



Faculteit Wetenschappen

Departement Chemie

**Numerical Modeling of a Hollow Cathode
Discharge**

**Numeriek Model van een Holle Kathode
Ontlading**

Proefschrift voorgelegd tot het behalen van de graad van
doctor in de Wetenschappen aan de Universiteit Antwerpen,

te verdedigen door

Neyda BAGUER

Prof. Dr. A. Bogaerts

Prof. Dr. R. Gijbels

Antwerpen 2005

Acknowledgements

Definitely a difficult part when writing a PhD thesis is the “Acknowledgements”. As it turns, it’s quite challenging to clearly and completely express in a few paragraphs so much received support, encourage, help, assistance and enlighten.

Immense gratitude goes to Prof. Annemie Bogaerts, in two parts, a) To Annemie, the friend, for your support and understanding, b) to Dr. A. Bogaerts for her constant guidance, creative inputs, always-insightful commentaries and immense effort in correcting my SpanGlish !!!.

I’m grateful as well, to Prof. Gijbels for giving me the opportunity of doing the PhD in your group and for your experienced guidance and confidence in my work.

I’m in debt to Prof. P. Van Espen who introduced me to Prof. Gijbels and Prof. Bogaerts and made possible the first step of this PhD thesis, which according to an old Chinese proverb it is already half the way. I also thank “Piet” for his kind support and friendship.

To see the discharge “on live” and to carry out some electrical and spectrometric measurements was possible thanks to the collaboration with Zoli Donko, from the Research Institute for Solid State Physics and Optics, Budapest, Hungary; who provided me with interesting and helpful discussion along all this years. I would like to thank as well his colleagues K. Kutasi, P. Hartmann and G. Bano for their help during the measurements.

The experimental work related to the Ar metastable population was carried out at the Laboratoire de Spectrometrie Physique from the Universite Joseph Fourier-Grenoble, France, thanks to the fructiferous collaboration with Prof. Nader Sadeghi and Dr. Z. Donko.

I’m grateful to M. Otte and his colleagues from University of Greifswald, Germany; for providing us the experimental data of the He discharge.

I would like to express my sincere thanks to Wim Goodheer for all the interesting and helpful discussions.

My gratitude to Prof. J. Broekaert for his interest in my work and useful advices.

Thanks to R. Capote for sharing with me his knowledge about Monte Carlo simulations as well as to L. Vincze.

I am most grateful to the help in software, programming languages and computer support provided by Hector, Koen and Luc.

All these years of hard work, long study hours, and difficult times would not have been bearable without the friendship and support of our research group colleagues and friends. Thanks to Min Yan, Ivan, Dieter, Miriam, Kathleen, Violeta, Chen, Liu, Erik, Andriy, Upendra, Igor, Vladimir and Misina.

Thanks Fabiana, Jasna and Gladis for all your support and encourage.

Thanks Nelly and Tania. Many thanks to Ingrid who wrote so efficiently the “Summary” of such complicated topic into “such complicated” language as it is Netherlands.

My gratitude to Martine Depauw for all her efficient work and kind support during my scholarships.

Finally, I want to express my “eternal” gratitude to my family: Gaby, Vicentico and Vicen, for being so patient, comprehensive and understanding. I sincerely apologize for all the time that I took from being with you !!! Thanks to my parents and sisters for all that support and encourage given at any time; no matter how far you were, you always managed to get here when I needed you.

Thanks also to those who were not directly related to this job, but in different ways contribute to it.

Many thanks to all of you,

Neyda

Wilrijk, October 2005

Table of Contents

| | | |
|---------|--|----|
| 1 | General introduction | 11 |
| 1.1 | Hollow cathode discharges..... | 11 |
| 1.1.1 | Applications | 12 |
| 1.2 | Modeling of hollow cathode discharges..... | 13 |
| 1.2.1 | Boltzmann kinetic equation's model | 13 |
| 1.2.2 | Fluid model | 15 |
| 1.2.3 | Fluid model in the drift and diffusion approximation..... | 16 |
| 1.2.3.1 | Local field approximation | 16 |
| 1.2.4 | Monte Carlo model..... | 17 |
| 1.2.5 | Particle-in-cell-Monte-Carlo model | 18 |
| 1.2.6 | Hybrid model | 18 |
| 1.3 | Aim of this Ph.D. thesis | 19 |
| 1.4 | References..... | 20 |
| 2 | Description of the hybrid model..... | 25 |
| 2.1 | Introduction..... | 25 |
| 2.2 | Assumption of the model | 26 |
| 2.3 | Monte Carlo models | 29 |
| 2.3.1 | Monte Carlo model for fast electrons | 29 |
| 2.3.2 | Monte Carlo model for fast Ar ⁺ ions and fast Ar ^f atoms | 32 |
| 2.3.2.1 | Monte Carlo model for fast Ar ⁺ ions | 32 |
| 2.3.2.2 | Monte Carlo model for the fast Ar atoms | 35 |
| 2.3.3 | Monte Carlo model for fast Cu atoms (sputtered atoms)..... | 36 |
| 2.3.4 | Monte Carlo model for fast Cu ⁺ ions..... | 39 |
| 2.4 | Fluid models..... | 45 |
| 2.4.1 | Fluid model for slow electrons and carrier gas ions | 45 |
| 2.4.2 | Fluid model for the metastable gas atoms | 48 |
| 2.4.2.1 | Fluid model for the He ^m metastable atoms | 48 |
| 2.4.2.2 | Fluid model for the Ar ^m metastable atoms | 50 |
| 2.4.3 | Fluid model for the Cu ⁺ ions and Cu atoms..... | 53 |
| 2.5 | Coupling of the Models..... | 55 |
| 2.6 | References..... | 61 |

| | | |
|-------|--|-----|
| 3 | Fundamental electric and spectrometric characteristics of the HCD..... | 67 |
| 3.1 | Introduction..... | 67 |
| 3.2 | Geometry and discharge conditions | 67 |
| 3.3 | Experimental set up..... | 68 |
| 3.4 | Electrical conditions and emission intensities | 69 |
| 3.5 | Calculated quantities as a function of discharge conditions | 74 |
| 3.5.1 | Electron collision rates | 76 |
| 3.5.2 | Charged particle densities | 78 |
| 3.5.3 | Electric potential | 79 |
| 3.5.4 | Electric field..... | 80 |
| 3.6 | Influence of the bottom and top of the hollow cylinder | 82 |
| 3.6.1 | Cathode bottom | 82 |
| 3.6.2 | Anode..... | 83 |
| 3.7 | Conclusions..... | 85 |
| 3.8 | References..... | 86 |
| 4 | Study of the He-Ni HCD: Relevance of the He metastable atoms | 89 |
| 4.1 | Introduction..... | 89 |
| 4.2 | Geometry and discharge conditions | 90 |
| 4.3 | Collision rates | 91 |
| 4.3.1 | Comparison to the asymmetric HCD configuration | 92 |
| 4.3.2 | Collision processes at the anode region..... | 95 |
| 4.3.3 | Contribution of the different ionization sources to the total ionization rate..... | 95 |
| 4.3.4 | Excitation rates and line intensities distribution..... | 96 |
| 4.4 | Electron, ion and metastable densities..... | 98 |
| 4.4.1 | Production and loss processes determining the He ^m metastable atom density | 100 |
| 4.4.2 | He ^m metastable atoms: their role in the electrical discharge properties..... | 100 |
| 4.5 | Potential and electric field distribution..... | 101 |
| 4.6 | Conclusions..... | 104 |
| 4.7 | References..... | 105 |
| 5 | Role of the fast Ar atoms and Ar ⁺ ions in a hollow cathode glow discharge.. | 109 |
| 5.1 | Introduction..... | 109 |

| | | |
|---------|---|-----|
| 5.2 | Ionization collision rate | 111 |
| 5.2.1 | Relative contribution of the various ionization processes to the total ionization..... | 111 |
| 5.2.2 | Heavy particle ionization collisions in the CDS..... | 111 |
| 5.2.3 | Pressure and current dependence..... | 113 |
| 5.2.4 | Influence of the heavy particles ionization collisions on the discharge parameters | 115 |
| 5.2.4.1 | Current-voltage characteristic | 115 |
| 5.2.4.2 | Charge density distribution..... | 115 |
| 5.3 | Mean energy of the fast electrons, fast Ar ⁺ ions and fast Ar atoms..... | 118 |
| 5.4 | Ar ⁺ ion flux at the CDS-NG interface | 121 |
| 5.5 | Conclusions | 124 |
| 5.6 | References | 125 |
| 6 | Study of the Ar ^m metastable atom population in a hollow cathode discharge by means of a hybrid model and spectrometric measurements | 129 |
| 6.1 | Introduction | 129 |
| 6.2 | Experimental set-up | 130 |
| 6.3 | Calculated two-dimensional Ar ^m metastable atom density profiles | 133 |
| 6.4 | Comparison between calculated and measured metastable density..... | 136 |
| 6.5 | Production and loss processes determining the Ar ^m metastable atom density | 141 |
| 6.6 | Influence of the electron quenching rate coefficient | 145 |
| 6.7 | Influence of the electron, fast Ar ⁺ ion and fast Ar ^f atom impact excitation cross sections..... | 147 |
| 6.8 | Discrepancy between experiment and model in the CDS..... | 150 |
| 6.9 | Conclusions | 151 |
| 6.10 | References | 152 |
| 7 | Study of the sputtered Cu atoms and Cu ⁺ ions in a hollow cathode glow discharge using a hybrid model..... | 157 |
| 7.1 | Introduction..... | 157 |
| 7.2 | Fluxes of bombarding species at the cathode | 160 |
| 7.3 | Flux of sputtered atoms | 162 |
| 7.4 | Density of the Cu atoms | 167 |
| 7.5 | Ionization processes of Cu atoms | 173 |

| | | |
|-----|--|-----|
| 7.6 | Density of the Cu ⁺ ions | 178 |
| 7.7 | Conclusions | 182 |
| 7.8 | References | 183 |
| 8 | Influence of the gas flow on the sputtered atoms and the deposition flux | 187 |
| 8.1 | Introduction | 187 |
| 8.2 | Gas flow inside the HCD | 189 |
| 8.3 | Effect of gas flow on the sputtered atom behavior | 192 |
| 8.4 | Conclusion | 200 |
| 8.5 | References | 201 |
| | Summary & Conclusions | 205 |
| | Samenvatting & Besluit | 215 |
| | Appendix..... | 225 |
| | a) Publications..... | 225 |
| | b) Contributions at Conferences..... | 226 |
| | c) Scientific Visits..... | 227 |

Chapter 1

General introduction

In the present chapter the distinctive characteristics of the hollow cathode discharge, i.e., the so-called “hollow cathode effect” and the “pendulum effect” are described as well as the geometric configurations of conventional hollow cathode discharges, its operating conditions, and applications fields. A short overview is given of the basic kinetic description of the plasma and how to obtain the macroscopic fluid equations of the plasma from the microscopic kinetic equations. Moreover, the different approaches used to model glow discharge plasmas are mentioned, i.e., models based on the solution of the kinetic Boltzmann equation, on the moments of the Boltzmann equation (fluid model of the plasma), particle approaches, like Monte Carlo and particles-in-cell models, and the hybrid approach, which is a combination of the fluid and Monte Carlo models.

1 General introduction

1.1 Hollow cathode discharges

The cylindrical hollow cathode discharge (HCD) is a kind of glow discharge and it was first used by Paschen for the study of helium spectral lines.¹ In a HCD, the cathode is wrapped onto itself to form a hollow cylinder. For the study of conventional (cylindrical) HCDs, two glow discharge regions are the most important: a dark space adjacent to the cathode surface, where the electric field is strong, which is called the cathode dark space (CDS) or sheath, and a rather luminous part beyond it, where the field is weak and which is called the negative glow (NG) or plasma region. Hence the plasma and sheath region are surrounded by the cathode surface. The cathode can be built in different shapes, for example as a spherical segment or as a pair of plane parallel plates or as a hollow cylinder. The anode (or anodes) is placed mostly at the ends of the cathode cylinder and can be chosen in different shapes, such as a disc, a ring, a cylinder, etc. If the distance between the anode and cathode is larger than the cathode region (i.e., CDS plus NG) for a given pressure, a positive column can be formed (PC).² Usually the anode (or anodes) is placed at such a distance from the cathode that no positive column can be formed and that the NG can be confined inside the discharge cavity.

A glow discharge is sustained by the cathode emission of secondary electrons and by the creation of new charged particles as results of electron, ion and metastable atom ionization collisions inside the discharge. The emitted secondary electrons are accelerated in the strong electric field of the CDS to high energies, and ionize the neutrals there, creating a new pair of charged particles. The latter also gain energy from the electric field and therefore are able to induce new ionization collisions. Because the electrons move again in the direction of the electric field, and because of their low mass, they lose only a small amount of energy in collisions, and therefore they propagate to the region of low electric field (i.e., to the NG) having still enough energy to induce there inelastic collisions. Moreover, in the case of the HCD, some of these electrons can penetrate into the CDS opposite to the cathode of their origin (“pendulum effect”)^{3,4} and cause ionization collisions there, which enhance even more the avalanche of high energetic particles.

The operating voltage of the HCD is lower than in a glow discharge with single planar cathode for the same current density. Moreover, the voltage-current dependence

shows two different regions: one with a steep slope at low current and the other with a smaller slope at higher current.

The most specific characteristic of the HCD is the so-called “hollow cathode effect”⁵ i.e., a large increase in the current density and light intensity, which is observed when the distance between the opposite cathode surfaces and the gas pressure are set in a way that the NG regions from facing cathode surfaces overlap.

These properties are mostly due to the very efficient use of the fast electrons and ions in the HCD.⁶⁻⁸ Indeed, most of the ions, which usually get lost at the boundaries of the NG with the anode and with the surrounding walls in the case of a plane cathode, can reach here the surface of the cathode and release more electrons. In the case of the fast electrons, their loss is also considerably reduced due to the “pendulum effect”. Moreover, some of these electrons penetrate into the dark space opposite to the cathode of their origin and cause ionization collisions there. The new electrons thus created will also be accelerated in the high CDS field, and they generate new electrons, so that an enhanced ionization rate in the CDS as well as in the NG is obtained.

Conventional HCDs usually operate⁹⁻¹¹ at pressures up to 10 Torr, with a cathode voltage ranging from 200 to 500 Volt and a discharge current from a few mA up to 1 A.

1.1.1 Applications

HCDs are used for a wide variety of applications, for example in plasma processing (ion etching, thin film deposition, surface treatment),¹²⁻¹⁵ in ion gas lasers¹⁶⁻¹⁹ and in spectroscopic analysis, where the hollow cathode is used as an emission source, allowing direct excitation and analysis of samples, or as a light source in absorption spectrometry because of its sharp and intense spectral lines.^{9,11,20,21}

To improve the results in these application fields, it is important to understand the different mechanisms involved in the discharge. This can be achieved by numerical modeling.

For example, in the specific case of atom emission spectroscopy, when the spatial distribution of the analyte can be inferred from the model results, better spectral line emission intensities can be archived.^{22,23}

For depth profiling analysis, this kind of modeling work shows that the variation of the depth profile can be a consequence of the change in the bombarding, sputtered and deposition fluxes and not necessarily to a change in sample composition, etc.

For deposition reactors the present simulation can help to find optimal geometries and conditions, as it gives the deposition profile. Moreover, since the growth and adhesion of the film depends on the energy of the sputtered particles upon arrival at the substrate, which is calculated in the model, this kind of work makes it possible to predict (and improve) the quality of the film growth.²⁴

Also in the metal vapor and metal vapor-ion laser technology, where the sputtered atoms and the corresponding ions constitute the active medium, it is useful to know their density distribution as well as the density distribution of the metastable atoms and ions from the carrier gas, in order to optimize the lasing transitions and therefore to improve the laser construction.²⁵

1.2 Modeling of hollow cathode discharges

Numerical simulations are very useful in areas where the gap between theory and experiment is large. The first step to study a physical phenomenon by means of computer simulations is to find a mathematical model to represent most of the properties of the physical phenomenon of interest. The continuous equations of the mathematical model have to be converted through different skins into discrete algebraic equations, for which a numerical solution can be found. I.e., continuous variables of the mathematical model are replaced by an array of values, and differential equations by algebraic equations.²⁶

The glow discharge gas can be considered as weakly ionized plasma, in which the temperature of the electrons is considerably higher than the other species present in the discharge. In general, plasma is considered as a quasineutral gas of charged and neutral particles, which exhibits a collective behavior, i.e., the motion depends not only on local conditions but on the state of the plasma in remote regions.²⁷

Different kinds of numerical models are used to describe the behavior of the plasma in glow discharges: models based on the solution of the kinetic Boltzmann equation, fluid models and particles models, such as Monte Carlo and particle-in-cell simulations. In the following these models will be briefly described focusing on the advantages and disadvantages.

1.2.1 Boltzmann kinetic equation's model

The basic description of the plasma lies in the kinetic theory.²⁸ One defines a distribution function for each gas constituent, depending of position, velocity and time $f(\vec{r}, \vec{v}, t)$, such that $f d\vec{r} d\vec{v}$ is the probability of finding particles within the six-

dimensional volume element $d\vec{r}d\vec{v}$ centered at the point (\vec{r}, \vec{v}) . Observable properties of the plasma can be obtained by taking various velocity moments of the distribution function $f(\vec{r}, \vec{v}, t)$. For example, the particle density, n , mean velocity, \vec{u} , and particle flux density, \vec{j} , in the volume element $d\vec{r}$, are defined as:

$$n(\vec{r}, t) = \int f(\vec{r}, \vec{v}, t) d\vec{v}$$

$$\vec{u}(\vec{r}, t) = \frac{\int \vec{v}f(\vec{r}, \vec{v}, t) d\vec{v}}{\int f(\vec{r}, \vec{v}, t) d\vec{v}} = \frac{\int \vec{v}f(\vec{r}, \vec{v}, t) d\vec{v}}{n(\vec{r}, t)}$$

$$\vec{j}(\vec{r}, t) = en\vec{u} = e \int \vec{v}f(\vec{r}, \vec{v}, t) d\vec{v}$$

Considering that the number of particles in the volume will change in time as dn/dt , then the rate of change of the number of particles will be given by the flux of particles through the surfaces of the volume element:

$$\frac{\partial}{\partial t} \int f(\vec{r}, \vec{v}, t) d\vec{r}d\vec{v} = - \int f\vec{v}d\vec{S}_r d\vec{v} - \int f\vec{a}d\vec{r}d\vec{S}_v$$

where $\vec{a} = \vec{F}/m$, is the acceleration that the particles experience due to the action of a total force F (The sum of external and internal forces). Applying Gauss' theorem, taking in account that r and v are independent variables and that the volume is arbitrary in the space $\vec{r} \vec{v}$. We obtain the kinetic equation for the distribution function of the particles in the element of volume $d\vec{r}d\vec{v}$ of the six-dimensional space.

$$\frac{\partial}{\partial t} f + \vec{v} \cdot \frac{\partial}{\partial \vec{r}} f + \frac{\partial}{\partial \vec{v}} \vec{a} f = 0 \quad (1.1)$$

The field depends on f and its evaluation therefore requires a self-consistent solution of the kinetic equation for each kind of particles present in the plasma. The average electric field due to the charged particles can be expressed through f . This relation is given by the Poisson's equation:

$$\vec{\nabla} \cdot \vec{E} = \frac{\rho}{\epsilon_0} = \frac{1}{\epsilon_0} \sum_i e_i \int f d\vec{v}$$

However, the field due to the internal forces cannot be easily represented because of the strong fluctuation of the internal forces. Hence the total rate of change of the number of particles in time will be taken as the sum of two terms: one due to the action of the external force (in our case only the electric force is considered), and the other due to the internal forces (i.e., collisions between the particles).

$$\frac{\partial f}{\partial t} = \left(\frac{\partial f}{\partial t} \right)_{ext} + \left(\frac{\partial f}{\partial t} \right)_{coll}.$$

Then the kinetic equation can be re written as:

$$\left(\frac{\partial f}{\partial t} \right)_{ext} + \vec{v} \cdot \frac{\partial f}{\partial \vec{r}} + \frac{e\vec{E}}{m} \frac{\partial f}{\partial \vec{v}} = \left(\frac{\partial f}{\partial t} \right)_{coll} \quad (1.2)$$

The form of the collision term depends upon the assumptions made about the collisions. The best known is the Boltzmann collision integral, which is based on random binary collisions. To solve the Boltzmann kinetic equation it is necessary to know the

form of the collision term $\left(\frac{\partial f}{\partial t} \right)_{coll}$, which is for any realistic model a complicated function of f .

Simulation models based on the solution of the Boltzmann kinetic equation²⁹⁻³¹ are capable to calculate the electron energy distribution function and therefore give a self-consistent electric field distribution. However, the models become computationally too expensive, especially for calculations lasting for a longer time than a few collisions. Moreover the coupling of Boltzmann equation to the Poisson's equation is a difficult numerical problem. One approach to deal with this problem is the fluid model of the plasma.

1.2.2 Fluid model

The fluid model is a hydrodynamic model of the plasma. It considers the plasma as a continuum, which is characterized by macroscopic, ensemble-averaged variables, like temperature and pressure. The transport of this continuum is described by solving, for each sort of particles, a set of moment equations. These macroscopic equations are obtained from the Boltzmann collisional kinetic equation by multiplying with n , nv , nvv , etc and integrating over velocity space, i.e., in a similar way as the macroscopic variables like density n and mean velocity u were obtained from the distribution function $f(r, v, t)$. The zeroth-moment equation (nv^0) expresses the conservation of mass (charge), the first-moment equation (nv^1), expresses the momentum density conservation and the second-moment equation (nv^2) expresses the energy conservation. With this procedure the one equation for the distribution function $f(\vec{r}, \vec{v}, t)$, which describes the particles behavior in a six-dimensional space is replaced by a set of equations for quantities defined in a three-dimensional space: the moment equations.

Each moment equation has a term involving higher moments, which makes it necessary to perform some approximations in order to close the equations set. This is only possible if we assume that the fluid is in hydrodynamic equilibrium, then the velocity distribution is isotropic in the velocity space and can be assumed Maxwellian, therefore the pressure tensor becomes scalar that can be expressed through the temperature $p = p(\rho, T)$. Hence the transport of each fluid can be described by the first three moment equations. However, by assuming an isotropic velocity distribution the average velocity, u , becomes zero and then the flux density $j = nu$, must be zero. This is not valid for glow discharges, where a flux of charged particles to each electrode is present.

1.2.3 Fluid model in the drift and diffusion approximation

In the drift and diffusion approximation of the fluid model, it is assumed that the velocity distribution of each kind of charged particle is isotropic in the direction perpendicular to the flux. The dependence of the distribution function f with respect to the velocity is then expanded in the first two terms of the Legendre polynomials where the two-term truncation of the spherical-harmonics expansion is applied. Substituting f in the kinetic Boltzmann equation (eq.1.2) in which the collision term is given by the Boltzmann collision integral and after handling this integro-differential equation in a proper way (see for example, page 549-552 from appendix B of Ref. 32), we obtain the continuity equation in which the particle flux is expressed as a linear combination of the drift due to the electric field and diffusion due to the density gradient: $\vec{j} = n\vec{u} = e\mu n\vec{E} - D\nabla n$, where μ is the mobility and D is the diffusion coefficient. In that case the momentum balance equation is disregarded and replaced by the flux equation. However, the transport coefficients μ and D , which depend on the local velocity distribution function f , should be calculated.

1.2.3.1 Local field approximation

In order to calculate the mobility and diffusion coefficients, which are a function of the velocity distribution, it is assumed that the local velocity of each fluid is in hydrodynamic equilibrium with the local electric field.³² I.e., the velocity distribution of each kind of charged particles is assumed to be the equilibrium velocity distribution of the particles in a uniform dc electric field. Therefore, the mobility and diffusion coefficients are supposed to be functional of the electric field and to be the same as if

they were measured or calculated under an equivalent but uniform electric field. Hence, the energy balance equation is substituted by the assumption of the local field approximation and the transport of each fluid can be described by the continuity and flux equations.³² In the case of charged fluids, it is necessary to couple these equations with the Poisson's equation, $\vec{\nabla} \cdot \vec{E} = \frac{e}{\epsilon_0} (n_+ - n_-)$, in order to calculate the electric field.

Then the relevant equations for each fluid are:

$$\frac{\partial n}{\partial t} + \vec{\nabla} \cdot \vec{j} = S$$

$$\vec{j} = \pm \mu n \vec{E} - D \vec{\nabla} n$$

The fluid model in the local field approximation has been used in a number of numerical models.³³⁻³⁵ The main advantage of fluid simulations is that they can be computationally efficient. However, the electron velocity distribution function at high energies is not in equilibrium with the local electric field. In the CDS due to the high field and large field gradient, the energy gained by the electrons from the field is not locally balanced by the energy lost through collisions, so that a flux of high-energy electrons can enter the NG, where they will produce inelastic collisions in spite of the weak electric field. Hence for the energetic tail of the electron velocity distribution the hydrodynamic equilibrium approach is not valid. When using such a model the ionization rates, especially by electron impact collisions, which are the main component of the source term of the continuity equations, are not very reliable. This can be accurately calculated with a Monte Carlo model.

1.2.4 Monte Carlo model

The MC simulations³⁶⁻³⁹ can be used to handle situations characterized by strong thermal non-equilibrium, such as for the description of the fast electrons all over the discharge. The particles are followed one after another and the collision rates are calculated based on the energy-dependent cross sections and random numbers. Hence, an accurate energy distribution function of the particles can be calculated. The dynamics of the particles are determined by Newton's law of motion: $m_i \frac{dv}{dt} = q_i \vec{E}$, where m_i and q_i are the mass and the charge of the particle i , respectively, and E is the electric field strength. The velocity of the particles is determined from the integral of motion. The particle position is calculated from the integration of the velocity equation. However, a

MC model is not self-consistent, because the electric field is not calculated in the model, but needs to be given as input.

1.2.5 Particle-in-cell-Monte-Carlo model

With the particle-in-cell-Monte-Carlo (PIC-MC) method,⁴⁰⁻⁴² the problem can be solved self-consistently. The collision rates are calculated based on the energy-dependent cross sections, and the particle energy is calculated from the electric field, which is obtained self-consistently from Poisson's equation using the charged species densities. This method is very time-consuming because a large number of particles should be followed for statistically valid results.⁴³

1.2.6 Hybrid model

Another way of solving the problem self-consistently is the so-called hybrid model⁴⁴⁻⁴⁹ e.g., a MC model combined with a fluid model, (i.e., a transport model, where the Poisson equation is solved together with the continuity and flux equations for ions and electrons, see above). Such a hybrid model combines the advantages of both methods, Indeed, the source terms for the continuity equations in the fluid model are taken from the collision rates, which are calculated in the MC models, based on the energy-dependent cross sections, while the particle energy is calculated from the electric field, and this approach is considerably faster than a PIC-MC model.^{43,50} The hybrid approach was used to describe the plasma behavior, and the behavior of the sputtered species in HCD's, for example in Ref. 51, for a segmented HCD and in Ref. 52 for a longitudinal HCD, respectively. These models were concerned with modified HCD configurations, which operate at higher pressures and currents than conventional HCD's.⁷ In the present work we will study, by means of a hybrid model the cylindrical HCD. This approach will allow us to calculate in a self-consistent manner, the electric field and the energy distribution functions of the energetic particles, which is not only crucial for the correct description of the electrical properties of the discharge but also for the description of the sputtering. Hence, a better description of excitation and ionization processes of the gas and sputtered atoms can be achieved, which is crucial for application purposes.

1.3 Aim of this Ph.D. thesis

The aim of the present work is to study the cylindrical HCD by means of a hybrid model. In order to check the validity of the model, some calculated results will be compared to experimental data, obtained for the same or very similar discharge conditions and geometric configuration.

In this thesis, we will focus in the processes determining physical and spectrometric discharge properties as well as processes important for the sputtering of the cathode.

The first part of the work is concerned to the study of the electrical and spectrometric characteristic (voltage-current dependence, excitation and ionization rate, etc) of the HCD. Special attention will be given to explore conditions at which the hollow cathode effect is observed. In order to investigate the influence of discharge geometry and filling gas, the model will be applied to the two most frequently used geometry configuration.

In the second part, all the fast particles, whose collision processes are relevant for the production of charged particles and/or for the cathode sputtering, will be followed with a MC approach. Therefore, the influence of fast gas ions and atoms and metal atoms and ions in the calculation of the charged density and electric field distribution can be inferred. Moreover, as the flux energy distribution of the particles bombarding the cathode is calculated, the sputtering can be accurately described as well as the interaction of the sputtered atoms with the plasma species. Also we will investigate how the gas flow affects the sputtered atom density profiles and the fluxes, which is important for sputter deposition applications. Finally, special attention will be paid to the study of the metastable atoms in He and Ar HCDs.

In that way we are able to present an overall picture of the discharge, in which the main physic and chemistry aspect of the HCD are considered.

1.4 References

- ¹ F. Paschen, *Ann. d. Phys.* **50** 901 (1916).
- ² A. von Engel, *Ionized gases* (Claredon, Oxford, 1965).
- ³ A. Guntherschulze, *Zeitschr. f. Phys.* **19**, 313 (1923).
- ⁴ A. Guntherschulze, *Zeitschr. f. Phys* **2**, 49 (1930).
- ⁵ P. F. Little and A. von Engel, *Proc. R. Soc. London A* **224**, 209 (1954).
- ⁶ H. Helm, *Z. Naturf.* **27a**, 1812 (1972).
- ⁷ R. R. Arslanbekov, A. A. Kudryavtsev and R. C. Tobin, *Plasma Sources Sci. Technol.* **7**, 310 (1998).
- ⁸ V. I. Kolobov and L. D. Tsendin, *Plasma Sources Sci. Technol.* **4**, 551 (1995).
- ⁹ P. J. Slevin, W. W. Harrison, *Appl. Spectr. Reviews* **10**, 201 (1975).
- ¹⁰ K. Rozsa, *Z. Naturf.* **35a**, 649 (1980).
- ¹¹ S. Caroli, *Prog. Analyt. Atom. Spectrosc.* **6**, 253 (1983).
- ¹² D. M. Manos and D. L. Flamm, *An Introduction to Plasma Etching* (Academic, New York, 1989).
- ¹³ A. Goldamn and J. Amoroux, *Gases: Macroscopic Processes and Discharges* (Plenum Press, New York, 1983).
- ¹⁴ H. Baránková and L. Bárdos, *Surf. Coat. Technol.* **163-164**, 649 (2003).
- ¹⁵ Z. Hubicka, M. Cada, Z. Potucek, P. Ptacek, H. Síchová, Z. Málková, L. Jastrabík and B. Trunda, *Thin Solid Films* **447-448**, 656 (2004).
- ¹⁶ K. Rozsa, *Z. Naturforsch.* **35a**, 649 (1980).
- ¹⁷ D. C. Gerstenberger and R. Solanki, J.G. Collin, *IEEE J. QuantElectron.* **16**, 820(1980).
- ¹⁸ I. G. Ivanov, E. L. Latush and M. F. Sem, *Metal Vapour Ion Lasers: Kinetic Processes and Gas Discharges* (Wiley & Sons Ltd, Chichester, 1996).
- ¹⁹ N. K. Vuchkov, K. A. Temelkov and N. V. Sabotinov, *IEEE J. Quantum Electron* **35**, 1799 (1999).
- ²⁰ C. Scheperrs and J. A. C. Broekaert, *J Anal. At. Spectrom* **15**, 61 (2000).
- ²¹ C. Yang and W. W. Harrison, *Spectrochim. Acta Part B* **56**, 1195 (2001).
- ²² M. A. Dempster and R. K. Marcus, *Spectroch. Acta B* **55**, 599 (2000).
- ²³ F. Chen and J. C. Williams, *Ana. Chem.* **62**, 489 (1990).
- ²⁴ A. Bogaerts, A. Okhrimovskyy, A. Bagger, *Plasma Source, Sci. Technol.* **14**, 191 (2005).
- ²⁵ G. Bano, L. Szalai, P. Horvath, K. Kutasi, Z. Donko, K Rozsa, T. M. Adamowicz, *J. Appl. Phys.* **92**, 6372 (2002).
- ²⁶ F.W. Hockney and J. W. Eastwood, *Computer simulation using particles* (Adam Hilger, Bristol, 1988).
- ²⁷ R.J.Goldston, and P. H.Rutherford, *Introduction to plasma physics and controlled fusion, Vol. 1* (Plenun, NY, 1984)

-
- ²⁸ T. J. M. Boyd and J. J. Sanderson, *Plasma Dynamics* (Nelson LTD, London, 1969)
- ²⁹ T. J. Sommerer, W.N. G. Hitchon, R. E. P. Harvey and J. E. Lawler, *Phys. Rev. A* **43**, 4453 (1991).
- ³⁰ Y. A. Mankelevich, A. T. Rakhimov and N. V. Suetin, *IEEE Trans. Plasma Sci.* **19**, 520 (1991).
- ³¹ W. P. Allis, G. Fournier and D. Pigache, *J. Phys.* **38**, 915 (1977).
- ³² I. P. Shkarofsky, T. W. Johnston and M.P. Bachiynski, *The Particle Kinetic of the Plasma* (Wesley, Reading (MA), 1966).
- ³³ J. P. Boeuf, *Phys Rev.* **36**, 2782 (1987).
- ³⁴ J. P Boeuf, *J. Appl. Phys.* **63**, 1342 (1988)
- ³⁵ D. Paschier and W. J. Goedheer, *J. Appl. Phys.* **74**, 3744 (1993).
- ³⁶ A. Tran Ngoc, E. Marode, P. C. Johnson, *J. Phys. D* **10**, 2317 (1977).
- ³⁷ M. J. Kushner, *J. Appl. Phys.* **54**, 4958 (1983).
- ³⁸ A. Bogaerts, M. van Straaten, R. Gijbels, *Spectrochim. Acta Part B* **50**, 179 (1995).
- ³⁹ Z. Donko, K. Rozsa and R. C. Tobin, *J. Phys. D* **29**, 105 (1996)
- ⁴⁰ M. Surendra, D. B. Graves, *IEEE Trans. Plasma Sci.* **PS-19**, 144 (1991).
- ⁴¹ H.B. Smith, C. Charles, R. W. Boswell and H. Kuwahara, *J. Appl. Phys.* **82**, 561 (1997).
- ⁴² C. K. Birdsall, *IEEE Trans. Plasma Sci.* **19**, 65 (1991).
- ⁴³ H. C. Kim, F. Iza, S. S. Yang, M. Radmilovic and J. K. Lee, *J. Phys. D* **38**, R283 (2005).
- ⁴⁴ M. Surendra, D. B. Graves, G. M. Jellum, *Phys. Rev. A* **41**, 1112 (1990).
- ⁴⁵ J. P. Boeuf, L. C. Pitchford, *IEEE Trans. Plasma Sci.* **19**, 286 (1991).
- ⁴⁶ A. Bogaerts, R. Gijbels, W. J. Goedheer, *J. Appl. Phys.* **78**, 2233 (1995).
- ⁴⁷ A. C. Dexter, T Farrell, M I Lees, *J. Phys. D* **22**, 413 (1989).
- ⁴⁸ A. Bogaerts, R. Gijbels, W. J. Goedheer, *J. Appl. Phys.* **78**, 2233 (1995).
- ⁴⁹ A. Bogaerts, R. Gijbels, W. J. Goedheer, *Anal. Chem.* **68**, 2296 (1996).
- ⁵⁰ T. J. Sommerer, M. Kushner, *J. Appl. Phys.* **71**, 1654 (1992).
- ⁵¹ G. Bano, L. Szalai, P. Horvath, K. Kutasi, Z. Donko, K Rozsa, T. M. Adamowicz, *J. Appl. Phys.* **92**, 6372 (2002).
- ⁵² A. Bogaerts and R. Gijbels, *J. Appl. Phys.* **92**, 6408 (2002).

Chapter 2

Description of the hybrid model.

The hybrid model presented here comprises the principles of Monte Carlo and fluid simulations. In the Monte Carlo sub-models the fast electrons, fast gas and metal atoms and ions are treated individually as particles. Their trajectory and interactions are described by the classical Newton laws of movements and by the energy-dependent collision cross sections, respectively. In the fluid sub-models, the slow electrons, slow ions (gas and metal), metastable atoms and metal atoms are treated as a continuum. In the fluid formalism the behaviour of this continuum is described by the continuity and flux equations. In the case of charged particles, these transport equations are solved together with the Poisson's equation in order to obtain the electric field distribution. Typical results from the MC models are, among others, the fast atom, fast ion and fast electron collision rates and the respective energy distribution function and fluxes. With the fluid models, on the other hand, the atom and ion density and flux distributions as well as the electric field profile can be obtained. By coupling those models, the main properties of the hollow cathode discharges, as well as the behavior of the plasma and the sputtered species are described self-consistently. This is so, because the source terms for the continuity equations in the fluid sub-models are taken from the collision rates, which are calculated mainly in the MC models, based on the energy-dependent cross sections, while the particle energy is calculated from the electric field strength, calculated in the fluid model for charged particles.

2 Description of the hybrid model

2.1 Introduction

The hybrid model¹⁻⁶ presented here is a combination of two models: Monte Carlo and fluid models. In the CDS the condition for equilibrium approach is not fulfilled for electrons due to the high electric field and the large field variation over the electron mean free path. Indeed, the energy gained by electrons from the field is not locally balanced by the energy lost through collisions. Hence a flux of high-energy electrons will enter the NG, producing inelastic collisions. For these high-energy electrons a microscopic model based on a three-dimensional Monte Carlo method is used in the entire discharge (CDS and NG).

The slow electrons in the NG, the positive gas and metal ions and the metal atoms, in the whole discharge are treated with a classical equilibrium approach, i.e., the fluid model of the plasmas. In the fluid model the transport of particles is represented by the continuity and flux equations. The drift velocity and diffusion coefficients of the transport equations are supposed to be functionals of the local electric field, and thus they can be calculated using an equivalent but uniform electric field (i.e., local field approximation). This is valid when:⁷ $\lambda \gg \lambda_c$ and $\tau \gg \tau_c$, i.e., the characteristic length (λ) and the time (τ) over which the plasma quantities change considerably, should be much larger than the mean free path (λ_c) and the collision time (τ_c). In our case this is true for the slow electrons, in the negative glow, which is the only region where they are present and for the gas and metal ions through the entire discharge. It should be mentioned that at the CDS, close to the CDS-NG interface, in a region of a length around 3 to 5 times of the gas ion mean free paths, the variation of the electric field over the ion mean free path is not so small. However, keeping in mind that for the present discharge conditions, the ratio of CDS length to the average gas ions mean free path, varies from 80 to 300,⁸ the local field approximation can be assumed valid all over the CDS and therefore over the complete discharge volume.⁹

The model will be applied to the two most frequently used configurations of cylindrical HCD's:

- a) a HCD where the cathode cylinder is closed at one end, and at some distance from the open end, an anode is placed (asymmetric configuration, see Fig. 2.1a).

- b) a HCD where the cathode cylinder is open at both ends, close to which the anodes are located (symmetric configuration, see Fig. 2.1 b).

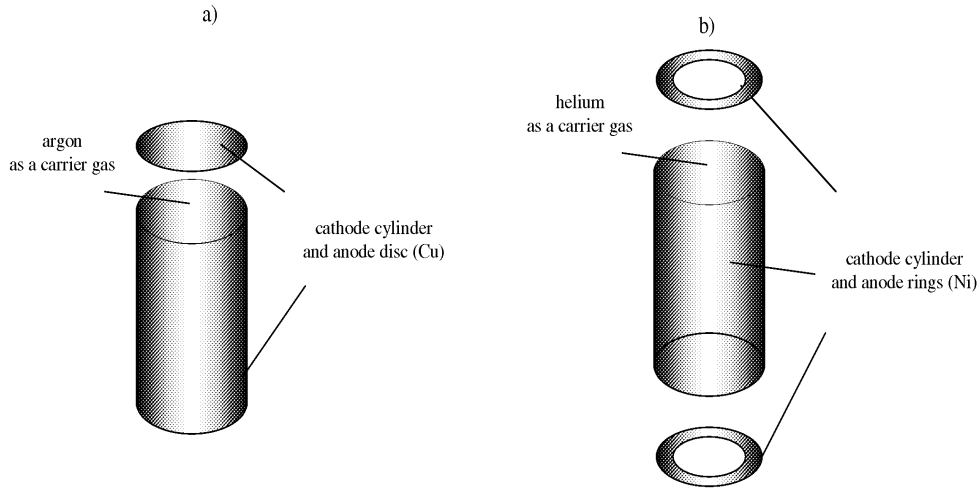


Fig. 2.1 Schematic picture of the HCD geometries simulated in the model: (a) symmetric configuration, Ar-Cu HCD, (b) asymmetric configuration, He-Ni HCD.

Moreover, also different cathode materials and background gases are used in the simulation. For the asymmetric HCD configuration (a) the cathode and anode were both made of copper and argon was the carrier gas, while for the symmetric HCD (b) nickel and helium were used instead. Here, these discharges will be termed as Ar-Cu HCD and He-Ni HCD, respectively.

2.2 Assumption of the model

1. The discharge gas is assumed to be at room temperature and uniformly distributed throughout the complete discharge, i.e., the thermal motion of the gas atoms is neglected.
2. Due to the low degree of ionisation of the discharge gas (around 10^{-4})¹⁰ the collision between the ions and electrons can be neglected, i.e., the movement of ions and electrons can be considered independent from each other, and treated separately in corresponding MC codes.¹¹

3. The species considered in the model are: neutral ground state gas atoms, metastable gas atoms, slow positive gas ions and fast and slow electrons. In the case of the Ar-Cu HCD, due to the efficient sputtering of the Ar gas, the species important for this process were also included, i.e., fast Ar atoms and Ar^+ ions, fast and slow Cu atoms and Cu^+ ions. Table 2.1 summarizes the different models used to describe the behavior of these species in the discharge.
4. The metastable levels have been combined into one collective level. This assumption was made because for our purpose only the total metastable density is important.
5. As fast particles are considered the particles for which it is necessary to get the energy distribution in order to accurately calculate the (inelastic or elastic) collision and/or sputtering rates.
6. The electrons are split up in two groups:¹² the fast electrons, with high enough energy to cause inelastic collisions, and the slow electrons, which do not have enough energy.
7. The Ar^f atoms are formed by elastic collisions of Ar^+ ions and Cu^+ ions with the background Ar gas and are assumed to have energies higher than 1 eV. The fact that we consider a fraction of the Ar atoms as fast particles, does not contradict the assumption that the gas is uniformly distributed throughout the discharge, because the fast Ar^f atom density is much lower (four orders of magnitude) than the density of the discharge gas.⁸ Nevertheless, these fast Ar^f atoms can be important in the discharge, because they play a role in ionization and excitation of Ar atoms and in the cathode sputtering
8. The fast Cu atoms (Cu^f) are the sputtered atoms from the cathode. Indeed the Cu atoms are emitted with an initial energy of several eV¹³ and they are considered as fast particles until they are thermalized, i.e., mainly due to elastic collisions with the background gas.
9. The fast Ar^+ and fast Cu^+ ions are considered in the cathode dark space (CDS), where these ions gain energy from the electric field and they are described through a Monte Carlo approach.
10. The plasma-surface interaction processes taken into account are: gas ion and metastable gas atom induced secondary electron emission from the cathode and secondary electron emission from the anode due to the arriving electrons. Beside

those processes, the cathode sputtering due to the bombarding flux of Ar^+ ions, fast Ar atoms and Cu^+ ions were also included for the Ar-Cu HCD discharge.

11. In order to obtain a better understanding of the HCD the model should be developed at least in two directions:

- The direction perpendicular to the cathode sidewalls, i.e., the radial direction, where the pendulum effect occurs. (See paragraph 1.1)
- The direction parallel to the cathode sidewalls, i.e. the longitudinal direction, in which the external discharge current will flow because of the position of the anode (anodes) at the open end (ends) of the cathode (see Fig. 2.1, above).

Table 2.1 Overview of the species incorporated in the model and the corresponding sub-models used to describe their behavior throughout the different regions of the HCD.

| Species followed | Sub-models | Discharge region |
|---|-------------|------------------|
| Fast electrons | Monte Carlo | CDS+NG |
| Fast gas ions (Ar^+ or He^+) | Monte Carlo | CDS |
| Fast gas atoms (Ar) | Monte Carlo | CDS+NG |
| Fast metal atoms (Cu) | Monte Carlo | CDS+NG |
| Fast metal ions (Cu^+) | Monte Carlo | CDS |
| Slow electrons | Fluid model | NG |
| Slow gas ions (Ar^+ or He^+) | Fluid model | CDS+NG |
| Metastable gas atoms (Ar^m or He^m) | Fluid model | CDS+NG |
| Slow metal atoms (Cu) | Fluid model | CDS+NG |
| Slow metal ions (Cu^+) | Fluid model | CDS+NG |

2.3 Monte Carlo models

2.3.1 Monte Carlo model for fast electrons

The model simulates the trajectories and collisions of electrons emitted by the cathode and the ones created within the discharge gap by ionization. Beside the new cascade electrons, created by electron impact ionization, also the electrons created by gas atom and gas ion impact ionization, metastable-metastable ionization and by Penning ionization collisions were followed (see below).

The electrons move under the influence of a spatially dependent electric field through a gas of neutral gas atoms, assumed to be at rest in comparison with the high speed of the electrons. The position at which the secondary electrons are ejected from the cathode is determined based on the flux distribution of the ion and metastable gas atoms to the cathode, obtained from the corresponding fluid model (see below paragraphs 2.4.1-2). The electrons are assumed to be emitted in the forward direction with an initial energy of 4 eV.¹⁴

In each time step the trajectory of the electron is calculated according to Newton's law:

$$x = x_0 + v_{0x} t - \frac{1}{2m_e} \bar{E}_{fr} \cos \alpha \Delta t^2 \quad (2.1) \quad v_x = v_{0x} - \frac{1}{m_e} \bar{E}_{fr} \cos \alpha \Delta t \quad (2.4)$$

$$y = y_0 + v_{0y} \Delta t - \frac{1}{2m_e} \bar{E}_{fr} \sin \alpha \Delta t^2 \quad (2.2) \quad v_y = v_{0y} - \frac{1}{m_e} \bar{E}_{fr} \sin \alpha \Delta t \quad (2.5)$$

$$z = z_0 + v_{0z} \Delta t - \frac{1}{2m_e} \bar{E}_{fz} \Delta t^2 \quad (2.3) \quad v_z = v_{0z} - \frac{1}{m_e} \bar{E}_{fz} \Delta t, \quad (2.6)$$

Where m_e is the electron mass, $\bar{E}_{fz}, \bar{E}_{fr}$ are the axial and radial electric field strength, α is the azimuthal angle of the radial position, m_e the electron mass, Δt the time interval and x, y, z (v_x, v_y, v_z) and x_0, y_0, z_0 (v_{x0}, v_{y0}, v_{z0}) are the positions (velocities) after and before Δt , respectively.

The probability of collision during the time step Δt is calculated by:

$$P = 1 - \exp\left(-\Delta s \left(n_g \sigma_j(\varepsilon) + n_m \sigma_{ion}^m(\varepsilon) + n_{sput} \sigma_{ion}^{sput}(\varepsilon)\right)\right) \quad (2.7)$$

where Δs is the distance traveled by an electron with energy, ε , during the interval Δt , and n_g , n_m , n_{sput} are the density of the discharge gas atoms in the ground and metastable state and of the ground state sputtered atoms, respectively. $\sigma_j(\varepsilon)$ is the electron impact cross sections of the “j” collisions with gas atoms in the ground state (elastic, excitation and ionization collisions). $\sigma_{\text{ion}}^m(\varepsilon)$ and $\sigma_{\text{ion}}^{\text{sput}}(\varepsilon)$ are the electron impact ionization cross sections of the collision with the carrier gas atoms in the metastable state and with sputtered metal atoms in the ground state, respectively. The calculated collision probability is compared with a random number (rn), uniformly distributed in the interval between 0 and 1. If $rn < P$, a collision occurs. To determine the kind of collision a second rn is generated and compared with the relative probability of each collision. Moreover, also electron impact excitation from the ground state gas atom to the metastable level is explicitly taken into account. Indeed, if an excitation collision happens, then the relative probability of the excitation to the metastable state to the total excitation ($P_{\text{em/et}}$) is calculated and compared with a rn ; if the $rn < P_{\text{em/et}}$ an excitation collision to the metastable level takes place. Table 2.2 summarizes all collision processes of the fast electrons included in the model for Ae-Cu HCD; while in Fig. 2.2 shows the corresponding collision cross sections (see below). Similarly, Table 2.3 and Fig. 2.3 show the corresponding reactions and the respective cross sections for the He-Ni HCD (see below).

After a collision, the new direction is determined by anisotropic scattering. The scattering angle χ and the azimuthal angle of scattering ϕ (i.e., in the center-of-mass system) are calculated using two rn and the electron angular differential cross section, $\sigma(\varepsilon, \chi)$. $\sigma(\varepsilon, \chi)$ was adopted from Ref. 15, where it was deduced based on the first Born approximation of the quantum elastic electron scattering theory, and assuming a screened Coulomb interaction potential.

$$rn = \frac{2\pi}{\sigma_j(\varepsilon)} \int_0^\chi \sigma(\varepsilon, \chi') \sin \chi' d\chi', \quad \chi = \arccos\left(1 - \frac{2rn}{1 + 8\xi(1-rn)}\right), \quad \xi = \frac{\varepsilon}{\varepsilon_0} \quad (2.8)$$

$$rn = \frac{1}{2\pi} \phi, \quad \phi = 2\pi rn \quad (2.9)$$

where $\sigma(\varepsilon)$ is the total electron scattering cross section, obtained upon integration of $\sigma(\varepsilon, \chi)$ over all possible χ , ξ is the dimensionless energy and $\varepsilon_0 = 27.21 \text{ eV}$ is the atomic unit of energy. $\sigma(\varepsilon, \chi)$ is assumed to be equal for all the analyzed electron collision

processes.¹ From these angles the new axial and azimuthal velocity angles (i.e., in the laboratory system) are found by transformation of the coordinate frame of reference.¹⁶

After each collision, the electron energy is calculated depending on the type of the collision. In the case of elastic collisions, the electron kinetic energy loss is assumed to be equal to the transfer energy in a binary encounter between two impenetrable spheres,¹⁷

$$\varepsilon = \varepsilon_0 \left(1 - 2 \frac{m_e}{m_{\text{gas}}} (1 - \cos \chi) \right) \quad (2.10)$$

In the inelastic collisions it is assumed that the energy exchange takes place between the projectile and the target atom orbital electron, and not to the atom as a whole, as it is assumed in elastic collisions.¹⁷ Hence, the kinetic energy loss in electron impact excitation and ionization collisions can be assumed to be equal to the excitation (ε_{exc}) and ionization (ε_{ion}) potential threshold of the target atom, respectively. The electron energy after excitation collisions is calculated as,

$$\varepsilon = \varepsilon_0 - \varepsilon_{\text{exc}} \quad (2.11)$$

In the case of electron impact ionization collisions, the resulting energy after the collision, $\varepsilon_0 - \varepsilon_{\text{ion}}$, is divided between the impacting electron (original) and the electron created in the ionization collision (emitted electron) based on the generation of a m as follows:

$$\varepsilon_{\text{ori}} = (\varepsilon_0 - \varepsilon_{\text{ion}})m, \quad \text{and} \quad \varepsilon_{\text{emi}} = \varepsilon_0 - \varepsilon_{\text{ion}} - \varepsilon_{\text{ori}} \quad (2.12)$$

If the differential energy ionization cross section ($\sigma_{\text{ion,diff}}$) is known the m can be defined as the probability that after the collision the original electron with an energy ε_0 will have an energy ε_{ori} :

$$m = \frac{\int_0^{\varepsilon_{\text{ori}}} \sigma_{\text{ion,diff}}(\varepsilon_0, \varepsilon') d\varepsilon'}{\sigma_{\text{ion}}(\varepsilon_0)} \quad (2.13)$$

and in this way, ε_{ori} can be obtained.

When the electrons collide at the anode they can be absorbed, reflected or produce secondary electron emission. The occurrence of one of these processes is decided based on the generation of a m and on the value of the secondary electron emission coefficient, δ . At the concerned energy range here (less than 300 eV) δ for Cu and Ni is less than 1.¹⁸ Then it is assumed that an electron emission happens when $\delta \leq m$. It was considered that 10% of the secondary electrons, are just the primary electrons, that where reflected from

the anode.¹⁹ In the opposite case, i.e., $\delta \geq m$, the impinging electron is assumed to be absorbed by the anode.

This procedure is repeated, until the electrons collide at the anode, or until the electrons are transferred to the slow group. Indeed, when the energy of the fast electrons drops below the energy of the lower threshold for inelastic collisions, they are transferred to the slow-electron group, because then, they are not capable of inelastic collisions. Hence they are not important as fast particles anymore and can be treated with the fluid model.

2.3.2 Monte Carlo model for fast Ar^+ ions and fast Ar^f atoms

Because the main production source of fast Ar atoms are the Ar^+ ion elastic collisions, (which include the symmetric charge transfer collisions), the fast Ar^+ ions and Ar^f atoms are followed in the same MC code. In the code they are treated separately, as independent particles, i.e., the movement equations, the collision rates, the time step, etc, are defined separately for the ions and fast atoms. The advantage of this way is the reduction in computer time and memory, as all the energy and coordinate data of the new particle are stored only during the complete cycle in time for each ion.

2.3.2.1 Monte Carlo model for fast Ar^+ ions

The MC simulation of the Ar^+ ions is done in a similar fashion as for the electrons, but the ions are followed only as fast particles inside the CDS. The ions start at the CDS-NG boundary, or within the CDS, with an assumed initial energy of 0.04 eV, which correspond to the assumed temperature of the discharge gas (i.e., 300 K) and a velocity direction parallel to the electric field. For the Ar^+ ions starting at the CDS-NG interface, the initial position is determined from the radial and axial ion flux diffusing from the NG to the CDS, calculated in the charged particle fluid model (see paragraph 2.4.1). As a result of the electron impact ionization and metastable-metastable ionization collisions, also some Ar^+ ions are created inside the CDS. The initial position of these ions is obtained from the corresponding ionization rates (calculated in the fast electron MC model (see above, 2.3.2.1) and in the fluid model for metastable atoms (see below, 2.4.2), respectively). Also the new Ar^+ ions created as a result of the Ar^+ ion or fast Ar^f atom impact ionization are followed.

During each time-step the trajectory and velocity of the ions are calculated with Newton's laws:

$$\vec{r} = \vec{r}_0 + \vec{v}_0 \Delta t + \frac{q\vec{E}_f}{2m_{\text{Ar}}} \Delta t^2, \quad (2.14)$$

$$\vec{v} = \vec{v}_0 + \frac{q\vec{E}_f}{m_{\text{Ar}}} \Delta t \quad (2.15)$$

where \vec{E}_f is the electric field, m is the Ar atomic mass, q is the particle charge, Δt is the time interval and \vec{r}_0, \vec{v}_0 and \vec{r}, \vec{v} are the position and velocity vectors before and after Δt , respectively.

The probability of collision during the time step Δt is calculated by: $P = 1 - \exp(-\Delta s n_{\text{Ar}} \sigma_t(\varepsilon))$, (2.16)

where Δs is the distance traveled by the Ar^+ ion with energy ε during the interval Δt , n_{Ar} is the density of the Ar atoms in the ground state, $\sigma_t(\varepsilon)$ is the total Ar^+ ion collision cross section. The cross sections for Ar^+ ion elastic collisions (including symmetric charge transfer) are taken from Ref. 20, whereas the cross sections for Ar^+ ion impact ionization and for excitation to the Ar metastable levels were adopted from Ref. 21. The calculated collision probability is compared with a rn , uniformly distributed in the interval between 0 and 1. If $rn < P$, a collision occurs. To determine the kind of collision a second rn is generated and compared with the relative probability of each collision, similar as in the MC model for the fast electrons. Table 2.2 summarizes all of the fast Ar^+ ion collision processes included in the model, while Fig. 2.2 shows the corresponding collision cross section plotted as function of the ion energy (see below).

Due to the lack of information about differential angular scattering cross sections, we have assumed the elastic scattering as isotropic in the centre of mass²⁰ and we have neglected the angular scattering in inelastic collisions. The latter assumption (i.e., conservation of velocity direction after ion impact ionization and excitation) will have almost no influence on the mean energy of the Ar^+ ions and Ar^f atoms. Indeed, the energy is primarily determined by the elastic (including charge transfer) collisions, due to their higher cross section at the energy range of interest here.^{22,23} After each collision, the new Ar^+ ion energy and velocity direction are calculated depending on the type of the collision:

- a) Elastic collision: In this model the elastic differential scattering cross section in the centre-of-mass is approximated by the sum of two components:²⁰ a backward (or 180 deg) scattering component and an isotropic component.

- I. The backward scattering component of elastic scattering and a cold (or stationary) atom results in a slow ion and a fast atom. The new ion starts “at rest” and the initial velocity direction is assumed to be parallel to the electric field. The new created fast atom is assumed to have the energy and velocity direction equal to the original ion²³ and it will be followed in the MC model for fast Ar atoms (see below). At high collision energies, this backward scattered component is equal to the charge transfer cross section. At low energies this component becomes very small as the elastic scattering becomes more isotropic.
- II. Based on the assumption of isotropic scattering in the centre-of-mass frame, the polar χ and azimuthal Φ angles of scattering with respect to the incident ion velocity direction are calculated as follows:

$$\chi = 0.5 \arccos(1 - 2m), \quad (2.17)$$

$$\phi = 2\pi m \quad (2.18)$$

From these angles the new velocity angles are found by transformation of the coordinate frame of reference. The ion energy is

$$\varepsilon = \varepsilon_{\text{ini}} [1 - (\sin \chi)^2], \quad (2.19)$$

where ε_{ini} is the incident ion energy.

If the transferred energy to the background atom is higher than the threshold energy, i.e. $\varepsilon_{\text{ini}} (\sin \chi)^2 > 1 \text{ eV}$, the atom is considered as a fast particle and hence followed in this MC code in the part for fast atoms (see below, 2.3.2.2).

- b) Excitation collision: No change in velocity direction is assumed and the energy after the collision is calculated as:

$$\varepsilon = \varepsilon_{\text{ini}} - \varepsilon_{\text{exc}}, \quad (2.20)$$

- c) Ionisation collision: It is assumed that the energy is shared equally between the projectile and the newly formed ion, so that:

$$\varepsilon = (\varepsilon_{\text{ini}} - \varepsilon_{\text{ion}}) / 2. \quad (2.21)$$

Further, like for the excitation collision, no change in velocity direction is assumed and the newly created ion is followed also in this MC model.

This procedure of following the ions with Newton’s laws and describing their collisions with cross sections and m is repeated, until the Ar^+ ions collide at the cathode walls or at the anode, where they are neutralized and disappear from the calculations.

The positions of the new-formed particles (electrons as a result of Ar^+ ion impact ionization and fast Ar^f atoms as a result of elastic collisions) are stored in an array, and later treated in the corresponding codes.

It should be mentioned that because of the asymmetric charge transfer collisions (ACT) of Ar^+ ions with Cu atoms, Ar^+ ions are lost. This loss is considered in the present MC model through the ACT collision rate (calculated in the fluid model for Cu^+ ions and Cu atoms (see below 2.4.3)). Note that the loss and creation of charged particles, especially of the Ar^+ ions and electrons, should always be carefully considered, because the Ar^+ ions, together with the electrons, determine the electrical properties of the glow discharge and they are important in this respect for the current balance. Therefore, in the present MC model, the loss of Ar^+ ions through ACT of Ar^+ ions with Cu atoms, is considered by feeding back to this model the ACT collision rate (calculated in the fluid model for Cu^+ ions and Cu atoms (see below 2.4.3))

2.3.2.2 Monte Carlo model for the fast Ar atoms

This sub-program handles the Ar atoms formed from elastic collisions from the Cu^+ ions and Ar^+ ions (including charge transfer), and which have energies above 1 eV. Atoms with energy below 1 eV are assumed to belong to the thermalized group.

The initial energy and velocity directions of the fast atom are determined by the mechanism of its creation:

- If the fast Ar^f atom was formed after a symmetric charge transfer collision, its energy and velocity direction are equal to the projectile Ar^+ ion (see 2.3.1).
- If the fast Ar^f atom was formed after an ion elastic collision, its energy and velocity direction are calculated based on the assumption of isotropic scattering in the centre-of-mass,

$$\varepsilon_{\text{Ar}} = \varepsilon_{\text{ion}} \sin^2 \chi \quad (2.22)$$

$$\chi_{\text{Ar}}^{\text{Lab}} = \frac{\pi - \chi}{2} \quad (2.23)$$

$$\phi_{\text{Ar}}^{\text{Lab}} = 2\pi r n \quad (2.24)$$

where χ is the scattering angle in the centre-of-mass

The fast Ar atoms are followed in the entire discharge because they do not feel the electric field and hence they are not exclusively directed to the cathode walls, but to all directions. Their trajectory and velocity are calculated also by the equations 2.14 and 2.15, but the term including the electric field disappears. For determining the occurrence

and kind of collisions and also the energy and velocity direction after collisions, the same assumptions as for the Ar^+ ions were made. The collision processes considered here are: elastic collisions, atom impact ionization as well as excitation from the ground state to the metastable level. The corresponding cross sections were taken from Refs. 20 and 21, respectively. The positions of the new-formed particles (Ar^+ ions and electrons as a result of Ar atom impact ionization and fast Ar atoms as a result of Ar atom elastic collisions) are stored in an array, and later treated in the corresponding codes. The fast Ar atoms are followed until their energy drops below 1eV or until they reach the cathode or anode walls, where they can be implanted or reflected. It was assumed that 10% of the fast atoms arriving at the wall are reflected.

2.3.3 Monte Carlo model for fast Cu atoms (sputtered atoms)

The cathode sputtering can be treated as a probability process, in which every time that an energetic particle (atom or ion) impinges the cathode, the ejection of the atoms will occur with a certain probability, given by the energy and angle of incidence of the impinging particle, i.e., following the principle of particle-in-cell simulations. However to accomplish it, a very long calculation time is required. Therefore, in the present model, we have opted to calculate the sputtered flux based on the Matsunami formula²⁴ for the sputtering yield and the energy flux distribution of the particles bombarding the cathode. This approach is sufficiently accurate and much faster.

The sputtered flux (J^{Cu}) is calculated as the product of the sputter yields as a function of energy (ε), i.e., the number of atoms ejected per incident particle,²⁴ and the bombarding particle flux energy distributions (f_{cat}), integrated over the complete energy range:

$$J^{\text{Cu}} = - \int \left[Y^{\text{Ar}^+, \text{Cu}}(\varepsilon) (f_{\text{cat}}^{\text{Ar}^+}(\varepsilon) + f_{\text{cat}}^{\text{Ar}^f}(\varepsilon)) + Y^{\text{Cu}^+, \text{Cu}}(\varepsilon) f_{\text{cat}}^{\text{Cu}^+}(\varepsilon) \right] d\varepsilon \quad (2.25)$$

where the negative sign indicates that the sputtered flux is in the opposite direction as the bombarding fluxes.

The spatial dependence of the sputtered flux was calculated based on an approximation of eq. (2.25), where instead of the flux energy distribution, the particle flux at the cathode (at each grid point of the cathode, i), was used and the sputtering yield was calculated for the average energy (ε_{ave}) at each i :

$$j_i^{\text{Cu}} = - \left(Y^{\text{Ar}^+, \text{Cu}}(\varepsilon_{\text{ave}}) j_{i, \text{cat}}^{\text{Ar}^+} + Y^{\text{Ar}^f, \text{Cu}}(\varepsilon_{\text{ave}}) j_{i, \text{cat}}^{\text{Ar}^f} + Y^{\text{Cu}^+, \text{Cu}}(\varepsilon_{\text{ave}}) j_{i, \text{cat}}^{\text{Cu}^+} \right) \quad (2.26)$$

Subsequently, the relative spatial distribution, $j_i^{\text{Cu}} / \sum_i j_i^{\text{Cu}}$, was factorized by the value of the total sputtered flux (J^{Cu}), calculated in eq. (2.25).

The initial position of the Cu atoms, i.e., the position from where they are ejected from the cathode surface, was determined by the relative spatial distribution of the sputtered flux ($j_i^{\text{Cu}} / \sum_i j_i^{\text{Cu}}$), and by generation of random numbers (rn 's). The Cu atoms are assumed to be ejected from the cathode following the Sigmund-Thompson distribution²⁵ from where the initial energy ε_0 , and the axial (θ) and azimuthal (Φ) angles of the initial velocity were calculated as: $\varepsilon_0 = U / (rn^{-0.5} - 1)$, $\theta = 0.5 \arccos(1 - 2rn)$ and $\phi = 2\pi rn$, respectively. U is the surface binding energy of the cathode material, which is taken equal to the heat of sublimation. Based on the fact that the maximum energy which a colliding particle can transfer in a collision, corresponds to the energy transfer in a head-on elastic collision, it was assumed in the model that the maximum initial Cu atom energy, ($\varepsilon_{\text{max}}^{\text{Cu}}$) will be equal or less than $\frac{4m^{\text{Cu}}m^{\text{Ar}}}{(m^{\text{Cu}} + m^{\text{Ar}})^2} \varepsilon_{\text{ave}}^{\text{Ar}^+}$, where $\varepsilon_{\text{ave}}^{\text{Ar}^+}$ is the average Ar^+ ion energy at the point of emission. Due to elastic collisions, this initial energy is transferred very effectively to the background gas. In Ref. 26 it was shown that the thermalization of the sputtered atoms occurs on a very short time-scale and can be considered to be finished when the diffusion starts, hence both processes can be modeled separately. This MC sub-model handles the evolution of the sputtered Cu atoms toward the thermalization, while in the fluid sub-model for Cu^+ ions and Cu atoms (see below, 2.4.3) the transport by diffusion of the Cu atoms is described.

During each time-step, the trajectory of the Cu atoms is calculated with Newton's laws: $\vec{r} = \vec{r}_0 + \vec{v}\Delta t$, where Δt is the time interval and \vec{r}_0, \vec{r} are the position vectors before and after Δt , respectively and \vec{v} is the velocity vector. We considered here that the slow-down of the sputtered Cu atoms is only due to elastic collisions with background Ar atoms, because this process has the highest cross section and the densities of the other species present in the discharge are at least four orders of magnitude lower than the background Ar atom density.⁸ Due to a lack of information about experimental Cu elastic cross sections with Ar atoms ($\sigma(\varepsilon_0)$), the value of $\sigma(\varepsilon_0)$ was obtained from Lindhard's differential scattering cross section,²⁷ $\sigma(\varepsilon_0, T)$, after integration over all possible values of energy transfer, T , from a projectile of energy ε_0 , to an atom at rest. The interatomic

interaction potential was taken in the form proposed by Sielanko,²⁸ i.e., a power-law potential that approximates the Molier potential by taking the inverse power potential parameter (n) as a function of the impinging energy:

$$n = 1 + \frac{4}{\exp(1.9\xi^{0.1})}, \text{ where } \xi, \text{ is the reduced energy, in units [eV,cm] defined as}$$

$$\xi = 6.94 \times 10^6 a \frac{m_{\text{Ar}}}{Z_{\text{Cu}} Z_{\text{Ar}} (m_{\text{Cu}} + m_{\text{Ar}})} \varepsilon.$$

Here, $a = \frac{4.68 \times 10^{-9}}{(\sqrt{Z_{\text{Cu}}} + \sqrt{Z_{\text{Ar}}})^{2/3}}$, is the Firsov screening length, and the parameter

$$\beta_n = \frac{3n-1}{8n^2}.$$

$$\text{Then } \sigma(\varepsilon) \text{ is obtained as: } \sigma(\varepsilon) = \frac{2\pi}{n-1} a^2 \frac{\beta_n^{1/n}}{\xi^{2/n}} \quad (2.28)$$

The probability of elastic collisions during the time-step, Δt , is calculated by: $P = 1 - \exp(-\Delta s n_{\text{Ar}} \sigma(\varepsilon_0))$, where Δs is the distance travelled by the Cu atoms with energy ε_0 during the interval Δt , and n_{Ar} is the density of the background Ar atoms. Subsequently, P is compared to a rn in order to determine if a collision takes place. After each collision, the new energy and velocity direction are calculated.

The axial scattering angle, χ , was calculated from the Sielanko formula,²⁸

$$\chi = 2 \arcsin \left(1 + \left(\frac{b}{a} \right)^2 \left(\frac{\xi}{\beta_n} \right)^{\frac{2}{n}} \right)^{\frac{n}{2}} \quad (2.29)$$

where b is the impact parameter. The impact parameter is calculated as proposed by Wronski.²⁹ In the Firsov analysis¹⁷, the differential (scattering) elastic cross section is related to the impact parameter by $\sigma(\varepsilon, \chi) = 2\pi b db$. Hence, the total elastic cross section is given by the maximum value of impact parameter, b_{max} , as $\sigma(\varepsilon) = \pi b_{\text{max}}^2$, therefore,

$$\text{we can calculate } b \text{ by the formula, } rn = \int_0^b \frac{2\pi b'}{\pi b_{\text{max}}^2} db', \quad b = \sqrt{rn} b_{\text{max}}.$$

The azimuthal angle of scattering is calculated as $\phi = 2\pi rn$,

$$\text{and the energy after the collision, } \varepsilon, \text{ as: } \varepsilon = \varepsilon_0 - T, \text{ where } T = \varepsilon_0 \frac{4m^{\text{Cu}} m^{\text{Ar}}}{(m^{\text{Cu}} + m^{\text{Ar}})^2} \sin^2 \frac{\chi}{2}.$$

The conversion of the scattering angles into the laboratory frame of reference was done by the ordinary transformation of the coordinate frame of reference.³⁰

This procedure of following the atoms with Newton's laws and describing their collisions with cross sections and m 's is repeated, until the Cu atoms collide at the cathode walls or at the anode, where they can be absorbed or reflected (we assumed a sticking coefficient equal to 0.5, i.e., 50% are reflected), or until their energy drops below 0.03 eV, i.e., when they can be considered as thermalized Cu atoms.

By following in this way a large number of sputtered atoms, the thermalization profile (i.e., the spatial distribution of thermalized Cu atoms) is calculated, and this yields the initial distribution for the further diffusion transport of the thermalized Cu atoms.

2.3.4 Monte Carlo model for fast Cu⁺ ions

The MC simulation for the Cu⁺ ions is carried out in a similar way as for the Ar⁺ ions, i.e., they are followed only as fast particles inside the CDS. The Cu⁺ ions start at the CDS-NG boundary or within the CDS with an assumed initial energy of 0.04 eV and a velocity direction parallel to the electric field. For the ions starting at the CDS-NG interface the initial position is determined from the radial and axial Cu⁺ ion flux diffusing from the NG to the CDS, as calculated in the Cu, Cu⁺ fluid model (see below 2.4.3). As a result of the electron impact ionization, Penning ionization and ACT collisions, some new ions are created inside the CDS. The initial position of these ions is obtained from the corresponding ionization rates (calculated in the fast electron MC model and in the Cu, Cu⁺ fluid model, respectively). During each time-step the trajectory of the ions is calculated with Newton's laws:

$$\vec{r} = \vec{r}_0 + \vec{v}_0 \Delta t + \frac{q\vec{E}_f}{2m_{\text{Cu}}} \Delta t^2, \quad \vec{v} = \vec{v}_0 + \frac{q\vec{E}_f}{m_{\text{Cu}}} \Delta t \quad (2.30)$$

where \vec{E}_f is the electric field, m^{Cu} is the Cu atomic mass, q is the particle charge, Δt is the time interval and \vec{r}_0, \vec{v}_0 and \vec{r}, \vec{v} are the position and velocity vectors before and after Δt , respectively. The only collision process considered for the fast Cu⁺ ions was the elastic collisions with the background Ar atoms. In the Lindhard's differential scattering cross section, no difference was made for neutral or charged projectiles. Therefore, we have applied the same analytical formula for the calculation of the Cu⁺ ion elastic cross section as for the fast Cu atom cross section. Hence, for determining the occurrence of collisions and also the energy and velocity direction after collisions, the same

assumptions as for the fast Cu^f atoms were made. This procedure is repeated until the Cu^+ ions collide at the cathode walls or the anode, where they are neutralized and disappear from the calculations. As a result of Cu^+ ion elastic collisions with the background Ar atoms, fast Ar^f atoms can be formed. These fast Ar^f atoms are followed in the MC model for Ar^+ ions and fast Ar^f atoms.

Table 2.2 Overview of the collision processes incorporated in the different MC sub-models for the numerical simulation of the Ar-Cu HCD, as well as the references where the cross sections were taken from.

| fast electrons | | References |
|--|---|---|
| 1) $e_f + \text{Ar} \rightarrow e_f + \text{Ar}$ | e^- elastic collision | A. Phelps, jilawww.colorado.edu/research/colldata.html |
| 2) $e_f + \text{Ar} \rightarrow e_f + \text{Ar}^*$ | e^- impact excitation | A. V. Phelps and Z. Lj. Petrovich, Plasma Sources Sci. Technol. 8 , R21 (1999). |
| 3) $e_f + \text{Ar} \rightarrow e_f + \text{Ar}^m$ | e^- impact excitation to the Ar^m level | N. J. Mason and W. R. Newell, J. Phys. B 20 , 1357 (1987). V. Puech and L. Torchin, J. Phys 19 , 2309 (1986). A. Phelps, jilawww.colorado.edu/research/colldata.html |
| 4) $e_f + \text{Ar} \rightarrow 2e_f + \text{Ar}^+$ | e^- impact ionization | A. V. Phelps and Z. Lj. Petrovich, Plasma Sources Sci. Technol. 8 , R21 (1999). |
| 5) $e_f + \text{Ar}^m \rightarrow 2e_f + \text{Ar}^+$ | e^- impact ionization from the Ar^m level | H. A. Hyman, Phys. Rev. A 20 , 855 (1979). |
| 6) $e_f + \text{Cu} \rightarrow 2e_f + \text{Cu}^+$ | e^- impact ionization of the Cu atoms | L. Vriens, Phys. Lett. 8 , 260 (1964). |
| fast Ar^+ ions | | |
| 7,8) $\text{Ar}^+ + \text{Ar} \rightarrow \text{Ar}^+ + \text{Ar}^f$ | Ar^+ elastic collision (including SCT) | A. V. Phelps, J. Appl. Phys. 76 , 747 (1994) |
| 9) $\text{Ar}^+ + \text{Ar} \rightarrow \text{Ar}^+ + \text{Ar}^m$ | Ar^+ -impact excitation to the Ar^m level | A. V. Phelps, J. Phys. Chem. Ref. Data 20 , 557 (1991). |
| 10) $\text{Ar}^+ + \text{Ar} \rightarrow 2\text{Ar}^+ + e_f$ | Ar^+ -impact ionization | A. V. Phelps, J. Phys. Chem. Ref. Data 20 , 557 (1991). |
| fast Ar^f atoms | | |
| 11) $\text{Ar}^f + \text{Ar} \rightarrow 2\text{Ar}^f$ | Ar^f elastic collision | A. V. Phelps, J. Appl. Phys. 76 , 747 (1994) |
| 12) $\text{Ar}^f + \text{Ar} \rightarrow \text{Ar}^f + \text{Ar}^m$ | Ar^f -impact excitation to the Ar^m level | A. V. Phelps, J. Phys. Chem. Ref. Data 20 , 557 (1991). |

| | | | |
|--|---|----------------------------------|---|
| 13) | $\text{Ar}^f + \text{Ar} \rightarrow \text{Ar}^f + \text{Ar}^+ + e_f$ | Ar^f -impact ionization | A. V. Phelps, J. Phys. Chem. Ref. Data 20 , 557 (1991). |
| <hr/> fast Cu^f atoms <hr/> | | | |
| 14) | $\text{Cu}^f + \text{Ar} \rightarrow \text{Cu} + \text{Ar}^f$ | Cu^f elastic collision | J. Linhard, M. Scharff and H.E. Schiott, Mat. Fys. Medd. Dan. Vid. Selsk, 33 , No 14 (1963). |
| <hr/> fast Cu^+ ions <hr/> | | | |
| 15) | $\text{Cu}^+ + \text{Ar} \rightarrow \text{Cu}^+ + \text{Ar}^f$ | Cu^+ elastic collision | J. Linhard, M. Scharff and H.E. Schiott, Mat. Fys. Medd. Dan. Vid. Selsk, 33 , No 14 (1963). |

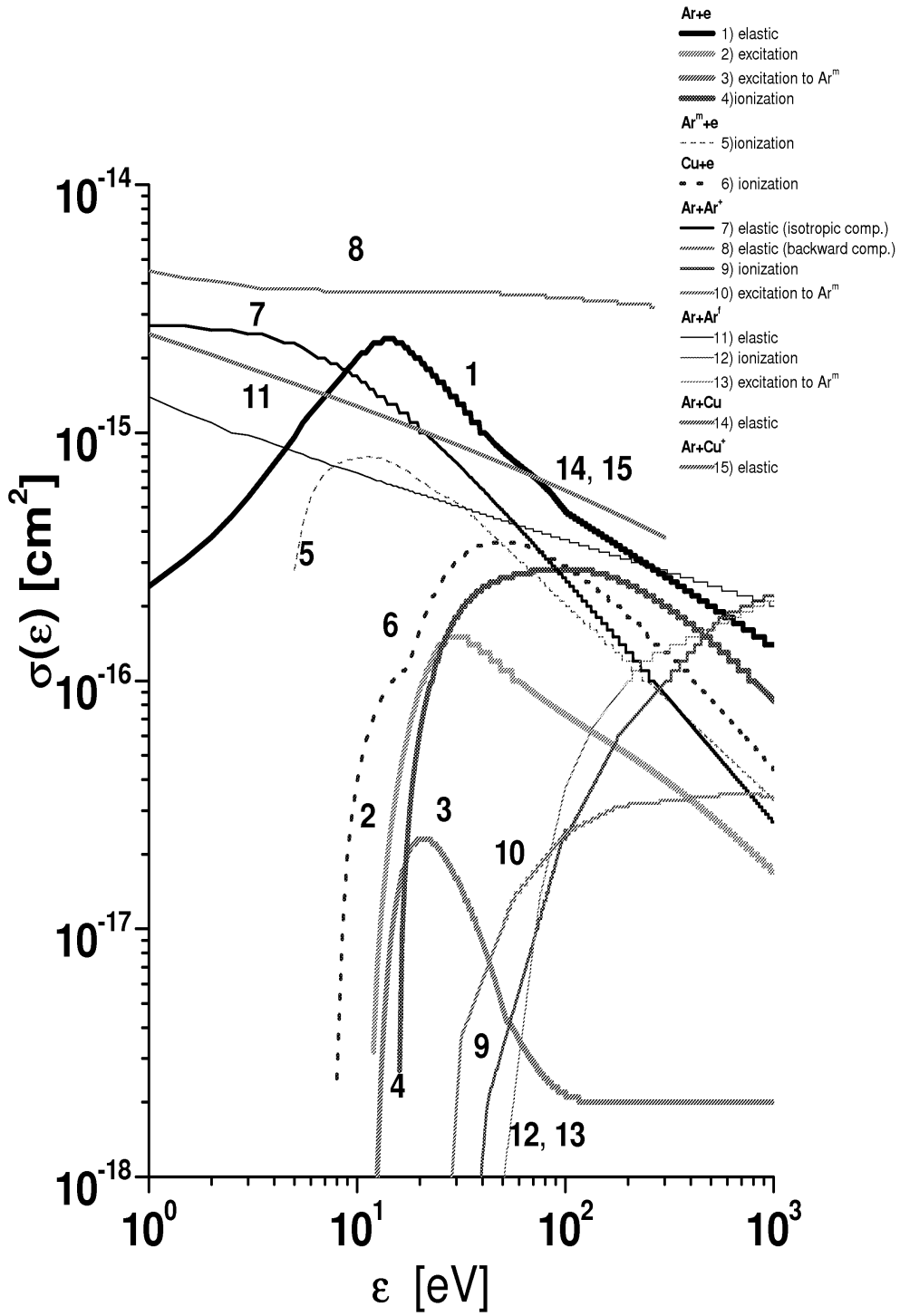


Fig. 2.2 Cross sections of fast electrons, fast Ar+ ions, fast Ar f atoms, fast Cuf atoms and fast Cu+ ions collision processes included in the Ar-Cu HCD model, as a function of the respective energies.

Table .2.3 Overview of the collision processes incorporated in the fast electron MC sub-model for the numerical simulation of the He-Ni HCD, s well as the references where the cross sections were taken from.

| fast electrons | | References | |
|-----------------------|--|--|---|
| 1) | $e_f + \text{He} \rightarrow e_f + \text{He}$ | e^- elastic collision | A. Phelps, jilawww.colorado.edu/research/colldata.html |
| 2) | $e_f + \text{He} \rightarrow e_f + \text{He}^m$ | e^- impact excitation to He^m metastable level | Fig. 8 from L. L. Alves, C M Ferreira, J. Phys. D 24 , 591 (1991). |
| 3) | $e_f + \text{He} \rightarrow e_f + \text{He}^*$ | e^- impact excitation | A. Phelps, www.colorado.edu/www/research/colldata.html |
| 4) | $e_f + \text{He} \rightarrow 2e_f + \text{He}^+$ | e^- impact ionization | A. Phelps, jilawww.colorado.edu/research/colldata.html |
| 5) | $e_f + \text{He}^m \rightarrow 2e_f + \text{He}^+$ | e^- -impact ionization from He^m metastable level | T. Kato and R. K. Janev, Atomic and Plasma-Material Interaction Data for Fusion 3 , 33 (1992). |

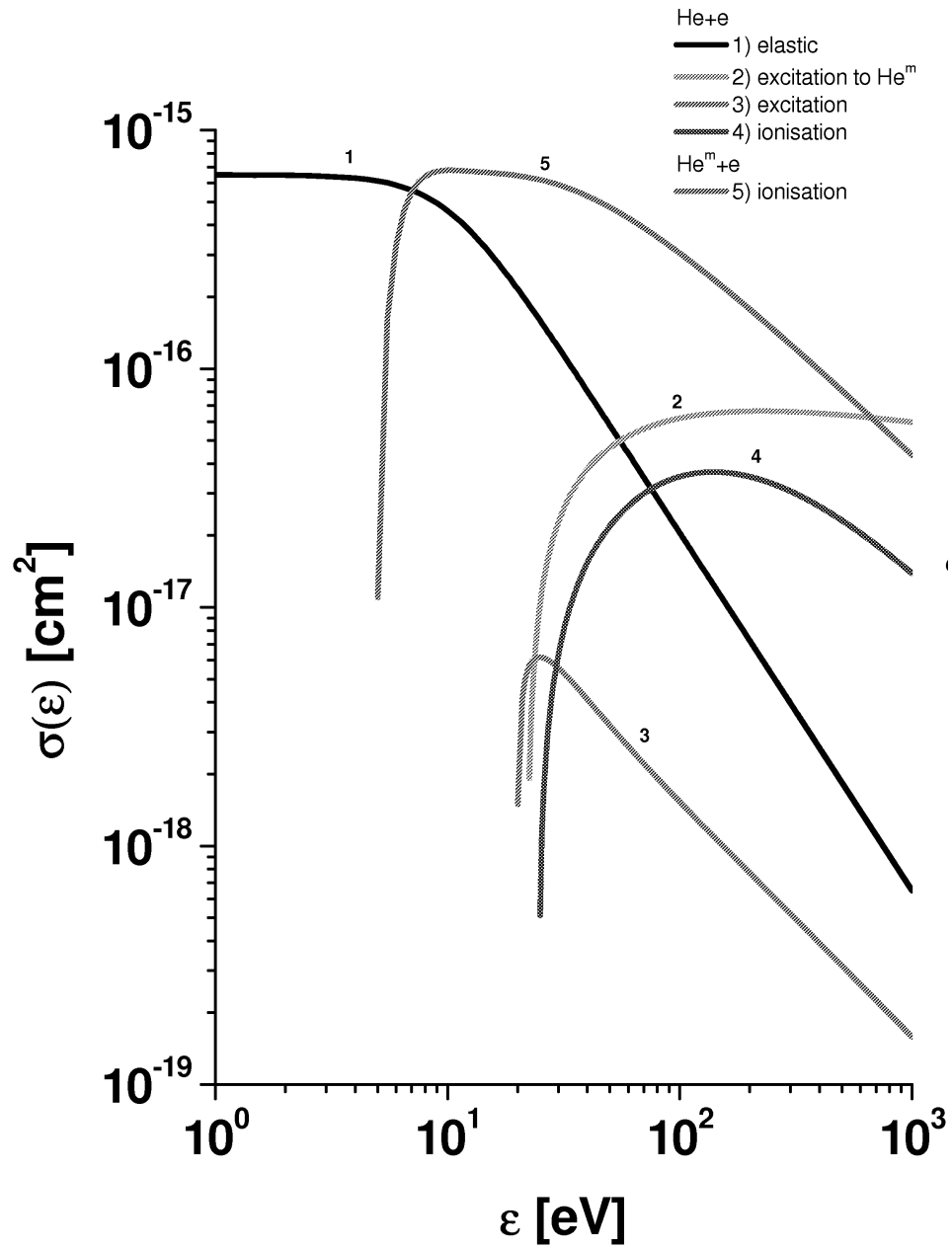


Fig. 2.3 Cross sections of fast electron collision processes included in the He-Ni HCD model, as a function of the electron energy.

2.4 Fluid models

2.4.1 Fluid model for slow electrons and carrier gas ions

In the fluid model the slow electrons and the gas ions are considered in hydrodynamic equilibrium with the electric field and they can be treated as a continuum. The transport of the slow electrons and the gas ions is described with the continuity (eq. 2.31 and 2.32, respectively) and flux equations. (eq. 2.33 and 2.34, respectively), in which the ion and electron fluxes are expressed as a linear combination of a drift, due to the electric field, and a diffusion, due to the particle density gradient. In order to obtain a self-consistent electric field, these equations are coupled with the Poisson equation (eq. 2.35). Because of the cylindrical symmetry of the discharge cell, the fluid model is developed in cylindrical coordinates.

$$\frac{\partial n_e}{\partial t} + \vec{\nabla} \cdot \vec{j}_e = S_{\text{slow}} \quad (2.31)$$

$$\frac{\partial n_{g^+}}{\partial t} + \vec{\nabla} \cdot \vec{j}_{g^+} = S_{\text{prod}}^{g^+} \quad (2.32)$$

$$\vec{j}_e = n_e \mu_e \vec{\nabla} V - D_e \vec{\nabla} n_e \quad (2.33)$$

$$\vec{j}_{g^+} = -n_{g^+} \mu_{g^+} \vec{\nabla} V - D_{g^+} \vec{\nabla} n_{g^+} \quad (2.34)$$

$$\nabla^2 V = \frac{e}{\epsilon_0} (n_{g^+} + n_{\text{Cu}^+} - n_e - n_{e_{\text{fast}}}), \quad \vec{E} = -\vec{\nabla} V \quad (2.35)$$

Here, ϵ_0 is the permittivity of the free space, e the electron charge, V the electric potential, \vec{E} the electric field strength. n_{g^+}, n_{Cu^+} are the gas and Cu^+ ion densities, respectively. $n_e, n_{e_{\text{fast}}}$ are the slow and fast electron densities, respectively. \vec{j}_e, \vec{j}_{g^+} are the electron and gas ion fluxes, respectively. $S_{\text{prod}}^{g^+}$ and S_{slow} are the source terms obtained as output from the Monte Carlo model for the fast electrons, representing the number of gas ions and slow electrons created per unit volume and per unit time, respectively. D_{g^+}, D_e and μ_{g^+}, μ_e are the corresponding gas ion and electron diffusion and mobility coefficients, respectively. μ_e was chosen to be equal to D_e , upon the assumption that the characteristic energy of the slow electrons was constant^{2,3,5,31} and equal to 1 eV. This

value was chosen based on the measurements of the electron energy distribution function in a cylindrical HCD in He, where the average energy of the electrons was found to be 1.2 eV at 1 Torr.³² As a consequence of this approximation the energy of the slow electrons will be not realistic obtained, as the electrons treated in the fluid model gain energy diffusing against the field in the CDS. Therefore some parameters of the discharge, which depend directly on the slow electron temperature, like the electron density and plasma potential in the NG will not so accurately be calculated, but for the correct description of the CDS and the NG, its length, the current-voltage characteristic, etc, the most important parameter to be calculated should be the ionization rate, specially by fast electrons,^{3,33} whose energy distribution is calculated accurately in the MC model. On the other hand, with this approximation the model is less complicated because one does not have to include the energy balance equation in this fluid model and one can obtain the energy distribution function for the fast electrons in the corresponding MC model.

Based on the comparison between experimental and calculated ion and electron current densities, Ward³⁴ proposed that the diffusion coefficients for the ions and electrons as well as the electron mobility can be considered independent of the electric field, while for the ions he found that a constant mobility was not valid to obtain a good agreement with experimental data of ion velocity in the NG, due to so a low field in the NG compare with the high electric field in the CDS. Ward proposed, to calculate the ion mobility as a function of the reduced electric field as follows,³⁴

$$\mu_{g^+} = \mu_{01} \frac{E}{p} \left(1 - CE/p\right) [\text{cm}^2 \text{V}^{-1} \text{s}^{-1}] \quad \text{for} \quad \frac{E}{p} \leq W \quad (2.36)$$

$$\mu_{g^+} = \mu_{02} \sqrt{\frac{E}{p}} \left(1 - G\sqrt{p^3/E^3}\right) [\text{cm}^2 \text{V}^{-1} \text{s}^{-1}] \quad \text{for} \quad \frac{E}{p} > W \quad (2.37)$$

In the present model the diffusion coefficients were taking as follows,^{1,3,5,}

$$\text{for the electrons } D_e = D_{0e} / p [\text{cm}^2 \text{s}^{-1}], \quad (2.38)$$

$$\text{for the ions } D_{g^+} = D_{0g^+} / p [\text{cm}^2 \text{s}^{-1}], \quad (2.39)$$

where p is the pressure of the background discharge gas in units of Torr. The values of the different constants appearing in the equations 2.36-2.39 are given in table 2.4.

The following boundary conditions were assumed for the solution of the set of transport and Poisson equations (eqs. 2.31-2.35): The electric potential at the cathode is taking equal to the discharge voltage and at the anode (anodes) equal to zero. For the charged particle densities the boundary conditions are the so-called ‘‘mixed boundary

conditions”,³⁵ i.e., for the electrons a total recombination at the electrodes is assumed, i.e., the electron density is taken equal to zero at all the electrodes, while for the gas ions the gradient of the density was taking equal to zero, $\vec{\nabla} n_{g^+} = 0$. This implies that the gas ion flux toward the electrodes is totally governed by the drift term, which was a necessary condition in order to avoid numerical instabilities by solving the system equations.

Table 2.4 Constants needed to calculate the mobility and diffusion coefficients of the electron and gas ions moving through their parent background gas.

| Transport coefficients constant | For Ar-Cu HCD | | For He-Ni HCD | |
|--|-----------------------|-----------|----------------------|-----------|
| D_{0e} | 2×10^{-5} | (Ref. 3) | 1×10^6 | (Ref. 35) |
| D_{0g^+} | 1×10^2 | (Ref. 3) | 4.1×10^2 | (Ref. 36) |
| μ_{01} | 1×10^3 | (Ref. 34) | 8×10^3 | (Ref. 34) |
| μ_{02} | 8.25×10^3 | (Ref. 34) | 4.1×10^4 | (Ref. 34) |
| C | 2.22×10^{-3} | (Ref. 34) | 8×10^{-3} | (Ref. 34) |
| G | 86.52 | (Ref. 34) | 27.44 | (Ref. 34) |
| W | 60 | (Ref. 34) | 25 | (Ref. 34) |

The system of equations 2.31-2.35 is solved numerically following the procedure developed by Passchier and Goedheer,^{37,38} i.e., the Scharfetter-Gummel implicit exponential scheme is used for the discretization of the transport equations.^{39,40} The main advantage of this method is its ability to deal with situations where either the drift or the diffusion component of the particle flux density is dominant, i.e. the high electric field in the plasma sheath and the low electric field in the NG, respectively. The continuity equations for slow electrons and the Poisson equation are solved simultaneously, using the Newton-Raphson method¹⁶ and the continuity equation for the gas ions is solved using the Thomas algorithm.⁴¹

2.4.2 Fluid model for the metastable gas atoms

The behavior of the metastable atoms is also described by continuity and flux equations, in which the flux is only determined by diffusion.^{36,42} The different production and loss processes considered in the model for He-Ni and Ar-Cu HCDs are summarized in Table 2.5 and 2.6, respectively.

Taking into account the production and loss processes summarized in Tables 2.5-6, the transport of the metastable atoms are described with the following balance equation:

$$\frac{\partial n_m}{\partial t} - D_m \nabla^2 n_m = S_{\text{prod}}^m - S_{\text{loss}}^m \quad (2.40)$$

Equation (2.40) is discretized and solved with the Thomas algorithm.⁴¹

2.4.2.1 Fluid model for the He^m metastable atoms

The plasma species considered in the model for the He^m atoms are: neutral ground state and metastable He atoms, slow positive ions (He^+) and fast and slow electrons. The two metastable levels of He, i.e., the triplet 2^3S and singlet 2^1S metastable levels lying at 19.82 eV and 20.61 eV above the ground state, respectively, have been combined into one collective level lying at 19.82 eV. It is found in the literature that the triplet state has a higher density than the singlet state, because the singlet metastables are converted into the triplet metastables by superelastic collisions with slow electrons in the NG; hence, the population of the 2^1S metastable level is typically around 20% of that of the 2^3S metastable level.⁴²⁻⁴⁴

The production processes incorporated in the model are: electron impact excitation from the He ground state by fast electrons and dielectronic recombination of He^+ ions with thermal electrons, while the following processes were included as loss mechanisms: fast electron impact ionization from the He^m metastable state, de-excitation induced by thermal electrons, metastable atom-metastable atom collisions, resulting in the ionization of one of the atoms (also called pooling ionization), two body collisions with ground state He atoms and three body collisions with two ground state He atoms, resulting in the formation of He_2^* and finally, diffusion to the walls followed by de-excitation at the walls. In the simulation, electron impact excitation of the metastables to higher radiating states is not included as a loss channel because of radiation trapping, i.e., most of the electrons excited from the metastables to the radiating states come back to the

metastable level due to reabsorption of the emitted light from transition to the ground state.^{28,30,33}

Taking in account the above-mentioned processes, the source terms of the continuity equation for the He^m metastable atom density are given by:

$$S_{\text{prod}}^{\text{He}^m} = S_{\text{exc}} + k_{\text{rec}} [n_e]^2 n_{\text{He}^+}$$

$$S_{\text{loss}}^{\text{He}^m} = S_{\text{ion}} + k_{\text{dexc}} n_{\text{He}^m} n_e + 2k_{\text{met}} [n_{\text{He}^m}]^2 + k_{2\text{B}} n_{\text{He}^m} n_{\text{He}} + k_{3\text{B}} n_{\text{He}^m} [n_{\text{He}}]^2$$

The reaction coefficients and the collision rates involved in these terms are presented in Table 2.5.

Table 2.5 Production and loss processes considered for the calculation of the He^m metastable atom density. The respective collision rate coefficients or the collision rates (when the collision processes involve fast particles) are also presented.

| Production processes | | Rates or rates coefficients |
|---|---------------------------------|--|
| $\text{He} + e_f \rightarrow \text{He}^m + e_f$ | electron- impact excitation | S_{exc} (calculated in MC-efast) |
| $\text{He}^+ + 2e \rightarrow \text{He}^m + e$ | dielectronic recombination | $k_{\text{rec}} = 6.0 \times 10^{-20} \text{ cm}^6 \text{ s}^{-1}$ (Ref. 36) |
| Loss processes | | |
| $\text{He}^m + e_f \rightarrow \text{He}^+ + 2e_f$ | electron-impact ionization | S_{ion} (calculated in MC-efast) |
| $\text{He}^m + e \rightarrow \text{He} + e + h\nu$ | electron- impact de-excitation | $k_{\text{dexc}} = 4.2 \times 10^{-9} \text{ cm}^3 \text{ s}^{-1}$ (Ref. 36) |
| $\text{He}^m + \text{He}^m \rightarrow \text{He}^+ + \text{He} + e_f$ | metastable-metastable collision | $k_{\text{met}} = 1.5 \times 10^{-9} \text{ cm}^3 \text{ s}^{-1}$ (Ref. 36) |
| $\text{He}^m + \text{He} \rightarrow \text{He} + \text{He}$ | two-body collision | $k_{2\text{B}} = 6.0 \times 10^{-15} \text{ cm}^3 \text{ s}^{-1}$ (Ref. 42) |
| $\text{He}^m + 2\text{He} \rightarrow \text{He}_2^* + \text{He}$ | three-body collision | $k_{3\text{B}} = 2.5 \times 10^{-34} \text{ cm}^6 \text{ s}^{-1}$ (Ref. 42) |
| Diffusion to the walls, followed by de-excitation at the walls | | $D_{\text{He}^m} = 470 \text{ cm}^2 \text{ s}^{-1}$ (Ref. 42) |

2.4.2.2 Fluid model for the Ar^m metastable atoms

In the Ar-Cu HCD model, beside the plasma species also the sputtering species are included. Therefore the species considered in this sub-model for the calculation of the Ar^m atom density are: neutral ground state and metastable Ar atoms, slow and fast positive Ar^+ ions, fast and slow electrons, fast Ar atoms, and Cu atoms and Cu^+ ions. The two metastable levels of Ar, 3P_2 and 3P_0 , which are lying at 11.55 eV and 11.72 eV above the ground state, respectively, have been combined into one collective level, lying at 11.55 eV.^{45,46} This assumption was made based on the fact that according to their statistical weights, $g = 2J+1$, where J is the total angular momentum of the state, the 3P_0 level is expected to be 5 times less populated than the 3P_2 level and in our experiments, density ratios close to 1/7 were measured in the HCD.⁴⁷ This significantly lower population of the 3P_0 level was also confirmed in previous studies in different kinds of discharges.^{48,49} Beside that, our interest in studying the metastable Ar^m atoms is concerned with their influence on the electrical properties of the discharge, on the secondary electron emission and on the ionization of the sputtered Cu atoms, for which only the total metastable density is important.

The transport of Ar^m metastable atoms is described by the continuity and flux equations. The production and loss terms of the continuity equation are given by the following processes: radiative recombination of Ar^+ ions with thermal electrons, and excitation by impact of fast electrons, fast Ar^+ ions and fast Ar^f atoms, were considered as production processes to the metastable state, while the following processes were included as loss mechanisms: fast electron impact ionization from the metastable state, electron impact transfer (also called electron quenching) to the resonance level, which decays to the ground state, (note that the resonance levels 3P_1 and 1P_1 have been lumped together into a collective level symbolized by Ar^*), pooling ionization, Penning ionization of the sputtered Cu atoms, two body collisions and three body collisions with ground state Ar atoms, and diffusion to the walls followed by de-excitation at the walls. Electron impact excitation of metastable atoms to the $3p^54p$ levels and other higher lying states was not considered as a loss process, because the majority of atoms excited to higher levels radiate down again to the $3p^54s$ state and hence the net loss of the metastable will be very small. The fast electron, fast Ar^+ ion, and fast Ar^f atom collision rates were calculated in the corresponding Monte Carlo models through the energy dependent cross sections. The cross section for electron impact excitation to the metastable state, was taken from

Mason,⁵⁰ and factorized to the maximum value of the cross section reported (values presented only till 19 eV) by Puech,⁵¹ which was recommended by Phelps.⁵²

Taking into account the production and loss processes summarized in Table 2.6 and the fact that the flux is only determined by diffusion, the density of the collective metastable state is calculated with the equation 2.40, where

$$S_{\text{prod}} = S_{e,\text{exc}} + S_{\text{Ar}^+,\text{exc}} + S_{\text{Ar}^f,\text{exc}} + k_{\text{rec}} n_e n_{\text{Ar}^+},$$

$$S_{\text{loss}} = S_{e,\text{ion},m} + k_{\text{sela}} n_{\text{Ar}^m} n_e + 2k_{\text{pool}} [n_{\text{Ar}^m}]^2 + k_{\text{Pen}} n_{\text{Ar}^m} n_{\text{Cu}} + k_{2B} n_{\text{Ar}^m} n_{\text{Ar}} + k_{3B} n_{\text{Ar}^m} [n_{\text{Ar}}]^2,$$

The boundary conditions are defined based on the fact that a rather high population of Ar^m metastable atoms was experimentally observed at the cathode walls. Note that in the fluid model for the He^m atoms and in previous works,^{8,53} it was assumed that the metastable atom density at the walls was equal to zero. The processes, which can be responsible for the presence of the metastables at the cathode walls, are most probably:

1. Recombination of Ar^+ ions with electrons at the cathode, yielding the formation of atoms in excited metastable state,
2. When fast Ar^f atoms bombard the cathode, a fraction of them might come back to the discharge in an excited metastable state.
3. A part of the metastable atoms impinging on the cathode surface are not quenched and comes back to the gas phase as metastable atoms. This mechanism has been recently observed with a glass surface.⁵⁴ However, quenching probabilities higher than 99% were measured for metal surfaces.⁵⁵

We selected the first possibility because at the concerned energy range, i.e., energies less than 300 eV, the mechanism to induce secondary electron emission by Ar^+ ions at a clean cathode surface is by potential emission,^{56,57} which means neutralization and Auger de-excitation, i.e., the formation of the metastable atoms is implicitly included.

Table 2.6 Production and loss processes considered for the calculation of the Ar^m metastable atom density. The respective collision rate coefficients or the collision rates (when the collision processes involve fast particles) are also presented.

| Production processes | | Rates or rates coefficients |
|--|------------------------------|--|
| $\text{Ar} + e_f \rightarrow \text{Ar}^m + e_f$ | electron-impact excitation | $S_{\text{exc},e}$ (calculated in MC-efast) |
| $\text{Ar} + \text{Ar}^+ \rightarrow \text{Ar}^m + \text{Ar}^+$ | ion-impact excitation | $S_{\text{exc},\text{Ar}^+}$ (calculated in MC- Ar^+) |
| $\text{Ar} + \text{Ar}^f \rightarrow \text{Ar}^m + \text{Ar}^f$ | atom-impact excitation | $S_{\text{exc},\text{Ar}^f}$ (calculated in MC- Ar^f) |
| $\text{Ar}^+ + e \rightarrow \text{Ar}^m + h\nu$ | radiative recombination | $k_{\text{rec}} = 1 \times 10^{-11} \text{cm}^3 \text{s}^{-1}$ (Ref. ⁵⁸) |
| Loss processes | | |
| $\text{Ar}^m + e_f \rightarrow \text{Ar}^+ + 2e_f$ | electron-impact ionization | $S_{\text{e,ion,m}}$ (calculated in MC-efast) |
| $\text{Ar}^m + \text{Ar}^m \rightarrow \text{Ar}^+ + \text{Ar} + e_f$ | pooling ionization | $k_{\text{met}} = 6.4 \times 10^{-10} \text{cm}^3 \text{s}^{-1}$ (Ref. ⁵⁹) |
| $\text{Ar}^m + e \rightarrow \text{Ar}^* + e \rightarrow \text{Ar} + h\nu + e$ | effective electron quenching | $k_q = 1 \times 10^{-8} \text{cm}^3 \text{s}^{-1}$ (Ref. ⁵⁹) |
| $\text{Ar}^m + \text{Cu} \rightarrow \text{Ar} + \text{Cu}^+ + e$ | Penning ionisation | $k_{\text{Pen}} = 2.6 \times 10^{-10} \text{cm}^3 \text{s}^{-1}$ (Ref. ⁴⁶) |
| $\text{Ar}^m + \text{Ar} \rightarrow \text{Ar} + \text{Ar}$ | two-body collision | $k_{2B} = 2.3 \times 10^{-15} \text{cm}^3 \text{s}^{-1}$ (Ref. ⁴⁸) |
| $\text{Ar}^m + 2\text{Ar} \rightarrow \text{Ar}_2^* + \text{Ar}$ | three-body collision | $k_{3B} = 1.4 \times 10^{-34} \text{cm}^6 \text{s}^{-1}$ (Ref. ⁴⁸) |
| Diffusion to the walls, followed by de-excitation at the walls | | $D_{\text{Ar}^m} = 54 \text{cm}^2 \text{s}^{-1}$ (Ref. ⁶⁰) |

In the present fluid model, the Ar^m metastable atom density at the cathode surface was taken equal to the measured Ar^m metastable atom density and it is assumed that this population is produced by a fraction of the bombarding Ar^+ ion flux at the cathode, which after recombination, come back to the discharge as Ar^m metastable atoms. At the anode, the Ar^+ ion flux is low; most of the discharge current is given by the electron flux.¹⁰ Hence the metastable atom density was taken equal to zero. With these boundary conditions, the continuity equation for the Ar^m atom density is discretized and solved using the Thomas algorithm.⁴¹

2.4.3 Fluid model for the Cu⁺ ions and Cu atoms

This model describes the behavior of the thermalized Cu atoms and the corresponding Cu⁺ ions. The ionization processes considered for the Cu atoms are: electron impact ionization, Penning ionization by Ar^m metastable atoms and asymmetric charge transfer (ACT) with Ar⁺ ions. The transport of the thermalized Cu atoms is diffusion dominated, while the Cu⁺ ion transport is determined by drift and diffusion.

The following continuity and flux equations describe the behavior of the Cu atoms and Cu⁺ ions:

$$\frac{\partial n_{\text{Cu}}}{\partial t} + \vec{\nabla} \cdot \vec{j}_{\text{Cu}} = S_{\text{prod}}^{\text{Cu}} - S_{\text{loss}}^{\text{Cu}} \quad (2.41)$$

$$\vec{j}_{\text{Cu}} = -D_{\text{Cu}} \vec{\nabla} n_{\text{Cu}} \quad (2.42)$$

$$\frac{\partial n_{\text{Cu}^+}}{\partial t} + \vec{\nabla} \cdot \vec{j}_{\text{Cu}^+} = S_{\text{prod}}^{\text{Cu}^+} \quad (2.43)$$

$$\vec{j}_{\text{Cu}^+} = -n_{\text{Cu}^+} \mu_{\text{Cu}^+} \vec{\nabla} V - D_{\text{Cu}^+} \vec{\nabla} n_{\text{Cu}^+} \quad (2.43)$$

where,

$$S_{\text{prod}}^{\text{Cu}} = J^{\text{Cu}} F_t,$$

$$S_{\text{loss}}^{\text{Cu}} = S_{\text{prod}}^{\text{Cu}^+} = S_{e,\text{ion,Cu}} + k_{\text{ACT}} n_{\text{Cu}} n_{\text{Ar}^+} + k_{\text{Pen}} n_{\text{Cu}} n_{\text{Ar}^m}$$

n_{Ar^+} , n_{Ar^m} are the Ar⁺ ion and Ar^m metastable atom densities, respectively.

n_{Cu} , n_{Cu^+} , \vec{j}_{Cu} , \vec{j}_{Cu^+} , D_{Cu} , D_{Cu^+} are the densities, fluxes and diffusion coefficients of Cu and Cu⁺, respectively. μ_{Cu^+} is the mobility of Cu⁺ ions in Ar gas. The values of these

coefficients were adopted from Ref. 61 as follows: $\mu_{\text{Cu}^+} = 1837.4 \text{ cm}^2 \text{ s}^{-1} \text{ V}^{-1}$.

$D_{\text{Cu}^+} = D_{\text{Cu}} = 144.6 \text{ cm}^2 \text{ s}^{-1}$ at 1 Torr. In Ref. 61 the diffusion coefficient for the Cu

atoms diffusing in Ar was calculated from a formula for a mixture of two chemical species,⁶² because no experimental values were found for it and neither for the Cu⁺ ions.

Hence, it was assumed in a first approximation that diffusion is not determined by the charge of the particle and therefore the same diffusion coefficient was adopted for the Cu atoms and Cu⁺ ions in Ar.

The production of Cu atoms ($S_{\text{prod}}^{\text{Cu}}$) is given by the normalized thermalization profile of the Cu atoms (F_t) factorized by the total sputtered flux of Cu atoms: $J^{\text{Cu}} = J_r^{\text{Cu}} + J_z^{\text{Cu}}$, where J_r^{Cu} , J_z^{Cu} and F_t are calculated in the MC model for fast Cu atoms (see above, paragraph 2.3.3) and the subscripts r and z denote the sputtering from the the cylinder side-walls and cathode bottom, respectively. The term $S_{\text{loss}}^{\text{Cu}}$ represents the loss of Cu atoms due to the ionization processes considered. Hence this term also gives the creation rate of the Cu^+ ions. $S_{\text{e,ion,Cu}}$ is the electron impact ionization rate of Cu, calculated in the MC model for the fast electrons. The second and third terms of $S_{\text{loss}}^{\text{Cu}}$ stand for the ionization rate of Cu atoms by ACT with Ar^+ ions and by Penning ionization with Ar^m metastables, respectively. The rate coefficient for ACT with Ar^+ ions (k_{ACT}) and for Penning ionization (k_{pen}) were taking equal to 2×10^{-10} and $2.6 \times 10^{-10} \text{ cm}^3 \text{ s}^{-1}$, respectively.⁶¹

The continuity equations of Cu^+ ions and Cu atoms are coupled through $S_{\text{loss}}^{\text{Cu}} = S_{\text{prod}}^{\text{Cu}^+}$. Both equations are discretized and solved with the extended Thomas algorithm for a pentadiagonal matrix.⁴¹ The boundary conditions for this system were determined by the sticking coefficients of copper atoms and ions. For the Cu atoms, a sticking coefficient of 0.5 was assumed, which means that at the walls, the Cu atoms will be reflected or absorbed in the same proportion. This value was assumed based on the experimental evidence that the sticking coefficient for the sputtered atoms should be less than one⁶³ and on the comparison between measured and calculated sputtered densities presented in Ref. 64. As boundary conditions for the Cu^+ ions, a complete recombination at the walls (anode and cathode) is assumed, i.e., a sticking coefficient equal to 1, $n^{\text{Cu}^+} = 0$.

2.5 Coupling of the Models

The various sub-models are coupled to each other, because of the interactions between the various species. Hence, the output of one sub-model is used as input in the other sub-models. The coupling is shown schematically in Fig.2.4, and will be explained in more detail below.

First the Monte Carlo model for fast electrons (e^f -MC) is run. In the first iteration an initial electric field has to be proposed. Our initial assumption was a linearly decreasing electric field in the CDS and a constant electric field in the NG. At the “cylinder corner”, i.e., in the CDS belonging both to the cathode bottom and the cathode sidewalls, the electric field was assumed to have an axial and a radial component and each component is a function of the radial and the axial coordinates. Also for the first iteration, a uniform gas ion flux to the cathode walls was assumed, based on the value of measured discharge current. The secondary electron emission coefficient (γ), equal to 0.08⁶⁵ and 0.3^{66,67} were used only for the first iteration in the Ar-Cu and He-Ni HCD simulations, respectively

For further iterations, beside the electrons emitted from the cathode walls, and the electrons formed by electron impact ionization, also all the new electrons, created by metastable-metastable ionization (and in the case of Ar-Cu HCD, also by fast Ar⁺ ion, fast Ar^f atom, Ar^m and Penning ionization collisions), are followed. γ was calculated in each e^f -MC cycle of the model, based on the condition for a self-sustained discharge (see below, paragraph 3.2). Assuming that the gas ion and metastable induced secondary electron emission coefficients are similar,⁶⁸ the electron flux at the cathode (J^e) is calculated through the γ coefficient and the gas ion ($J_{cat}^{g^+}$) and metastable ($J_{cat}^{g^m}$) fluxes at the cathode, as $J^e = \gamma (J_{cat}^{g^+} + J_{cat}^{g^m})$. The flux of fast Ar^f atoms was not considered in the electron-induced emission, because at a clean cathode surface (as a result of sputtering) the threshold for this process is 500 eV.^{65,69} Output of the e^f -MC used as input in the gas ion and slow electron fluid model (g^+ ,e-fluid) includes the γ coefficient, used to calculate the electron component of the total current at the cathode, the fast electron density and the gas ion ($S_{e,ion}$) and slow electron creation (S_{slow}) rates.

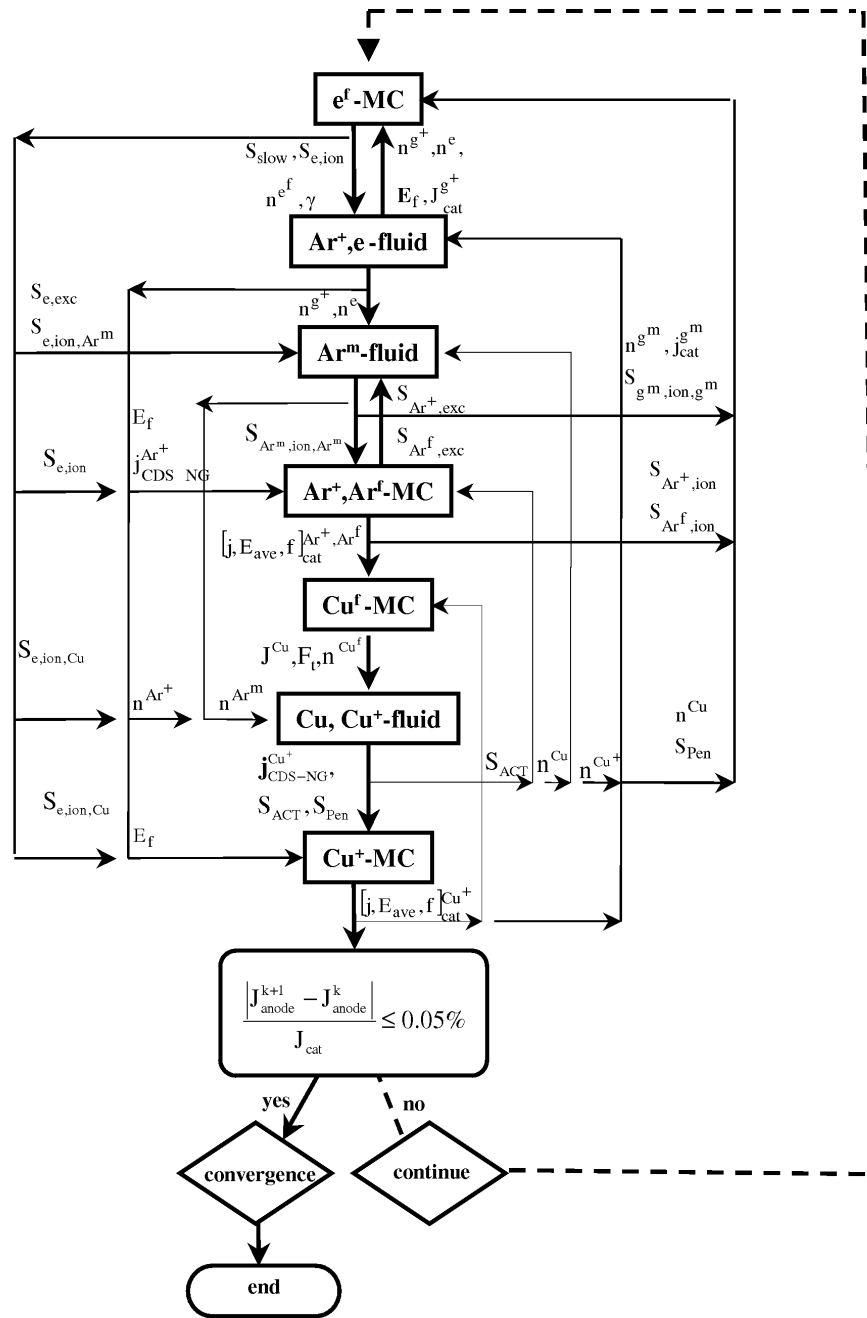


Fig. 2.4 Flowchart of the coupling of the various sub-models in the hybrid model for the HCD.

Output of the e^f -MC model, used for the metastable atom-fluid model (Ar^m -fluid), is the production rate of the metastable atoms due to electron impact excitation from the ground state ($S_{e,exc}$) as well as the loss rate due to electron impact ionization from the metastable level (S_{e,ion,Ar^m}).

Output of the e^f -MC model, used as input in the MC model for the fast Ar^f atoms and fast Ar^+ ions (Ar^+, Ar^f -MC), is the electron impact ionization rate ($S_{e,ion}$), which gives the number of Ar^+ ions created by electron impact ionization.

The electron impact ionization rate of Cu atoms ($S_{e,ion,Cu}$) calculated here is needed in the fluid model for the copper ions and atoms (Cu, Cu^+ -fluid), giving the loss of Cu atoms due to electron impact ionization, and it is also needed in the MC model for fast Cu^+ ions (Cu^+ -MC), where it gives the initial position of the Cu^+ ions created due to electron impact ionization.

Secondly, the g^+, e -fluid model is run with the source terms for the creation rate of gas ions and bulk electrons (i.e., $S_{e,ion}$ and S_{slow} , respectively). It yields the gas ion and electron densities, the axial and radial gas ion and electron density fluxes, and the axial and radial electric field distribution. The electric field and the gas ion flux to the cathode walls and gas ion density flux to the CDS-NG interface ($j_{CDS-NG}^{g^+}$) will be used as input for the MC models for fast electrons, fast Ar^+ ions, fast Ar atoms and fast Cu^+ ions. The ion and electron densities are used in the metastable and in the Cu^+ and Cu atom fluid models to calculate certain production and loss rates, which are not provided from the MC models.

Third, the Ar^m -fluid model is run with production and loss rates due to Ar^+ ion, fast Ar^f atom and fast electron collisions, calculated in the corresponding MC models, and the density of electrons (n^e) and Cu atoms, calculated in the respective fluid models. The output of this model includes the density of the collective metastable state (n^{g^m}) and the flux of metastable atoms bombarding the cathode ($J_{cat}^{g^m}$). These results are both used in the e^f -MC model, to determine the electron impact ionization from the metastable level (S_{e,ion,g^m}), and the secondary electron emission at the cathode due to the flux of metastable gas atoms, respectively. The fluid model for the metastable atoms also yields the ionization rate due to metastable-metastable collisions (S_{g^m,ion,g^m}), which is used in the Ar^+, Ar^f -MC model and in the e^f -MC model to determine the starting position of the

new Ar^+ ions and fast electrons, respectively. Moreover, the metastable atom density is required as input in the Cu, Cu^+ -fluid model for the calculation of the loss of Cu atoms (production of Cu^+ ions) due to Penning ionization.

Fourth, the Ar^+ , Ar^f -MC model is run. As input this sub-program requires the number of Ar^+ ions created inside the CDS, the Ar^+ ions starting at the CDS-NG interface and the electric field distribution in the CDS, as well as the loss of Ar^+ ions due to ACT collisions (calculated in the Cu, Cu^+ -fluid model) and the rate of newly created fast Ar^f atoms due to Cu^+ ion elastic collisions (calculated in the Cu^+ -MC model). This model yields, among others, the fast Ar^+ ion and fast Ar^f atom impact ionization rates, $(S_{\text{Ar}^+, \text{ion}}, S_{\text{Ar}^f, \text{ion}})$ giving the position for the newly created electrons to be followed in the e^f -MC model, the Ar^+ ion and fast Ar^f atom impact excitation rates to the Ar^m metastable levels, $(S_{\text{Ar}^+, \text{exc}}, S_{\text{Ar}^f, \text{exc}})$ used as input in the Ar^m -fluid model, as well as the bombarding fluxes (axial and radial), the average energy and the energy distribution at the cathode of the Ar^+ ions and fast Ar^f atoms, which are used as input in the Cu^f -MC model.

Fifth, the MC model for the fast (sputtered) Cu^f atoms (Cu^f -MC) is run. As input, this sub-program requires the bombarding flux (axial and radial), the average energy and the energy distribution at the cathode of the Ar^+ ions and fast Ar^f atoms. This sub-model also requires as input, the bombarding flux, the average energy and the energy distribution at the cathode of the Cu^+ ions. This is, however, added after it is calculated in the MC model for the fast Cu^+ ions. This Cu^f -MC model yields the sputtered Cu flux from the cathode (J^{Cu}), the thermalized Cu atom profile (F_t) and the density of the non-thermalized Cu atoms throughout the discharge (n^{Cu^f}), which are the input for the fluid model for Cu atoms and Cu^+ ions (Cu, Cu^+ -fluid).

Sixth, the Cu, Cu^+ -fluid model is run. It yields, among others, the densities and fluxes of the Cu atoms and Cu^+ ions. The Cu^+ ion density flux at the CDS-NG interface ($j_{\text{CDS-NG}}^{\text{Cu}^+}$) is required as input in the Cu^+ -MC model to determine the starting position of the Cu^+ ions. The Cu atom density (n^{Cu}) is needed in the metastable atom fluid model for the calculation of metastable atom loss due to Penning ionization, as well as in the e^f -MC model for calculating the electron impact ionization rate of Cu atoms. The Cu^+ ion density, n^{Cu^+} , is required as input in the Ar^+ ion and slow electron fluid model to calculate the total charge density, which is needed for the Poisson equation. Moreover, the Cu, Cu^+ -fluid model yields the creation rates of Cu^+ ions due to Ar^+ ion ACT

collisions (S_{ACT}) and Penning ionization (S_{Pen}) collisions, which define the position for the newly created Cu^+ ions and electrons to be followed in the Cu^+ -MC and e^f -MC models, respectively. The ACT collision rate of the Ar^+ ions with the Cu atoms is also given as input in the Ar^+ , Ar^f -MC model in order to account for the loss of Ar^+ ions that this process implies

Finally, the MC for fast Cu^+ ions is run. As input it requires the electric field distribution in the CDS, together with the number of Cu^+ ions created inside the CDS, as well as the Cu^+ ions starting at the CDS-NG interface, which are obtained from the e^f -MC and Cu, Cu^+ -fluid models, respectively. Among others, this Cu^+ -MC model gives the average energy ($E_{ave}^{Cu^+}$), the bombarding flux ($j_{cat}^{Cu^+}$) and the energy distribution at the cathode of the Cu^+ ions ($f_{cat}^{Cu^+}$), which are used to calculate the sputtered flux due to the bombardment of Cu^+ ions (self-sputtering) in the Cu^f -MC model (see above). As a result of elastic collisions of these energetic Cu^+ ions with the background Ar atoms, ($S_{Cu^+,ela}$) fast Ar^f atoms can be created, which are followed in the Ar^+ , Ar^f -MC model.

As mentioned before, to obtain a correct electric field distribution, the ionization rate due to the fast electrons is the main value. Therefore for the first iterations in order to obtain a good enough electric field distribution and at the same time to reduce time and effort, only the e^f -MC and the gas ion-slow electron- fluid sub-models for the Ar-Cu HCD were run iteratively until convergence was reached. In the case of the He-Ni HCD model, due to the importance of the metastable atoms for the production of charged particles, the fluid model for the He^m atoms was also included.

It was considered that the convergence was reached when the difference in the total current to the anode in two successive iterations, was below 1%. Typically, 7 to 12 iterations were carried out before convergence was reached (depending on the discharge conditions and discharge gas). The total current to the cathode was not taken as a criterion of convergence, because the difference between two successive iterations was already below to 10^{-2} after a few iterations, as can be seen from Fig. 2.5.

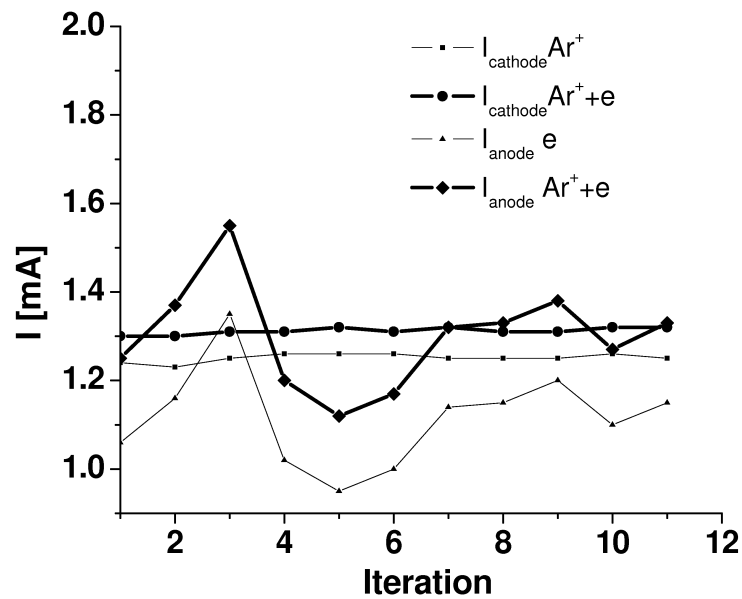


Fig. 2.5 Calculated value of the charged particle fluxes to the anode and cathode as a function of time (given by the number of iterations) for an Ar-Cu HCD at a pressure of 0.3 Torr and at 1.29 mA. Note how the gas ion flux to the cathode stays constant, while the amplitude of the curve representing the electron current to the anode decreases and become closer to the value of the total current to the cathode.

In Fig. 2.5 it is also possible to see how after successive iterations, the criterion adopted for convergence here, is reached. Indeed, the electron and total (ion and electron) fluxes to the anode as a function of time (i.e., represented through the number of iterations) oscillate from the value of total current to the cathode, until these oscillations become smaller and the total current to the anode and to the cathode become almost equal.

Next when a good enough electric field distribution was calculated the other sub-models for the descriptions of the fast Ar^+ ions and atoms and the sputtered species were added. Hence the above seven sub-models were run iteratively, until convergence was reached. The latter was determined by the difference in the total current to the anode in two successive iterations, which should be below 0.05 %. Typically, 3-4 iterations were carried out before convergence was reached.

2.6 References

- ¹ M. Surendra, D. B. Graves and G. M. Jellum, *Phys. Rev. A* **41**, 1112 (1990).
- ² J. P. Boeuf and L. C. Pitchford, *IEEE Trans. Plasma Sci.* **19**, 286 (1991).
- ³ A. Fiala, L. C. Pitchford and J. P. Boeuf, *Phys. Rev. E* **49**, 5607 (1994).
- ⁴ L. C. Pitchford, N. Ouadoudi and J. P. Boeuf, *J. Appl. Phys.* **78**, 77 (1995).
- ⁵ Z. Donko, *Phys. Rev. E* **57**, 7126 (1998).
- ⁶ A. Bogaerts, R. Gijbels and W. Goedheer, *J. Appl. Phys.* **78**, 2233 (1995).
- ⁷ J. M. Boyd and J. J. Sanderson, *Plasma dynamics*, (Nelson, London, 1969).
- ⁸ N. Bagger, A. Bogaerts and R. Gijbels, *J. Appl. Phys.* **94**, 2212 (2003).
- ⁹ J. E. Lawler, *Phys. Rev. A* **32**, 2977 (1985).
- ¹⁰ N. Bagger, A. Bogaerts, R. Gijbels, *Spectrochim. Acta Part B* **57**, 311 (2002).
- ¹¹ A. C. Dexter, T. Farrell, M. I. Lees, *J. Appl. Phys. D* **22**, 413 (1989).
- ¹² M. Surendra, D. B. Graves and G. M. Jellum, *Phys. Rev. A* **41**, 1112 (1990).
- ¹³ R. V. Stuart and G. K. Wehner, *J. Appl. Phys.* **35**, 1819 (1964).
- ¹⁴ H. Helm, *Z. Naturforsch.* **27a**, 1812 (1972).
- ¹⁵ A. Okhrimovskyy, A. Bogaerts and R. Gijbels, *Phys. Rev. E* **65**, 37402 (2002).
- ¹⁶ E. A. Rainville and P. E. Bedient, *Elementary differential Equations* (Collier-Macmillan Ltd, London, 1972).
- ¹⁷ J. B. Hasted, *Physics of Atomic Collisions*, (Butterworths, London, 1972).
- ¹⁸ N. R. Whetten, R. C. Wheat and M. J. Astle, *CRC Handbook of Chemistry and Physics*, p. E-372 (CRC, Boca Raton, 1982).
- ¹⁹ B. Chapman, *Glow Discharge Processes*, (Wiley, New York, 1988).
- ²⁰ A. V. Phelps, *J. Appl. Phys.* **76**, 747 (1994).
- ²¹ A. V. Phelps, *J. Phys. Chem. Ref. Data* **20**, 557 (1991).
- ²² E. W. McDaniel and E. A. Mason, *The mobility and diffusion of ions in gases* (Wiley, New York, 1973).
- ²³ W. D. Davis, T. A. Vanderslice, *Phys. Rev.* **131**, 219 (1963).
- ²⁴ N. Matsunami, Y. Yamamura, Y. Itikawa, N. Itoh, Y. Kazumata, S. Miyagawa, et al., *Atom. Data and Nucl. Data Tables* **31**, 1 (1984).
- ²⁵ P. Sigmund, *Topics in Applied Physics* (Springer, Berlin, 1984).
- ²⁶ J. A. Valles Abarca and A. Gras-Marti, *J. Appl. Phys.* **55**, 1370 (1984).
- ²⁷ J. Linhard, M. Scharff and H. E. Schiott, *Mat. Fys. Medd. Dan. Vid. Selsk.* **33**, No 14 (1963).
- ²⁸ J. Sielanko, *Radiat. Eff. Lett.* **86**, 185 (1984).
- ²⁹ Z. Wronski, *Vacuum* **42**, 635 (1991).

- ³⁰ T. C. Bradbury, *Mathematical Methods with Applications to Problems in the Physical Sciences* (Wiley, New York, 1984)
- ³¹ K. Kutasi, Z. Donko, J. Appl. Phys. **63**, 1081 (2000).
- ³² M. A. Khodorovskii, Ph. D. thesis, University of St. Petersburg, 1975.
- ³³ P. Boeuf, L. C. Pitchford, J. Phys. D **28**, 2083 (1995).
- ³⁴ A. L. Ward, J. Appl. Phys. **33**, 2789 (1962).
- ³⁵ P. Boeuf, J. Appl. Phys. **33**, 1342 (1988).
- ³⁶ R. Deloche, P. Monchicourt, M Cheret and F. Lambert, Phys. Rev. A **13**, 1140 (1976).
- ³⁷ D. Paschier, Ph. D. thesis, University of Utrecht, 1994.
- ³⁸ D. Paschier, W. J. Goedheer, J. Appl. Phys. **74**, 3744 (1993).
- ³⁹ H. K. Gummel, IEEE Trans. Electron Devices **11**, 455 (1964)
- ⁴⁰ D. L. Scharfetter and H. K. Gummel, IEEE Trans. Electron Devices **16**, 64 (1969)
- ⁴¹ D. U. Rosenberg, *Methods for the numerical solutions of partial differential equations* (New York, Elsevier, 1969).
- ⁴² A. V. Phelps, Phys. Rev. **99**, 1307 (1955).
- ⁴³ T. J. Sommerer, M. Kushner, J. Appl. Phys. **71**, 1654 (1992).
- ⁴⁴ H. M. Katsch, E. Quandt, Th. Schneider, Plasma Phys. Control Fusion **38**, 183 (1996)
- ⁴⁵ D. P Lymberopoulos and D. J. Economou, J. Appl. Phys. **73**, 3668 (1993).
- ⁴⁶ A. Bogaerts and R. Gijbels, Phys. Rev A **52**, 3743 (1995).
- ⁴⁷ N. Baguer, A. Bogaerts, Z. Donko, R. Gijbels and N. Sadeghi, J. Appl. Phys. **97**, in press (2005).
- ⁴⁸ K. Tachibana, Phys. Rev. A **34**, 1007 (1986).
- ⁴⁹ N. Sadeghi, M. Cheaib, and D.W. Setser, J. Chem. Phys. **90**, 219 (1989).
- ⁵⁰ N. J. Mason, W. R. Newell, J. Phys. B **20**, 1357 (1987).
- ⁵¹ V. Puech and L. Torchin, J. Phys. D **19**, 2309 (1986).
- ⁵² A. Phelps, jilawww.colorado.edu/research/colldata.html
- ⁵³ N. Baguer, A. Bogaerts and R. Gijbels, J. Appl. Phys. **93**, 47 (2003).
- ⁵⁴ P. Macko and N. Sadeghi, Plasma Source, Sci. Technol., **13**, 303 (2004).
- ⁵⁵ H. Conrad, G. Ertl, J. Küppers, W Sesselmann, B. Woratschek, and H. Haberland, *Surface Science* **117**, 98 (1982).
- ⁵⁶ H. D. Hagstrum, Phys. Rev. **96**, 336 (1954).
- ⁵⁷ G. Hohler, *Particle Induced Electron Emission II*, (Springer, Berlin, 1992)
- ⁵⁸ M. A. Biondi, Phys. Rev. **129**, 1181 (1963).
- ⁵⁹ C. M. Ferreira, L. Loureiro and A. Ricard, J. Appl. Phys. **54**, 2261 (1983)
- ⁶⁰ A. V. Phelps and J. P Molnar, Phys. Rev **89**, 1202 (1952).

-
- ⁶¹ A. Bogaerts and R. Gijbels, *J. Appl. Phys.* **79**, 1279 (1996).
- ⁶² J. O. Hirschfelder, C. F. Curtis and R. B. Bird, *Molecular Theory of Gases and Liquids*, (Wiley, New York, 1954)
- ⁶³ R. M. Allot, M Kubinyl, A. Grofcsik, W. J Jones and R. S. Mason, *J. Chem. Soc Faraday Trans.* **9**, 1297 (1995).
- ⁶⁴ A. Bogaerts, E Wagner, B.W. Smith, J.D. Winefordner, D. Pollmann, W.W. Harrison and R. Gijbels, *Spectr. Acta Part B* **52**, 205 (1997).
- ⁶⁵ A. V. Phelps and Z. Lj. Petrovic, *Plasma sources Sci. Technol.* **8**, R21-R44 (1999).
- ⁶⁶ F. Stebbings, *Proc. Roy. Soc. (London) A* **241**, 270 (1957).
- ⁶⁷ E. A. Den Hartog, D. A. Doughty, J. E. Lawler, *Phys. Rev. A* **41**, 2471 (1988).
- ⁶⁸ J. B. Hasted, *J. Appl. Phys.* **30**, 22 (1959).
- ⁶⁹ A. Bogaerts and R. Gijbels, *Plasma Sources Sci. Technol.* **11**, 27 (2002).

Chapter 3

Fundamental electric and spectrometric characteristics of the HCD

Some of the fundamental characteristics of the hollow cathode glow discharge are presented for different discharge conditions, based on a hybrid Monte Carlo-fluid model, and on electrical and spectroscopic measurements. The Monte Carlo model describes the movement of the fast electrons as particles, while in the fluid model, the slow electrons and positive gas ions are treated as a continuum. The transient continuity equations are solved together with the Poisson equation in order to obtain a self-consistent electric field. The source terms of the continuity equations and the electron multiplication coefficient (used for the determination of the secondary electron emission coefficient) are obtained from the Monte Carlo simulation. These two models are run iteratively until convergence is reached. Typical results are, among others, the charged particles densities, the fluxes, the electric field and potential distribution. It is found that the influence of the bottom of the cylindrical hollow cathode cannot be neglected. A very good agreement between calculations and experimental data was obtained

3 Fundamental electric and spectrometric characteristics of the HCD

3.1 Introduction

Most studies i.e., analytical models, experiments or mathematical simulations dealing with cylindrical HCDs are focused only on the radial properties of the discharge, assuming a hollow cathode of infinite length and hence a discharge uniform in the axial direction.¹⁻⁷ Here we intend to simulate the cylindrical geometry of a HCD as realistically as possible taking into account the effect of the ends of the hollow cathode in the discharge.

In this chapter some of the fundamental characteristics of the hollow cathode glow discharge are presented for different discharge conditions, based on a hybrid Monte Carlo-fluid model, and on electrical and spectroscopic measurements.

In the numerical simulation only the behavior of the electrons and slow ions were included, as these particles are the most important in determining the electrical properties of the discharge. Therefore in this part, the hybrid model is based on the coupling of the MC model for fast electrons and the fluid model for slow electrons and ions.

3.2 Geometry and discharge conditions

The discharge geometry consists of a cylindrical cathode closed at one end and a disc anode at the other end, separated by 0.2 cm (Fig. 3.1). In a classical HCD the length of the cylinder is typically 5 to 10 times larger than the radius in order to reduce the loss of electrons through the open end of the cylinder. We assumed a length of 3 cm and a radius of 0.5 cm.

The discharge conditions assumed in the model were taken from the experiments, i.e., the gas pressure was varied from 0.3 to 1 Torr, the discharge current ranged from 1 to 10 mA and a discharge voltage between 240 and 300 V was

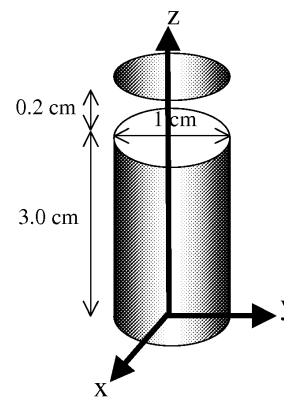


Fig. 3.1 Schematic picture of the cell geometry used in the model and in the experiments.

applied to the cathode, whereas the anode was grounded. The gas temperature was assumed to be at room temperature, 300K.⁸

The collision processes considered in the model were electron impact ionization, electron impact excitation and electron elastic collisions with the Ar ground state atoms. The corresponding cross sections were obtained from Phelps⁹ (see Table 2.2 and Fig. 2.2). The first excitation threshold of the ground state Ar atoms (11.55 eV) was taken as the energy threshold for considering the electrons as fast particles.

3.3 Experimental set up

The cylindrical HCD with the same dimensions as in Fig. 3.1 was placed in a Pyrex envelope. Both anode and cathode were made of high purity copper, and high purity argon was used as the discharge gas. The discharge was operated in dc mode and digital multimeters measured the discharge current and the voltage. The background pressure of the vacuum system was about 10^{-6} Torr.

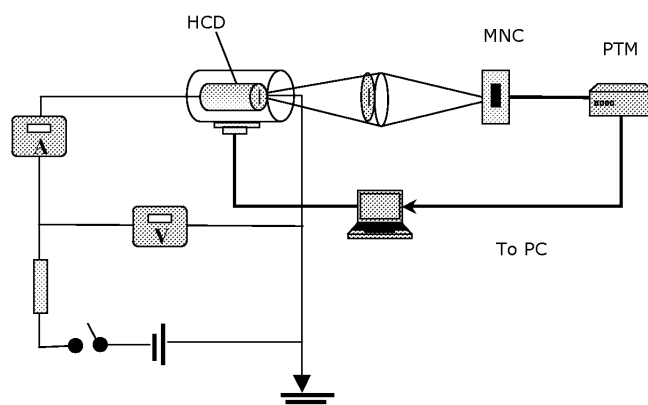


Fig. 3.2 Schematic overview of the experimental setup, where HCD stand for the hollow cathode discharge cell, MNC for the monochromator and PTM, for the photo multiplier tube.

The spatial distribution of the light emission intensity in the discharge was scanned in the radial direction. For this aim, a 0.05 cm slit was machined into the anode disc along its diameter and the discharge tube was mounted on a precision translator equipped with a stepping motor driven by a PC. A 10 cm focal length quartz lens imaged the light of the discharge onto the entrance slit of a monochromator (MNC). A diaphragm

was placed in front of the lens to obtain sufficient spatial resolution. For the recording of the spectral lines a photomultiplier tube (PMT) type EMI 9558B was used. The digitised signal of the PMT was sent to the PC, using an IEEE488 interface. The PC also controlled the wavelength positioning of the monochromator when recording the spectral scans (see Fig. 3.2).

3.4 Electrical conditions and emission intensities

The measured and calculated current-voltage dependence (V - I) in the pressure range from 0.3 to 1 Torr is presented in Fig. 3.3. For each pressure about 20 V - I points were measured. The symbols denote the conditions for which the calculations were performed (typically at 5 to 7 V - I values per pressure).

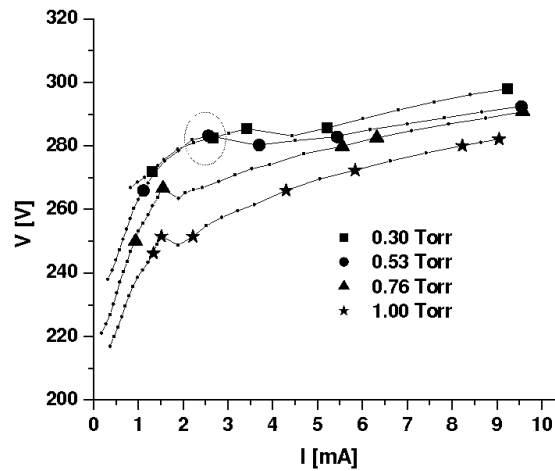


Fig. 3.3 Voltage-current dependence at different pressures. The lines with small points show the experimental measurements and the larger symbols represent the modeled discharge conditions. The spotlighted area shows the optimal discharge conditions for the occurrence of the hollow cathode effect.

In the calculations the total secondary electron emission coefficient, γ , was calculated in the Monte Carlo model based on the condition for the self-sustained discharge, under the assumption that the Ar^+ ions were the main source of electron emission from the cathode, and that there is no recombination in the plasma or other volume losses, which is a correct approximation in our pressure range.¹⁰ Then the condition for a self-sustained discharge can be written as: $\gamma = \frac{1}{M}$, where M is the so-

called electron multiplication coefficient, defined as the amount of electrons created in

the discharge per electron ejected from the cathode due to the Ar^+ ion induced secondary electron emission. In this way, γ was not taken constant¹¹⁻¹³ or used as a fitting parameter like in other works,¹⁴ but as a parameter really reflecting the amount of electron impact ionisation in the discharge. The obtained γ as a function of the reduced electric field at the cathode wall (i.e., the ratio of the electric field, (E) to the gas density (n)) is shown in Fig. 3.4.

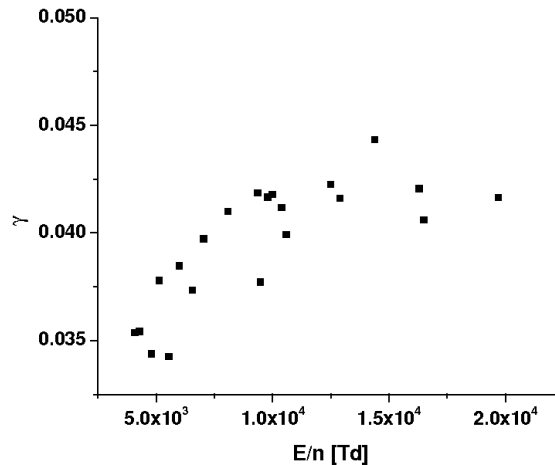


Fig. 3.4 Calculated secondary electron emission coefficient (γ) as a function of the reduced electric field (E/n).

Because the electric field is also a function of the axial position, we took as a representative value of the electric field at the cathode wall the value at $z = 1.5$ cm. The value of γ obtained here varies very little from 0.035 to 0.042 corresponding to a reduced electric field (E/n) from 5.10^3 Td to 2.10^4 Td, respectively. This value is in good agreement with the values obtained by Kruihof¹⁵ for an Ar discharge in which the copper cathode was cleaned by sputtering without high temperature flashing, which is also true in our case. With these values of γ , we obtained a good agreement between the experimental and calculated V - I dependence. Hence, we can conclude that the assumption is justified, that in a HCD in this range of discharge conditions, the secondary electron emission by Ar^+ ions is the predominant process.

In the review work of Phelps¹⁶ it is suggested that in this range of E/n the total secondary electron emission coefficient began to deviate from the ion-induced secondary electron emission coefficient. However, Ref. 16 deals with planar-cathode discharges in

Ar in normal and abnormal glow modes, where it is expected that at $E/n > 10^4$ Td (which corresponds for these glow modes, to a discharge voltage greater than 500 V) the role of ionization by heavy particles becomes important, and then the total secondary electron yield increases, while the ion-induced secondary electron emission coefficient stays constant. The ionisation by heavy particles begins to become important only for ion energies above 500 eV,¹⁷ which means that the discharge voltage should be at least 500 V. However we are dealing with a cylindrical HCD in which the discharge voltage is clearly below 500V (see Fig. 3.3 above). Although a cylindrical HCD is also a kind of glow discharge it can, due to its distinguished properties, not be classified as a normal or an abnormal discharge, but it is classified as a conventional hollow cathode discharge.¹⁸ It should be mentioned that in the conventional HCDs the discharge voltage is lower than in a glow discharge for the same current density and pressure. Hence, the same value for E/n can be reached as in a glow discharge, at the same current density and pressure but at a lower voltage, so that heavy particle ionization is not yet important in this range of E/n for cylindrical HCDs.

The $V-I$ dependence of a HCD has two well-defined regions (see Fig. 3.3, above): one at low current density characterized by a steep slope and the other one, at higher current density with a smaller slope. For all the curves a region of transition between steep and small slope was observed. Moreover, it appears also from Fig. 3.3 that the transition region is not continuous at certain points. This was experimentally checked many times; to be sure that it was not a systematical error in the measurements. In fact at these $V-I$ conditions of the discontinuity, the light emission was most intense, i.e., it looks as if at these conditions the hollow cathode effect is optimal. Indeed at conditions where the light emission is most intense, the excitation processes are the most efficient.¹⁹ This follows also from our simulation results. Indeed, it was found that for all pressures analysed here, the average amount of excitation per electron emitted by the cathode (M_{exc}) was maximal at the $V(I)$ points corresponding to the transition region, which suggests the most intense light emission.

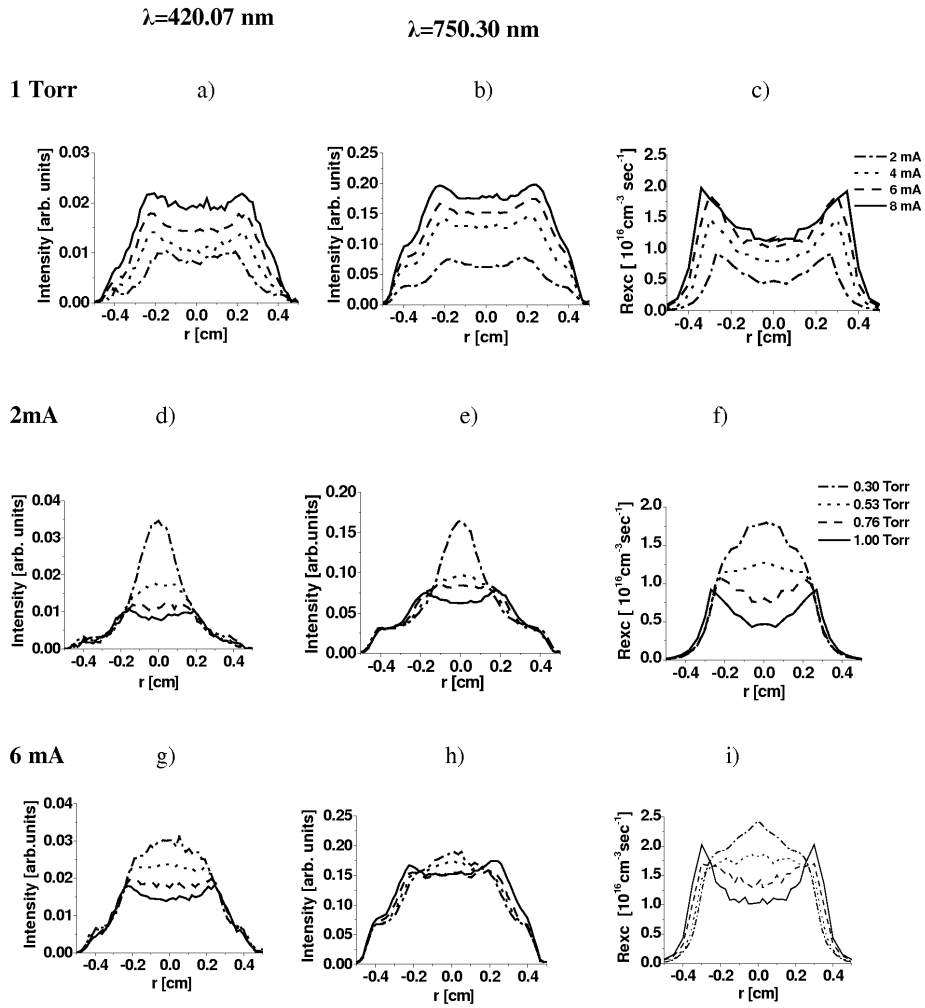


Fig. 3.5 Comparison of the radial profile of the recorded emission intensity for ArI 420.07 nm, ArI 750.30 nm and of the calculated electron impact excitation rate of the Ar atoms at $z = 1.5$ cm, at constant pressure (1 Torr) for different currents (a, b and c), and at constant current for different pressures at 2 mA (d, e and f) and at 6 mA (g, h and i), respectively.

Having in mind that the electron impact excitation is the main source of light in the NG²⁰ we have measured the spectral lines of ArI 420.07 nm, ArI 603.2 nm and ArI 750.3 nm, which are mainly produced by electron impact excitation.¹⁹ Fig. 3.5 shows the measured emission light intensities of some ArI lines (Figs. 3.5 (a), (d), (g) for ArI 420nm, and Figs. 3.5 (b), (e), (h) for ArI 750.3nm) and the calculated total electron impact excitation rate (Figs. 3.5 (c), (f), (i)) as a function of radial position. It is clear that

the results of the measurements and of the calculations show a similar shape and also behave similarly as a function of pressure and current.

In Refs. 18 and 21 it was suggested that the optimal discharge condition (pressure, current and voltage) for the occurrence of the hollow cathode effect is reached when at constant voltage, the current increases with a decrease in pressure, or when at constant current, the discharge voltage drops with a decrease in pressure. In order to check this, we plotted the current-pressure dependence (see Fig. 3.6).

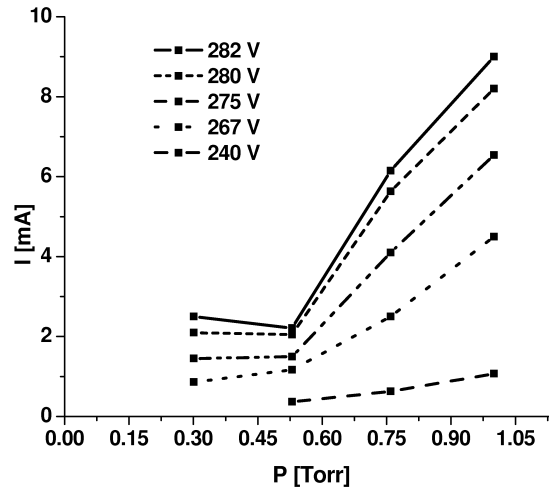


Fig. 3.6 Calculated and measured current-pressure dependence at constant voltage.

It appears that in our discharge this happens for a pressure between 0.3 and 0.53 Torr and for a current around 2 mA (see also Fig. 3.3). Hence at these conditions the intensity of the spectral lines should be maximal, as can indeed be observed in the second and third row of Fig. 3.5, where the spectral line intensities and the calculated electron impact excitation rate obtained for a discharge current of 2 mA and 6 mA are plotted at different pressures. For both currents (2 and 6 mA) the maximum intensities of the spectral lines, as well as the maximum of the electron impact excitation rate, were obtained at a pressure of 0.3 Torr and the effect is most pronounced at the current of 2 mA. From Fig. 3.6 this effect is only visible at the discharge voltage of 282 V. It appears from Fig. 3.3 that the optimal condition for the hollow cathode effect occurs in the voltage range from 279 to 283 V (see spotlighted area). At the other voltages in the $I(P)$ dependence, the current decreases very slowly or stays constant with decreasing pressure,

in the pressure range of 0.3 to 0.53 Torr. With further decrease in the pressure without increasing the voltage, the discharge current will drop until the discharge will burn out.

3.5 Calculated quantities as a function of discharge conditions

In the following part, the influence of the current and pressure on the discharge behaviour is analysed in more detail. The calculated two-dimensional profiles of the electron impact ionization rate, electron density, potential distribution and axial electric field for different conditions are shown in Figs. 3.7 to 3.9. Figs. 3.7 and 3.8 illustrate the results at 1 Torr and a current of 9 mA and 1.4 mA, respectively, which correspond to the region of small and steep slope, respectively. Fig. 3.9 shows the results at 0.3 Torr and 9 mA (small slope). The thick black lines in the figures represent the cathode walls.

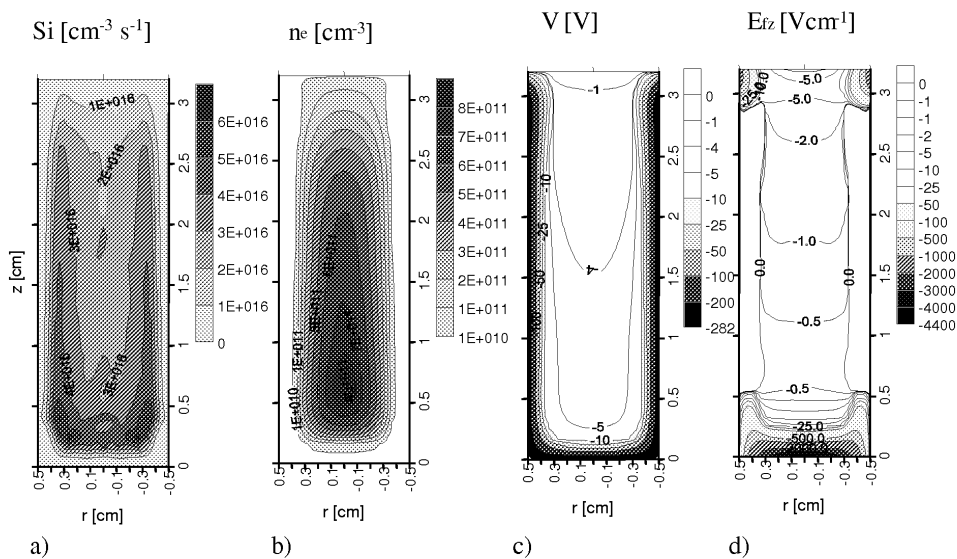


Fig. 3.7 Two-dimensional profile throughout the discharge at a pressure of 1 Torr and a current of 9 mA: (a) the electron impact ionization rate of the Ar atoms, (b) the slow electron density, (c) the potential distribution, (d) the axial electric field.

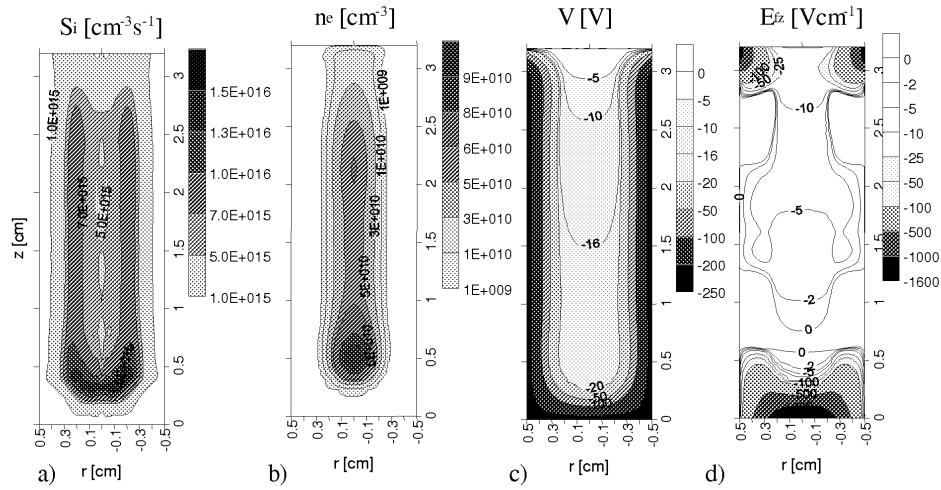


Fig. 3.8 Two-dimensional profile throughout the discharge at a pressure of 1 Torr and a current of 1.4 mA: (a) the electron impact ionization rate of the Ar atoms, (b) the slow electron density, (c) the potential distribution, (d) the axial electric field.

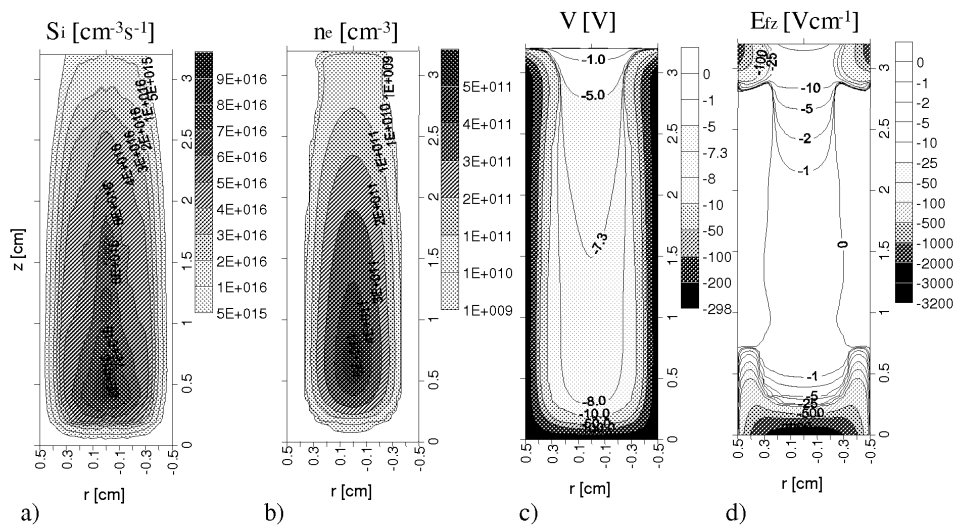


Fig. 3.9 Two-dimensional profile throughout the discharge at a pressure of 0.3 Torr and a current of 9 mA: (a) the electron impact ionization rate of the Ar atoms, (b) the slow electron density, (c) the potential distribution, (d) the axial electric field.

3.5.1 Electron collision rates

For all the conditions analyzed here, the absolute maximum of the electron impact ionization and excitation rates were observed near the bottom of the cathode cylinder in the NG region (Figs. 3.7a to 3.9a). This is a consequence of the strong axial and radial electric field in this region, which creates a flux of electrons with high energy in both directions.

Hence, a large amount of ionization will occur, while in the rest of the discharge only the radial electric field remains strong. At a pressure of 1 Torr, the excitation and ionization rate profiles are more or less uniform in the axial direction along the discharge and they show a peak in the radial direction in the NG near the CDS-NG interface for all currents (see Figs. 3.7a, 3.8a). This can also be observed in Fig. 3.5, where the measured spectral lines intensities for ArI 420.07 nm, ArI 750.3nm and the calculated electron impact excitation rates as a function of the radial distance at $z = 1.5$ cm, are plotted for different currents at 1 Torr pressure (Figs. 3.5 (a), (b), (c)). With decreasing current, the position of these peaks shifts toward the cylinder axis because the sheath length increases. Moreover, the absolute value of the rates decreases. With decreasing pressure, (compare Figs. 3.7a with 3.9a), the NG from the opposite sides of the cathode sidewalls start to collapse and at 0.3 Torr the collapse is completed, i.e. there are not two separate peaks at the two NG-CDS interfaces, but a common peak at the cylinder axis, corresponding to the best regime for the hollow cathode effect (HCE), as mentioned above (see also Figs. 3.5 (d)-(i)).

The variation in the radial positions of the collision rate maximum can be best explained based on the electron energy distribution function (see Fig 3.10). The electrons emitted from the cathode as well as the new ones created from ionisation collisions are accelerated by the strong electric field present in the CDS. The maximum possible energy for the electrons can be reached at the end of the CDS, i.e. close to the CDS-NG interface. Due to the inelastic collisions, the electron energy distribution is spread out over lower energies. At 1 Torr the electron collision frequency is high, and only a few electrons reach the axis region ($r = 0$) with enough energy to cause inelastic collisions (see Fig. 3.10a). Therefore a dip in the collisions rate profiles is observed. With decreasing pressure, the discharge gas density drops. Then, the collision frequency decreases, and in order to sustain the discharge the applied voltage and the length of the CDS should increase to provide for sufficient ionisations. Consequently at lower pressures, there will

be an increasing amount of electrons reaching the axis, with high enough energy, to produce inelastic collisions (see Fig 3.10b). Hence the electron excitation and ionization collision rates show a maximum at the cylinder axis.

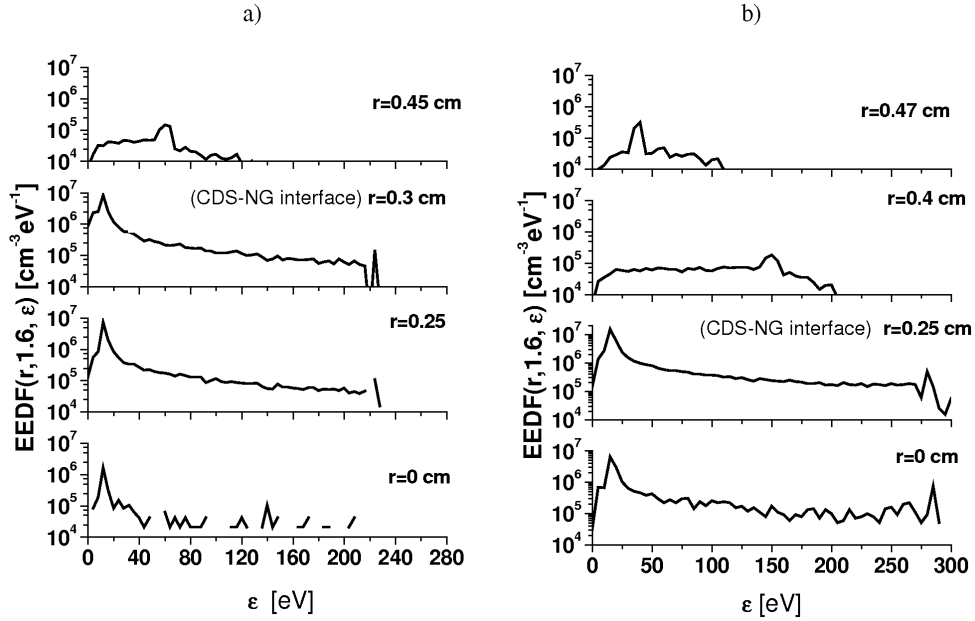


Fig. 3.10 The development of the EEDF at the discharge center ($z = 1.6$ cm) and at different radial positions for a discharge current of 4.5 mA at 1 Torr (a) and at 0.3 Torr (b).

The ionization processes inside the CDS were found important for all the conditions studied here, also at the currents corresponding to the region of the small slope in the V - I characteristic. This is in contrast to Ref. 18, where it was suggested, based on an analytical model, that for this region (small slope) the ionisation processes in the CDS can be neglected. The amount of ionization inside the CDS increases with decreasing current, as the length of the CDS increases, and it is almost independent of the pressure. For example at currents around 10 mA it was found that 40% of the total ionisation events occur inside the CDS while for currents around 1 mA this value increases to 65%. The rate at which the electrons are transferred to the slow group is zero in the sheath, where the electric field is strong and the electrons will remain fast, because they gain energy from the electric field. The maximum is reached in the beginning of the NG both in the axial and radial directions (not shown here).

3.5.2 Charged particle densities

The electron density in a HCD shows a tendency to decrease towards the open end of the cathode²² as is shown in Figs. 3.7b, 3.8b and 3.9b. Similar to the electron impact ionisation rate profiles, describe above, it reaches its maximum in the lower part of the cathode cylinder, near the cathode bottom, but unlike the rates, this maximum is found at the cylinder axis for all the conditions, which is expected for the pressure values under consideration.²²⁻²⁴

In almost the entire CDS the slow electron density is zero (because of their high mobility), while the ion density is low and rather constant. This positive space charge region near the cathode walls yields the strong electric field in the CDS (see below).

Both, electron and gas ion, densities begin to increase simultaneously at the end of the sheath. It is interesting to notice that the sheath region (indicated by the white region in the Fig. 3.7b, 3.8b and 3.9b) near the cathode bottom is shorter than at the cathode sidewalls, which will give rise to a higher axial electric field at the cathode bottom compared to the radial electric field at the cylinder sidewall (see below Fig. 3.7c, 3.8c and 3.9c). In the bulk plasma (or NG) the electron and ion density profiles are almost equal to each other, yielding a quasi-neutral region.

With decreasing current (compare Figs. 3.7b and 3.8b) the length of the sheath increases and the NG is more confined near the axis. Moreover the maximum of the density profile near the bottom is more pronounced and the density decreases faster toward the anode region, due to the increase of the loss of fast electrons to the anode. With the decrease in pressure (compare Figs. 3.7b with 3.9b), the profile of the densities in the axial direction show the same tendency as with the decrease in current as a consequence of the increasing loss of fast electrons to the anode (see also Fig. 3.14 below). Moreover, at the upper part of the cathode, near the anode, the sheath length increases compared with its lengths in the rest of the discharge cavity.

3.5.3 Electric potential

The electric potential distribution throughout the discharge is shown in Figs. 3.7c, 3.8c and 3.9c. The two characteristic regions of the HCD i.e., the sheath and the bulk plasma can be clearly distinguished. In the sheath the potential changes rapidly, for example, at 1 Torr (Fig. 3.7c), from -282 V at the cathode wall, to -10 V at the end of the sheath. The NG is characterized by a small potential gradient. It should be mentioned that this gradient increases with the drop in pressure and in current, as in the case of ion and electron densities

At 1 Torr, the plasma potential was found equal to -4 V at the centre of the discharge (Fig. 3.7c). With the decrease in current the plasma potential becomes more negative (e.g., -16 V at the centre of the discharge at 1.4 mA and 1 Torr; see Fig. 3.8c). Moreover the value of the plasma potential at the CDS- NG interface also decreases (for $p = 1$ Torr: from -10V at 9 mA to -20 V at 1.4 mA). The same tendency was observed at other pressures and the effects were even more pronounced at low pressure. Indeed at 0.3 Torr (Fig. 3.9c) the plasma potential at the discharge centre at 9 mA was found equal to -7 V and at 1.4 mA it was equal to -42 V.

In Fig. 3.11 the value of the plasma potential at the discharge axis and at $z = 1.5$ cm is plotted against the discharge current for all the conditions studied here.

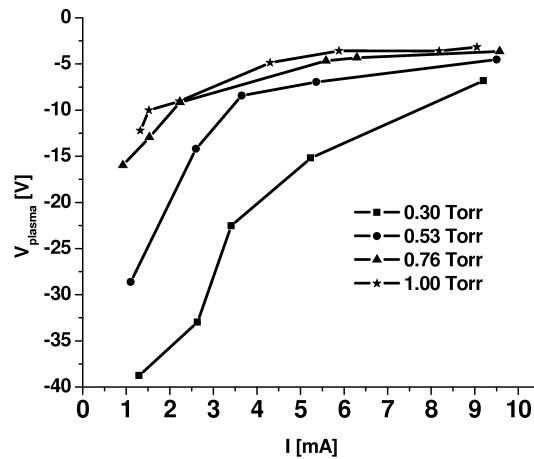


Fig. 3.11 Calculated plasma potential at the center of the discharge ($z=1.5$ cm, $r=0$ cm) as a function of the electric current at several pressures.

It is important to realize that for a cylindrical HCD the plasma potential was found negative throughout the entire discharge. However this is not the case for all kinds of HCDs, for example in Refs. 14 and 25, where segmented HCD and HCD with planar cathodes were modelled, positive plasma potential was found. We think that this difference is mainly due to the cathode geometry, i.e., in a cylindrical HCD the loss of fast electrons and ions to the anode and to the wall is lower for the same conditions than in the segmented HCD or in a HCD with planar cathodes. Hence in a cylindrical HCD there is no need for the plasma potential to be positive in order to guarantee the current balance as is the case for example in the abnormal glow discharges with planar electrodes where the electric potential in the NG is characterized by a positive value^{26,27}. Also in Ref. 18 it is mentioned that the fraction of ions that reach the cathode to produce electrons by secondary emission is similar in the modified (e.g. segmented) HCD as in the abnormal GD and they considered the modified HCD therefore as a discharge between and abnormal GD and conventional (cylindrical) HCD.

In our experimental work we were not able to measure the potential inside the discharge. However in Ref. 21, a negative plasma potential up to -30 V has been measured in a cylindrical HCD for Ar, Ne and He with cathode materials of Ni, Fe and Mo in a pressure range of 0.1 to 10 Torr and currents from 30 to 200 mA. Also in Ref. 28 has been reported a negative plasma potential for a He-Ni cylindrical HCD in a pressure range of 0.7 to 4 Torr and currents from 2 to 6 mA (see below, chapter 4).

3.5.4 Electric field

As can be deduced from the potential distribution, the electric field at the corner of the cylinder bottom is weaker compared to the field at the sidewall and bottom center. In Figs. 3.7d, 3.8d and 3.9d the axial electric field profiles are presented. Since the length of the sheath is defined here as the distance where the electric field gradient becomes very small in comparison with the field gradient inside the sheath, it is clear from these figures that the sheath length increases with decreasing current (Figs. 3.7d and 3.8d) and with decreasing pressure (Figs 3.7d and 3.9d and also Fig. 3.12).

The radial electric field is the predominant one in most of the discharge cavity (except at the cathode bottom and at the anode region) and it depends strongly on the radial distance, while it is almost uniform in the axial direction. In the NG the radial electric field changes slightly in the radial direction (not shown). Kazantsev et al.²⁹ have

also found the presence of a weak radial electric field in the NG of a HCD, by means of polarization spectroscopy.

The axial electric field is strong at the cathode bottom, especially at the centre, where it is a strong function of the axial distance. In the NG the axial electric field changes only a few V/cm in the entire NG. For example at 1 Torr and 9 mA it changes from 0 to -10 V/cm. This is in good agreement with the measurement of the axial electric field in the NG of a HCD carried out by Helm.¹ With decreasing pressure and current, the gradient in the axial direction increases, e.g., the axial electric field changes from -5 V/cm at the bottom CDS- NG interface to -50 V/cm at the cathode end at 0.3 Torr and 1.4 mA (not shown here).

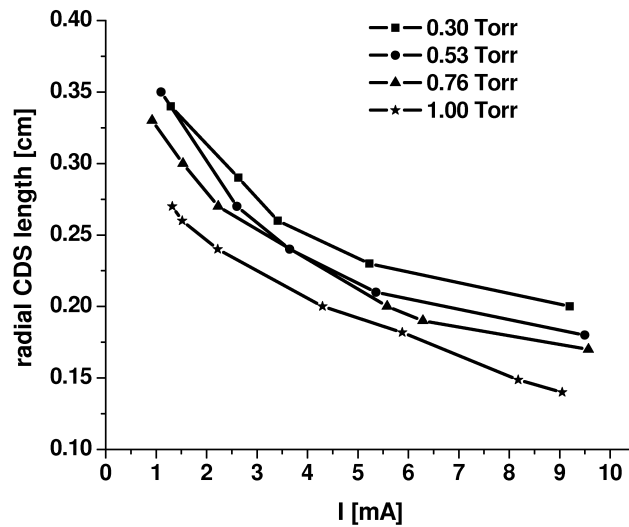


Fig. 3.12 Calculated radial CDS length at $z = 1.5$ cm as a function of the total current at several pressures.

At the cathode bottom “corners” and in the anode region, the axial and radial electric field shows a strong dependence of the radial as well as of the axial distance.

3.6 Influence of the bottom and top of the hollow cylinder

3.6.1 Cathode bottom

In some models, it is assumed that the influence of the cathode bottom of the HCD is negligible.¹⁻⁷ In order to test this approximation, we study the effect of the emission of electrons from the cathode bottom on the discharge behaviour, by comparing simulation results with and without emission from the bottom of the cylinder cathode.

When the electron emission from the bottom is not taken in account, the maxima of the ionization rate (i.e., ion source term) profiles are shifted in the axial direction toward the centre of the HCD. Hence the maximum in the electron and ion density profiles, the maximum in the radial electric field and in the radial ion current density are also shifted in the axial direction toward the HCD centre. When the electron emission from the cathode bottom is considered, all the maxima are found near the bottom of the HCD (as was shown in Figs. 3.7 to 3.9). Indeed, as a consequence of the strong axial and radial electric field near the bottom, a flux of high-energy electrons is created in both directions, increasing the number of electron impact ionization collisions, leading also to a maximum in the charged particle densities near the cathode bottom. We think that the special sputter and redeposition profiles observed at the bottom of the HCD “cylinder corners” is also a consequence of the presence of the strong axial and radial electric field there.

In Fig. 3.13 the electron density profile at the discharge axis is shown with and without taking into account secondary electron emission from the cathode bottom. It is interesting to mention that when the cathode bottom emission is not considered the potential distribution in the NG becomes slightly positive in the upper half of the HC, whereas with considering the cathode bottom emission it remains negative in the entire discharge volume (see Figs. 3.7c, 3.8c and 3.9c).

The discharge characteristics in the radial direction, on the other hand, do not change considerably with or without taking into account cathode bottom emission, as is expected.

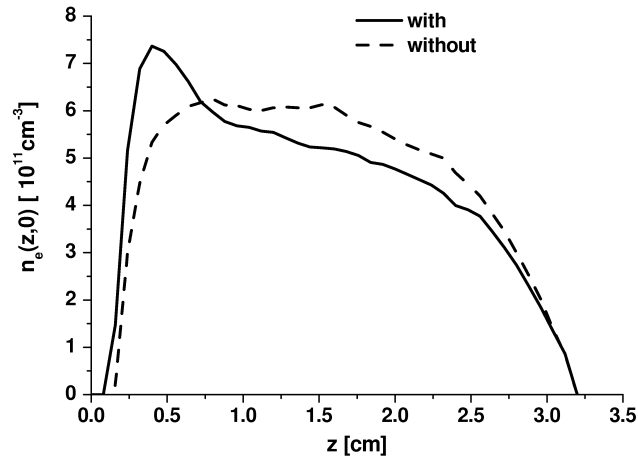


Fig. 3.13 Comparison of the calculated axial slow electron density profile at the discharge axis with and without taking into account secondary electron emission from the cathode bottom.

3.6.2 Anode

Fig. 3.14 shows the fraction of fast electrons reaching the anode, as a function of voltage at four different pressures.

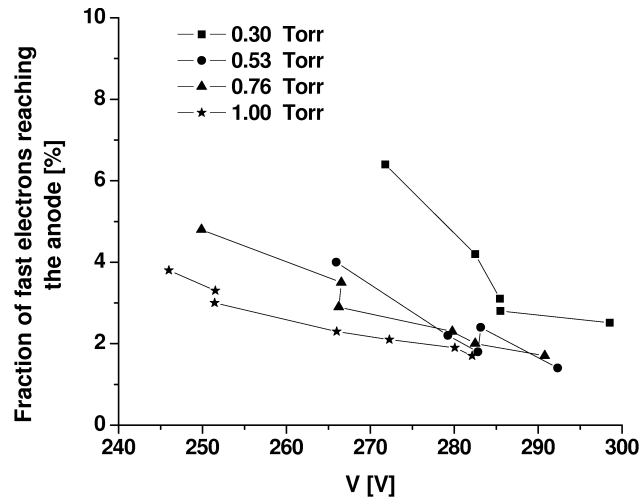


Fig. 3.14 Calculated fraction of fast electrons reaching the anode as a function of discharge voltage at several pressures.

At all conditions investigated, this fraction is in the range of 1 to 6%. Hence only a minority of the fast electrons gets lost at the anode. This fraction increases slightly at decreasing pressure, voltage and current, explaining why the axial profile of the

ionisation rate and consequently of the charged particle densities decreases toward the anode, as was mentioned above.

When a fast electron reaches the anode, it can induce the emission of a new electron, or it can be reflected or absorbed by the anode wall, depending on its energy. Most of the fast electrons that reach the anode are absorbed, i.e., between 80-90%, i.e., they are lost from the discharge.

3.7 Conclusions

Summarizing our results we can point out the following:

1. The γ coefficient was obtained almost constant in the range of the reduced electric fields studied here, with a value around 0.04, which agrees very well with reported data for a Cu cathode cleaned by sputtering without flashing.
2. At the conditions studied here the gas ions are the main source of electron emission from the cathode and that the fundamental process of electron production is by ionization collisions of electrons with Ar atoms.
3. The ionization collisions inside the CDS were found to be important for all conditions investigated, even at high currents.
4. The maximum in the profile of the collision rates, the charged particle densities, the potential and electric field was found near the cathode bottom of the HCD cylinder.
5. The plasma potential was found to be negative for all the discharge conditions investigated.
6. When the emission from the cathode bottom was not considered the maxima in the profiles were axially shifted to the cylinder centre and the plasma potential was found positive at the upper half of the cylinder cathode. This shows the importance of considering the cathode bottom in order to have a more realistic description of the discharge.
7. The loss of fast electrons to the anode increases and also the plasma potential becomes more negative with the decrease in pressure and in current.
8. The best regime for the hollow cathode effect to occur was obtained when at constant voltage the current increases with decreasing pressure, i.e. at pressures between 0.3 and 0.53 Torr and a current of 2 mA. These conditions are characterized in the experimental data by the most intense light emission, and in our calculations, when the maximum of the calculated total electron impact excitation rate is found at the cell axis, i.e., in the form of a disc shape instead of a ring shape.

3.8 References

- ¹ H. Helm, F. Howorka and M. Pahl, *Z. Naturf.* **27a**, 1417 (1972).
- ² Y. Kagan, *J. Phys. D.* **18**, 1113 (1985).
- ³ S. Hashiguchi and M. Hasikuni, *Japan. J. Appl. Phys.* **28**, 699 (1989).
- ⁴ S. Bukvic and L. M. Labat, *Phys. Scripta* **46**, 57 (1991).
- ⁵ R. R. Arslanbekov, A. A. Kudryavtsev and I. A. Movchan, *Sov. Phys. Tech. Phys.* **37 (6)**, 620(1992).
- ⁶ R. R. Arslanbekov, A. A. Kudryavtsev and I. Movchan, *Sov. Phys. Tech. Phys.* **37(4)**, 395 (1992).
- ⁷ J. P. Martinez and J. C. Amare, *J. Phys. D.* **31**, 312 (1998).
- ⁸ G. H. Copley and C. S. Lee, *Can. J. Phys.* **53**, 1705 (1975).
- ⁹ A. V. Phelps and Z. Lj. Petrovich, *Plasma Sources Sci. Technol.* **8**, R21 (1999).
- ¹⁰ V. I. Kolobov and L. D. Tsendin, *Plasma Sources Sci. Technol.* **4**, 551 (1995).
- ¹¹ M. Surendra, D. B. Graves and G. M. Jellum, *Phys. Rev. A* **41**, 1112 (1990).
- ¹² A. Fiala, L. C. Pitchford and J. P. Boeuf, *Phys. Rev. E* **49**, 5607 (1994)
- ¹³ M. Jugroot, P. Bayle, M. Yousfi and O. Eichwald, *J. Phys. D* **32**, 106 (1999).
- ¹⁴ K. Kutasi and Z. Donko, *J. Phys. D* **33**, 1081 (2000).
- ¹⁵ A. A. Kruithof and F. M. Penning, *Physica* **3**, 515 (1936).
- ¹⁶ A. V. Phelps and Z. Lj. Petrovich, *Plasma Sources Sci. Technol.* **8**, R21 (1999).
- ¹⁷ A. V. Phelps, *J. Phys. Chem. Ref. Data* **20**, 557 (1991).
- ¹⁸ R. R. Arslanbekov, A. A. Kudryavtsev and R. C. Tobin, *Plasma Sources Sci. Technol.* **7**, 310 (1998).
- ¹⁹ A. Bogaerts, Z. Donko, K. Kutasi, G. Bano, N. Pinhao and M. Pinheiro, *Spect. Acta* **655**, 1465 (2000).
- ²⁰ D. J. Sturges and H. J. Oskam, *J. Appl. Phys.* **37**, 2405 (1966).
- ²¹ V. I. Kirichenko, V. M. Tkachenko and V. B. Tyutyunnik, *Sov. Phys. Tech. Phys.* **21**, 1080 (1976).
- ²² S. Caroli, *Prog. Analyt. Atom. Spectrosc.* **6**, 253 (1983).
- ²³ J. P. Martinez and J. C. Amare, *J. Phys. D.* **31**, 312 (1998).
- ²⁴ F. Howorka and M. Pahl, *Z. Naturf.* **27a**, 1425 (1972).
- ²⁵ Z. Donko, *Phys. Rev. E* **57**, 7126 (1998).
- ²⁶ A. Bogaerts, R. Gijbels and W. Goedheer, *J. Appl. Phys.* **78**, 2233 (1995)
- ²⁷ A. Bogaerts and R. Gijbels, *Anal. Chemi.* **68**, 2296 (1996).
- ²⁸ S. Pfau, R. Kosakov, M. Otte and J. Rohmann, *Proc. XXIV ICPIG, Warsaw*, p 262 (1999).
- ²⁹ S. A. Kazantsev, A. G. Petrashen, N. T. Polezhaeva and V. N. Rebane, *Opt. Spectrosc.* **68**, 740 (1990).

Chapter 4

*Study of the He-Ni HCD: Relevance of the
He^m metastable atoms*

Hollow cathode discharge in He is studied based on a Monte Carlo-fluid hybrid model combined with a transport model for the metastable He atoms. The metastable model considers various production and loss mechanisms for the He^m metastable atoms. These three models are run iteratively until convergence is reached. Typical results are, among others, the excitation and ionisation rates, the electron, ion and metastable densities and fluxes, the electric field and potential distribution. Also the relative importance of different processes determining the metastable density in a He HCD is analysed, as well as the role of the He metastable atoms and He⁺ ions on the secondary electron emission at the cathode. The calculation results are compared with experimental data for the same discharge conditions and good agreement was obtained.

4 Study of the He-Ni HCD: Relevance of the He metastable atoms

4.1 Introduction

This chapter describes the study of a He-Ni HCD (symmetric configuration). The fundamental electrical and spectrometric properties of HCDs were already studied in the previous chapter. Therefore in this chapter, we focus on the discharge properties that best reflect the differences given by the discharge geometry and the carrier gas. Special attention is given to the study of the He^m metastable atoms, like for example, to the relative importance of the processes determining the metastable atom density, the contribution of the He^m atoms to the total ionization rate as well as to their role on the secondary electron emission at the cathode.

The general processes, which determine the He^m metastable atom density in a He discharge, were first studied by Ebbinghaus.¹ Since then many papers have been published, where the He^m metastable atoms are being studied either experimentally (using atomic absorption spectroscopy,^{2,3} plasma induced emission spectroscopy,⁴ Doppler shift Fourier transform spectroscopy,⁵ etc) as well as theoretically (where the transport of metastable atoms is described by continuity equations, yielding the metastable density).^{6,7} The metastable population in He was studied, experimentally and with the use of balance equations, in various kinds of discharges including afterglow discharges,⁸⁻¹⁰ dc,¹¹ rf¹² and HCDs.^{13,14} Also some studies have been performed with respect to the role of He^m metastable atoms in a glow discharge with formation of a positive column.^{15,16}

In the present chapter, we will analyze the role of He^m metastable atoms in a HCD, using a fluid model for the metastable He^m atoms, which is combined with a Monte Carlo model for the fast electrons and a fluid model for the slow electrons and He⁺ ions.

A similar combination of models has been applied in the literature for the simulation of glow discharges with planar cathode, both for a dc glow discharge in Ar¹⁷ and for an rf discharge in various gases.¹⁸ The advantage of this procedure is that it allows to follow the influence of the metastable atoms on the electron energy distribution, the ionization rates, the ion and electron densities, etc and vice-versa, i.e., how these parameters can influence the metastable atom density. Moreover, as will be shown later,

it appeared necessary to include the He^m metastables in our model, in order to account for sufficient ionization in the plasma.

The plasma species considered in this chapter are: neutral ground state and metastable He^m atoms, positive ions (He^+) and electrons. The two metastable levels of He, i.e., the triplet 2^3S and singlet 2^1S metastable levels lying at 19.82 eV and 20.61 eV above the ground state, respectively, have been combined into one collective level lying at 19.82 eV. This assumption was made because for our purpose only the total metastable density is important. It is found in the literature that the triplet state has a higher density than the singlet state, because the singlet metastables are converted into the triplet metastables by superelastic collisions with slow electrons in the NG; hence, the population of the 2^1S metastable level is typically around 20% of that of the 2^3S metastable level.^{7,9,12} The energy threshold for considering the electrons as fast particles was taken equal to the ionisation threshold of the combined He^m metastable level, i.e., 4.77 eV. Indeed, it is considered in the model that the electrons with lower kinetic energy than 4.77 eV are not able to produce inelastic collisions and can therefore better be described with a fluid model.

Our calculation results will be compared with experimental data¹⁹ obtained for the same discharge geometry and conditions, as well as with reported data in the literature.

4.2 Geometry and discharge conditions

The calculated results are illustrated here for the same geometry and discharge conditions as used in the experiments reported by S. Pfau et al.,¹⁹ in order to allow the best comparison between calculated and measured data. In Ref. 19, measurements in the NG were done with a radially moveable Langmuir-probe, while the investigation of the CDS was carried out by spatially and spectrally resolved measurements of the line radiation parallel to the axis of the HCD, as the electrical probes are not suitable for this region.

The electrodes of the discharge are schematically illustrated in Fig. 4.1. The hollow cathode is a nickel cylinder with 6 cm length and 3 cm inner diameter, open at both ends. The anodes are rings, with 2.4 cm inner diameter, also made of nickel and located at both ends of the cathode at a distance of 2.8 cm. The discharge conditions assumed in the model are also taken from the experiments, i.e., the gas pressure is 1 Torr,

the discharge current ranges from 2 to 6 mA and a discharge voltage between 158 and 170 V is applied to the cathode, whereas the anodes are grounded.

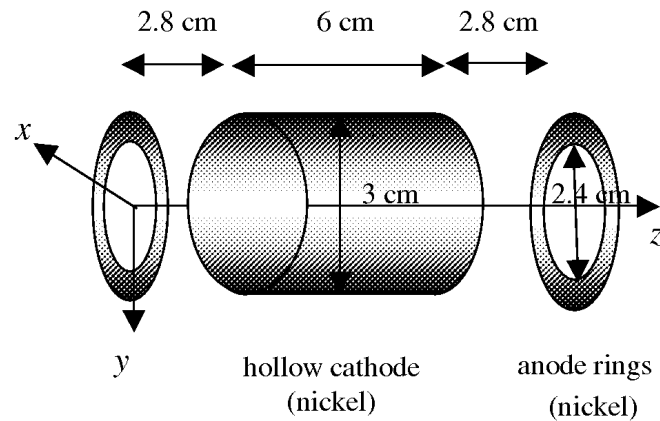


Fig. 4.1 Schematic picture of the cell geometry assumed in the model.

4.3 Collision rates

The calculated electron impact excitation rate to the metastable level is presented in Fig. 4.2, at a current of 4.5 mA, a voltage of 165 V and a pressure of 1 Torr. Fig. 4.3 shows the calculated total ionization rate (a), as well as the contributions by electron impact ionization from the He ground state atoms (b), from the He metastable level (c), and by the ionization due to the metastable-metastable atom collisions (d), at the same conditions as in Fig. 4.2. The thick black lines from $z = 2.8$ cm till $z = 8.8$ cm represent the hollow cathode, whereas the anode rings are located at $z = 0$ cm and $z = 11.6$ cm (i.e., the borders of the figure).

It appears from these figures that the maximum of all excitation and ionization rates occurs in the NG, more specifically at the discharge center (both in axial and radial direction). The occurrence of the maximum of the collision rate profiles at $z = 5.8$ cm., i.e., at the center in the axial direction differs to the corresponding profiles of the asymmetric configuration at 1 Torr, where the maximum was reached near the closed end of the hollow cathode cylinder (see Figs. 3.7a and 3.8a).

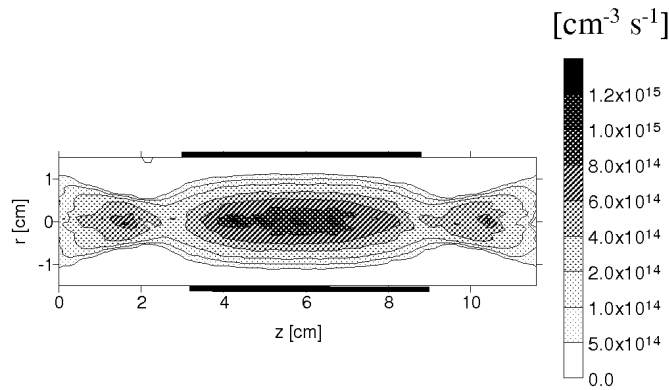


Fig. 4.2 Calculated two-dimensional electron impact excitation rate to the He m metastable level throughout the discharge at a pressure of 1 Torr and a current of 4.5 mA. The hollow cathode is represented by the thick black lines from $z = 2.8$ cm to $z = 8.8$ cm, whereas the anode rings are located at $z = 0$ cm and $z = 11.6$ cm.

4.3.1 Comparison to the asymmetric HCD configuration

Those axial profiles (Figs. 4.2 and 4.3) are a direct consequence of the discharge geometry. In the case of the asymmetric configuration the presence of a closed end gives rise to a strong electric field at the cathode bottom, which allows an enhanced ion and electron production there, while in the case of the symmetric configuration, the maximum electric field strength is found at $z = 5.8$ cm, i.e., at the center of the discharge because both cylinder ends are open and consequently the loss of the fast electrons toward the anodes increases (see below paragraph 4.5).

In the radial direction, the electron collision rate profiles also differ from the corresponding profiles of the asymmetric configuration at 1 Torr. Here at 1 Torr, all the inelastic collision rates peak at the cylinder axis, while in the Ar-Cu HCD a dip in the profiles was observed at the axis. The electron collision rate profiles for the He- Ni HCD at 1 Torr resemble more the corresponding radial profiles of the Ar-Cu HCD at 0.3 Torr.

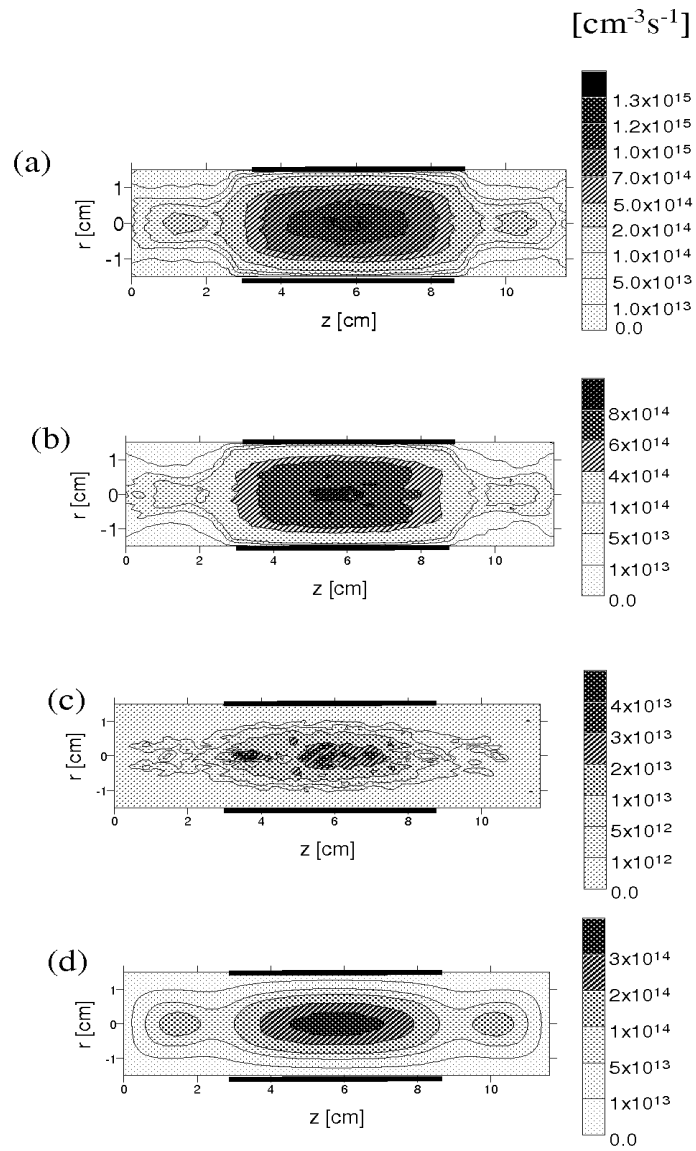


Fig. 4.3 Calculated two-dimensional ionization rates throughout the discharge at a pressure of 1 Torr and a current of 4.5 mA: (a) total ionization rate; (b) electron impact ionization rate of He ground state atoms; (c) electron impact ionization rate of He m metastable atoms; (d) ionization rate due to metastable-metastable collisions.

This can be understood by the analysis of the evolution in the radial direction of the EEDF (see Fig. 4).

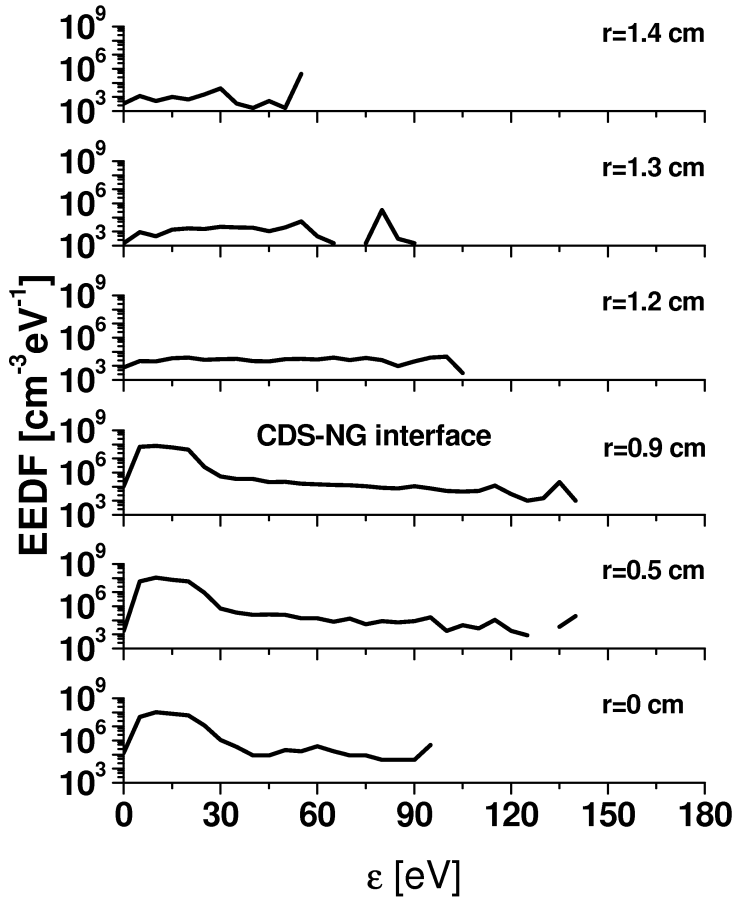


Fig. 4.4 The development of the EEDF at the discharge center ($z = 5.8$ cm) and at different radial positions at 1 Torr, 4.5 mA and a cathode voltage of -165 V. The CDS-NG interface is around $r = 0.9$ cm.

Fig. 4.4 shows that in the NG (i.e., at radial distances lower than 0.9 cm) there is a large amount of high-energy electrons. Moreover a considerable fraction of electrons still reach the axis ($r = 0$ cm), with high enough energy to produce inelastic collisions. Hence the electron excitation and ionisation collision rates peak at the cylinder axis. The reason why the profiles of electron inelastic collisions in a He discharge at 1 Torr, resemble the corresponding profiles at 0.3 Torr in Ar, is due to the lower value of the cross section for electron impact excitation and ionization collisions with the ground state He atoms (at its maximum, the value of both cross sections is around 10^{-17} cm²) compared with the cross sections of Ar atoms, which are one order of magnitude higher. Hence, compared with

the Ar discharge at similar conditions, the electron collision frequency in He discharge decreases, which is equivalent to the effect of dropping the pressure in the Ar-Cu HCD.

4.3.2 Collision processes at the anode region

It is interesting to notice that the electron impact excitation rate to the metastable level (Fig. 4.2) as well as the ionization rate due to metastable-metastable collisions (Fig. 4.3d), show a second maximum also at the cylinder axis, but in the region between cathode and anode (here termed as anode region). Especially for the electron impact excitation rate to the metastable level, the maximum in the anode region is nearly equal to the maximum at the discharge center, as follows from Fig. 4.2. Keeping in mind that this process is the main source for the production of He^m metastable atoms (indeed, electron-ion recombination is found to be negligible at pressures below 4 Torr)^{10,14} it will yield a metastable atom density in the anode region, which is comparable in magnitude with the metastable atom density at the discharge center (see below Fig 4.6c). Hence, this will give the profile with a second maximum in the anode region for the metastable-metastable collision rate, as is shown in Fig. 4.3d.

4.3.3 Contribution of the different ionization sources to the total ionization rate

As far as the total ionization rate in the discharge is concerned, it appears to reach only a maximum in the cathode region (i.e., the discharge cavity inside the cathode cylinder, i.e., from $z = 2.8$ cm to 8.8 cm; see Fig. 4.3a). The reason is that electron impact ionization from the He ground state is the dominant ionization mechanism in the discharge, and it reaches only a maximum in the cathode region (see Fig. 4.3b). The latter ionization mechanism is not only important in the NG, but also in the CDS, where 44% of the electron impact ionization takes place, according to our model calculations. The importance of electron impact ionization in the CDS of a HCD at pressures around 1 Torr was also observed for the Ar-Cu HCD.

Beside electron impact ionization from the He ground state, ionization due to metastable-metastable collisions (Fig. 4.3d) is of second importance, but it is more confined to the cylinder axis.

Electron impact ionization from the He metastable level, on the other hand, is clearly of minor importance at the conditions under study.

Integrated over the total discharge volume, the relative contributions of electron impact ionization from the ground state, ionization due to metastable-metastable

collisions, and electron impact ionization from the He metastable level, were calculated to be 81%, 18 % and 1%, respectively at the present condition (4.5 mA). With decreasing current, the role of electron impact ionization from the He ground state becomes even more dominant, e.g., at 2 mA, the relative contribution was calculated to be almost 86 %. Electron impact ionization from the He metastable level, on the other hand, becomes then almost negligible (i.e., calculated to be 0.2 % at 2 mA).

4.3.4 Excitation rates and line intensities distribution

Fig. 4.5a illustrates the calculated electron impact excitation rates to the He^m metastable level at $z = 5.8$ cm (i.e., at the discharge center in the axial direction), as a function of radial position, at three different currents. As expected, the excitation rate increases with rising current.

The shape of the curves is quite similar, with a maximum at the cylinder axis. This means that for the three conditions investigated, the NG regions of the two opposite cathode walls overlap, i.e., that the HC effect is present. The shapes of the three curves are compared in more detail in figure 4.5b, which shows the normalized excitation rates.

It appears that the excitation rate is more peaked at the discharge center at the lowest current investigated. In other words, the CDS is somewhat larger at the lowest current, as is expected.^{20,21} In Fig. 4.5c the normalized light intensity distributions are plotted as a function of radial position (again at $z = 5.8$ cm), at the three different currents, for the line $\lambda = 501.6$ nm, corresponding to the transition from 3^1P to 2^1S , as measured in Ref.19. Exact comparison between Figs 4.5b and 4.5c is not possible, because our calculation results show the excitation rate to the He^m metastable level, whereas the experimental light intensity originates from another excited level. However, the later still reflects the electron impact excitation rate.^{22,23} It is clear that the same behavior is observed in both calculated and measured results. Indeed, figure 4.5c shows that the light intensity distribution is also somewhat more peaked at the cylinder axis, i.e., that the CDS extends to slightly further distances from the cathode walls, at the lowest current of 2 mA, which is in accordance with our calculation results.

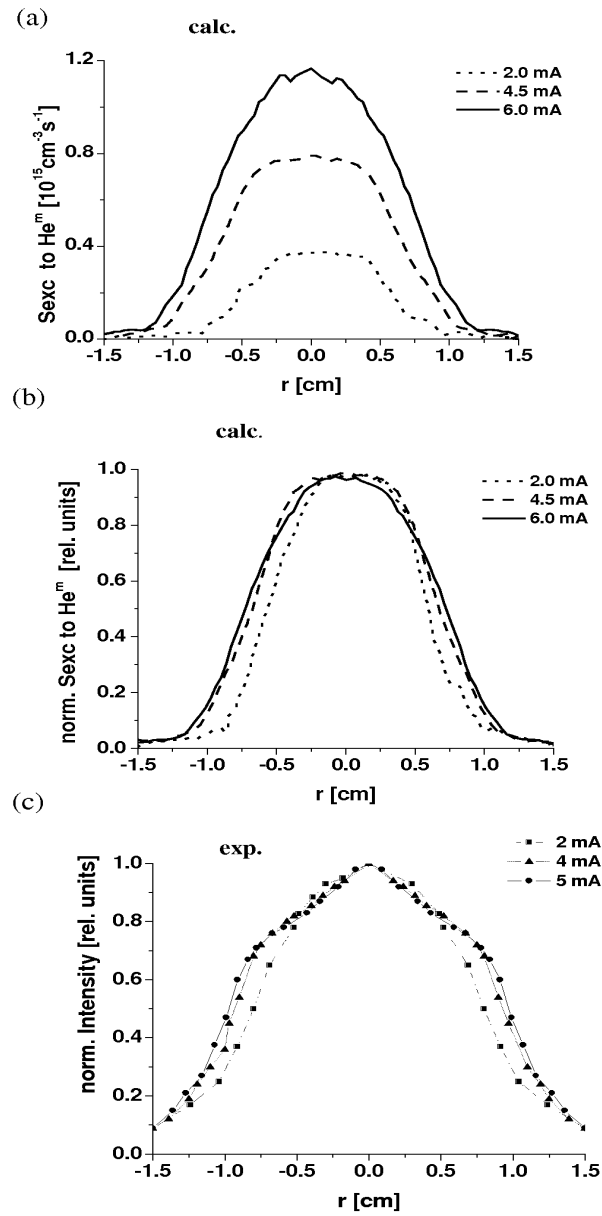


Fig. 4.5 Radial profiles at $z = 5.8$ cm for 1 Torr and three different currents: (a) calculated electron impact excitation rates to the He metastable level; (b) normalized calculated electron impact excitation rates to the He metastable level; (c) normalized measured light intensity distribution for the HeI line at 501.6 nm.

4.4 Electron, ion and metastable densities

Fig. 4.6 presents the calculated two-dimensional density profiles of electrons (a), He^+ ions (b) and He^m metastable atoms (c) at a current of 4.5 mA. Whereas the electron and He^+ ion densities reach only a maximum within the hollow cathode region, the He^m metastable atom density is characterized by a second maximum outside the hollow cathode region, i.e., in the so-called anode region, as was predicted by the shape of the electron impact excitation rate to the He^m metastable level (see above, Fig. 4.2).

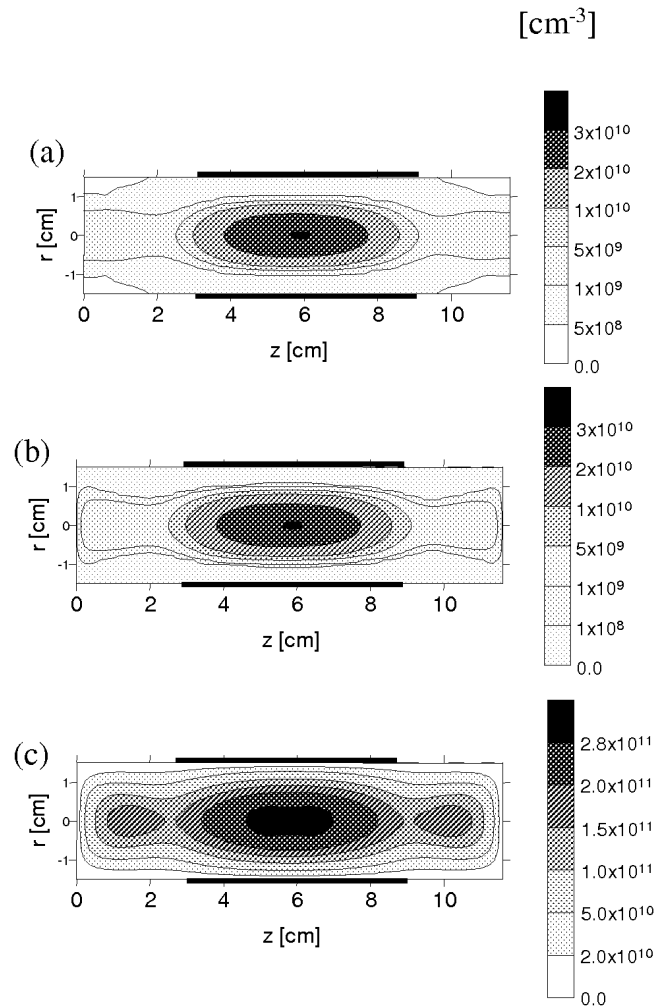


Fig. 4.6 Calculated two-dimensional density profiles throughout the discharge at a pressure of 1Torr and a current of 4.5 mA, for the slow electrons (a), the ions (b), and the He metastable atoms (c).

When comparing the absolute values of the densities, it appears that the He^m metastable atom density is about one order of magnitude higher than the He^+ ion and electron densities, at the current of 4.5 mA. The metastable atom density changes only slightly with variation of the current, i.e., the maximum value varies from $1.6 \times 10^{11} \text{ cm}^{-3}$ at 2 mA, over $2.8 \times 10^{11} \text{ cm}^{-3}$ at 4.5 mA, till $3.8 \times 10^{11} \text{ cm}^{-3}$ at 6 mA.

The electron and He^+ ion densities, on the other hand, are more dependent on current. Therefore, the ratio of He^m metastable to He^+ ion or electron densities is higher at lower current. For example, at 2 mA, the He^m metastable atom density at the discharge center was calculated to be 30 times higher than the electron and He^+ ion densities, whereas it was only 7 times higher at 6 mA.

Fig. 4.7 illustrates the calculated electron densities at $z = 5.8 \text{ cm}$, as a function of radial position, at the three currents under study (a), in comparison to the measured data (b), from Ref. 19.

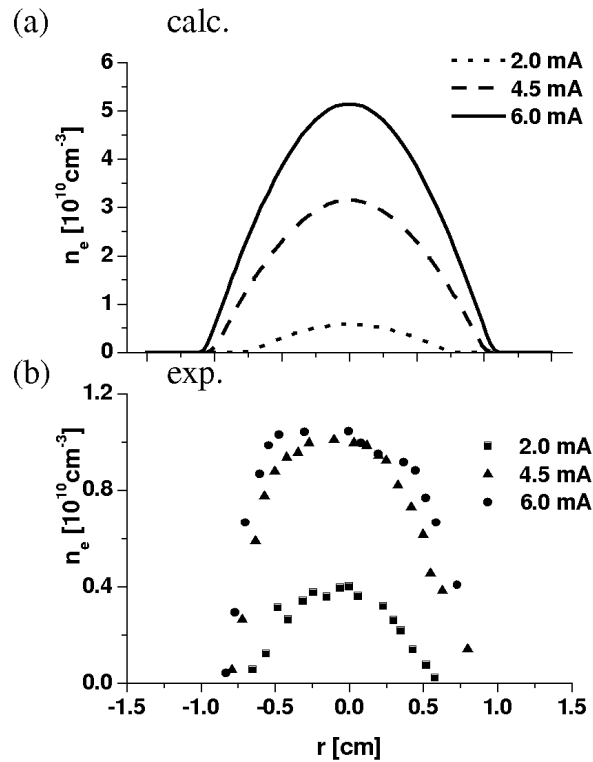


Fig. 4.7 Radial dependence of the slow electron density at $z = 5.8 \text{ cm}$ for a pressure of 1 Torr and three different currents: (a) calculated results; (b) experimental data obtained from Ref. 19.

The calculated electron densities appear to be somewhat higher, and they rise more uniformly with increasing current, in comparison with the experimental data (where the difference between 4.5 mA and 6 mA was found to be very small). This difference between the calculated and experimental value of the electron density can be a direct consequence of the assumption of constant electron temperature in the simulations. Nevertheless, keeping in mind that both calculations and measurements are subject to uncertainties, the agreement is already quite satisfactory, because both calculated and measured densities are in the same order of magnitude, and show the same radial dependence.

4.4.1 Production and loss processes determining the He^m metastable atom density

Concerning the importance of the different processes determining the He^m metastable atom density, it was found, for the conditions under study, that the production occurs almost completely by electron impact excitation, and that electron-ion recombination is negligible. Indeed, as reported from measurements in Ref. 14, recombination becomes only important for the production of He^m metastable atoms at pressures above 4 Torr. As far as the loss of metastables is concerned, diffusion and subsequent de-excitation at the walls is most significant (i.e., the relative contribution, integrated over the entire discharge region, is calculated to be 60% at 4.5 mA), followed by metastable-metastable collisions (28%) and two-body collisions with He ground state atoms (8%). The other loss processes considered in the model, are found to be negligible at the conditions under study. At decreasing current, the role of diffusion becomes even more important, with a calculated contribution of 76% at 2 mA.

4.4.2 He^m metastable atoms: their role in the electrical discharge proprieties

Because of the high He^m metastable atom density compared to the He⁺ ion and electron densities, it is expected that the flux of metastable atoms to the cathode walls plays an important role in secondary electron emission.⁹ Indeed, the metastable atom flux to the cathode walls is about 15% of the total flux (i.e., ion plus metastable) at 6 mA, and this value increases with decreasing current, i.e., 17% at 4.5 mA, and 20% at 2 mA. If we consider that the electron emission yield due to the He^m metastables is comparable in magnitude to the He⁺ ion induced emission yield, as was measured by Hasted,²⁴ then the role of He^m metastable atoms in secondary electron emission reflects the contribution to the total flux and hence is not negligible. As appears from above, it increases slightly

with decreasing current. The same tendency was observed for the γ coefficient, i.e., at 6 mA, 4.5 mA, 2 mA, γ was equal to 0.32, 0.38, 0.44, respectively. As was mentioned above, the γ coefficient calculated in this work reflects the total contribution of the ions and metastable atoms in the emission of secondary electrons from the cathode surface. Hence we can conclude that the γ increment at low currents is related to the increased efficiency of the metastable atoms in releasing electrons from the cathode surface. This can compensate to some degree for the drop in the relative contribution to ionization (i.e., electron multiplication in the discharge) by metastable-metastable collisions at lower currents.

In general, it can be concluded that the role of He^m metastables for the production of electrons and He^+ ions (and hence: electrical current), both with respect to secondary electron emission and to ionization in the discharge, is not negligible in the He HCD at the present conditions. In fact, we found that it was necessary to include the He^m metastable atoms in our model, in order to account for sufficient electron and ion production, and hence to calculate an electrical current in correspondence to the experimental values.

4.5 Potential and electric field distribution

The two-dimensional electric potential distribution throughout the discharge is depicted in Fig. 4.8.

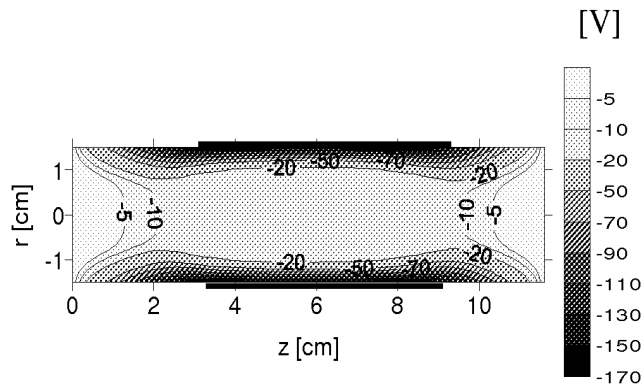


Fig. 4.8 Calculated two-dimensional potential distribution throughout the discharge at a pressure of 1 Torr and a current of 4.5 mA.

The two characteristic regions in the HCD, i.e., the CDS and NG, can be clearly distinguished. It is interesting to notice that the equipotential lines in the CDS are concave within the HC region, whereas they are convex outside this region. In this way, they will focus the electrons inside the hollow cathode region toward the discharge center, and outside this region toward the center of the anode rings.

It is clear that the potential in the CDS changes rapidly from -165 V at the cathode walls till about -20 V at about 5 mm from the cathode, i.e., at the CDS-NG interface. In the NG, no field reversal is observed, the plasma potential remains negative and it is rather constant (varying from -20V at the CDS-NG interface to about -11 V at the discharge center). Indeed, there is no need for the plasma potential to become positive, in order to guarantee the discharge current balance,²⁵ as is the case in other kinds of glow discharges.

In Ref. 26 it is argued that the field reversal appears in order to decrease the loss of fast electrons to the anode and in Ref. 27 it was mentioned that if almost all positive ions will flow to the cathode and if this is compensated by a flux of electrons to the anode, no field reversal will be necessary. Both conditions are fulfilled in a cylindrical HCD, i.e., due to its geometry, the positive ions in the NG will diffuse radially to the NG-CDS interface, while the slow electrons which are trapped radially, will flow in the axial direction to the anodes (only the slow electrons are trapped). Then the radial current (to the cathode) will be mainly carried by the ions, while the axial current (to the anodes) will be mainly due to the slow electrons, i.e. the ion and electron fluxes occur preferentially in different directions. Also the loss of fast electrons to the anode is reduced, because the fast electrons can oscillate between the opposite CDS (pendulum effect) releasing their energy inside the cathode cavity by inelastic collisions.

Figure 4.9 shows the calculated radial profiles, at $z = 5.8$ cm, of the electric potential (a) and radial electric field (b), at the three different currents under study. Also illustrated in these figures are the corresponding measured values, as obtained from Refs. 19, 28. Very good agreement is reached between calculated and measured data, both with respect to the length of the CDS (cf. the change in gradient in potential and electric field distribution) and to the value of the plasma potential in the NG. The latter is found to be negative and of similar magnitude in both calculated and measured results. Moreover, it becomes slightly more negative with decreasing current.

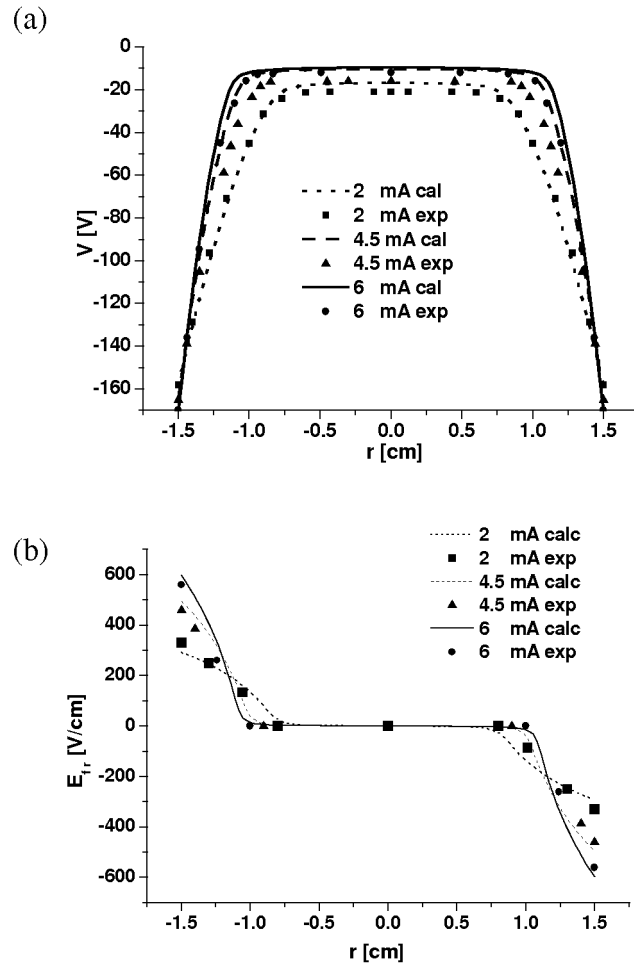


Fig. 4.9 Radial profiles of the calculated electric potential (a) and radial electric field distribution (b), at $z = 5.8$ cm for a pressure of 1 Torr at three different currents, (curves), compared with experimental data obtained from Refs. 19 and 28 (symbols).

4.6 Conclusions

It was found that:

1. The excitation and ionization rates, as well as the plasma species densities, reach the maximum at the discharge center, both in axial (i.e., in the middle of the HC region, at $z = 5.8$ cm) and in radial directions, (i.e., at the cylinder axis).
2. The He^m metastable atom density profile shows a maximum at the center of the hollow cylinder, but it exhibits also a second maximum outside the HC region, i.e., in the region between HC and anode rings. The reason is that the dominant production mechanism of the He^m metastables, i.e., electron impact excitation to the metastable level, reaches also a second maximum in this region.
3. The calculated He^m metastable atom density was found to be an order of magnitude higher than the calculated electron and He^+ ion densities
4. The role of He^m metastable atoms is clearly not negligible at the conditions under study, both with respect to secondary electron emission at the cathode walls, and to ionization in the plasma, by metastable-metastable collisions. The latter process typically accounts for about 20 % to the total ionization in the HCD, according to our model calculations.
5. It was found that including the He metastables in the model was necessary to be able to reproduce the experimental electrical current values.
6. Finally, the comparison made with the experimental data of Refs.19, 28, for the electrical current, and the radial profiles of electron density, potential and radial electric field (including the value of the plasma potential and the CDS length), shows that the model presents a realistic picture of the He HCD.

4.7 References

- ¹ E. Ebbinghaus, *Ann. Phys.* **7**, 267 (1930).
- ² A. McIntonsh, M. H. Dunn, I. K. Belai, *J. Phys. D* **11**, 301 (1978).
- ³ K. E. Greenberg, G. A. Hebner, *J. Appl. Phys.* **73**, 8126 (1993).
- ⁴ T. Kubota, Y. Morisaki, A. Ohsawa, M. Ohuchi, *J. Phys. D* **25**, 613 (1992).
- ⁵ H. S. Myeong, H. Xichun, T. A. Miller, *Chem. Phys.* **228**, 145 (1998).
- ⁶ T. Ledig, B. Schroder, *J. Phys. D* **25**, 1080 (1992).
- ⁷ T. J. Sommerer, M. Kushner, *J. Appl. Phys.* **71**, 1654 (1992).
- ⁸ A. V. Phelps, *Phys. Rev* **89**, 1202 (1952).
- ⁹ A. V. Phelps, *Phys. Rev* **99**, 1307 (1955).
- ¹⁰ R. Deloche, P. Monchicourt, M Cheret, F. Lambert, *Phys. Rev. A* **13**, 1140 (1976).
- ¹¹ E. A. Den Hartog, T.R. O'Brian, J.E. Lawler, *Phys. Rev. Lett.* **62**, 1500 (1989).
- ¹² H. M. Katsch, E. Quandt, Th. Schneider, *Plasma Phys. Control Fusion* **38**, 183 (1996).
- ¹³ P. Gill, C. E. Webb, *J. Phys. D* **10**, 299 (1977).
- ¹⁴ I. Kuen, F. Howorka, H. Stori, *Phys. Rev. A* **23**, 829 (1981).
- ¹⁵ P. G. Browne, M. D. Dunn, *J. Phys. B* **6**, 1103 (1973).
- ¹⁶ K. A. Hardy, J. W. Sheldon, *J. Appl. Phys.* **53**, 8532 (1982).
- ¹⁷ A. Bogaerts, R. Gijbels, *Phys. Rev A* **52**, 3743 (1995).
- ¹⁸ T. J. Sommerer, M. Kushner, *J. Appl. Phys.* **71**, 1654 (1992).
- ¹⁹ S. Pfau, R. Kosakov, M. Otte, J. Rohmann, Experimental investigation of cylindrical HCD, *Proc. XXIVICPIG, Warsaw*, p 33 (1999).
- ²⁰ A. von Engel, *Ionized gases* (Claredon, Oxford, 1965).
- ²¹ F. Howorka, M. Pahl, *Z. Naturforsch.* **27a**, 1425 (1972).
- ²² A. Bogaerts, R. Gijbels, J. Vleck, *Spectrochim. Acta, Part B* **53**, 1517 (1998).
- ²³ T. Kubota, Y. Morisaki, A. Ohsawa, M. Ohuchi, *J. Phys. D* **25**, 613 (1992).
- ²⁴ J. B. Hasted, *J. Appl. Phys.* **30**, 22 (1959).
- ²⁵ N. Baguer, A. Bogaerts, R. Gijbels, *Spectrochim. Acta, Part B* **57**, 311 (2002).
- ²⁶ T.J. Sommerer, W.N.G. Hitchon, J.E. Lawler, *Phys. Rev. A* **39**, 6356 (1989).
- ²⁷ R. A. Gottsho, A. Mitchell, R. Scheller, Y. Y. Chan, D. B. Graves, *Phys. Rev A* **40**, 6407 (1989).
- ²⁸ M. Otte (private communication).

Chapter 5:

Role of the fast Ar^f atoms and, Ar^+ ions in a hollow cathode glow discharge

The role of the fast Ar atoms and Ar⁺ ions in a cylindrical hollow cathode discharge is studied based on a self-consistent model based on the principle of Monte Carlo and fluid simulations. With Monte Carlo models the movement of the fast electrons, fast Ar atoms and fast Ar⁺ ions as particles is described, while with the fluid models, the slow electrons, ions and metastable atoms are treated as a continuum. Typical results are, among others, the fast atom, fast ion and fast electron collision rates, the energy distribution function and fluxes of the fast atoms, fast ions and fast electrons, etc. It was found that in spite of the fact that integrated over the complete discharge volume, the ionization rate due to the fast gas atoms and ions represent only a little percent of the total charged particle production, the role of the fast atoms and fast ions is important for determining the net charge distribution in the CDS. Indeed, close to the cathode walls, these ionization processes determine the total ionization rate profile

5 Role of the fast Ar atoms and Ar⁺ ions in a hollow cathode glow discharge

5.1 Introduction

Many applications of the HCDs in laser technologies,^{1,2} plasma surface treatments^{3,4} and analytical chemistry^{5,6} are based on the sputtering of the cathode material by high-energetic particles. HCDs are very useful discharges to obtain high rates of sputtering, due to the fact that most of the energy of the fast particles is spent inside the discharge,^{7,8} i.e., for the production of new electron-ion pairs, excitation collisions, charge transfer collisions, etc. In this chapter we will focus on the study of the gas ions and fast gas atoms, due to the importance of these species for the sputtering of the cathode material.

A very important step in the study of the role of ions and atoms in glow discharges was achieved by the experimental and theoretical work of Davis and Vanderslice.⁹ They pointed out the relevance of symmetric charge transfer collisions in determining the gas ion and gas atom energy distribution in the cathode dark space. Since then, different theoretical and computational approaches have been developed in order to study more precisely other processes, which are responsible for determining the energy distribution, fluxes, densities, etc of these species in GDs. For example a theoretical approach was followed in Ref.10, where analytical formulas for the energy distribution function of ions and neutrals in the CDS were derived based on the model of Davis and Vanderslice. In Ref. 11, this model was extended, using the transport formalism, to account for electron impact ionization collisions in the CDS. In Ref. 12 a transport model combined with a phenomenological method (viscous drag fluid model) was used to describe rf discharges. In transport models it is assumed that the particle energy is in hydrodynamic equilibrium with the local field.¹³ However, when using such a model in the CDS, the electron energy distribution of the fast electrons, which are responsible for most of the ionization collisions, is not correctly calculated, and consequently the calculated electron collisions rates are not very reliable. With Monte Carlo models (MC)^{14,15} the microscopic nature of a collision can be described. The particles are followed one after another and the collision rates are calculated based on the energy-dependent cross sections. Hence, a correct energy distribution function for the energetic

particles can be calculated. However a MC model is not self-consistent, because the electric field is not calculated in the model, but needs to be given as input. In Ref. 16 a MC model was used to calculate energy and angular distributions of He⁺ and Ar⁺ ions in the CDS considering symmetric charge transfer and elastic collisions. With the particle-in-cell-Monte-Carlo (PIC-MC) method,¹⁷ the problem can be solved self-consistently. The collision rates are calculated based on the energy-dependent cross section, and the particle energy is calculated from the electric field, which is obtained self-consistently from Poisson's equation using the charged species densities. This method is very time-consuming because a large number of particles should be followed for statistically valid results. Another way of solving the problem self-consistently is the so-called hybrid model^{18,19} e.g., a MC model combined with a fluid model, (i.e., a transport model, where the Poisson equation is solved together with the continuity and flux equations for ions and electrons).^{20,21} Such a hybrid model combines the advantages of both methods and it is considerably faster than a PIC-MC model.²²⁻²³ Hybrid models for describing the role of fast ions, neutrals and electrons were applied to GDs with planar cathode in hydrogen²⁴ and argon^{25,26} respectively. In the present chapter we will apply the hybrid approach to a cylindrical HCD in Ar to obtain the energy distribution of ions and fast atoms arriving at the cathode walls. These distributions will be used to calculate the density of the sputtered species i.e., the sputtered atoms and ions from the cathode material.

The species considered at this point in the model were: background Ar atoms, singly charged positive ions (Ar⁺), metastable Ar^m atoms, fast and slow electrons and fast Ar atoms (Ar^f). The Ar^f atoms are formed by elastic collisions of Ar⁺ ions with the background gas and are assumed to have energies higher than 1 eV. The energy threshold for considering electrons as fast particles was 4.6 eV, which corresponds to the ionization energy threshold of the common Ar^m metastable level. The collision processes included are, for the fast electrons, elastic and excitation collisions from the ground state and ionization from the ground and metastable states. For the ions, elastic collisions (including symmetric charge transfer), excitation to the metastable state and ionization from the ground state are taken into account. Finally, for the fast atoms, elastic collisions, excitation to the metastable state and ionization from the ground state collisions are considered.

The calculated results illustrated in this chapter and in the three following chapters for the Ar-Cu HCD were obtained with the same geometry and discharge conditions as assumed in chapter 3 (see paragraph 3.2).

5.2 Ionization collision rate

5.2.1 Relative contribution of the various ionization processes to the total ionization

To study the contribution of the various processes to the total ionization rate, Fig. 5.1 presents the calculated ionization rate profiles at 0.3 Torr and 9.2 mA. This condition is a representative example for all the discharge conditions investigated here. Note that the thick black lines in this figure and in all following contour plots represent the cathode walls.

The maximum in the ionization rate due to the metastable–metastable collisions (Fig. 5.1a) is observed in the centre of the CDS and it is three orders of magnitude less than the maximum rate due to atom and ion impact ionization collisions (Fig. 5.1b), which take place only very close to the cathode walls. Integrated over the total discharge volume, metastable–metastable ionization represents only 0.04 % of the total ionization, followed by 0.16% due to ion impact ionization and 2.8% due to fast atom impact ionization at the conditions under study here. Hence, electron impact ionization has a dominant contribution to the total ionization.

5.2.2 Heavy particle ionization collisions in the CDS

In previous chapters, it was already demonstrated that the ionizations collisions inside the CDS were important, even at high currents. In this chapter, some more ionization sources are included, and it is found that the importance of ionization in the CDS is even more pronounced, because these additional processes are most important inside the CDS

In spite of the fact that integrated over the total discharge volume these processes contribute only for 3% to the total ionization, their influence in the discharge is larger than that, as will be shown below. Indeed, most ion-electron pairs are created, due to these processes, inside the CDS. Hence these additional ions and electrons can gain energy from the electric field and contribute also to the enhancement of the total ionization. This enhancement can be observed if we compare figures 5.1c and 5.1d. Fig. 5.1c shows the total ionization rate profile when only electron impact ionization was considered, whereas Fig. 5.1d presents the total ionization rate, when also the ionization by heavy particles was included. In Fig. 5.1c we see that close to the cathode walls, the total ionization rate was less than $5 \times 10^{15} \text{ cm}^{-3} \text{ sec}^{-1}$, whereas in Fig. 5.1d it was higher

than this value (see the contour line corresponding to this value). Moreover in Fig. 5.1d the rate profile is a bit higher in magnitude and more uniform throughout the entire length of the HCD than in Fig. 5.1c.

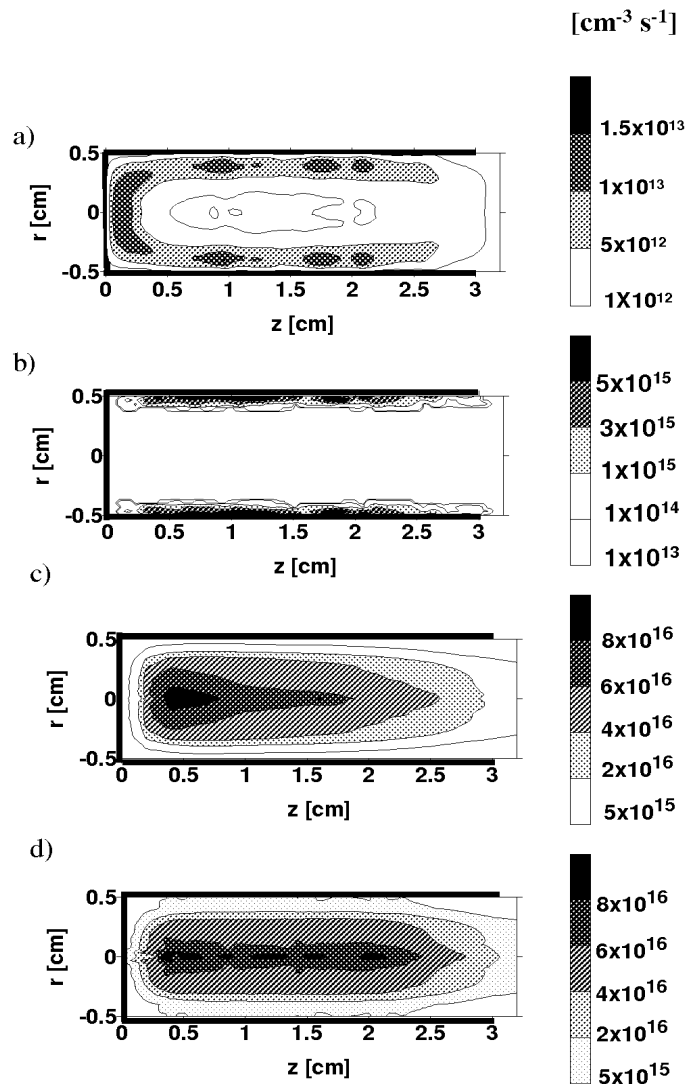


Fig. 5.1 Calculated two-dimensional ionization rate profiles throughout the discharge at a pressure of 0.3 Torr and a current of 9.2 mA, as a result of metastable-metastable atom collisions (a); ion and fast atom impact ionization (b); total ionization rate, calculated when only electron collisions were considered (c) and the total ionization rate considering electron, ion, fast atom and metastable-metastable ionization collisions (d). The hollow cathode is represented by the thick black lines from $z = 0$ cm to $z = 3$ cm, whereas the anode ring is located at $z = 3.2$ cm.

A direct measure of this enhancement in ionization rate can also be obtained from the electron multiplication coefficient i.e., the number of electrons created in the discharge per electron ejected from the cathode due to ion and metastable induced secondary electron emission. When only electron impact ionization was considered the multiplication coefficient was 28 (see Fig 3.4) and it rises to around 35 when all other ionization processes were included as well. This represents an increase of 20 % for the discharge conditions of Fig. 5.1, which is the discharge condition where this effect is more relevant due to the higher discharge voltage (see below).

5.2.3 Pressure and current dependence

For all the conditions investigated here, electron impact ionization of ground state Ar atoms was found to be the dominant process of electron production. The relative contribution of the additional ionization processes (i.e., due to the Ar^m , Ar^+ and Ar^f collisions) to the total ionization in the discharge, increases with decreasing pressure, as can be seen from Fig. 5.2a. For example, at a discharge current of 9 mA and at 1 Torr pressure, it represents 0.6% of the total ionization rate, increasing to 3 % at 0.3 Torr. With decreasing pressure at constant current, the CDS length increases; hence the ionization inside the CDS increases. Moreover, the discharge voltage increases also. The higher discharge voltage results in higher Ar^+ ion and fast Ar atom energies and consequently in more efficient ion and atom impact ionization, because the ionization cross sections increase with rising energy, in the energy range of interest here²⁷ (see Fig. 2.2).

At constant pressure, the contribution of these processes gains in importance at currents for which the ionization inside the CDS is predominant^{28,29} (i.e., low currents, corresponding to the step gradient of the voltage-current dependency) and also at high currents. Note that a higher discharge current at constant pressure arises from a higher voltage.

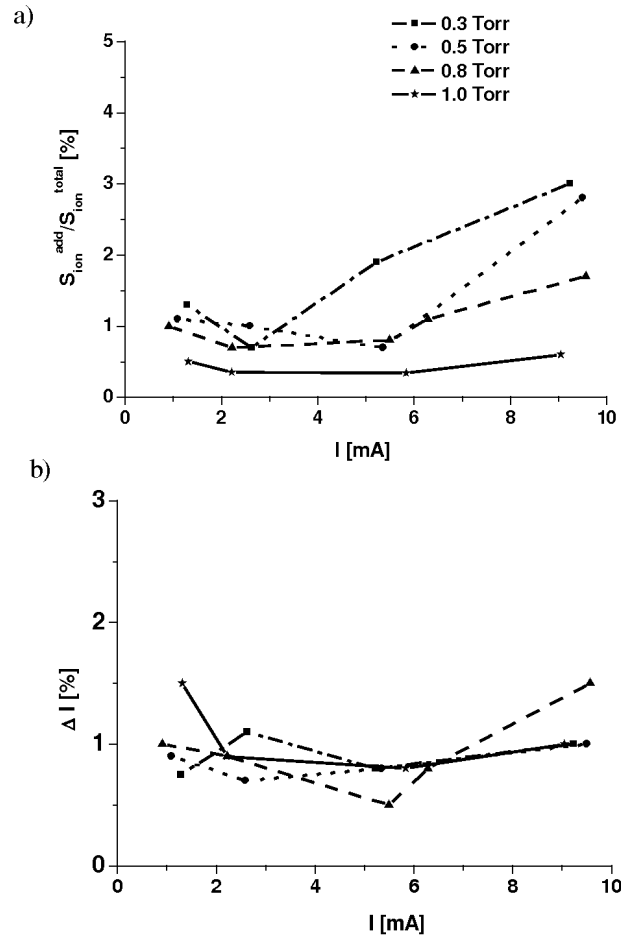


Fig. 5.2 Calculated relative contribution (in %) to the total ionization rate due to the ionization collisions of Ar⁺ ions, fast Ar atoms and metastable Ar atoms (i.e., the additional ionization rates; S_{ion}^{add}) for all the discharge conditions investigated here (a), and calculated rise of the total discharge current (in %) due to the additional ionization processes (b).

5.2.4 Influence of the heavy particles ionization collisions on the discharge parameters

5.2.4.1 Current-voltage characteristic

The influence of these new sources of ionization on the calculation of the current-voltage characteristic of the discharge is small. The total rise in discharge current due to the contribution of fast atom, ion and metastable ionization collisions is less than 2% for all the conditions investigated here, as can be seen from Fig. 5.2b. Indeed, the discharge current is an integrated value, i.e., it reflects the total amount of ionization, and the added ionization processes represent only a small fraction of the total ionization in the discharge (Fig. 5.2a).

However the additional ionization processes will have more effect on the calculation of parameters which directly depend on the ionization distribution in the CDS; i.e., the net charge density distribution in the CDS and consequently the voltage drop in the CDS, as well as the electric field and the plasma potential. Indeed, close to the cathode walls, these ionization processes determine the total ionization rate profile (see Fig. 5.1).

5.2.4.2 Charge density distribution

Fig. 5.3 illustrates the radial profiles (at $z = 1.6$ cm) of the net charge density, i.e., the Ar^+ ion density minus the electron density (Fig. 5.3a), the ion and electron densities (Fig. 5.3b), the electric potential (Fig. 5.3c) and the electric field (Fig. 5.3d) at a pressure of 0.3 Torr and a current varying from 1.3 to 9.2 mA. Note that $r = 0$ corresponds to the cylinder axis, whereas $r = 0.5$ cm denotes the cathode walls. The thick lines present the results calculated when ion, fast atom, metastable and electron ionization collisions were considered, whereas the thin lines correspond to the calculation results when only electron impact ionization from the ground state Ar atoms was included for the same discharge conditions.

Fig. 5.3a shows that when the additional processes are included, especially at low currents (1.3 mA and 2.6 mA), the net (positive) charge density increases. This will give rise to an increase in the potential drop in the CDS. Hence, the plasma potential becomes less negative and consequently, the radial electric field in the CDS increases, as can be observed from Figs. 5.3c and 5.3d, respectively.

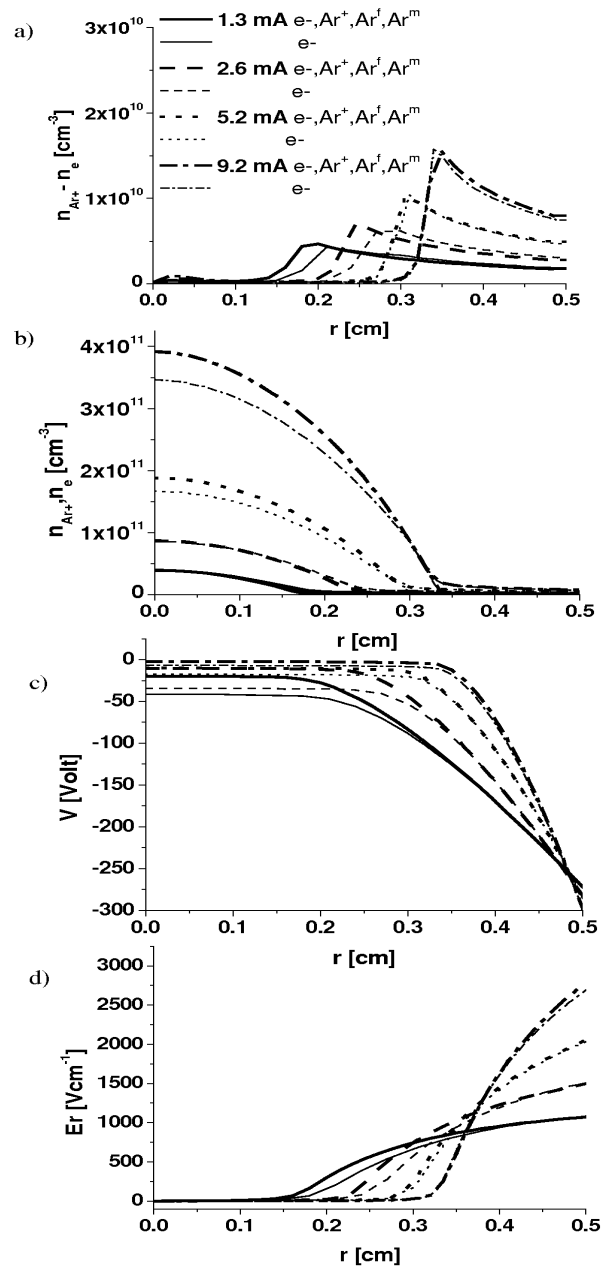


Fig. 5.3 Calculated radial profiles at the discharge center ($z = 1.6$ cm), of the calculated net positive charge density (a); ion and electron densities (b); electric potential distribution (c) and electric field distribution (d) for different discharge currents at 0.3 Torr. The thick lines represent the results calculated when considering the ionization due to electron, ion and fast atom impact collisions and metastable–metastable atom collisions, while the thin lines correspond to the model where only electron impact ionization was considered.

At high currents a rise in the ion and electron density in the NG is observed (see Fig. 5.3b, for example for the same discharge condition as in Fig. 5.1, the plasma density show an increases of around 12%), as a consequence of the rise in electron impact ionization in this region. However this rise does not influence the electric field, because the net space charge does not change.

To illustrate the effect of the additional ionization mechanisms in the entire discharge, Fig. 5.4 shows the two-dimensional (2D) potential distributions for a discharge current of 1.3 mA and an applied voltage of -271 V.

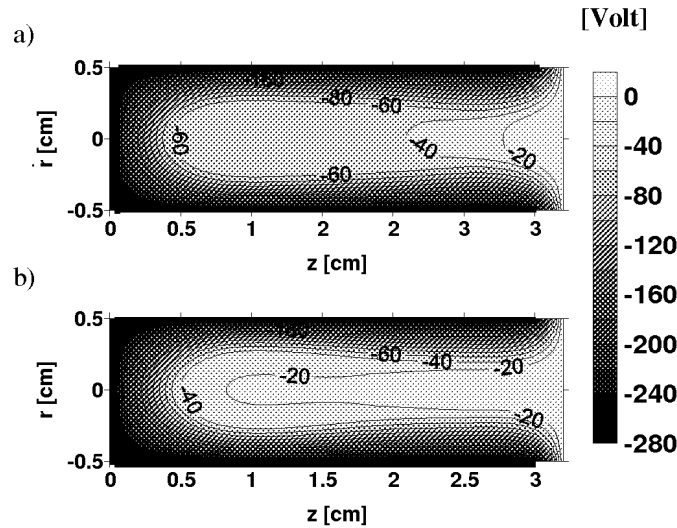


Fig. 5.4 Calculated two-dimensional potential distribution throughout the discharge at 1.3 mA and -271 V applied voltage at a pressure of 0.3 Torr, considering the ionization due to electron impact collisions (a); and considering the ionization due to electron, ion, fast atom and metastable-metastable collisions (b).

Fig. 5.4a presents the results for the case where only electron impact ionization was considered, whereas in Fig. 5.4b the other ionization collisions were also included. In Fig. 5.4a the equipotential curve at the NG-CDS interface corresponds to -60 V, giving a potential drop in the CDS of -211 V. The plasma potential at the cylinder centre was equal to about -40 V. In Fig. 5.4b, on the other hand the potential is equal to -40 V at the CDS-NG interface, yielding a potential drop in the CDS of -231 V and the plasma potential is about -20 V. The CDS length does not change; hence this gives rise to an increase in the electric field in the CDS.

5.3 Mean energy of the fast electrons, fast Ar⁺ ions and fast Ar atoms

In Fig. 5.5 the 2D mean energy distribution profiles of the fast Ar⁺ ions (a) fast Ar^f atoms (b) and fast electrons (c) are shown at 9.2 mA, 298 V and 0.3 Torr.

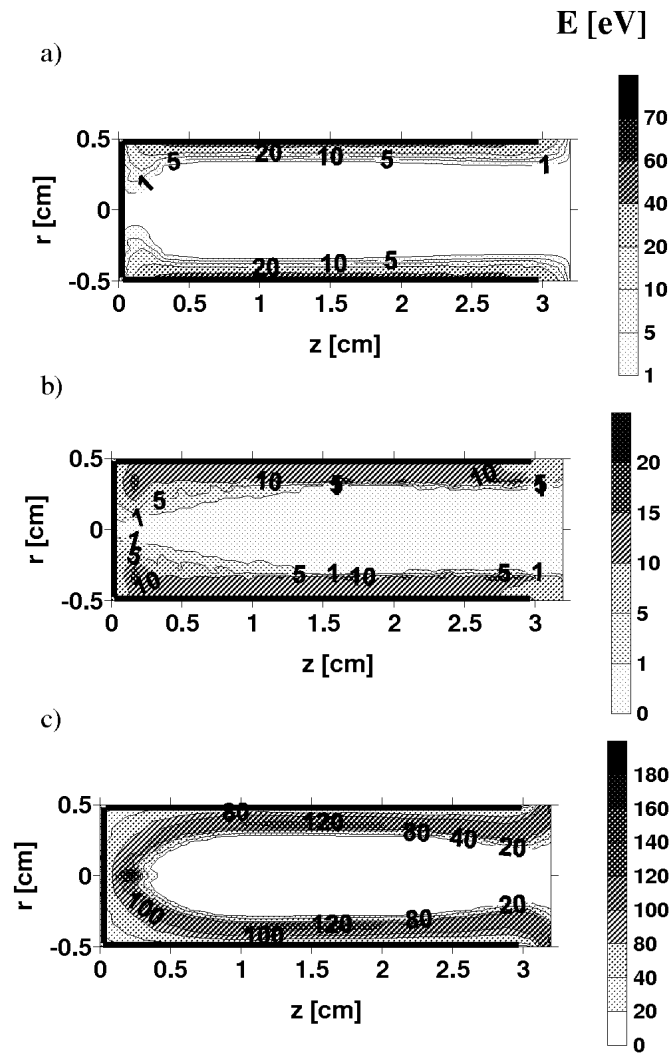


Fig. 5.5 Calculated two-dimensional mean energy profiles throughout the discharge of fast Ar⁺ ions (a); fast Ar atoms (b) and fast electrons (c) at 9.2 mA and a pressure of 0.3 Torr

The ions and atoms reach their maximum energy at the cathode walls, whereas the electrons have their maximum energy at the end of the CDS, because they are accelerated away from the cathode. The mean energy of the Ar⁺ ions close to the cathode was found to be lower than the mean energy of the electrons at the CDS–NG interface, because of the efficient energy transfer in the ion symmetric charge transfer collisions.^{9,13}

For the conditions under study, the Ar⁺ ion mean energy at its maximum was equal to 60 eV, which corresponds to 20% of the energy associated to the potential drop in the CDS.

With decreasing current, the ion mean energy drops, as is illustrated in Fig. 5.6. Indeed, a lower current at constant pressure arises from a lower voltage, which yields a lower energy. Moreover, the ratio of the CDS length to the mean free path of the Ar⁺ ions for charge transfer collision (d/λ) increases, so that, the ion energy transfer efficiency to the background gas atoms increases⁹ and consequently the ion mean energy decreases.

With a rise of pressure at constant current, d/λ increases considerably; hence the ion mean energy decreases. This follows clearly when comparing Figs. 5.6a with 5.6b and it explains why at a pressure of 1 Torr the rate of the ion and atom impact ionization collisions was so low (see Fig. 5.2).

The mean energy of the fast Ar^f atoms is lower than the mean energy of the Ar⁺ ions, because they are formed from the ions as a result of elastic (including symmetric charge transfer) collisions but they are not able to gain additional energy from the electric field (see Figs. 5.5b and 5.6). Close to the CDS–NG interface the fast Ar atom mean energy increases toward the cathode wall, following the pattern of the Ar⁺ ion energy, but further inside the CDS, their energy is more uniformly distributed than the ion energy, due to the energy broadening effect from the elastic collisions.³⁰ This is clearly illustrated in Fig. 5.5b. The fraction of the maximum fast atom mean energy which respect to the energy corresponding to the CDS potential drop, was found to be independent of the discharge current and changes only slightly with pressure: from 4% at 1 Torr to 5% at 0.3 Torr. In the NG no fast atoms were found.

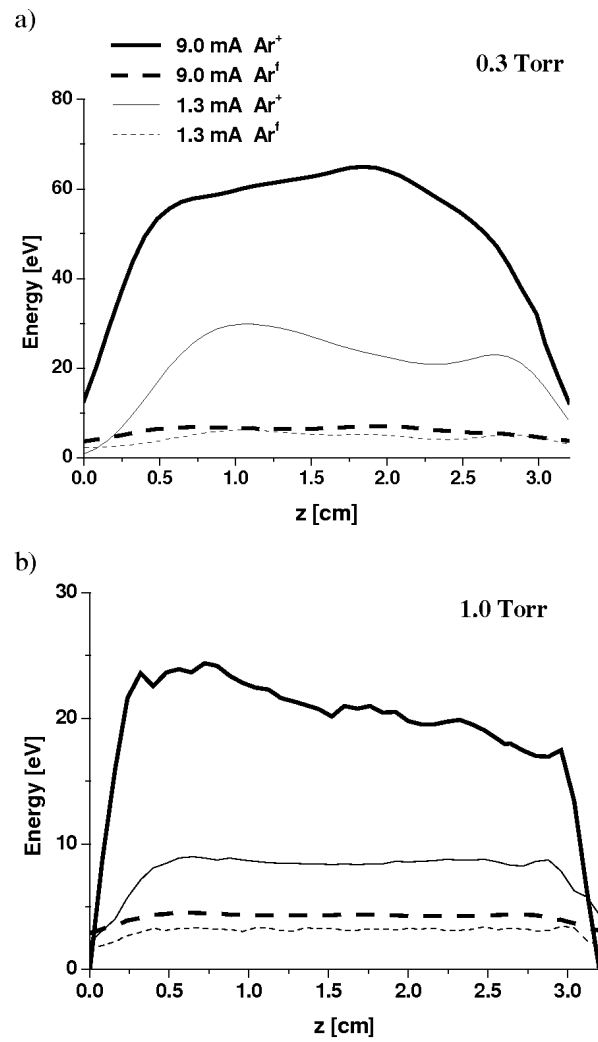


Fig. 5.6 Calculated Ar⁺ ion and fast Ar atom mean energies at the cathode wall for currents around 1 mA and 9 mA, and at two different pressures: 0.3 Torr (a) and 1 Torr (b). In these figures the solid lines represent the ion mean energy and the dashed lines correspond to the fast atom mean energy.

In Fig. 5.5c, we see that the mean energy of the fast electrons at the CDS-NG interface was equal to 180 eV, which correspond to 61% of the cathode fall potential. With decreasing current, this percentage decreases slightly, for example, at 1.3 mA it represents 54% of the cathode fall potential. In the NG, at 0.3 Torr, the mean electron energy was calculated to be between 10 and 20 eV, which is higher than the threshold of inelastic collisions. With rising pressure, the electron mean energy decreases due to:

- the decrease of the applied voltage and
- the increase of the ratio of the CDS length to the fast electron energy relaxation length.

The latter is determined by the total electron inelastic collision cross-section, because the energy exchange in the electron elastic collisions is negligible. At 1 Torr the mean energy of the fast electrons in the NG was between 5 and 10 eV. Hence, this is not enough to ionize the discharge gas. This explains why at 1 Torr the maximum of all inelastic collisions was found close to the CDS-NG interface, while at 0.3 Torr this maximum was located at the discharge axis.

5.4 Ar⁺ ion flux at the CDS-NG interface

To investigate which fraction of the Ar⁺ ion flux at the cathode arrives from the NG at the CDS-NG interface, we have plotted in Fig. 5.7 the Ar⁺ ion flux as a function of the radial distance, at different pressures, for a constant applied voltage (a); and at different currents, for a constant pressure (b).

In the figures the position of the CDS-NG interface is indicated with the small vertical lines. Furthermore, the ratio of the ion current at the beginning of the CDS to its value at the cathode wall, expressed in % is also indicated.

In our model, the coordinates of the CDS-NG interface were determined based on the position where the ion and electron densities begin to increase and become almost equal to each other (see Figs. 5.3a and 5.3b).

At constant voltage, the fraction of the Ar⁺ ion flux at the CDS-NG interface to the Ar⁺ ion flux at the cathode surface was found almost independent of the pressure (Fig. 5.7a)

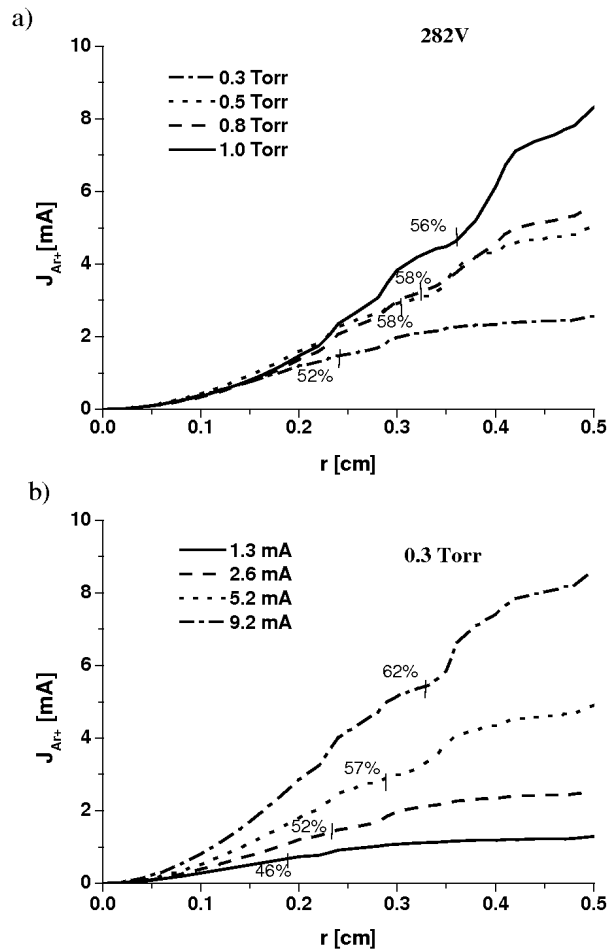


Fig. 5.7 Calculated radial ion current at constant applied voltage for different pressure values (a) and at constant pressure for four different currents (b). In the figures are also indicated the position corresponding to the CDS-NG interface (small vertical line) and the ratio of the ion current at the CDS-NG interface to its value at the cathode wall (expressed in %).

At constant pressure, this value increases with rising current (Fig. 5.7b). Indeed, at higher currents (i.e., higher voltage) the major increase in the ion current occurs in the NG, whereas at lower current, when the CDS length is larger, the major rise in current takes place inside the CDS. This is in agreement with the efficiency of electron multiplication in the CDS and in the NG, as pointed out in chapter 3 (paragraph 3.4). In fact the ratio of the total Ar⁺ ion flux coming from the NG at the CDS-NG to the total Ar⁺ ion flux at the cathode wall is approximately equal to the ratio of the electron

multiplication coefficient in the NG to the total electron multiplication coefficient in the discharge

5.5 Conclusions

We can conclude that:

1. In spite of the fact that integrated over the total discharge volume the ionization due to fast Ar atoms and Ar⁺ ions contributes only for 3% to the total ionization, their influence in the discharge was larger than that.
2. Close to the cathode walls, the ionization processes due to fast Ar atoms and Ar⁺ ions determine the total ionization rate profile
3. The inclusion in the model of Ar⁺ and Ar^f ionization collision processes is important for the correct calculation of parameters which directly depend on the ionization distribution in the CDS; i.e., the net charge density distribution in the CDS, the voltage drop in the CDS, as well as the electric field and the plasma potential.
4. The relative importance of the ionization by heavy particles increases with decreasing pressure, especially at low currents, where the ionization inside the CDS is predominant.
5. The mean energy of fast ions, fast atoms and fast electrons increases with decreasing pressure and with rising current.
6. The ratio of the Ar⁺ ion flux at the CDS-NG interface to the ion flux at the cathode is almost independent of pressure and rises with voltage

5.6 References

- ¹ I. G. Ivanov, E. L. Latush, M. F. Sem, Metal vapors ion lasers: Kinetic processes and gas discharges (Chichester, John Wiley & Sons Ltd, 1996).
- ² N. K. Vuchkov, K. A. Temelkov, N. V. Sabotinov, *IEEE J. Quantum Electron* **35**, 1799 (1999).
- ³ D. M. Manos, D. L. Flamm, An introduction to plasma etching (New York, Academic, 1989).
- ⁴ A. Goldamm, J. Amoroux, Gases: Macroscopic processes and Discharges (New York, Plenum Press, 1983).
- ⁵ P. J. Slevin, W. W. Harrison, *Appl. Spectrosc. Reviews* **10**, 201 (1975).
- ⁶ S. Caroli, *Prog. Analyt. Atom. Spectrosc.* **6**, 253 (1983).
- ⁷ H. Helm, *Z. Naturf.* **27a**, 1812 (1972).
- ⁸ V. I. Kolobov, L. D. Tsendin, *Plasma Sources Sci. Technol.* **4**, 551 (1995).
- ⁹ W. D. Davis, T. A. Vanderslice, *Phys. Rev.* **131**, 219 (1963).
- ¹⁰ I. Abril, A. Gras-Marti, J.A. Valles-Abarca, *Phys. Rev A* **28**, 3677 (1983).
- ¹¹ I. Abril, A. Gras-Marti, J.A. Valles-Abarca, *J. Vac. Sci. Technol. A* **4**, 1773 (1986).
- ¹² C. W. Jurgensen, E.S. G. Shaqfeh, *J. Appl. Phys.* **64**, 6200 (1988).
- ¹³ T. J. M. Boyd, J. J. Sanderson, *Plasma Dynamics* (London, Nelson LTD, 1969)
- ¹⁴ A. Tran Ngoc, E. Marode, P. C. Johnson, *J. Phys. D* **10**, 2317 (1977).
- ¹⁵ A. Bogaerts, M. van Straaten, R. Gijbels, *Spectrochim. Acta Part B* **50**, 179 (1995).
- ¹⁶ Z. Wronski, *Vacuum* **42**, 635 (1991).
- ¹⁷ M. Surendra, D. B. Graves, *IEEE Trans. Plasma Sci.* **PS-19**, 144 (1991).
- ¹⁸ M. Surendra, D. B. Graves, G. M. Jellum, *Phys. Rev. A* **41**, 1112 (1990).
- ¹⁹ J. P. Boeuf, L. C. Pitchford, *IEEE Trans. Plasma Sci.* **19**, 286 (1991).
- ²⁰ J. P. Boeuf, *J. Appl. Phys.* **63**, 1342 (1988).
- ²¹ D. Paschier, W. J. Goedheer, *J. Appl. Phys.* **74**, (1993).
- ²² T. J. Sommerer, M. Kushner, *J. Appl. Phys.* **71**, 1654 (1992).
- ²³ H. C. Kim, F. Iza, S. S. Yang, M. Radmilovic and J. K. Lee, *J. Phys. D* **38**, R283 (2005).
- ²⁴ A. C. Dexter, T. Farrell, M I Lees, *J. Appl. Phys. D* **22**, 413 (1989).
- ²⁵ A. Bogaerts, R. Gijbels, W. J. Goedheer, *J. Appl. Phys.* **78**, 2233 (1995).
- ²⁶ A. Bogaerts, R. Gijbels, W. J. Goedheer, *Anal. Chem.* **68**, 2296 (1996).
- ²⁷ A. V. Phelps, *J. Phys. Chem. Ref. Data* **20**, 557 (1991).
- ²⁸ R R Arslanbekov, A. A. Kudryavtsev, R C Tobin, *Plasma Sources Sci. Technol.* **7**, 310 (1998).
- ²⁹ N. Baguer, A. Bogaerts, R. Gijbels, *Spectrochim. Acta Part B* **57**, 311 (2002).

³⁰ R. S. Mason, R. M. Allot, *J. Phys. D* **27**, 2372 (1994).

Chapter 6

*Study of the Ar^m metastable atom population
in a hollow cathode discharge by means of a
hybrid model and spectrometric measurements*

The role of the metastable Ar^m atoms in a cylindrical HCD is studied self-consistently based on a hybrid model and experimental measurements in the pressure range of 0.3 to 1 Torr and currents of 1 to 10 mA. The Monte Carlo model describes the movement of the fast electrons, fast Ar^f and Cu atoms and fast Ar^+ and Cu^+ ions as particles, while in the fluid model, the slow electrons, Ar^+ , Cu^+ ions, Cu and Ar^m metastable atoms are treated as a continuum. Typical calculation results are, among others, the two-dimensional profiles of the production and loss rates of Ar^m metastable atoms, as well as the metastable atom densities and fluxes throughout the complete HCD. Moreover, the calculated radial profiles (averaged over the axial direction) of the Ar^m metastable atom density are compared with experimental radial density profiles recorded by laser absorption spectroscopy. The relative importance of the different processes determining the Ar^m metastable population is analyzed, as well as the influence of pressure and voltage on them. Experimental results evidence the presence of the metastable atom production source at the cathode surface, probably originating from fast Ar^+ ions and Ar^f atoms impinging on it. Comparison between experimental and calculated Ar^m metastable atom densities shows a good agreement at low pressures, but at 1 Torr the calculated values differ by a factor of two from the measured ones. Several possible explanations for this discrepancy are discussed.

6 Study of the Ar^m metastable atom population in a hollow cathode discharge by means of a hybrid model and spectrometric measurements

6.1 Introduction

In the present chapter, we will focus on the behaviour of the Ar^m metastable atoms and their interaction with the other particles present in the HCD.

The general processes, which determine the metastable atom density in glow discharges, were first studied by Ebbinghaus.¹ Since then many papers have been published, where the Ar^m metastables are being studied either experimentally (using atomic absorption spectroscopy,²⁻⁵ plasma induced emission spectroscopy,⁶ laser induced fluorescence,⁷ etc) as well as by numerical models (where the transport of metastable atoms is described by continuity equations, yielding the metastable density).⁸⁻¹⁰ The population of Ar^m metastable atoms was studied, experimentally and with the use of balance equations, in various kinds of plasmas including afterglow,^{11,12} dc,¹³ rf,¹⁴⁻¹⁶ and helicon⁴ discharges. Also some studies have been performed with respect to the role of metastables in the glow discharge with formation of a positive column (PC).^{17,18}

In the present chapter, we will analyze the role of Ar^m metastable atoms in a HCD, using a metastable fluid model, which is combined with other Monte Carlo and/or fluid models for electrons, Ar^+ and Cu^+ ions, fast Ar^f atoms and fast and thermal Cu atoms. A similar combination of models has been applied in the literature for the simulation of glow discharges with planar cathode, both in Ar, in dc¹⁹ and rf¹⁵ regimes. The advantage of this procedure is that it allows following the influence of the metastable atoms on the electron energy distribution, the ionization rates, the ion and electron densities, etc, as well as the influence of these parameters on the metastable atom density. Moreover, Ar^m metastables play a decisive role in the ionization of the sputtered Cu atoms.

From this chapter on, the sputtered species have been included in the model. Hence as fast Ar^f atoms are considered the Ar atoms formed by elastic collisions of Ar^+ ions and Cu^+ ions with the background Ar gas and which have energies higher than 1eV. The fast Cu atoms (Cu^f) are the sputtered atoms from the cathode. Indeed the Cu atoms are emitted with an initial energy of several eV and they are considered as fast particles

until they are thermalized, i.e., mainly due to elastic collisions with the background gas. The fast Ar⁺ and fast Cu⁺ ions are considered in the cathode dark space, where these ions gain energy from the electric field.

The energy threshold for considering electrons as fast particles was 4.6 eV, which corresponds to the ionization energy of the Ar metastable levels.

In the following, calculated metastable atom density profiles (axially averaged) are compared with experimental density profiles measured by laser absorption in a similar discharge geometry (1 cm diameter, 3 cm long) and at the same conditions (0.3 to 1 Torr pressure and 1 to 10 mA current).

6.2 Experimental set-up

The HCD geometry consists of a cylindrical hollow cathode copper tube of 1 cm inner diameter and 3 cm length, with a copper made disk at each tube end. One of those disks acted as anode, while the other disk was connected to the cylindrical hollow cathode (asymmetrical configuration). A narrow slot of 0.1cm wide and 1 cm long has been machined into each disk in order to allow the map of the laser beam passing through the discharge. This HCD was surrounded by a Pyrex envelope and placed inside a vacuum vessel evacuated by a turbo molecular pump. To eliminate eventual introduction of impurities from outgasing or from micro-leaks, the vacuum vessel was continuously flushed with 3 sccm of high purity (99.998%) argon gas. The gas pressure, measured with a capacitance manometer, was varied from 0.3 to 1 Torr by adjusting the pumping speed with a control valve. The discharge was operated at currents between 0.5 to 10 mA, for which the measured discharge voltage was ranging from 230 to 316 V.

The population of the two metastable states (³P₂ and ³P₀) was measured using optical absorption, with a tunable Littman type external-cavity diode laser (LD110, Sacher Lasertechnik) as light source. The laser was tuned on the transitions $\lambda = 772.42$ nm and 772.38 nm, originating from the ³P₂, ³P₀ metastable levels, respectively. Fig. 6.1 shows the optical arrangement.

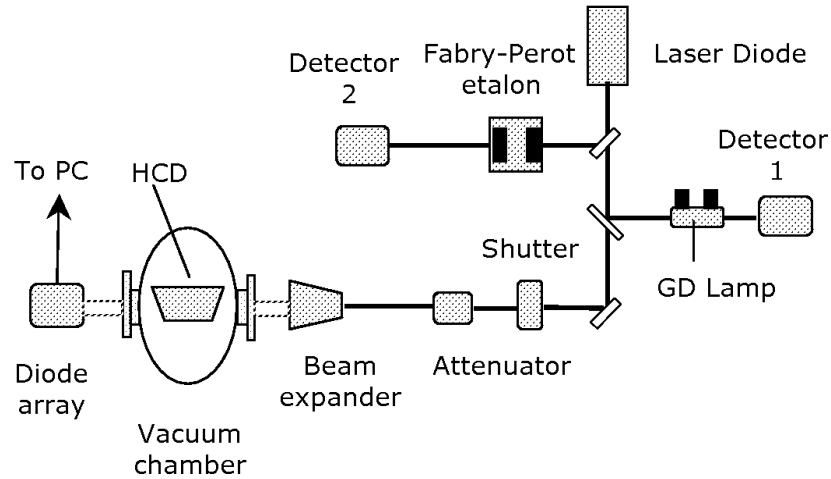


Fig. 6.1 Schematic overview of the experimental setup.

Two secondary beams have been obtained using beam splitters. The first beam was used for the precise frequency calibration with a Fabry-Perot interferometer and the absorption signal from the second beam, crossing a low pressure reference argon glow discharge cell, helped for the exact setting of the laser wavelength at the center of the absorption lines.^{4,20} Before entering the vacuum vessel, the main laser beam was attenuated and then horizontally expanded with a set of 4 successive grazing angle incidence prisms, which provided a beam map covering the entire surface of the anode slot. Therefore, a 1.0 x 0.1 cm laser map crossed the HCD cylinder parallel to its axis and exited from the second slot, which was perfectly aligned with the entrance slot. The laser beam was then detected with a photodiode array (PDA-697, Andor Technology), whose 1024 pixels were also aligned with the slots. Hence, each radial position, r , in the HDC corresponds to a pixel number, n . Given the 25 μm step of the pixels; the laser map covered only 400 pixels of the detector. The PDA was controlled by a PC computer. To record the radial profile of the maximum absorption signal, when the laser wavelength was set at the center of the line, the acquisition of 4 files was needed:

$L_p(n)$: (plasma and laser on)

$L_0(n)$: (laser with plasma off)

$P(n)$: (plasma without laser beam, stopped by a shutter)

$B(n)$: (plasma and laser beam off: background, dark counts and readout noise)

According to the Beer-Lambert law, the radial profile of the metastable atoms density, $N(r)$, can be deduced from the following relation:

$$\langle N(r) \rangle = 4\pi\epsilon_0 \frac{mc}{\pi e^2} \frac{\delta\nu_D}{2\sqrt{\ln 2/\pi}} \frac{1}{lf} \ln \left(\frac{L_p(n) - P(n)}{L_0(n) - B(n)} \right)$$

where m and e are the electron mass and charge, c is the light speed,

$\delta\nu_D = \frac{2\sqrt{\ln 2}}{\lambda_0} \sqrt{\frac{k_B T(t)}{M}}$ is the Doppler width (FWHM) related to the temperature $T(r)$ of

the metastable atoms, l is the length of the HCD and f is the oscillator strength of the line, whose values are 0.028 and 0.31 for the 772.38 and 772.42 nm lines, respectively.²¹ We estimate a radial resolution better than 0.01 cm, corresponding to 4 pixels. We should point out that the measured populations represent axially averaged values. To avoid saturation phenomena leading to an underestimation of the densities,²² the intensity of the monitoring laser map was reduced to about 10 $\mu\text{W}/\text{cm}^2$.

In a preliminary experiment, the laser beam was limited to 0.1 cm in diameter, the PDA was replaced with a photodiode (PD), the laser frequency was modulated (at 10 Hz) around the line center (about 10 GHz modulation) and the signal from the PD, together with signals from detectors #1 and #2, were recorded with a digital oscilloscope (see for details Refs. 4 and 20). This was done in order to deduce from the Doppler profile of the absorption line the temperature of metastable atoms, which is similar to the gas temperature T_g , under our pressure conditions.²⁰ When moving the laser beam along the diameter of the HCD, we did not observe any radial dependence of T_g , but a slight increase of T_g with pressure and discharge current was observed. However, to simplify, this dependence of T_g on the plasma parameters, is neglected in the model.

6.3 Calculated two-dimensional Ar^m metastable atom density profiles

The models were applied to the Ar-Cu HCD (asymmetric configuration), described in chapter 3 (see Fig. 3.1). The discharge conditions assumed in the model were the same as in paragraph 3.2.

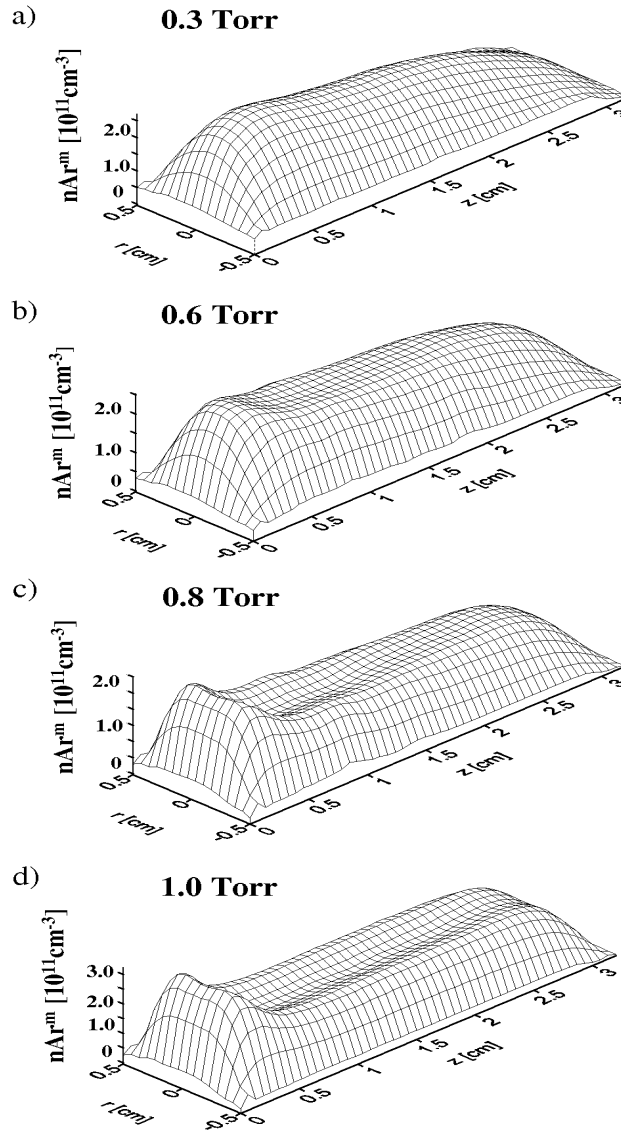


Fig. 6.2 Calculated two-dimensional profiles of the Arm metastable atom population at 6 mA at 0.3 Torr (a), 0.6 Torr (b), 0.8 Torr (c), and at 1 Torr (d).

Fig. 6.2 shows the calculated two-dimensional Ar^m metastable atom density profiles, obtained under the following assumptions, which yielded the best agreement with experiment:

1. At the walls, a fraction (in the order of several %, see below: Fig. 6.6) of the Ar⁺ ion flux comes back as Ar^m metastable atoms.
2. The electron quenching rate coefficient is assumed to be equal to $10^{-8} \text{ cm}^3 \text{ s}^{-1}$.
3. It is assumed that the production of Ar^m metastable atoms is due to direct electron impact excitation from the ground state, as well as cascading from higher-lying states, and the electron impact excitation cross section of Puech and Torchin²³ is adopted.

It is clear from Fig. 6.2 that, for all the conditions, the Ar^m metastable atom density is at maximum near the closed end of the HCD (i.e., at the “cathode bottom”). At 0.3 Torr, the Ar^m metastable atom density is more spread out in the entire discharge, due to diffusion, and is characterized by a parabolic shape in the radial direction. With increasing pressure, on the other hand, the Ar^m metastable atoms become more concentrated near the cathode bottom, and the metastable density distribution shows a more flat profile in the radial direction, with even the appearance of a dip at the discharge axis.

The metastable density was found to be in the same order of magnitude as the density of charged particles, i.e., in the order of 10^{11} cm^{-3} . Hence, their role in the ionization of the plasma was found to be negligible. The flux of metastable atoms to the cathode walls was found much lower than the Ar⁺ ion flux for all the conditions (see Fig. 6.3). At 1 Torr, the ratio of metastable atom flux to the ion flux at the cathode was 1/40 (Fig. 6.3b). This ratio increases till 1/20 at 0.3 Torr (Fig. 6.3a), but still, it is too low to play a significant role in the emission of secondary electrons.²⁴

In chapter 4 a similar fluid model was applied to investigate the He^m metastable atom behavior in a HCD at 1 Torr for the same range of currents as in the present chapter. It was found that the He^m metastable atom density was at least one order of magnitude higher than the He⁺ ion and electron densities and consequently the role of metastables in secondary electron emission at the cathode and in the ionization of the discharge was rather important. The metastable-metastable ionization collisions were found to be responsible for about 20% to the total ionization in the He HCD, according to our previous model calculations (see paragraph 4.3).

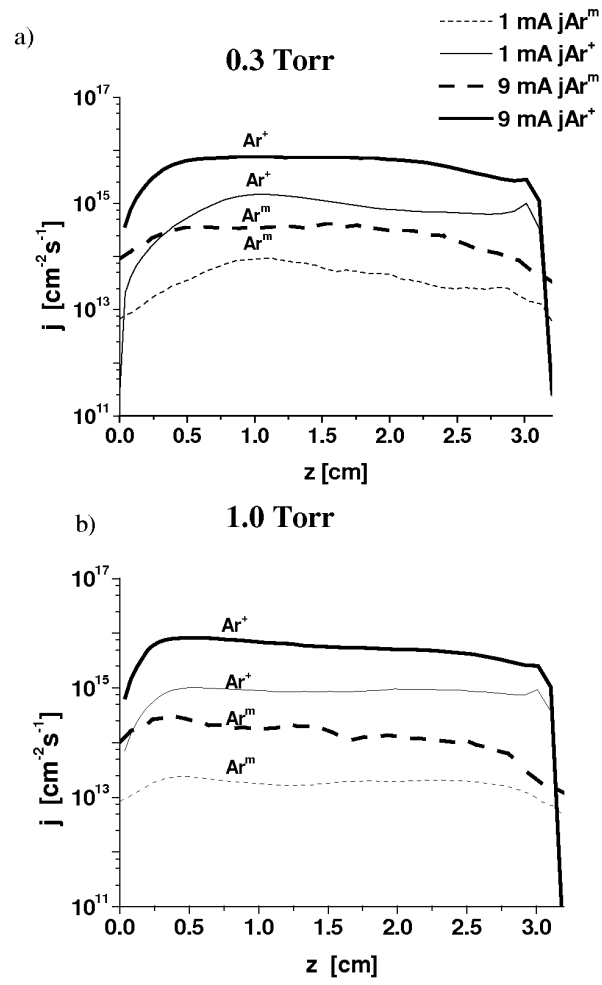


Fig. 6.3 Calculated ion and metastable flux densities at the cathode surface for two discharge currents at 0.3 Torr (a) and at 1.0 Torr (b). In these figures the solid lines represent the ion flux whereas the dashed lines correspond to the metastable flux.

6.4 Comparison between calculated and measured metastable density

To allow comparison with the measured density profiles (left column of Fig. 6.4), the calculated two-dimensional Ar^m metastable atom density profiles were averaged over the axial distance, and the radial profiles obtained in that way, are shown in the right column of Fig. 6.4.

The calculated and measured profiles are in reasonable agreement. At all pressures investigated, the calculated and experimental profiles show a similar radial dependence as well as variation with current. For instance, at 0.3 Torr, all Ar^m metastable densities peak at the HCD axis, and show a nearly parabolic profile, which suggests that the loss is dominated by diffusion to the walls and subsequent de-excitation at the walls²⁵ (Fig. 6.4 (a) and (b)). With increasing pressure, at 0.6 Torr, the profiles begin to flatten at the center, (except at 1 mA), which shows that other loss processes are gaining importance (Fig. 6.4 (c) and (d)). With further increase in pressure, at 0.8 Torr, a dip appears at the axis for the profiles corresponding to the high currents (Fig. 6.4 (e) and (f)), and finally, at 1 Torr, two maxima in these profiles are clearly observed at the high currents (Fig. 6.4 (g) and (h)).

At the current of 1 mA, the densities peak at the center, for all pressures, as in the experiment.

One should point out that the calculated density of the metastable atoms at the cathode walls was adjusted to the experimental values by imposing the boundary conditions (see paragraph 2.4.2.2). Indeed, in agreement with our experimental observations, it was assumed in the present model that the Ar^m metastable population at the cathode walls was not zero. Hence, we assumed that a fraction of the Ar⁺ ions arriving at the cathode, after recombination with the electrons of the conduction band of the metal surface, come back to the discharge as Ar^m metastable atoms. As we can see from Fig. 6.4, the Ar^m metastable density at the walls increases with increasing current (at constant pressure) and with decreasing pressure (at constant current) i.e., at conditions where the reduced electric field increases (see Fig. 6.5).

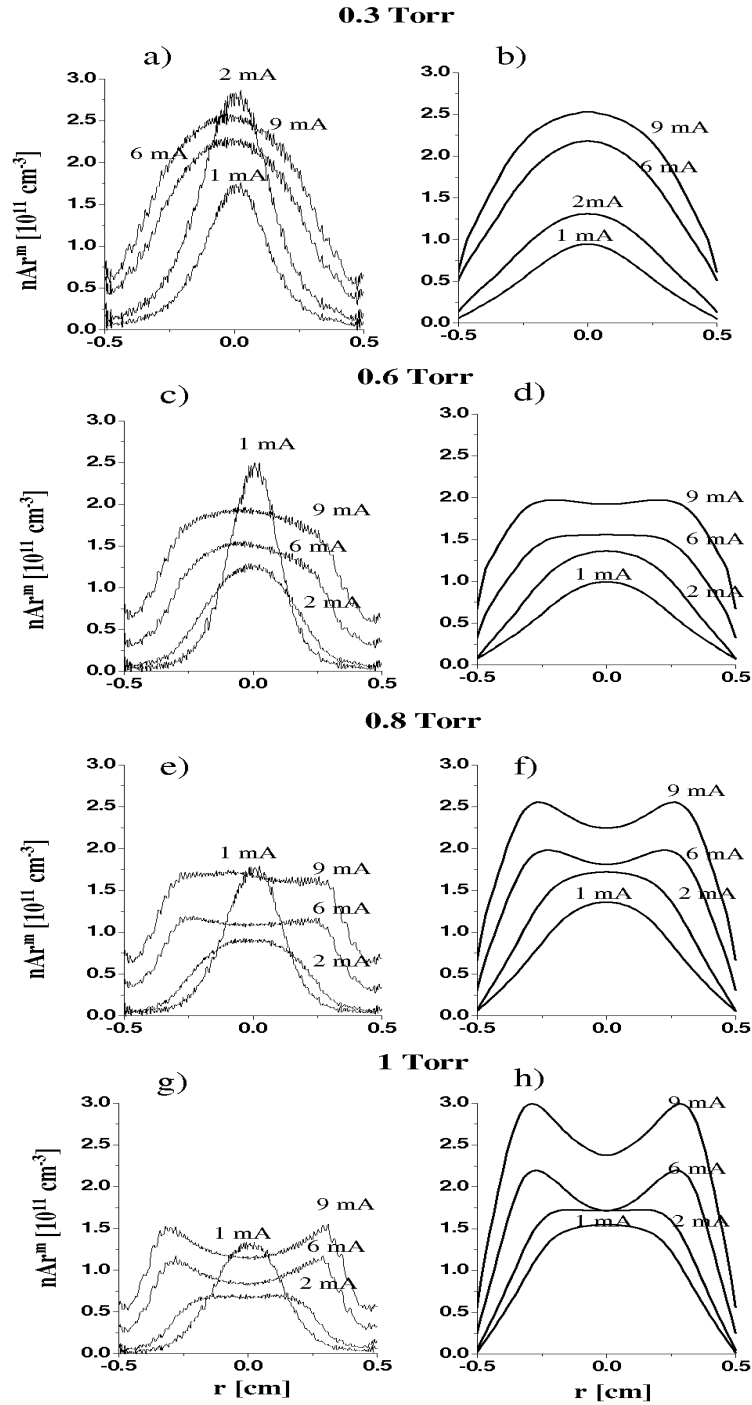


Fig. 6.4 Radial dependence of the (axially averaged) Ar metastable atom density profiles at four different pressures: experimental profiles (a, c, e, g) and calculated profiles (b, d, f, h).

The increase of the reduced electric field means a rise in the average energy of all charged particles. The fact that the metastable atom density at the walls increases with the average energy of the impinging Ar⁺ ions, may confirm our assumption that the metastable population at the walls is the result of Ar⁺ ion resonant neutralization at the cathode surface, as the probability of this process increases with rising incoming ion energy.²⁶

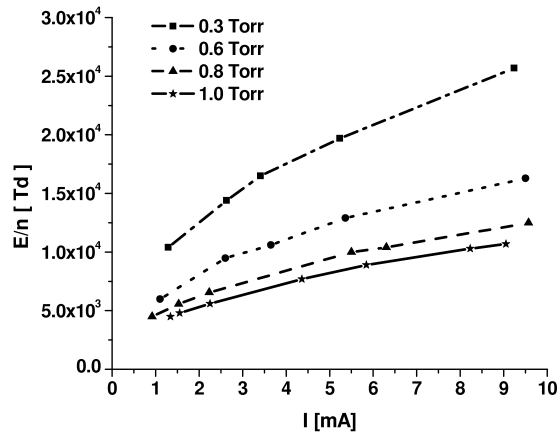


Fig. 6.5 Calculated (axially averaged) value of the electric field strength at the cathode wall, as a function of electrical current, for different values of gas pressure.

The percentages of Ar⁺ ion flux needed to reproduce the metastable density at the walls are shown in Fig. 6.6, for all the discharge conditions analyzed here. At constant discharge current, this fraction decreases with increasing pressure. This is because at constant current, the ion current to the cathode remains almost constant as the pressure increases, while the diffusion flux of metastable atoms to the wall decreases almost as (pressure)⁻¹. At constant pressure, this fraction also decreases with increasing current; because the Ar⁺ ion flux to the cathode increases linearly with the discharge current, while the Ar^m metastable flux to the wall changes only slightly. (Cfr. the curves of 1 mA and 9 mA in the left column of Fig. 6.4).

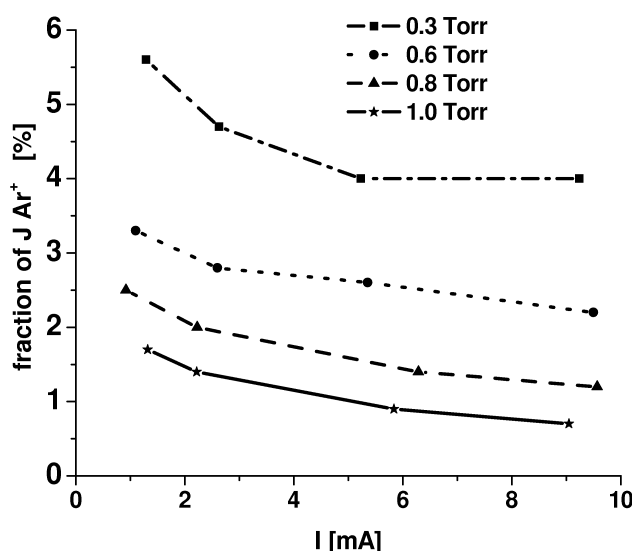


Fig. 6.6 Calculated fraction (in %) of the Ar^+ ion flux at the cathode walls coming back to the discharge as Ar^m metastable flux, as a function of the discharge current.

Some features of the measured profiles can, however, not yet correctly be reproduced by the model:

(a) *At constant pressure, the calculated Ar^m metastable atom densities increase with current, while experimentally this is not the case for the lower currents.* Indeed, the measured metastable population at 1 mA, at its maximum, is higher than the corresponding values at higher currents for 0.6, 0.8 and 1 Torr, and at 0.3 Torr the maximum metastable density is the highest at 2 mA. The reason for the rise of calculated Ar^m metastable atom density with rising current is the increase of total production rate with current, as is shown in Fig. 6.7. Indeed, the fast electron, Ar^+ ion and fast Ar^f atom fluxes, which define all production mechanisms, are directly proportional to current. Hence, in order to obtain a drop in calculated Ar^m metastable density with rising current, as is observed in the experimental results, the rates of the loss mechanisms should increase more than linearly with current, in order to compensate for the increased production. However, at high current, hence high electron density, the main loss is due to electron quenching (see below, paragraph 6.5), for which the rate is only linearly proportional to the current. At low current, hence low electron density, diffusion is the dominant loss mechanism, but it does not depend on current at all. Hence, our model is not able to predict a higher metastable population at low current (e.g., 1 or 2 mA) than at high current (6 or 9 mA).

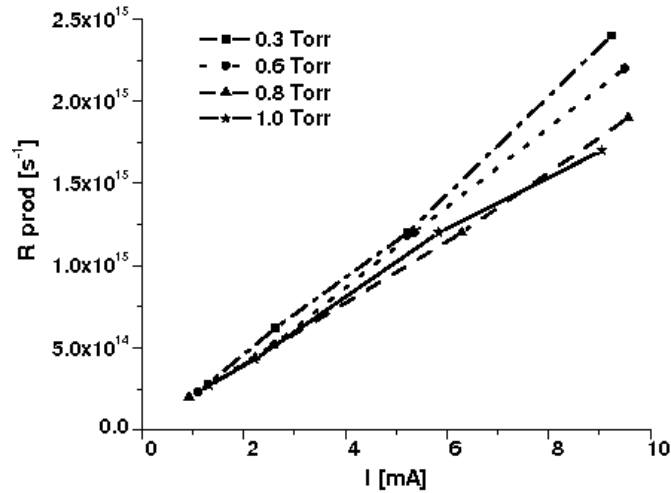


Fig. 6.7 Total production rate determining the Ar^m metastable atom density, integrated over the entire discharge, as a function of total discharge current, at four pressures.

(b) At constant current, with increasing pressure, the calculated metastable density increases, while in the experiment the opposite tendency is observed. As shown in Fig. 6.7, the total production rate increases slightly with decreasing pressure, although it is worth to mention that the pressure effect is much less pronounced than the current effect, described above. The reason for this increasing production rate with decreasing pressure results from the increasing contribution of fast Ar⁺ ions and Ar^f atoms. Indeed, at lower pressures, the reduced electric field increases, as the discharge voltage increases (at constant current), and moreover, the energy relaxation length of Ar⁺ ions inside the CDS rises. So the fast Ar⁺ ions and Ar^f atoms have higher energy, and consequently, fast Ar⁺ ion and Ar^f atom impact excitation become more efficient as production mechanisms. (See previous chapter, paragraph 5.2.3). However, in spite of the increasing production rate with decreasing pressure, the calculated metastable density decreases with decreasing pressure. This is a consequence of the increasing role of diffusion at lower pressure^{2,18,27} spreading out the metastable atoms to the walls, where they are destroyed upon collisions with the wall. At 0.3 Torr, diffusion is the main loss mechanism (see also below, paragraph 6.5), as can be deduced from the nearly parabolic shape of the calculated radial profiles.

A similar behavior of increasing Ar^m metastable population with increasing pressure and current was also found in an Ar glow discharge with planar cathode in dc^{7,13}

and in rf^{15,28} regimes, where the Ar^m metastable population has been measured (by laser induced fluorescence or by optical emission) and calculated (with a hybrid model) at similar conditions as under study here. Experimental and calculation studies performed in Ar PC discharges^{17,18,29} at [0.075-4] Torr show that the metastable population increases up to 0.1 Torr and then decreases, i.e., the metastable population appears to saturate by the effect of pressure at much lower values. This results from the much larger vessel dimensions in these experiments, so that the diffusion rate is significantly reduced, and hence, the relative importance of volume quenching mechanisms increases.

Hence, although it should be noted that in absolute values, the difference between calculated and experimental densities is not large (i.e., at maximum a factor of 2, cfr. Figs. 6.4(g) and (h)), and can even be considered rather small, in view of the uncertainties in the model and experiment we want to investigate in more detail why our model, in its current state, i.e., with the rate coefficients and cross sections used as presented in Table 2.6, predicts a pressure dependence of the metastable atom population, which is the opposite to the experimental observations.

In the following sections, we will investigate in somewhat more detail the relative contributions of the different production and loss mechanisms, as well as the influence of the rate coefficients and cross sections, in order to find out, how a better agreement with experimental data might be obtained.

6.5 Production and loss processes determining the Ar^m metastable atom density

The effect of the different production and loss mechanisms in modeling the metastable atom density profiles can be understood from Fig. 6.8, where the radial dependence of the production and loss rates, averaged over the axial distance, is shown for a discharge of 6 mA, at 1 Torr and 0.3 Torr, as a representative example for all discharge conditions investigated here.

At 1 Torr, electron impact excitation (exc,e) is the main production source for the metastable atom population, and the maximum of the electron impact excitation rate (Fig. 6.8a) is found almost at the same radial position as the maximum in the metastable density (Figs. 6.4g, h), i.e., in the NG close to the boundary with the CDS. At this pressure, only a few heavy particles have enough energy for excitation (see paragraph 5.3).

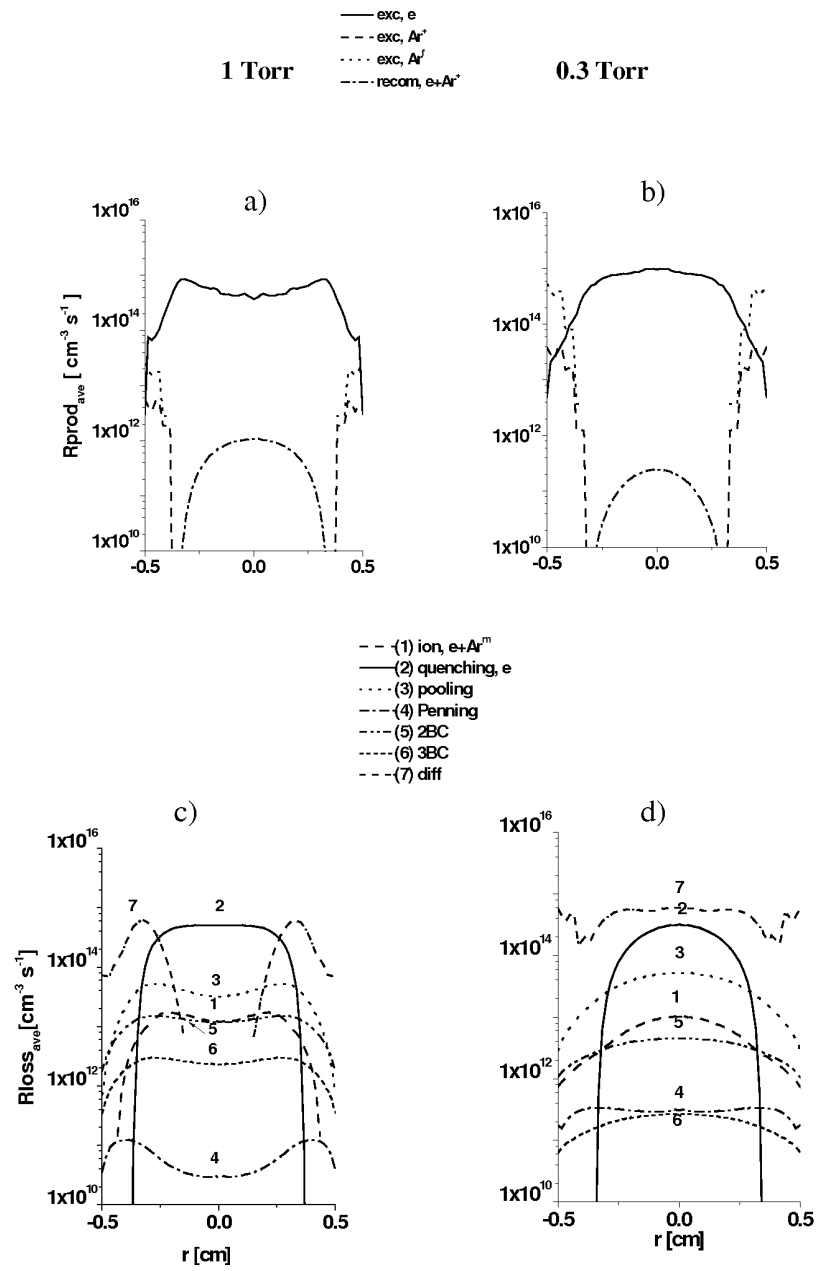


Fig. 6.8 Calculated radial profiles of the axially averaged production (a,b) and loss (c,d) rates determining the Ar^m metastable atom population at 6 mA, at 1 and 0.3 Torr, respectively.

With decreasing pressure, as the mean energy of the fast particles increases and taking in account that at energies above 50 eV the cross sections for Ar⁺ ion and Ar^f atom impact excitation to the metastable state become higher than the electron impact excitation cross section, (see Fig. 2.2) the production rate by heavy particles (exc,Ar⁺; exc,Ar^f) increases, and they turn out to be the main production source for the metastable Ar atoms in the CDS (see Fig. 6.8b). Electron impact excitation remains the main production source in the NG and its rate peaks at the center (HCD axis), similar to the metastable atom density profile (Fig. 6.8b). At low pressures, due to the increase of the reduced electric field and the CDS length (see Figs. 6.5 and 3.12, respectively), the average electron energy, at the discharge axis, will be high enough to cause excitation collisions to the metastable state, while at high pressure, very few electrons will reach the discharge axis, with sufficient energy to undergo inelastic collisions (see Fig. 3.10).

The role of electron-ion recombination (e,Ar⁺ recom) was found negligible for all the conditions, due to the low ionization degree of the plasma (10^{-5} to 10^{-4}).

Concerning the losses, we see that at 1 Torr the main mechanism of destruction is electron transfer to the resonance level (q,e). Diffusion to the walls (diff) becomes important only in the CDS, as the maximum of the metastable atom profile is found in the NG, close to the NG-CDS interface (Fig. 6.8.c). This is in contrast to the calculated results at 0.3 Torr, where diffusion predominates over the other loss processes all over the discharge volume and spreads out the metastable atom population toward the walls, where the metastable atoms undergo de-excitation (see Fig. 6.8d).

Fig. 6.9 shows the relative contributions of the different production (a) and loss (b) processes, integrated over the entire discharge, as a function of current, for the different pressures investigated.

It is clear from Fig. 6.9a that electron impact excitation (thin lines) is the dominant production mechanism of Ar^m metastable atoms, at all conditions investigated, with a contribution ranging from 60 till almost 100 %. The contribution decreases slightly with increasing current and decreasing pressure. The reason is that the fast Ar^f atoms start to play a quite important role at higher current and lower pressure, as is also observed in Fig. 6.9a (thicker lines). Indeed, a higher current (at constant pressure) and a lower pressure (at constant current) correspond to a higher discharge voltage, hence to a higher reduced electric field (see Fig. 6.5) and consequently higher energies of the fast Ar⁺ ions and Ar^f atoms, so that these species become more efficient in excitation to the Ar^m metastable level. The contribution of fast Ar⁺ ions to the production of Ar^m metastables

(not shown in Fig. 6.9a, for the sake of clarity) increases also slightly with current, and with decreasing pressure, but it was always less than 4%, because of the lower fast Ar⁺ ion flux and impact excitation cross section compared to the fast Ar^f flux and impact excitation cross section. Finally, the contribution of electron-ion recombination is calculated to be negligible as production mechanism for the Ar^m metastable atoms, with a typical contribution of less than 0.1%.

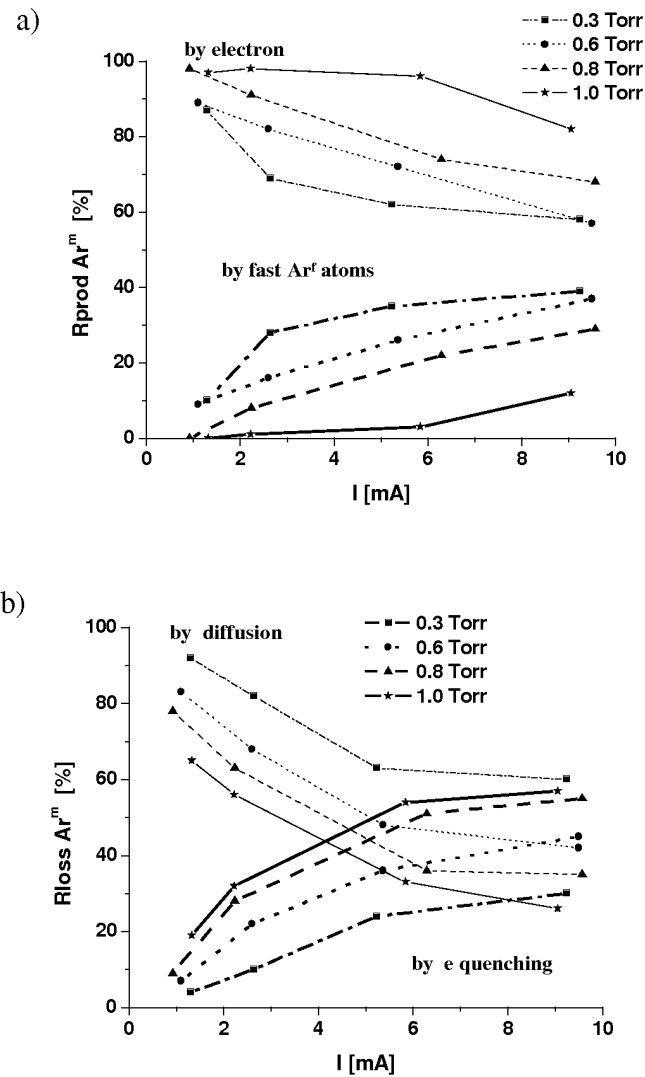


Fig. 6.9 Calculated relative contributions of the main production (a) and loss (b) processes, integrated over the entire discharge, as a function of current, at four pressures.

Concerning the loss mechanisms (Fig. 6.9b), diffusion to the walls, followed by de-excitation at the walls (thin lines), is calculated to be the dominant loss mechanism at 0.3 Torr and for low currents at all pressures investigated, with contributions ranging from 60 till over 90%. Electron impact transfer of the metastable to the resonance level (thicker lines) becomes increasingly important at higher current and pressure, and it reaches a contribution of 60% at the highest current and pressure investigated. This is like expected, because of the higher electron densities at higher current and pressure. Some other loss processes (not shown in the figure), like electron impact ionization ($\text{ion,e} + \text{Ar}^m$) from the metastable level, pooling ionization (pooling) and two-body collisions with Ar gas atoms (2BC), contribute for a few % to the total loss of Ar^m metastable atoms, whereas three-body collisions with Ar gas atoms (3BC) and Penning ionization of the sputtered Cu atoms (Penning), were calculated to contribute for less than 1 %.

We can conclude that the Ar^m metastable atom profiles at pressures of 0.8 and 1 Torr and at currents of 6 and 9 mA are mainly determined by two factors: (1) enhanced production through electron impact excitation collisions from the ground state, which peaks near the CDS-NG interface, coupled by (2) enhanced loss, due to thermal electron quenching, at the cylinder axis, i.e., at the position where the maximum of the electron density is found for all the conditions investigated (see for example Figs. 3.7b-3.9b). With decreasing pressures, the main source of metastable atom production remains electron impact excitation from the ground state, but due to the increase of the electron energy relaxation length, the maximum of the electron impact excitation rate is now shifted to the discharge axis. Moreover, as the discharge pressure drops, the diffusion increases, becoming the main loss, which is reflected by the nearly parabolic radial profile of metastable atom densities at low pressures.

Integrated over the total discharge volume, ionization due to the metastable atoms was found to be less than 0.5 % of the total ionization rate.

6.6 Influence of the electron quenching rate coefficient

We have found that the profile of the metastable atom population was greatly dependent of the electron-quenching coefficient (k_q) employed in the calculations. For example in Ref. 30 we have used a $k_q = 2 \times 10^{-7} \text{ cm}^3 \text{ s}^{-1}$, which is a value commonly used in models in the literature, when a collective metastable level is assumed,^{9,14,19,29} and we obtained for the higher currents (6 and 9 mA), that the dip of the calculated Ar^m radial

profile at the HCD axis was much more pronounced at 0.8 Torr and 1 Torr. Moreover, at low pressures, the calculated metastable density profiles show also a dip at the HCD axis, (see Fig. 8 of Ref. 30) in contrast to the experimental observations.

We assumed in the present work that the effective electron quenching coefficient for the collective Ar metastable level should be in the same order as the electron impact transfer coefficient from the metastable 3P_2 level to the radiative level 3P_1 , because these two are the most populated levels of the $3p^54s$ group. In an Ar afterglow, Sadeghi³¹ measured an electron impact rate coefficient for transfer from the 3P_2 level to the 3P_1 level of $3.7 \times 10^{-8} \text{ cm}^3 \text{ s}^{-1}$.

We used an effective quenching coefficient equal to $10^{-8} \text{ cm}^3 \text{ s}^{-1}$, because this yielded calculated density profiles in good agreement with the experimental values (see Fig. 6.10). We call this an effective electron-quenching coefficient, because our model does not consider explicitly all the four $3p^54s$ levels. Hence, this coefficient implies the total loss of the metastable atoms due to electron impact transfer from the metastable levels to the radiative levels and also the reverse process. Indeed, the radiative levels 3P_1 and 1P_1 are resonant, i.e., due to the imprisonment of resonance radiation, their lifetimes are much higher than their radiative lifetime.^{11, 27}

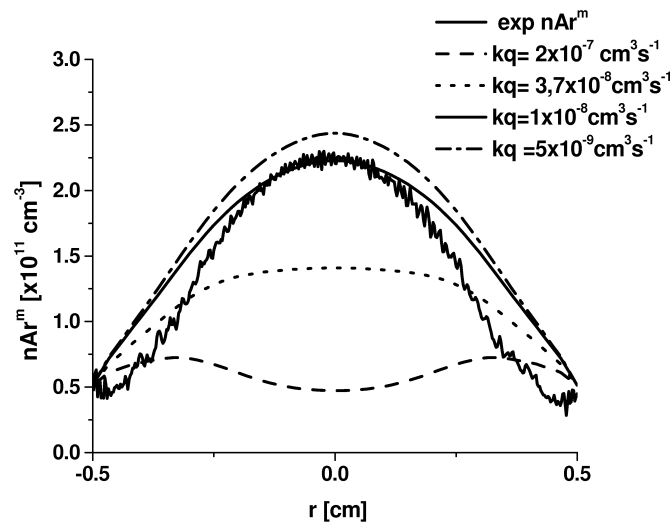


Fig. 6.10 Effect of considering different values for the electron quenching coefficients on the calculated Ar^m metastable atom density profile, illustrated for a discharge at 0.3 Torr and 6 mA.

Using this value of k_q , the comparison between the calculated and experimental results shows that the metastable fluid model at 0.3 Torr works well (see Fig. 6.4(a) and

(b)), but at higher pressures (0.8 and 1 Torr) it overestimates the metastable atom population (cfr. Figs. 6.4 (e/f) and (g/h)). This can be a consequence of not considering the interaction between the different excited levels within the $3p^54s$ state, because at this pressure range, electron quenching was found the main loss process, while at 0.3 Torr diffusion to the walls was found the dominant loss mechanism. Also, k_q could be electron temperature dependent, hence pressure dependent, a fact that was ignored in our model. However, another reason can be that the total production at higher pressures is overestimated.

6.7 Influence of the electron, fast Ar⁺ ion and fast Ar^f atom impact excitation cross sections

To calculate the rate of electron impact excitation to the metastable state, which is the main source of production, the integrated electron impact excitation cross-section, also called the optical-excitation cross section was used for all conditions. This cross section represents the direct excitation from the ground state plus the contributions of excitation to, and subsequent cascading from, higher-lying states. The contribution of the cascading from the higher-lying states in determining the population of the metastable state increases with increasing the reduced electric field strength.^{2,23} At constant current, the reduced electric field increases with decreasing pressure (see Fig. 6.5), because a constant current at lower pressure arises from a higher discharge voltage. For example, at 9 mA, the reduced electric field, at its maximum value, i.e., at the cathode wall, in the first half of the cylinder cathode, at 0.3 Torr, is 2.7 times larger than at 1 Torr, as can be seen from Fig. 6.11. Hence it can be deduced that the contribution of cascading from higher states is less important at higher pressure.

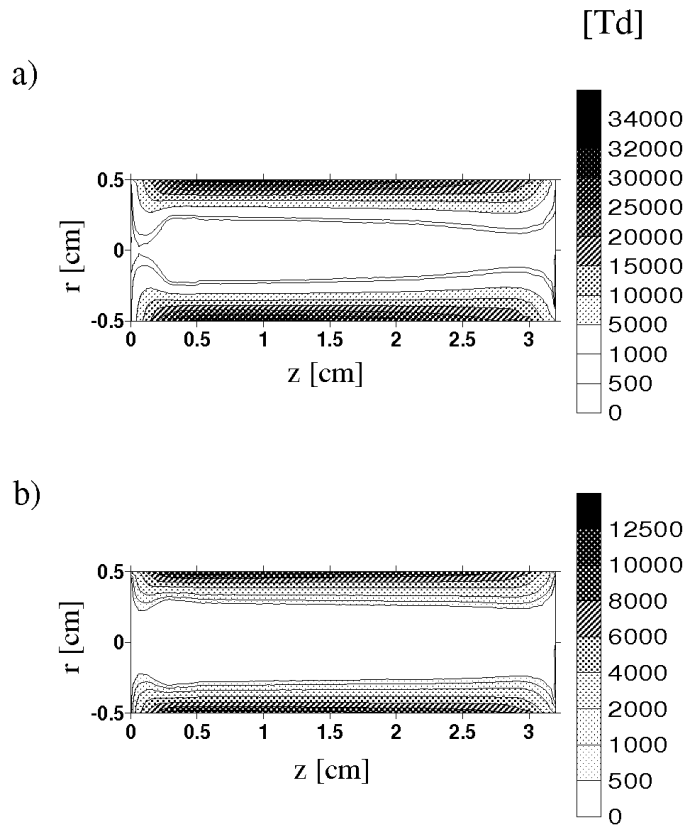


Fig. 6.11 Calculated radial electric field distribution throughout the HCD, at 9mA and at 0.3 Torr (a), and at 1 Torr (b).

At its maximum, the integrated electron impact excitation cross-section to the metastable state presented by Puech,²³ which includes the contribution of cascading, was equal to $2.4 \times 10^{-17} \text{ cm}^2$, which is 2.58 times larger than the maximum of the direct electron impact excitation cross section,³² equal to $9.3 \times 10^{-18} \text{ cm}^2$.

Hence, in order to investigate how better agreement can be reached between calculated and measured metastable densities, we have done some additional calculations, assuming that at 1 Torr the metastable atom population is only due to the contribution of direct excitation from the ground state. For this purpose we have reduced the electron excitation cross section of Puech²³ by a factor of 2.58. Moreover, we have also reduced by the same factor the Ar⁺ ion and fast Ar^f atom impact excitation cross sections to the metastable state, because they were adopted from Phelps,²⁴ and he considered them as upper limits.

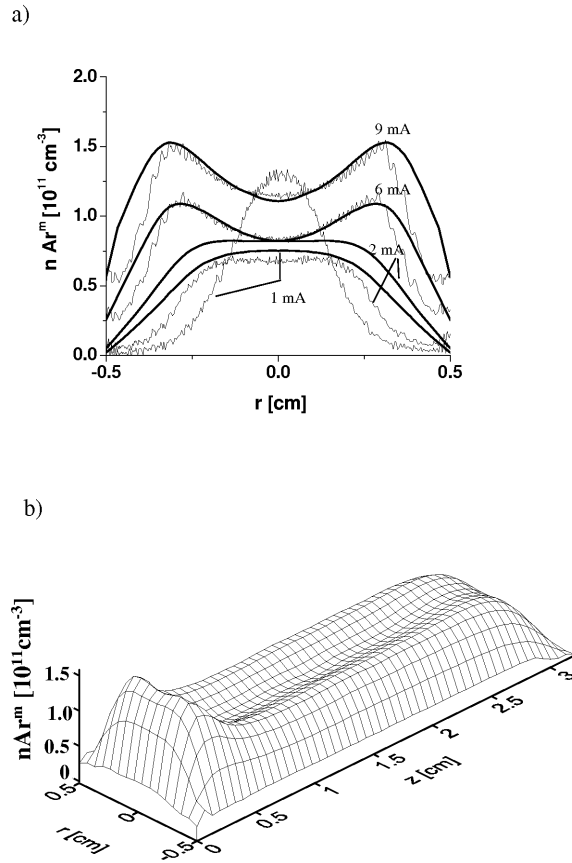


Fig. 6.12 Comparison of the calculated (axially averaged) and measured Ar^m metastable atom density radial profiles at four different currents (a) and the calculated two-dimensional profile of the Ar^m metastable atom population at 6 mA (b), after reduction of the total production rate at 1 Torr.

Using these assumptions, the calculated metastable atom populations at 1 Torr have dropped, and averaged over the axial distance, they are in much better agreement with the experimental profiles, as is illustrated in Fig. 6.12a. Beside that, the two-dimensional profiles of the Ar^m metastable atom density stay (almost) the same (cfr. Fig. 6.12b and 6.2d). The only difference in the profiles is given by the increase of the ratio of the metastable population at the walls compared to its maximum value, as the population at the walls was imposed by the boundary conditions, according to its measured value, and hence it stays the same for these calculations.

6.8 Discrepancy between experiment and model in the CDS

It is, however, apparent from Fig. 6.4, and Fig. 6.12a that for all pressures investigated, the calculated metastable atom population was still found to be a bit higher in the CDS than the experimental values. This can be a consequence of different factors or a combination of them:

1) Maybe the Ar⁺ ion and fast Ar atom impact excitation cross sections are too high, which gives an overestimated production in the CDS, or

2) It might be that, beside the considered mechanisms, still other loss processes should be included in the model, or

3) Maybe the rate coefficients of some processes were not accurate enough. For instance, in the CDS, the sputtered Cu atom density, as well as the Ar^m metastable density itself, are calculated to be fairly high. Although the overall contribution of Penning ionization (of sputtered Cu atoms) integrated over the entire discharge region is relatively low, this process might play a non-negligible role in the CDS, where the density of the sputtered Cu atoms is quite high. However, the rate coefficient of this process is subject to considerable uncertainty. Indeed, this rate coefficient was only estimated¹⁹ from an empirical formula.³³ Also the rate coefficient of pooling ionization (by collision of two Ar^m metastable atoms) was taken from Ref. 18, where it was adapted from the corresponding cross section for a similar process in Ne and He. If for these rate coefficients higher values would be adopted, these loss mechanisms might be more important in the CDS, thereby reducing the calculated metastable atom population, so that the latter could be in better agreement with experiment.

However, we do not want to adapt the rate coefficients like fitting parameters, without any scientific basis, in order to reach better agreement with experiment. We think that more insight can be obtained about the role of different mechanisms, by discussing the discrepancies between model and experiment.

6.9 Conclusions

We have shown the calculation results for the Ar^m metastable atoms compared to their experimental density measured by laser absorption for an Ar HCD with Cu cathode,. Based on experimental results, the following assumptions were made in the model:

- A fraction (in the order of several %) of the Ar⁺ ion flux at the cathode walls returns back to the discharge as Ar^m metastable atoms;
- The value for the electron quenching rate coefficient is assumed to be equal to $10^{-8} \text{ cm}^3 \text{ s}^{-1}$, which is reasonable, compared to measured values

It was found that:

1. At low pressure, the metastable atom densities show a nearly parabolic profile at all currents investigated, because of the important role of diffusion.
2. When the pressure increases, the density profiles become flatter, and at high currents, they even exhibit two peaks at the CDS-NG boundaries, with a dip at the discharge axis, which is determined mainly by the enhanced production by electron impact excitation close to the CDS-NG boundaries and the increasing role of electron quenching as a loss mechanism of the metastable atom population.
3. The contribution of metastable atoms to the formation of charges in the discharge is found to be negligible for the conditions under study, both as ionization source as well as in secondary electron emission from the cathode.
4. Finally, from the comparison between calculations and experiment, we could obtain a better insight in the relative importance of different production and loss mechanisms, and their corresponding rate coefficients and cross sections.
5. The metastable atom densities, calculated in this way, can be used in our model, to predict their importance in the HCD, for instance for Penning ionization of sputtered Cu atoms.

6.10 References

- ¹ E. Ebbinghaus, *Ann. Phys.* **7**, 267 (1930).
- ² K. Tachibana, *Phys. Rev. A* **34**, 1007 (1986).
- ³ K. E. Greenberg and G. A. Hebner, *J. Appl. Phys.* **73**, 8126 (1993).
- ⁴ B. Clarenbach, B. Lorenz, M. Krämer, and N. Sadeghi, *Plasma Source, Sci. Technol.* **12**, 345 (2003).
- ⁵ P. Macko and N. Sadeghi, *Plasma Source, Sci. & Technol.*, **13**, 303 (2004).
- ⁶ G. R. Scheller, R. Gottsho, B. D. Graves and T. Itrator, *J. Appl. Phys.* **64**, 598 (1988).
- ⁷ B. K. McMillan and M. Zachariah, *J. Appl. Phys.* **77**, 5538 (1995).
- ⁸ J. Vlcek, *J. Phys. D.* **22**, 623 (1989).
- ⁹ D. P Lymberopoulos and D. J. Economou, *J. Appl. Phys.* **73**, 3668 (1993)
- ¹⁰ P.A. Sa, J. Loureiro and C.M. Ferreira, *J. Phys. D* **27**, 1171 (1994).
- ¹¹ E. Ellis and N. D. Twiddy, *J. Phys. B*, **2**, 1366 (1969).
- ¹² A. V. Phelps and J. P Molnar, *Phys. Rev* **89**, 1202 (1952).
- ¹³ A. Bogaerts, R. D. Guenard, B.W. Smith, J.D. Winefordner, W.W. Harrison and R. Gijbels, *Spectrochim. Acta Part B*, **52**, 219 (1997).
- ¹⁴ T. Makabe, N. Nakano and Y. Yamaguchi, *Phys. Rev. A* **45**, 2520 (1992).
- ¹⁵ S. Rauf and M. J. Kushner, *J. Appl. Phys.* **82**, 2805 (1997).
- ¹⁶ G. A. Hebner and P. A. Miller, *J. Appl. Phys.* **87**, 8304 (2000).
- ¹⁷ K.A. Hardy and W. Sheldon, *J. Appl. Phys.* **53**, 8532 (1982).
- ¹⁸ C. M. Ferreira, L. Loureiro and A. Ricard, *J. Appl. Phys.* **54**, 2261 (1983).
- ¹⁹ A. Bogaerts and R. Gijbels, *Phys. Rev A* **52**, 3743 (1995).
- ²⁰ R. Engeln, S. Mazouffre, P. Vankan, D.C. Schram and N. Sadeghi, *Plasma Source, Sci. Technol.*, **10**, 595 (2001).
- ²¹ W.L. Wiese, J.W. Brault, K. Danzmann, V. Helbig and M. Kock, *Phys. Rev. A* **39**, 2461 (1989).
- ²² N. Sadeghi, *J. Plasma and Fusion Res.* **80**, 767 (2004).
- ²³ V. Puech and L. Torchin, *J. Phys. D* **19**, 2309 (1986).
- ²⁴ A. V. Phelps, *J. Phys. Chem. Ref. Data* **20**, 557 (1991).
- ²⁵ A. von Engel, *Ionized Gases* (Clarendon Press, Oxford, 1955).
- ²⁶ H. D. Hagstrum, *Phys. Rev.* **96**, 336 (1954).
- ²⁷ A. Phelps, *Phys. Rev* **114**, 1011 (1959).
- ²⁸ F. Tochikubo, Z. L. Petrovic and S. Kakuta, *Jpn. J. Appl. Phys.* **33**, 4271 (1994).
- ²⁹ E. V. Karoulina and Yu A Lebedev, *J. Phys. D.* **25**, 401 (1992).

- ³⁰N. Baguer, A. Bogaerts and R. Gijbels, *J. Appl. Phys.* **94**, 2212 (2003).
- ³¹N. Sadeghi, Ph. D thesis, Grenoble (1974).
- ³²N. T. Padial, G. D. Meneses, F. J. Paixao and Gy. Csanak, *Phys. Rev. A* **23**, 2194 (1980).
- ³³L. A. Riseberg, W. F. Parks and L. D. Scheerer, *Phys. Rev. A* **8**, 1962 (1973).

Chapter 7

*Study of the sputtered Cu atoms and Cu⁺ ions
in a hollow cathode glow discharge*

The role of the Cu atoms sputtered from the cathode material in a cylindrical hollow cathode discharge and the corresponding Cu^+ ions is studied with a self-consistent model based on the principle of Monte Carlo (MC) and fluid simulations. In order to obtain a more realistic view of the discharge processes, this model is coupled with others sub-models, which describe the behavior of electrons, fast Ar^f atoms, Ar^+ ions and Ar^m metastable atoms, also based on the principles of MC and fluid simulations. Typical results are, among others, the thermalization profile of the Cu atoms, the fast Cu^f atom, the thermal Cu atom and Cu^+ ion fluxes and densities and the energy distribution of the Cu^+ ions. It was found that the contribution of the Ar^+ ions to the sputtering was the most significant, followed by the fast Ar^f atoms. At the cathode bottom, there was no net sputtered flux but a net amount of redeposition. Throughout the discharge volume, at all the conditions investigated, the largest concentration of Cu atoms was found in the lower half of the HCD, close to the bottom. Penning ionization was found the main ionization mechanism for the Cu atoms. The ionization degree of copper atoms was found to be in the same order as for the argon atoms (10^{-4}).

7 Study of the sputtered Cu atoms and Cu⁺ ions in a hollow cathode glow discharge using a hybrid model

7.1 Introduction

When the ions and neutral gas atoms bombard the cathode surface of a glow discharge, different processes may occur: the atoms and ions can be reflected or implanted, can provoke structural rearrangements in the surface layers of the cathode material, induce secondary electron emission and can also generate a series of collisions between the atoms of the cathode surface. This can lead to the ejection of some atoms of the target surface (i.e., so-called sputtering) or the cascade can go deep into the interior of the target, transferring the energy to lattice vibrations (heat).^{1,2} When sputtering happens, the ejected particles are mostly single ground state neutral atoms, but moving away from the cathode, they can react with the other species present in the discharge, and the sputtered atoms can become ionized.

HCD are extensively used in laser technologies,^{3,4} spectroscopic analysis⁵⁻⁷ and plasma processing (ion etching, thin film deposition, surface treatment).^{8,9} Many of these applications are based on the sputtering of the cathode material by energetic ions and atoms. HCD's are a good medium to obtain high fluxes of energetic particles. The loss of energetic particles (to the anode(s) and to the walls) is considerably reduced in HCD's due to its geometric configuration.^{10,11} Hence, most of the energy of the fast particles is spent inside the discharge for the production of new electron-ion pairs, which allows lower operating voltages than in conventional planar cathode glow discharges. Consequently HCD's give high rates of sputtering while maintaining the discharge voltage relatively low, which decreases the probabilities of overheating the cathode surface as well as the radiation damage of the substrate.

Due to the non-homogeneity of the discharge, the spatial distribution of the sputtered particles is not uniform. Therefore, in order to improve the use of HCD's for the above-mentioned applications, it is important to study the fundamental aspects of the sputtering, such as the spatial distribution of the sputtered particles, their transport and interaction with the other plasma species, as well as the best conditions for optimal sputtering.

The sputtering process in HCD's has been investigated by means of atomic emission,^{5,6,12} absorption,¹³⁻¹⁵ fluorescence¹⁶ and mass spectrometry.¹⁷ Theoretical works are mainly based on numerical simulations. By modelling the sputtering process in HCD's, the metal atom population is calculated based on the solution of the continuity and flux equations. In some works¹⁸⁻²¹ the creation rate for the sputtered atoms is deduced from the total discharge current (to obtain a value for the impinging ion flux to the cathode) and from the applied potential (i.e., the average energy of the bombarding gas ions, needed to determine the sputtering yield, is taken in accordance with the cathode fall potential). This source term can also be given by the thermalization profile, like for example in the work of Oliver and Finlayson,²² where the initial flux of sputtered metal atoms was generated by a MC model in combination with experimental data, and the thermalization profile was calculated based on the "continuous slowing down approximation".²³ However, by tracking the sputtering in that way, the solution is not self-consistently calculated. Indeed, the energy distribution of the particles bombarding the cathode, which is the most important parameter for determining the sputtered flux, is not calculated in the model, but is deduced based on experimental parameters (discharge current and cathode fall potential). Hence it is not possible to obtain the spatial dependence of the sputtered flux. A self-consistent calculation of the sputtered atom density can be carried out, for example, by calculating the energy distribution function of the energetic particles analytically²⁴ or by solving the Boltzman transport equation²⁵ and subsequently the Poisson equation together with the continuity equations, in order to obtain the particle densities and the electric field strength.

Another way of self-consistently calculating the sputtered atom density is given by the hybrid approach, based on a combination of MC and fluid models. With the MC approach^{26,27} the microscopic nature of particles and their interaction can be considered explicitly. On the other hand, the fluid method^{28,29} considers no individual particles but treats them as a continuum. The transport of each kind of particles is described by solving the continuity and flux equations. Moreover, in the case of charged particles the transport equations are coupled with the Poisson equation in order to obtain the electric field strength. The source terms for the continuity equations in the fluid model are taken from the collision rates, which are calculated in the MC models, based on the energy-dependent cross sections, while the particle energy is calculated from the electric field. In that way not only the flux energy distribution of the particles bombarding the cathode can be calculated, but also the interaction of the sputtered atoms with the plasma species can

be followed in a more realistic way. The hybrid approach was used to describe the plasma behavior, and the sputtered species in HCD's, for example in Ref. 30, for a segmented HCD and in Ref. 31 for a longitudinal HCD, respectively. These models were concerned with modified HCD configurations intended for laser applications, which operate at higher pressures and current than conventional HCD's.³²

In the present chapter we will study, by means of a hybrid model, the processes responsible for the cathode sputtering, the transport of the sputtered atoms and the corresponding ions, as well as their interaction with the other species in a HCD. This approach will allow us to calculate in a self-consistent manner, the electric field and the energy distribution functions of the energetic particles, which is not only crucial for the correct description of the electrical properties of the discharge but also for the description of the sputtering. Indeed, in this way, the energy and particle fluxes of the energetic particles bombarding the cathode, as well as the fluxes and densities of the sputtered atoms and corresponding ions, are calculated directly and self-consistently in the model. Hence, a better description of excitation and ionization processes of the sputtered atoms can be achieved, which is useful for application purposes. For example in analytical chemistry, where cathode sputtering is the way of sample atomization, it is important for atom absorption spectrometry to find the place where the concentration of sample (sputtered) atoms and ions is highest in order to improve the absorption signal. Moreover, for atom emission spectrometry, it is useful to improve the analyte spectral line emission intensity, and for mass spectrometric analysis, it is important to optimize the out-coming ion flux. Also in the metal vapor and metal-ion laser technology, where the sputtered atoms and the corresponding ions constitute the active medium, it is useful to know their density distribution as well as the density distribution of the metastable atoms and ions from the carrier gas, in order to optimize the lasing transitions and therefore to improve the laser construction.

The model was applied to the Ar-Cu HCD with the same geometry and discharge conditions as assumed in chapter 3 (see paragraph 3.2 and Fig. 3.1). The particles considered to be present in the discharge are ground state Ar atoms, singly charged positive Ar^+ and Cu^+ ions, metastable Ar^m atoms, Cu atoms, fast and slow electrons, fast Ar^f atoms, fast Cu^f atoms and fast Ar^+ and Cu^+ ions. The criterion for considering particles as fast, the collision processes included, etc are the same as in chapter 6. (See also Table 2.2 and Fig. 2.2).

7.2 Fluxes of bombarding species at the cathode

The sputtered flux from the cathode (eq. 2.25) is determined by the flux energy distribution of the heavy particles bombarding the cathode (i.e., atoms and ions from the discharge gas, as well as ions from the cathode material (so-called self-sputtering)), multiplied with the sputtering yield.

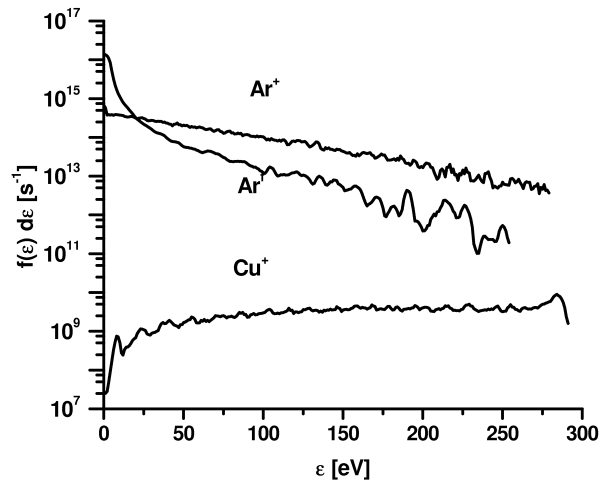


Fig. 7.1 Calculated flux energy distribution of the Ar⁺ ions, fast Ar^f atoms and Cu⁺ ions bombarding the cathode surface at 0.3 Torr and 9 mA.

The relative importance of Ar⁺ ions, fast Ar^f atoms and Cu⁺ ions for the sputtering process can be inferred from Fig. 7.1, where the flux energy distributions at the hollow cathode surface are plotted for a discharge current of 9 mA and a pressure of 0.3 Torr, which is a representative example for all the conditions investigated.

The fast Ar^f atoms have a dominant role, but only at low energies, because their energy distribution decreases rapidly with increasing energy. The same is true, but less pronounced for the Ar⁺ ions. The Cu⁺ ion energy distribution function shows the opposite behavior, because it increases with rising energy. On the other hand, the Cu⁺ ion flux is always several orders of magnitude lower than the Ar⁺ ion and fast Ar^f atom fluxes. Hence in the concerned energy range, the highest flux at the cathode corresponds to the Ar⁺ ions. Keeping in mind that there is a threshold energy for the sputtering to occur,³³

and that the sputtering yield is an increasing function of the bombarding energy up to energies of 1000 eV,³⁴ the sputtered flux will be little for low bombarding energies.

Integrated over the total energy range the contribution of the Ar^+ ions to the sputtering was found to be the most significant, followed by the fast Ar^f atoms. For example at the condition under study, the Ar^+ ions and fast Ar^f atoms contribute for about 85% and 15 % to the total amount of sputtering, respectively. The role of self-sputtering was found to be negligible (less than 0.1%).

The relative contribution of the fast Ar^f atoms rises slightly with decreasing current at low pressures. Indeed, when the discharge current drops, the CDS length increases, hence the Ar^+ ion elastic collision rate inside the CDS increases, and consequently, the ratio of fast Ar^f atom flux to Ar^+ ion flux increases as well. (Note that fast Ar^f atoms are created mainly by Ar^+ ion elastic collisions (including SCT) with the carrier gas atoms).

As the pressure rises, the situation changes. At low currents, the sputtering is almost completely caused by the Ar^+ ions, due to the low energy of the fast atoms. Indeed, with increasing pressure, the Ar^+ ion elastic collision rate increases, and consequently the amount of fast Ar^f atoms increases, as before. However, the discharge voltage decreases as well (at constant current), hence the mean energy of the Ar^+ ions drops, and therefore also the energy transferred to the Ar atoms. Moreover, the fast atom energy relaxation length (determined by the elastic collision cross section) decreases and becomes smaller than the CDS length. Hence the energy of the fast atoms, when they strike the cathode, drops below the sputtering threshold.

It is interesting to notice that, while the Ar^+ ion and fast Ar^f atom energy distributions peak at low energies, the Cu^+ ion energy distribution peaks at the maximum attainable energy, i.e., at the energy corresponding to the cathode fall potential. This is so, because the energy relaxation length of the Cu^+ ions (λ^{Cu^+}) is similar to the CDS length (d), while the energy relaxation length of the Ar^+ ions was found to be about 6 times lower than d . For example at 0.3 Torr and 9 mA, our calculations predict $d = 0.18$ cm and $\lambda^{\text{Cu}^+} = 0.15$ cm, while $\lambda^{\text{Ar}^+} = 0.03$ cm. Moreover, due to the difference in mass between the Cu^+ and Ar^+ ions, the maximum energy transfer of Cu^+ ions to the discharge gas atoms will be less than for the Ar^+ ions. Hence, the Cu^+ ions traverse the CDS without many collisions with the gas atoms, while the collision frequency of the Ar^+ ions is higher and the energy transfer to the discharge gas more effective. Experimentally, this

was also suggested by Hang and Harrison,³⁵ based on metal ion measured intensity profiles in GD's, and it corresponds also to findings by experimental and modeling work in planar GD's.^{36,37}

7.3 Flux of sputtered atoms

The net flux of sputtered Cu atoms at the cathode consists of two contributions, one due to the ejected (sputtered) energetic atoms and another due to the transport by diffusion of the thermalized Cu atoms back to the cathode. In Fig. 7.2 the sputtered (ejected) flux, the back-diffusion flux and the net sputtered Cu atom flux at the cathode are plotted at 0.3 Torr and 9 mA, as a representative example for all the conditions investigated.

At the cathode bottom, (Fig.7.2a) the ejected flux is very low at the border ($r = 0.5$ cm) and increases toward the center, where it stays almost constant. The flux due to back-diffusion of the thermalized Cu atoms shows a sharp maximum at the center, decreasing very rapidly with the radial distance. The diffusion flux is always directed toward the cathode (i.e., back-diffusion), as the density of thermalized atoms decreases in that direction, which is like expected because of the relatively high energy (between 5 eV and 15 eV)³⁸ of the atoms when sputtered from the cathode. Over the entire bottom surface, the back-diffusion flux predominates over the ejected flux. This results in a net flux of atoms re-depositing at the cathode bottom ($jz_{\text{net}}^{\text{Cu}}$ is negative).

At the cathode sidewalls (Fig. 7.2b), the ejected Cu atom flux is very low at the "cathode corner" ($z = 0$); it reaches a maximum at about 0.7 cm from the cathode bottom (i.e., in the first half of the cylinder) and then it decreases toward the anode.

Note that a negative flux now indicates a flux away from the cathode surface and this is opposite from the axial direction (sputtering from the cathode bottom). The back-diffusion flux predominates over the ejected flux only at the region close to the bottom and at the open end of the cathode, where only the diffusion flux is present. Hence, there is a net sputtering from the cathode sidewalls ($jr_{\text{net}}^{\text{Cu}}$ is negative), except near the open end and especially near the cathode bottom, where there is significant redeposition ($jr_{\text{net}}^{\text{Cu}}$ is greatly positive).

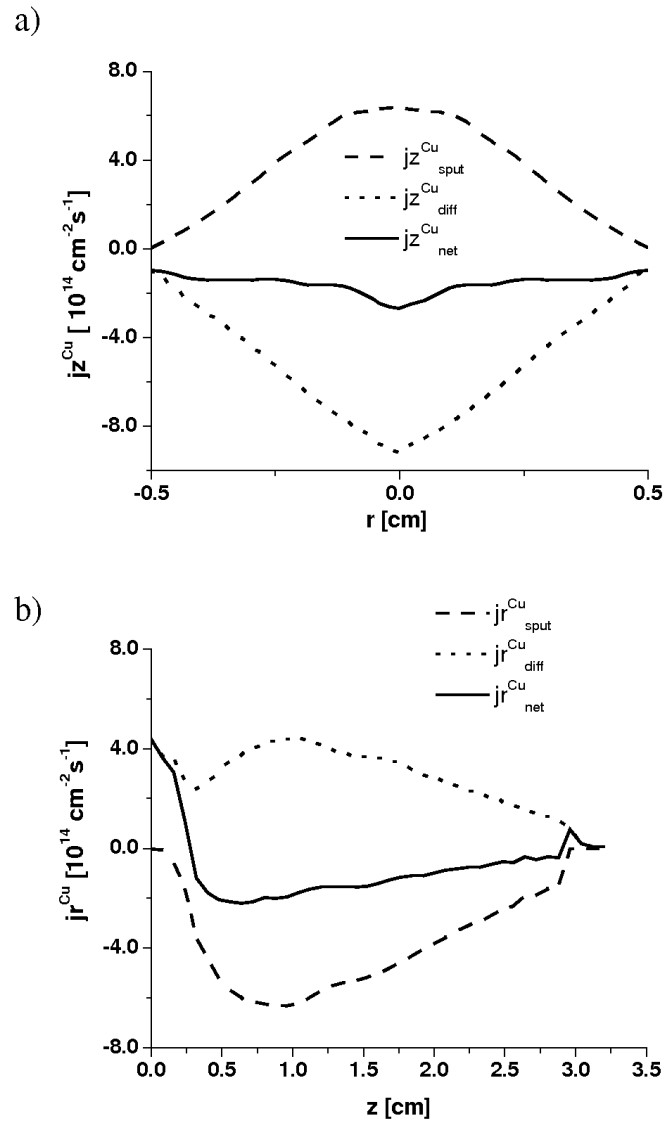


Fig. 7.2 Calculated ejected ($j_{\text{sput}}^{\text{Cu}}$), back-diffusion ($j_{\text{diff}}^{\text{Cu}}$) and net sputtered ($j_{\text{net}}^{\text{Cu}}$) Cu atom axial (a) and radial (b) fluxes at the cathode bottom and sidewalls, respectively, at 0.3 Torr and 9 mA.

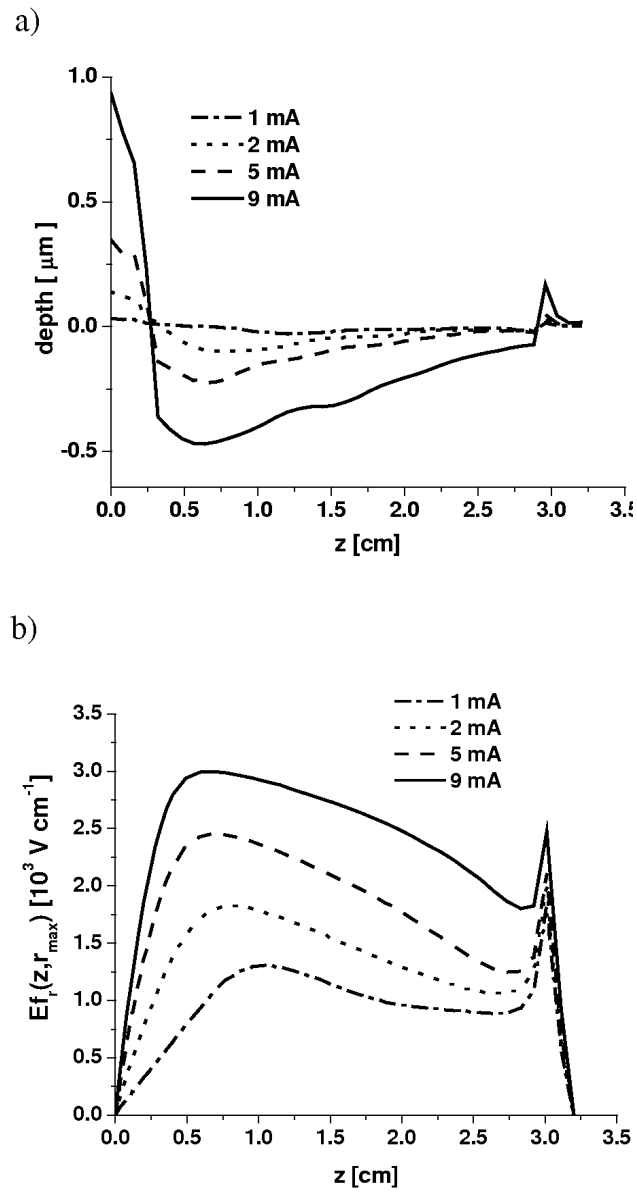


Fig. 7.3 Calculated depth profile at the cathode sidewalls after sputtering for 5 hours (a), compared to the electric field distribution at the sidewalls (b), at 0.3 Torr and at four currents.

This spatial behavior of the sputtered flux is common for all the discharge conditions investigated here: Along the bottom and sidewalls, the profile of the Cu atom fluxes (ejected, back-diffusion and net flux) is rather non-uniform. At the cathode bottom, there is a net flux of redeposition instead of sputtering. At the cathode sidewalls, the various fluxes are larger near the closed end of the hollow cathode. This is a direct consequence of the strong axial and radial electric field here, whereas in the rest of the CDS belonging to the cathode sidewalls, only the radial component of the electric field is strong (except at the open end).

From the comparison of Figs. 7.3a and 7.3b we can indeed see that the cathode depth profile (Fig. 7.3a) due to the net sputtered flux at the cathode sidewalls reflects the spatial distribution of the electric field strength at the cathode sidewalls. A weak radial electric field corresponds to a large amount of redeposition because of the small bombarding flux.

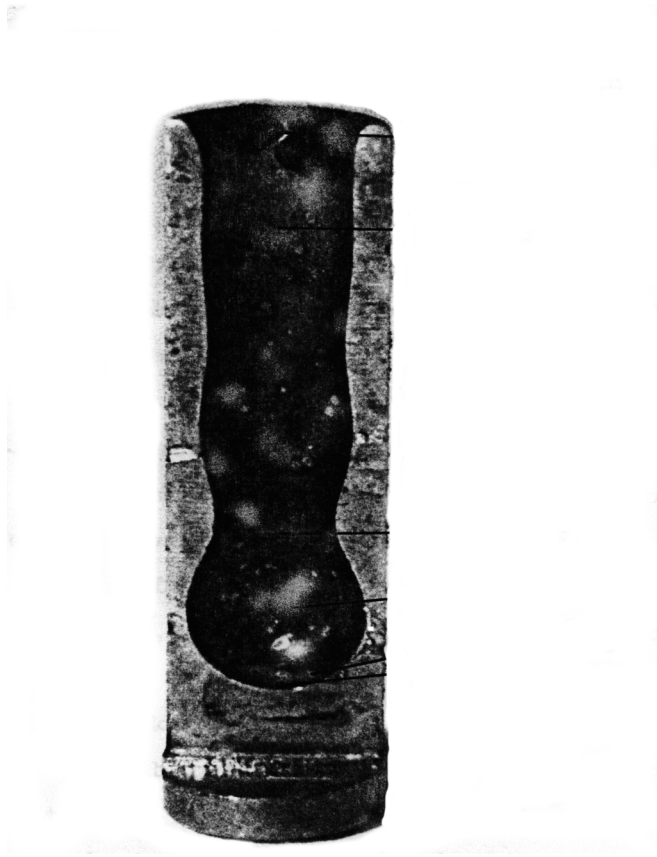


Fig. 7.4 Effect of the cathode sputtering in a Ar-Cu HCD at 1 Torr and at 200 mA after 15 hours sputtering (This figure. was reproduced from Ref. 5).

Our calculated Cu atom depth profiles are consistent with the experimental observations of cut hollow cathodes, which show that the deeper crater is found in the first half of the HCD, i.e., that part of the HCD near the bottom and that the cathode bottom after sputtering is thicker than before, as can be seen at the Fig. 7.4, (reproduced from Ref. 5). (See also for example Fig.14 from Ref. 5 and Fig. 6 from Ref. 22).

Integrated over the entire cathode surface, (i.e., bottom and side-walls), the net sputtered Cu atom flux corresponds to about 20% of the total ejected flux at 0.3 Torr, due to the large amount of redeposition. It should be mentioned that the net sputtered flux from the cathode sidewalls represents 23% of the total ejected flux. This means that a certain fraction of the atoms ejected from the sidewalls, redeposits at the cathode bottom. This ratio of about 20% was found the same for all values of the discharge current. Indeed, with decreasing current (at constant pressure), the net sputtered Cu atom flux drops (see Figs. 7.3a and 7.5), because a decrease in current means a lower discharge voltage (at constant pressure) and lower particle fluxes, hence a drop in the flux energy distribution. However, the ratio of the net sputtered flux to the ejected flux stays nearly constant.

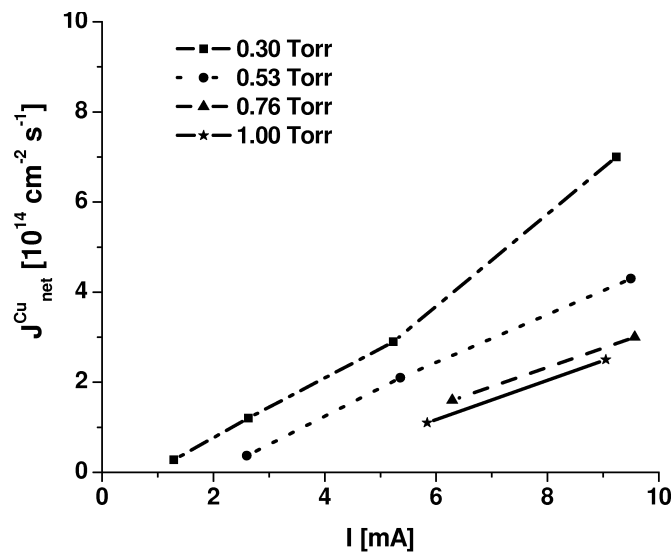


Fig. 7.5 Calculated net sputtered Cu atom flux, integrated over the complete cathode surface, as a function of electrical current and at four different pressures.

With increasing pressure, when the current is held constant, the net ejected flux of Cu atoms decreases (see Fig. 7.5), but the ratio of the net sputtered flux to the total

ejected flux rises slightly. For example at 1 Torr, the net sputtered flux represents about 26% of the ejected flux, while at 0.3 Torr it was found to be around 20%. This can be explained as follows: when the pressure increases at constant current, a lower voltage is needed to sustain the discharge, implying a shift of the flux energy distribution to lower energies, hence less sputtering, but at the same time, due to the increase in pressure, the diffusion drops, hence the back-diffusion is slightly reduced.

7.4 Density of the Cu atoms

The ejected Cu atoms transfer most of their initial energy (typically 5-15 eV) very efficiently to the background discharge gas and consequently, the majority of the sputtered atoms become thermalized already after a few collisions. This is clear from Fig. 7.6a, which shows that the non-thermalized Cu atom density profile has a maximum adjacent to the cathode walls and becomes negligible after 1-2 mm from the cathode surface. Also the thermalized Cu atom density profile (Fig. 7.6b) exhibits a maximum near the cathode walls, i.e., at about 1.2 mm for a discharge at 0.3 Torr and 9 mA.

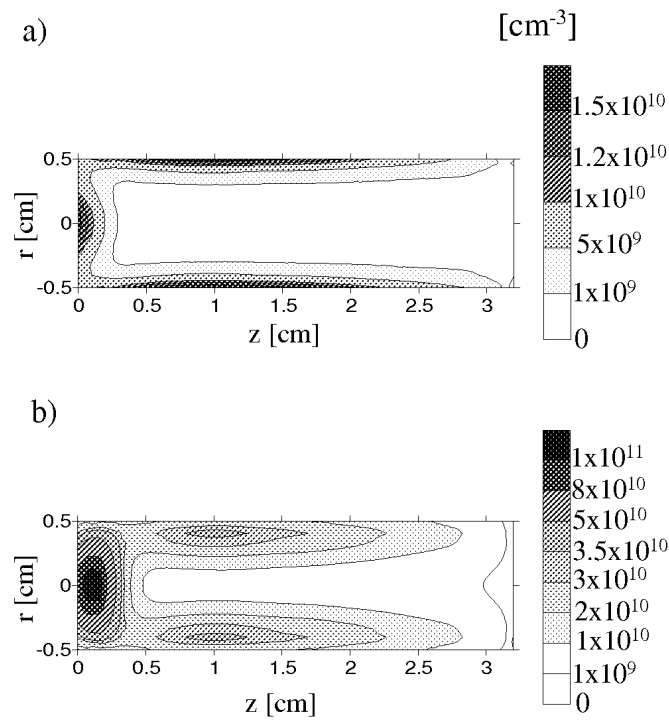


Fig. 7.6 Calculated two-dimensional density profiles of the non-thermalized (a) and thermalized (b) Cu atoms at 9 mA and 0.3 Torr.

The total Cu atom population is given by the sum of both groups: the non-thermalized and the thermalized Cu atoms. It should be noted that the density of the non-thermalized Cu atoms is much lower than that of the thermalized atoms: even at its maximum, it is still one order of magnitude lower, and throughout the discharge volume, their density is negligible compared to the thermalized Cu atom density. Hence the profile of the total Cu atom density resembles closely the corresponding thermalized Cu atom density profile, as can be seen from Fig. 7.7a, which shows the total Cu atom density profile at 9 mA and 0.3 Torr.

Fig. 7.7 illustrates the total Cu atom two-dimensional density profiles at 0.3 Torr and four different currents, and Fig. 7.8 shows the density profiles at 9 mA and four different pressures.

In general, the total Cu atom density peaks at the cell axis, close to the bottom surface. A second maximum is found between 0.5 and 1.5 cm from the cathode bottom, very close to the cathode sidewalls. Around the cylinder axis, away from the cathode bottom and sidewalls, the Cu atom density is very low. At all the conditions investigated, the largest concentration of Cu atoms was always found in the lower half of the HCD, where the bombarding fluxes of energetic Ar⁺ ions and atoms were at maximum (see above).

As appears from Fig. 7.7, the Cu population decreases with decreasing discharge current at constant pressure, because the sputtered flux drops. At 0.3 Torr and all currents investigated, the maximum density is always reached at around 1 mm from the cathode surface, both from the cathode bottom and the sidewalls. Due to the increase of the CDS length at lower currents, the maximum of the Cu atom density at the cathode sidewalls shifts in the direction of increasing z , from $z = 1$ cm at 9 mA, to $z = 1.5$ cm at 1 mA. At 1 mA, a region of very low density appears at a distance of 0.6 cm from the cathode bottom, as if two independent zones of sputtering exist in the discharge, one due to the cathode bottom and another due the cathode sidewalls.

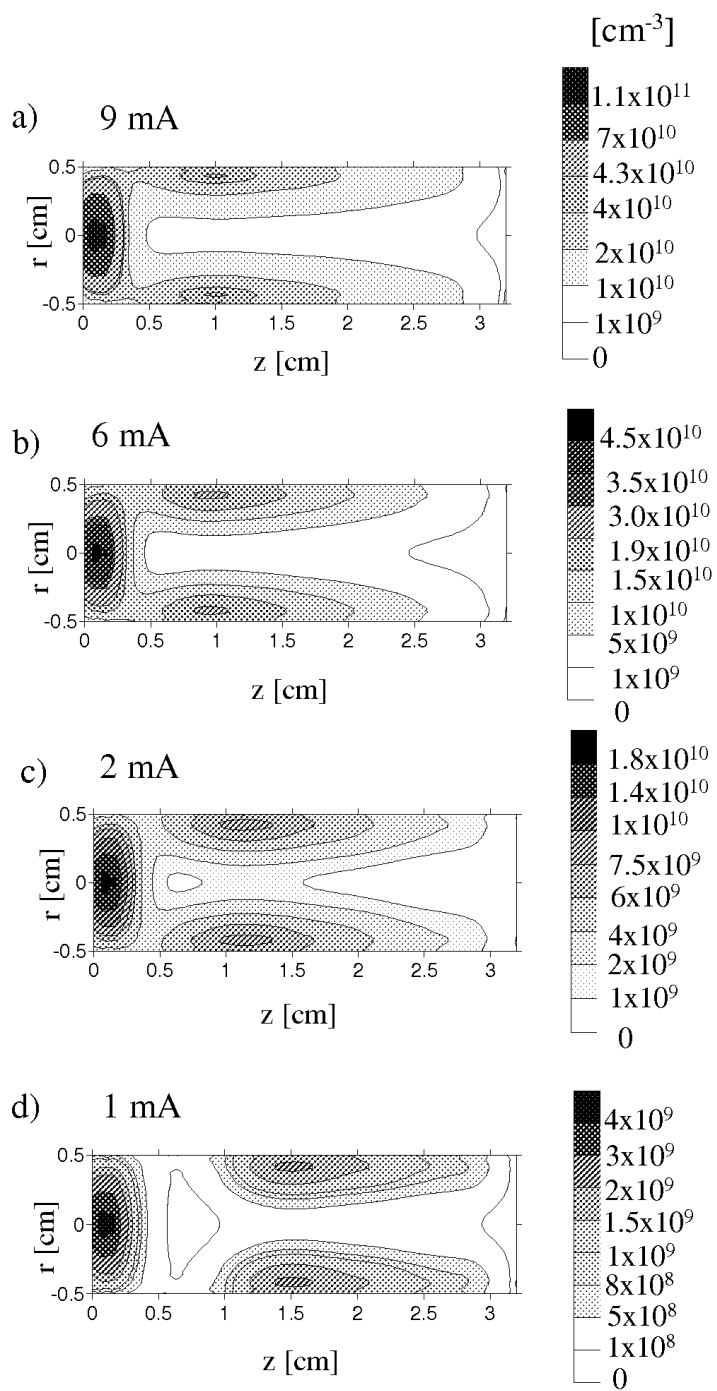


Fig. 7.7 Calculated two-dimensional profiles of the Cu atom density at 0.3 Torr and four different currents: 9 mA (a), 6 mA (b), 2 mA (c) and 1 mA (d).

It is clear from Fig. 7.8 that with increasing pressure, the Cu atom population decreases and its maximum near the cathode bottom is found somewhat closer to the cathode surface, i.e., at 1 mm, 0.7 mm, 0.5 mm and 0.3 mm from the cathode bottom for 0.3 Torr, 0.53 Torr, 0.76 Torr and 1 Torr, respectively. The reason is that the thermalization happens faster due to the decrease of the Cu mean free path.

Also, with increasing pressure, the first maximum near the cathode bottom drops, but the second maximum near the cathode sidewalls, increases. For example, at 0.3 Torr (Fig. 7.8a) the maximum Cu atom density, in front of the cathode bottom, is 2.5 times higher than the second peak at the cathode sidewalls. At 0.76 Torr, (Fig. 7.8c) both density peaks, near the cathode bottom and the sidewalls, have similar values, around $5 \cdot 10^{10} \text{ cm}^{-3}$. At still higher pressure (1 Torr, Fig. 7.8d) the maximum population of Cu atoms is found in front of the cathode sidewalls.

This is probably the consequence of the lower diffusion with increasing pressure. At 1 Torr, the ejected (sputtered) Cu atom flux from the cathode bottom represents 8% of the total ejected flux, integrated over the entire cathode surface, which corresponds exactly to the ratio of the cathode bottom area to the total area of the cathode cylinder. At 0.3 Torr, the ejected flux from the bottom represents only 2% of the total ejected flux. Moreover, at the cathode bottom, there is no net sputtered flux, but a net redeposition flux. Hence, the shift in the position of the Cu atom maximum density from near the cathode bottom to near the cathode sidewalls when the pressure increases, cannot be a consequence of the lower sputtering from the cathode bottom, because the latter in fact increases. For this reason, we think it is due to lower diffusion.

Moreover, at higher pressure, the drop in the density in the axial direction, as well as in the radial direction, is much more pronounced. This results in a significant dip at the cylinder axis, and in much lower Cu density values near the open end of the cylinder. For example at 9 mA and at 0.3 Torr the calculated Cu density at the cylinder axis, at $z = 3$ cm, is approximately 10^9 cm^{-3} while at 1 Torr it has dropped till $5 \cdot 10^7 \text{ cm}^{-3}$, at $z = 3$ cm (see Fig. 7.8).

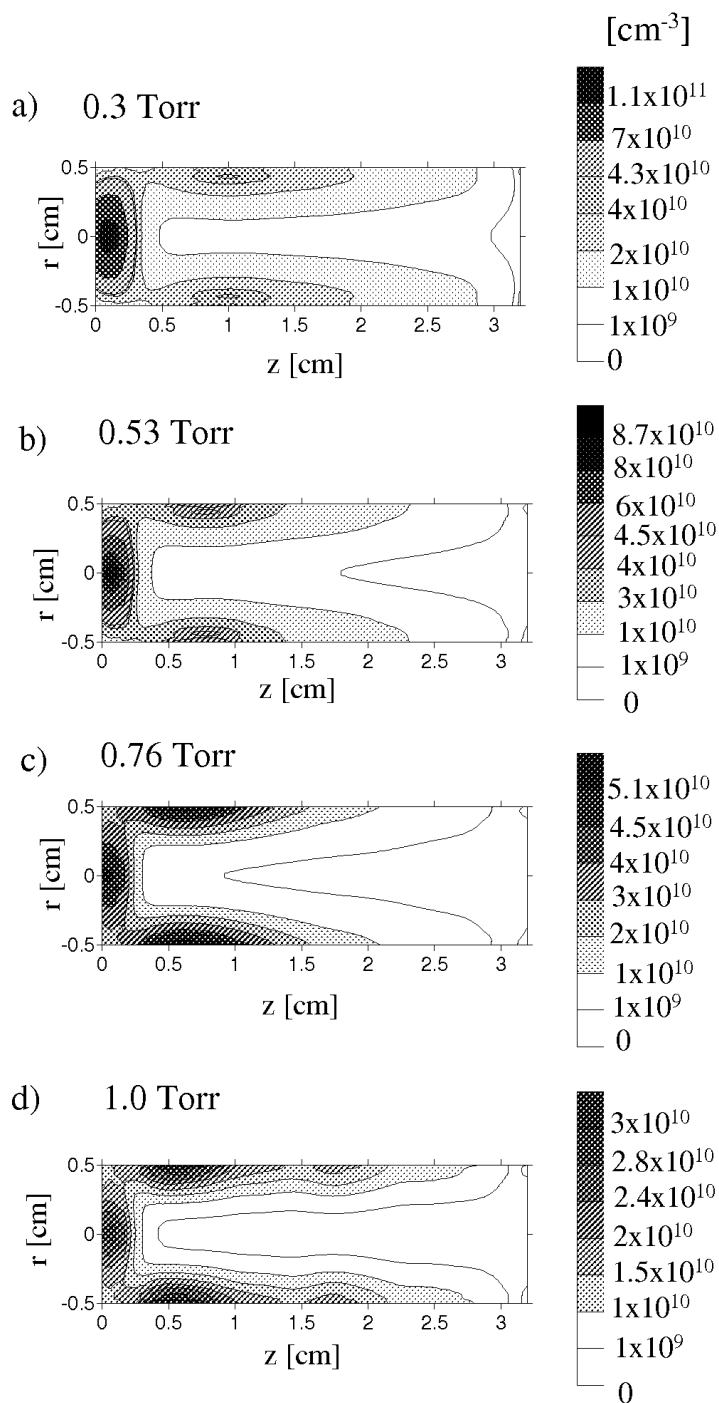


Fig. 7.8 Calculated two-dimensional profiles of the Cu atom density at 9 mA and four different pressures: 0.3 Torr (a), 0.53 Torr (b), 0.76 Torr (c) and 1.0 Torr (d).

It is interesting to notice that, at a pressure of 1 Torr, a third (small) peak appears near the cathode sidewalls at $z = 1.8$ cm (see Fig. 7.8d), indicating that regions of higher metal density alternate with regions of lower density. It should be pointed out that regions with well-defined different microstructure along the hollow cathode surface, as well as the formation of consecutive hollow spheres along the cathode sidewalls have also been observed experimentally^{5,22,39} (see Fig. 4). In our opinion, the main reason for this spatial dependence of the Cu atom density is the non-uniform distribution of the ion velocity at the cathode sidewalls, which is ultimately determined by the spatial distribution of the electric field.

It is clear that in the CDS, for the cathode bottom near the axis, and for the sidewalls, between $z = 0.5$ to 2.5 cm, the electric field lines, i.e., the lines perpendicular to the equipotential surfaces, along which the ions move towards the cathode, are normal to the cathode surface and the electric field gradient is high, since the equipotential surfaces are close to each other (see for example Figs. 3.7c-3.9c). Consequently, the ions strike the cathode here perpendicularly and with high average kinetic energy, while at the corner and at the upper region of the hollow cathode, near the open end, the electric field lines become slanted and the field strength decreases, hence the ions strike the surface at an angle and with less energy.

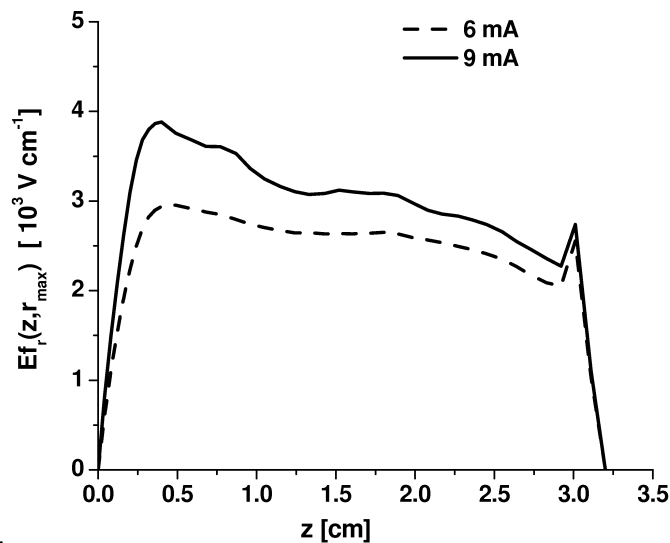


Fig. 7.9 Calculated electric field distribution as a function of axial position, at 1 Torr and 6 mA and 9 mA.

Specifically at 1 Torr, the relation between the appearance of the alternate hollow cathode spheres and the electric field distribution can be seen more clearly by observing the axial dependence of the electric field distribution at the cathode sidewalls, as is represented in Fig. 7.9. Beside the major peak of the electric field at $z = 0.4$ cm, a second small maximum can be observed at $z = 1.8$ cm, for a discharge current of 6 and 9 mA. This is in contrast to the case of 0.3 Torr, where only a maximum around $z = 0.5$ cm was observed (see Fig. 7.3b).

7.5 Ionization processes of Cu atoms

The ionization mechanisms for Cu atoms included in the model are Penning ionization by metastable Ar^m atoms, asymmetric charge transfer collision by Ar^+ ions (ACT) and (fast) electron impact ionization. The electron impact ionization rate was calculated directly in the MC model for the fast electrons through the energy-dependent cross section, while the ionization rates for Penning ionization and ACT collisions were obtained through the corresponding collision rate coefficients and the calculated Ar^m metastable and Ar^+ ion densities, respectively. The rate coefficients of ACT and Penning ionization are in the same order of magnitude, hence, the difference in the corresponding collision rates is mainly given by the metastable Ar^m atom and Ar^+ ion density distributions throughout the discharge. Therefore, in order to calculate accurate values for these rates, realistic Ar^+ ion and metastable Ar^m atom densities are needed.

The Ar^+ ion density can be considered to be more or less correctly calculated in our model, as a very good agreement between calculated and measured current-voltage and spectrometric properties of the discharge were obtained (see chapter 3 for more details).

Concerning the metastable Ar^m density, we found in chapter 6 that the agreement between experimental and calculated (axially averaged) radial profiles was in reasonable agreement for all conditions investigated. Indeed, the density values were in the same order of magnitude and similar radial profiles, as well as electrical current behavior was obtained. The agreement was especially good at 0.3 Torr (see Fig. 7.10a). However, with increasing pressure, at constant current, the calculated metastable density values became higher than the measured ones, although it should be noted that the difference was not large: at its maximum, i.e. at 1 Torr, it was only a factor of two.

In chapter 6, it was shown that, at 1 Torr a better agreement with experimental results could be achieved if the production of the collective Ar metastable level (³P₂ and ³P₀ levels) by fast electrons, fast Ar⁺ ions and fast Ar^f atoms was assumed to be only due to direct excitation from the ground state. The resulting comparison between calculated and experimental values is illustrated in Fig. 7.9d. This suggestion was done, based on the fact that the contribution of the cascading from the higher-lying states in determining the metastable population, increases with the reduced electric field strength,^{40,41} and that at constant current, the reduced electric field increases with decreasing pressure. Consequently, it can be deduced that the contribution of cascading from higher states is less important at higher pressure.

In the present work, we have interpolated the suggestion made in chapter 6 for 1 Torr to the other intermediate pressures, 0.53 and 0.76 Torr, as well.

Indeed, if we assume that at 1 Torr, the production of the collective Ar metastable level (³P₂ and ³P₀ levels) by fast electrons, fast Ar⁺ ions and fast Ar^f atoms is only due to direct excitation from the ground state, while at 0.3 Torr, it arises from contributions of direct excitation from the ground state as well as from cascading of the higher-lying states, then it seems straightforward to use some intermediate production rate for the metastable population at 0.53 and 0.76 Torr.

In practice, this corresponds to reducing the total production rate by some factor i.e., by 20% at 0.53 Torr and by 40% at 0.76 Torr. The resulting calculated densities are then in reasonable agreement with the experimental values, as is clear from Fig. 7.10b and 7.10c.

Summarized, the solid lines in Fig. 7.10 (a-d) represent the calculated Ar^m densities used in our model to calculate the Penning ionization rate. Because they are in good agreement with the measured Ar^m metastable density profiles, we expect that the Penning ionization rate in our model yields also realistic values.

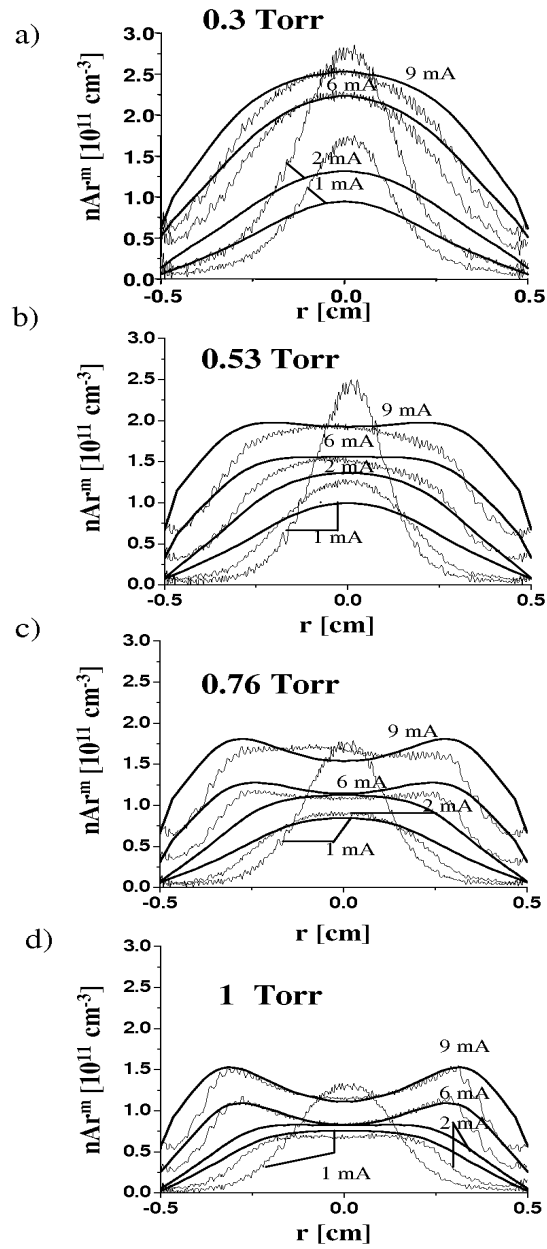


Fig. 7.10 Comparison of the calculated (axially averaged) and measured Ar^m metastable density radial profiles at 0.3 Torr (a), 0.53 Torr (b), 0.76 Torr (c) and 1.0 Torr (d), after reduction of the total excitation rate to the metastable state (see text). Thick and thin solid lines represent the calculated and experimental results, respectively.

To illustrate the relative importance of the different ionization mechanisms throughout the discharge, the two-dimensional rate profiles of electron impact ionization, Ar⁺ ion ACT collisions and Penning ionization are presented in Fig. 7.11 for a discharge at 9 A and 0.3 Torr.

The maximum of all the rates was found around the cylinder axis, and at a few millimeters from the cathode bottom. Throughout the rest of the discharge, the spatial distribution of the rates is somewhat different.

The electron impact ionization rate (Fig. 7.11a) is low near the cathode sidewalls and increases towards the NG, since the electrons are accelerated away from the cathode, and reach their maximum energy at the end of the CDS. Hence, in spite of the fact that the Cu atom density is high near the cathode surface, the electron impact ionization rate is low here, since there are not enough energetic electrons. In the NG, the electron impact ionization rate of the Cu atoms is more or less uniformly distributed. This is a consequence of the oscillatory movement of the electrons between the two opposite CDS regions, (“pendulum effect”) and the fact that the Cu ionization threshold (i.e., 7.7 eV) is low compared to the maximum achievable electron energy, so that in the entire NG, there are enough electrons with sufficient energy for the Cu ionization.

In the CDS, Penning ionization is the main mechanism for ionization of the Cu atoms, as the density of the Ar^m metastable atoms is one order of magnitude higher than the Ar⁺ ion density in this region. The Penning ionization rate peaks at the CDS-NG interface (see Fig. 7.11b). Throughout the NG, Penning ionization is still the most important ionization mechanism, but ACT is only slightly less important. This is like expected since the densities of the Ar⁺ ions and Ar^m metastable atoms are similar in value and both densities peak at the discharge axis.

Compared to the spatial profile of the Penning ionization rate, the maximum of the ACT profile is shifted toward the cylinder axis and is also more concentrated to the first half of the HCD (see Fig. 7.11c). This is the result of the Ar⁺ ion density profile, which exhibits a similar behavior, (see Figs. 3.7b-3.9b), while the Ar^m metastable atoms are more uniformly distributed in the axial direction (see Fig. 6.2).

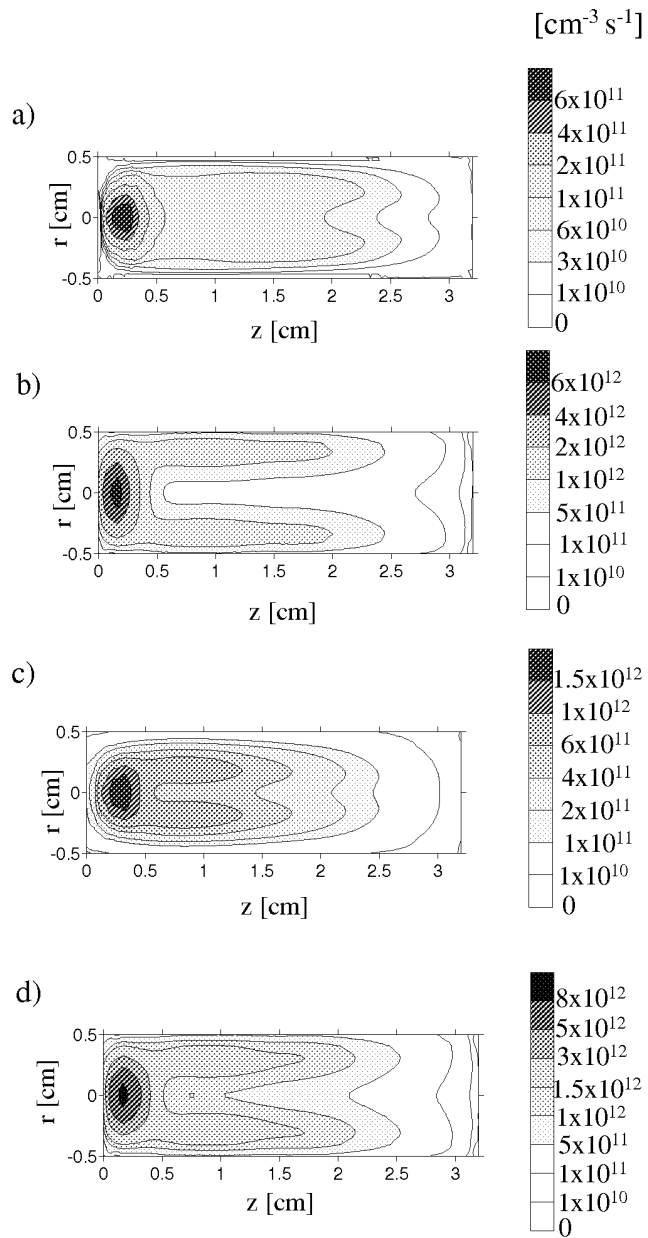


Fig. 7.11 Calculated two-dimensional collision rates of Cu atoms due to: electron impact ionization (a), Penning ionization (b), Ar⁺ ion ACT collision (c) and the total Cu ionization rate (d), at a pressure of 0.3 Torr and a current of 9 mA.

Integrated over the entire discharge volume, Penning ionization was calculated to be the dominant ionization mechanism of the Cu atoms, for all the conditions investigated, followed by ACT collisions and electron impact ionization. For example, at 9 mA and 0.3 Torr, the relative contribution of Penning ionization, ACT and electron impact ionization amount to 78%, 18% and 4%, respectively.

With decreasing current, at constant pressure, the role of Penning ionization still increases, as the densities of the Ar⁺ ions and electrons decrease much faster with current than the Ar^m metastable atom density. For the lower currents investigated (1 and 2 mA) at 0.3 and 0.53 Torr, Penning ionization is almost completely responsible for the Cu atom ionization (i.e., 86% and 91% at 2 mA and 1 mA, respectively).

With increasing pressure, at constant current, the opposite tendency is observed. As the pressure rises, the density of the Ar⁺ ions and electrons increases, while the Ar^m metastable density decreases. Moreover, due to the higher electron density, the loss of metastable atoms by thermal electron quenching becomes more important at higher pressures and currents. Hence, at higher pressures and currents, the radial profiles of the Ar^m metastable atoms change, compared with the profiles at low pressure. Indeed, the Ar^m metastable atom density then shows a minimum at the position where the slow electron density has a maximum, i.e., at the discharge axis. Therefore, the relative importance of Ar⁺ ion ACT collisions in the NG increases. However, integrated over the entire HCD volume, Penning ionization is still the main production mechanism of Cu⁺ ions. For example, for a discharge at 1 Torr and 9 mA, the relative contribution of Penning ionization, ACT and electron impact ionization amount to 68%, 26% and 6%, respectively.

7.6 Density of the Cu⁺ ions

The metal ion population is the result of both the density and the ionization efficiency of the sputtered atoms. Figs. 7.12 and 7.13 illustrate the two-dimensional Cu⁺ ion density profiles, at 0.3 Torr and four different currents, and at 9 mA and four different pressures, respectively.

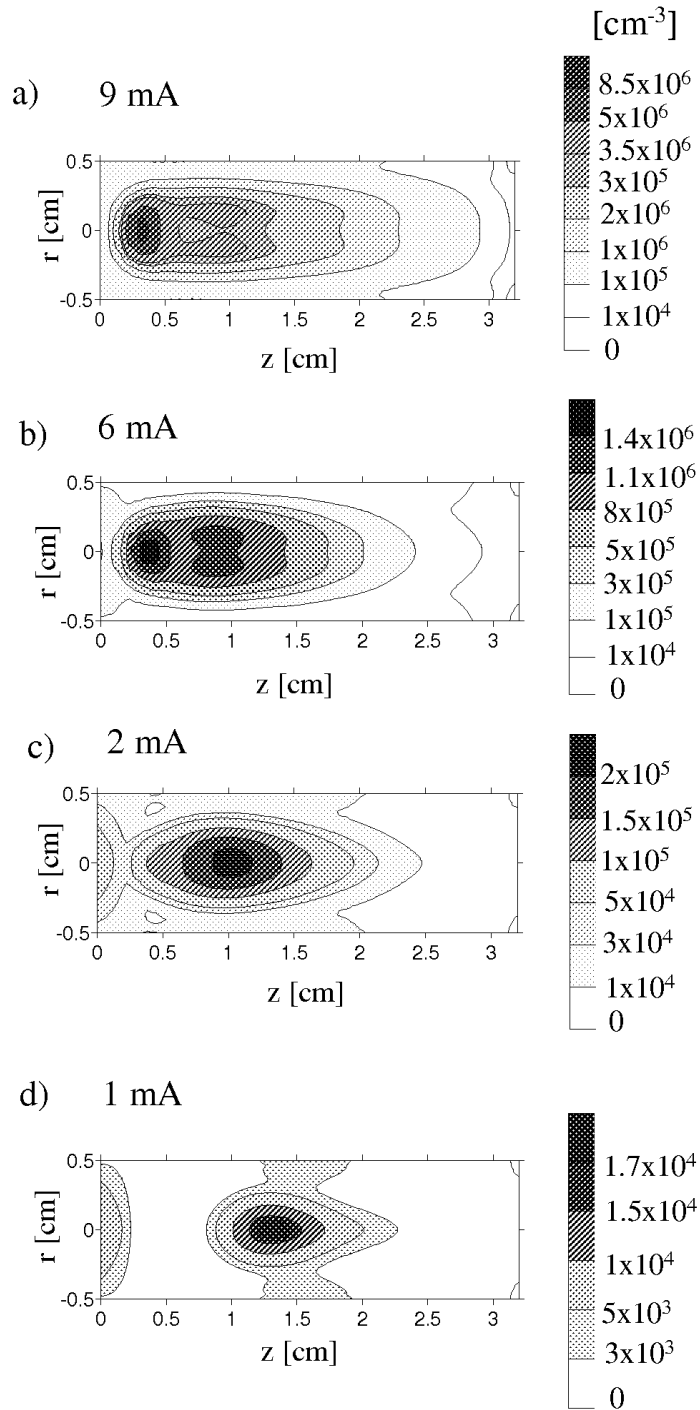


Fig. 7.12 Calculated two-dimensional profiles of the Cu⁺ ion density at 0.3 Torr, and four different currents 9 mA (a), 6 mA (b), 2 mA (c) and 1 mA (d).

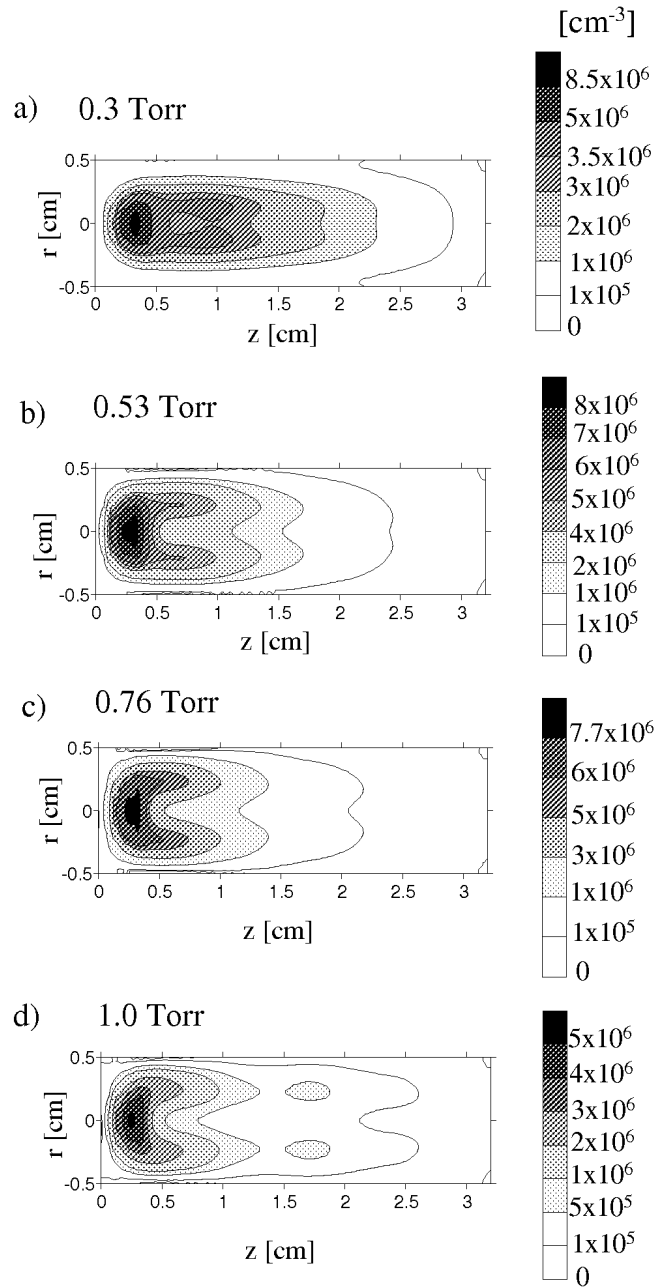


Fig. 7.13 Calculated two-dimensional profiles of the Cu⁺ ion density at 9 mA and four different pressures: 0.3 Torr (a), 0.53 Torr (b), 0.76 Torr (c) and 1.0 Torr (d).

Compared to the Cu atom spatial distribution, the Cu⁺ ion population is more shifted in the radial direction toward the axis, because the ionization is mainly caused by Penning ionization and ACT collisions (see above) and the densities of the Ar^m metastable atoms and Ar⁺ ions are low near the cathode wall. At 0.3 Torr and 9 mA the Cu⁺ ion density profile peaks at the cylinder axis in the lower half of the cylinder. Further away from the cathode bottom, the Cu⁺ ion density profile shows a small dip at the cylinder axis and two small maxima at both sides off-axis (like a donut-shape), as can be observed in Fig. 7.12a.

With decreasing current, the Cu⁺ ion density drops drastically close to the bottom cathode and the two small peaks off-axis begin to merge (i.e., the donut closes in the middle). At low currents, the maximum population is found at the center of the discharge (Fig. 7.12d).

With increasing pressure (see Fig. 7.13), the Cu⁺ ion population decreases and becomes concentrated almost completely in the lower half of the cylinder. In the radial direction, the density profiles do not change very much, i.e., they exhibit two peaks at high currents and a common peak at the cylinder axis, at low currents (similar as in Fig. 7.12).

The ionization degree of the Cu atoms was found to be around 10^{-5} for all conditions investigated. In the case of Ar atoms, the ionization degree was in the same order of magnitude. Therefore, the relation of the Cu⁺ ion population to the Ar⁺ ion population is similar to the ratio of the Cu atom to Ar atom population, and is in the order of 10^{-4} .

7.7 Conclusions

It was found that:

1. The energetic Ar⁺ ions play the most important role for the sputtering of the cathode.
2. The role of self-sputtering was negligible, in contrast to planar GD's, where the contribution of self-sputtering was typically in the order of several percentages.⁴²
3. At the cathode bottom, there is no net sputtered flux, but there is a net amount of redeposition.
4. At the cathode sidewalls, redeposition predominates only close to the cathode bottom and near the open end towards the anode.
5. Throughout the discharge volume, at all the conditions investigated, the largest concentration of Cu atoms was found in the lower half of the HCD, close to the bottom, at some distance from the cathode surface (both at the cathode bottom and at the cathode sidewalls).
6. At low pressure, the Cu atom population is more uniformly distributed along the discharge length and the density profiles show a maximum at the cylinder axis, close to the cathode bottom.
7. At high pressures, the maximum was found close to the cathode sidewalls.
8. At 1 Torr, regions of high Cu atom density alternate with region of low density, which corresponds to the formation of the characteristic consecutive hollow spheres observed experimentally in HCD's.
9. Penning ionization was found the main ionization mechanism for the Cu atoms, followed by Ar⁺ ion ACT.
10. The ionization degree of the Cu atoms was found to be in the order of 10⁻⁵ for all conditions investigated.

7.8 References

- ¹ G. K. Wehner, *Phys. Rev.* **102** 690 (1956).
- ² B. Chapman, *Glow Discharge Processes: Sputtering and Plasma Etching* (Wiley-Interscience, New York, 1980).
- ³ I. G. Ivanov, E. L. Latush and M. F. Sem, *Metal Vapour Ion Lasers: Kinetic Processes and Gas Discharges* (Wiley & Sons Ltd, Chichester, 1996).
- ⁴ N. K. Vuchkov, K. A. Temelkov and N. V. Sabotinov, *IEEE J. Quantum Electron* **35**, 1799 (1999).
- ⁵ P. J. Slevin and W. W. Harrison, *Appl. Spectrosc. Reviews* **10**, 201 (1975).
- ⁶ S. Caroli, *Prog. Analyt. Atom. Spectrosc.* **6**, 253 (1983).
- ⁷ C. Yang and W. W. Harrison, *Spectrochim. Acta Part B* **56**, 1195 (2001).
- ⁸ D. M. Manos and D. L. Flamm, *An Introduction to Plasma Etching* (Academic, New York, 1989).
- ⁹ A. Goldamm and J. Amoroux, *Gases: Macroscopic Processes and Discharges* (Plenum Press, New York, 1983).
- ¹⁰ H. Helm, *Z. Naturf.* **27a**, 1812 (1972).
- ¹¹ V. I. Kolobov and L. D. Tsendin, *Plasma Sources Sci. Technol.* **4** 551 (1995).
- ¹² C. Yang and W. W. Harrison, *Spectroc. Acta Part B* **56**, 1195 (2001).
- ¹³ E. H. Daughtrey, D. L. Donohue, P. J. Slevin and W. W. Harrison, *Anal. Chem.* **47**, 683 (1975).
- ¹⁴ R. M. Allot, M Kubinyl, A. Grofcsik, W. J Jones and R. S. Mason, *J. Chem. Soc Faraday Trans.* **9**, 1297 (1995).
- ¹⁵ D. R. Oliver and T. R. Finlayson, *J. Analyt. Atom. Spectr.* **13**, 443 (1998).
- ¹⁶ G. Gergelyi and Z. Szilvassy, *ACH-Models in Chemistry* **136**, 69 (1999).
- ¹⁷ W. Hang and W.W. Harrison, *Anal. Chem.* **69**, 4957 (1997).
- ¹⁸ B. E. Warner and K. B. Persson, *J. Appl. Phys.* **50**, 5694 (1979).
- ¹⁹ E. M. van Veldhuizen and F. J. Hoog, *J. Phys. D* **17**, 953 (1984).
- ²⁰ S.C. Rae and R.C. Tobin, *J. Appl. Phys.* **64**, 1418 (1988).
- ²¹ A. J. Lichtenberg and M. A. Lieberman, *J. Appl. Phys.* **87**, 8191 (2000).
- ²² D. R. Oliver and T. R. Finlayson, *J. Phys. D* **31**, 1857 (1998).
- ²³ J. A. Valles Abarca and A. Gras-Marti, *J. Appl. Phys.* **55**, 1370 (1984).
- ²⁴ R. R. Arslanbekov, R. C. Tobin and A. A. Kudryatsev, *J. Phys. D* **81**, 554 (1997).
- ²⁵ G. J. Fetzter and J. J. Rocca, *IEEE J. Quantum Electron* **28**, 1941 (1992).
- ²⁶ A. Tran Ngoc, E. Marode and P. C. Johnson, *J. Phys. D* **10**, 2317 (1977).
- ²⁷ A. Bogaerts, M. van Straaten and R. Gijbels, *Spectrochim. Acta Part B* **50**, 179 (1995).
- ²⁸ J. P Boeuf, *J. Appl. Phys.* **63**, 1342 (1988).
- ²⁹ D. Paschier and W. J. Goedheer, *J. Appl. Phys.* **74**, 3744 (1993).

- ³⁰ G. Bano, L. Szalai, P. Horvath, K. Kutasi, Z. Donko, K. Rozsa, T. M. Adamowicz, J. Appl. Phys. **92**, 6372 (2002).
- ³¹ A. Bogaerts and R. Gijbels, J. Appl. Phys. **92**, 6408 (2002).
- ³² R. R. Arslanbekov, A. A. Kudryatsev and R. C. Tobin, Plasma Sources Sci. Technol. **7**, 310 (1998).
- ³³ N. Matsunami, Y. Yamamura, Y. Itikawa, N. Itoh, Y. Kazumata, S. Miyagawa, et al, Atom. Data and Nucl. Data Tables **31**, 1 (1984).
- ³⁴ R. V. Stuart and G. K. Wehner, J. Appl. Phys. **33**, 2345 (1962).
- ³⁵ W. Hang and W.W. Harrison, Anal. Chem. **69**, 4957 (1997).
- ³⁶ M. van Straaten, A. Bogaerts and R. Gijbels, Spectrochim. Acta Part B **50**, 583 (1995).
- ³⁷ A. Bogaerts and R. Gijbels, J. Appl. Phys. **79**, 1279 (1996).
- ³⁸ R. V. Stuart and G. K. Wehner, J. Appl. Phys. **35**, 1819 (1964).
- ³⁹ J. Hamish, J. de la Rosa, J. Appl. Phys. B. **43**, 189 (1987).
- ⁴⁰ K. Tachibana, Phys. Rev. A **34**, 1007 (1986).
- ⁴¹ V. Puech and L. Torchin, J. Phys. D **19**, 2309 (1986).
- ⁴² A. Bogaerts and R. Gijbels, Anal. Chem. **68**, 2676 (1996).

Chapter 8

Influence of the gas flow on the sputtered atoms and the deposition flux

In this chapter we have investigated how the gas flow affects the sputtered atom density profiles and the fluxes, which is important for sputter deposition. For this aim we combined our hybrid model with a commercial computational fluid dynamics program “Fluent” to compute the axial gas flow (entering through a hole in the cathode bottom). The sputtered atom density profiles are not much affected by the gas flow. The flux, on the other hand, is found to be significantly enhanced by the gas flow, but in the present set-up it is far from uniform in the radial direction at the open end of the HCD, where a substrate for deposition could be located.

8 Influence of the gas flow on the sputtered atoms and the deposition flux

8.1 Introduction

When hollow cathode discharges are used for thin film deposition, a gas flow, through the cathode, can be applied to enhance the deposition rate, because it facilitates the material transport towards the substrate.¹⁻¹⁰ Often the gas flow forces the plasma out of the hollow cathode discharge, and the so-called plasma-jet then interacts with the substrate.⁶⁻¹⁰ It is also worth to mention that the particular route of the gas flow may also decrease the residual gas influence on the target and substrate.¹ In order to understand better the influence of a gas flow on the plasma behavior in a hollow cathode discharge, the effect of the gas flow was incorporated in the model.¹¹

There exist some models in the literature that incorporate the gas flow in gas discharge plasmas. At the Eindhoven University of Technology, a general plasma simulation tool, called "PLASIMO" is developed, and applied to various types of plasmas with gas flow, such as an argon cascaded arc plasma, microwave plasmas, inductively coupled plasmas (ICPs), plasma light sources.¹²⁻¹⁵ At the von Karman Institute for Fluid Dynamics, a powerful tool for the numerical simulation of an ICP with laminar flow was developed.¹⁶ The convection transport mechanism was also taken into account in low pressure ICP plasma models in chlorine¹⁷ for plasma processing applications, but here the gas flow was only included in the mass balance equation as a relaxation term with gas residence time. This approach can, of course, not show in detail the local effects of the gas flow on the plasma characteristics. In Refs. 18 and 19 the gas flow was included in the flux equation, in models for ICP discharges in nitrogen. In our group, we have recently developed some models, which incorporate the effect of gas flow, by adding a convection term in the flux equations, for two types of discharges: a dc glow discharge in argon, used as ion source for mass spectrometry,²⁰ and a cc rf discharge in CH₄, used for plasma-enhanced chemical vapor deposition, to study the effect on the deposition rate and the uniformity of the deposition flux.²¹ In this chapter we will apply the same approach assumed in Refs. 20-21 to study the influence of the gas flow on the sputtered Cu atom density profiles and fluxes, which is of importance for sputter deposition purposes.

The description of the gas flow, and its effect on the plasma behavior, is done by a combination of a commercial computational fluid dynamics (CFD) program, called FLUENT, and our hybrid model, in which the fluid model for the sputtered species has been modified.

The CFD program, FLUENT,²² is based on the balance equations for mass, momentum and energy, which are solved with an implicit scheme. A laminar gas flow is assumed for our calculations, and a two-dimensional axisymmetric approximation is used. The program calculates the gas flow pattern (convection velocity as a function of position) inside the HCD, using the gas flow at the inlet, and the pressure at the outlet, as input values. From this, also the gas pressure and temperature distributions inside the HCD are obtained. More information can be found in Ref. 22.

In order to account for the influence of the gas flow in the sputtered atom density and flux, the flux equations for the Cu atoms and Cu⁺ ions in the fluid model for the sputtered species (2.4.3) have been modified. Indeed, a convection term has been added to the Cu⁺ ion and Cu atom flux equations, which is attributed to the fact that the atoms and ions move together with the (argon) gas flow. Hence, the flux equation for the neutral species (Cu atoms) becomes a summation of diffusion (first term) and convection (second term):

$$\vec{j}^{\text{Cu}} = -D^{\text{Cu}} \vec{\nabla} n^{\text{Cu}} + n^{\text{Cu}} \vec{U}_{\text{conv}}$$

Similarly, the flux equation for the Cu⁺ ions becomes the sum of diffusion (first term), migration in the electric field (second term) and convection (third term):

$$\vec{j}^{\text{Cu}^+} = -D^{\text{Cu}^+} \vec{\nabla} n^{\text{Cu}^+} + n^{\text{Cu}^+} \mu^{\text{Cu}^+} \vec{E} + n^{\text{Cu}^+} \vec{U}_{\text{conv}}$$

where $D^{\text{Cu}}, D^{\text{Cu}^+}$ are Cu atom and Cu⁺ ion diffusion coefficients. The diffusion coefficient for the Cu⁺ ions was taking equal to that of the Cu atoms, under the assumption that in a first approximation, the diffusion is not determined by the charge of the particle. $\vec{j}^{\text{Cu}}, \vec{j}^{\text{Cu}^+}$ are the Cu atom and Cu⁺ ion fluxes, $n^{\text{Cu}}, n^{\text{Cu}^+}$ are the respective densities and U_{conv} stands for the convection velocity, which is adopted from the FLUENT calculations. μ^{Cu^+} and \vec{E} symbolize the mobility of the ion and the electric field strength. The values of the transport coefficients are defined in paragraph 2.4.3.

It is also possible to make a coupling back from the plasma models to the CFD code, for instance, when there is a lot of heating in the discharge, which then needs to be

used as source term in the energy balance equation in the gas flow model. However, for the conditions under investigation here (pressure ranging from 0.3 to 1 Torr and discharge currents from 1 to 10 mA), the effect of gas heating is very small (see paragraph 6.2), so that the profiles of gas pressure, temperature and velocity are not significantly disturbed by the plasma, and a coupling back to the CFD code was not necessary.

8.2 Gas flow inside the HCD

To investigate the effect of a gas flow in the HCD, and more specifically on the behavior of the sputtered species, which is highly relevant for deposition purposes, we consider a hole, with 2 mm diameter, in the bottom of the cathode, through which the gas flows in, and the other end of the cylinder tube is open. For deposition applications, the substrate could then be placed at this open end. It should be noted that in the calculations, no substrate was explicitly included. Hence, it is assumed, like it is mostly the case in experimental setups that the substrate is far away, so that it does not affect our calculated gas flow pattern inside the HCD. Of course, in reality, the substrate will always influence the gas flow to some extent. However, the main purpose of the present calculations is to show how the gas flow will behave inside the HCD, in the general case, i.e., when no particular substrate is specified.

The input gas velocity is varied between 50 m/s and 250 m/s. This corresponds to a gas flow between 12 and 60 cm², for the assumed hole in the cathode bottom of 2 mm diameter. Comparison is also made with the case of no gas flow. In the following, all calculation results are shown for an electrical current of 6 mA and a pressure of 1 Torr, unless mentioned otherwise. The observed effects are, indeed, found to be very similar for the other conditions investigated (i.e., pressure ranging between 0.3 and 1 Torr, and current varying between 1 and 9 mA).

Fig. 8.1 illustrates the gas velocity distributions inside the HCD, for input velocities ranging from 50 to 250 m/s. The thicker lines at the figure borders (in this and all following figures) symbolize the walls of the HCD, whereas the thin lines represent the open end (at $z = 3.2$ cm) and the hole (gas inlet) in the cathode bottom (at $z = 0$).

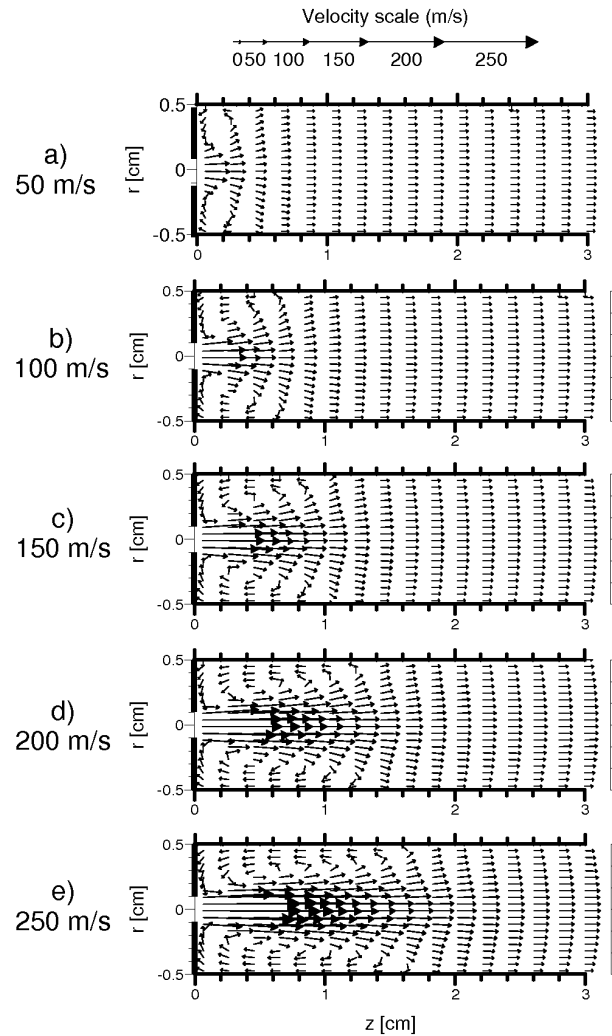


Fig. 8.1 Vector plots of the calculated gas velocity distributions in the HCD, for different values of gas inlet velocity, at 1 Torr. The thicker lines at the figure borders denote the walls of the cathode, whereas the thin lines represent the open end (at $z=3.2$ cm) and the hole in the cathode bottom ($z=0$).

It is clear that the velocity is highest at the gas inlet, and that the gas expands mainly in the axial direction. Note that the length of the vectors is a measure for the magnitude of the velocities, i.e., the largest arrow in Fig. 8.1a corresponds to 50 m/s and the largest arrow in Fig. 8.1e corresponds to 250 m/s. In general, except near the sidewalls in the first cm from the inlet, where the influence of the gas inlet is felt, the gas moves mainly in the axial direction throughout the HCD, i.e., towards the open end of the HCD. The flow distribution shows a paraboloid shape, with maximum velocities at the

cylinder axis and minimum values at the side walls, as is expected from Poiseuille's law. This paraboloid shape is of course more pronounced for the higher inlet gas velocities. Near the inlet, the gas velocity slows down dramatically after the initial expansion, but later on, it remains more or less constant, or decreases slightly in the axial direction. The calculated values (at the cylinder axis) at the open end of the HCD are tabulated in Table 8.1, for each value of the inlet gas velocity.

Table 8.1 Calculated values for the gas velocity at the open end of the hollow cathode, at the cell axis, for different values of gas velocity at the inlet.

| Gas velocity at inlet (m/s) | Gas velocity at open end of HCD (m/s) |
|------------------------------------|--|
| 50 | 4 |
| 100 | 8 |
| 150 | 13 |
| 200 | 17 |
| 250 | 21 |

A higher velocity at the inlet leads also to a higher velocity at the open end, and the effect is slightly more than linear. The ratio between inlet and outlet velocities is about 12 for all conditions, which is expected, based on conservation laws and the different diameters of inlet hole and open end.

As a result of the gas flow, the argon gas pressure and temperature are not completely uniform inside the HCD. The variation is, however, not very pronounced, as is shown in Fig. 8.2, for the inlet gas velocity of 250 m/s.

The gas pressure (Fig. 8.2a) is 1 Torr (i.e., the base pressure for all conditions) in most of the HCD, but it reaches a maximum of 1.01 Torr at the position of the gas inlet (i.e., a rise of only 5%), and a local minimum of about 0.9 Torr at the edge of the gas inlet. Except near the inlet, the gas pressure is calculated to be very uniform in the radial direction. The gas temperature (Fig. 8.2b) shows a local minimum of 295 K near the gas inlet, as a result of the gas expansion, and a broad maximum of about 320 K at about 1 cm from the inlet. Further in the HCD, the gas temperature drops gradually in the axial direction, to about 300 K near the open end of the HCD. The variations of pressure and

temperature for the other (lower) inlet gas velocities investigated are calculated to be even smaller.

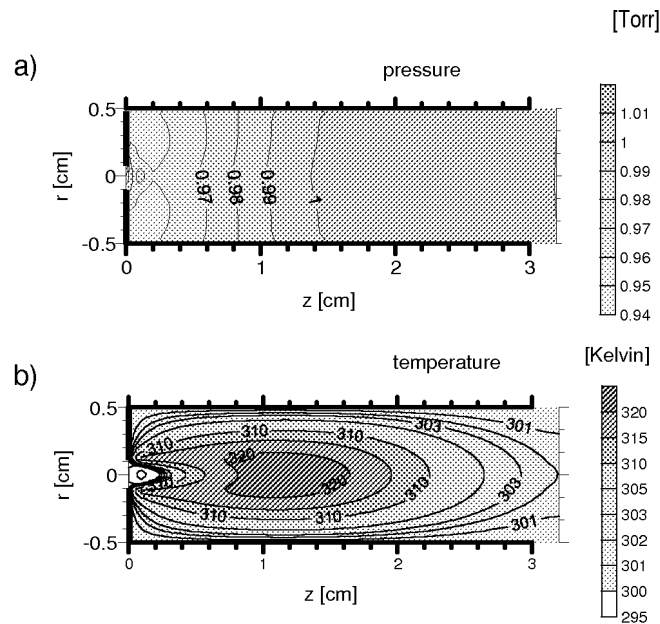


Fig. 8.2 Contour plots of the calculated distribution of gas pressure (a) and temperature (b) inside the HCD, for the inlet gas velocity of 250 m/s, and a base pressure of 1 Torr.

8.3 Effect of gas flow on the sputtered atom behavior

Fig. 8.3 (left column) shows vector plots of the calculated fluxes of the sputtered Cu atoms inside the HCD, for the various conditions of inlet gas velocity (Figs. 8.3 b-f).

Note that this is the flux of thermalized Cu atoms, as calculated in the fluid model of the Cu atoms and Cu^+ ions, because the Cu atoms become thermalized almost immediately after sputtering from the cathode (see paragraph 7.4). The flux distribution in the absence of a gas flow is also shown (Fig.8.3a). In this case, the flux of sputtered Cu atoms is mainly in the radial direction and directed towards the cylinder axis, as a result of sputtering from the side walls of the HCD and radial diffusion. The radial flux is at maximum in the order of $10^{13} \text{ cm}^{-2} \text{ s}^{-1}$ (close to the side walls and between 0.5 and 1 cm from the cathode bottom). In the main region of the HCD, it is typically in the order of $10^{12} \text{ cm}^{-2} \text{ s}^{-1}$, and it drops to zero at the cylinder axis. There is only a very small axial

component in the flux (in the order of $10^{10} \text{ cm}^{-2} \text{ s}^{-1}$), which is the result of diffusion, due to the Cu atom concentration gradient in the axial direction (see below, Fig. 8.4).

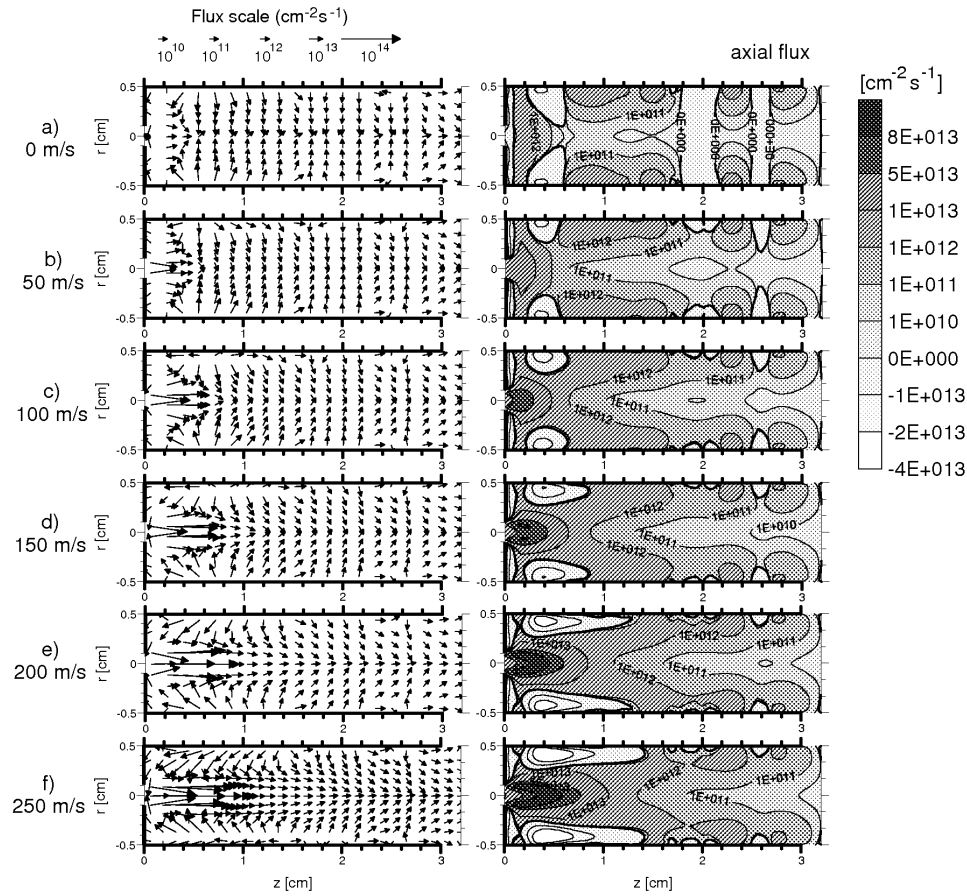


Fig. 8.3 Vector plots (left column) of the calculated fluxes of sputtered Cu atoms in the HCD at 1 Torr, in the absence of a gas flow (a) and for different values of gas inlet velocity (b-f). (The size of the arrows gives the total value of the flux, which is a combination of the axial and radial value.) Also shown are the contour plots of the axial flux distribution (right column), where the logarithmic scale enables us to illustrate the large difference in flux values throughout the HCD.

When a gas flow is applied, the Cu atoms are carried away from the gas inlet, in the axial direction, towards the open end of the HCD. Hence, the resulting Cu atom flux is a superposition of the axial flux (due to the gas flow) and the radial flux (as a result of sputtering and diffusion). It is clear that the axial component becomes increasingly important for higher values of the inlet gas velocity. For the inlet velocity of 250 m/s, the axial flux component reaches values in the order of $10^{14} \text{ cm}^{-2} \text{ s}^{-1}$ around 5 mm from the cathode bottom, and it drops gradually to 10^{10} - $10^{11} \text{ cm}^{-2} \text{ s}^{-1}$ near the open end of the HCD.

The radial flux component remains the same for all conditions, and has the same values as mentioned above.

The axial flux at the open end is not uniform in the radial direction, but it varies from $3 \times 10^9 \text{ cm}^{-2} \text{ s}^{-1}$ at the cylinder axis, till $7.7 \times 10^{10} \text{ cm}^{-2} \text{ s}^{-1}$ at 4 mm from the center. This is, however, not visible in Fig 8.3, because the sizes of the arrows in the figure correspond to flux values ranging from ca. $10^9 \text{ cm}^{-2} \text{ s}^{-1}$ to $10^{14} \text{ cm}^{-2} \text{ s}^{-1}$. Hence, the relatively small difference between $3 \times 10^9 \text{ cm}^{-2} \text{ s}^{-1}$ and $7.7 \times 10^{10} \text{ cm}^{-2} \text{ s}^{-1}$ is not reflected in a visible difference in sizes of the arrows. For this reason, the countour plots of the axial flux distribution are also shown in Fig. 8.3 (right column), because they enable us to illustrate large differences in flux values, because of the logarithmic scale. It is indeed clear that the axial flux at the open end of the HCD is not uniform in the radial direction. This radial variation is presented more clearly later (see below Figs. 8.6-8.7).

Moreover, the calculated flux at the open end of the HCD is also higher for higher gas flow, as will also be shown in more detail below (see below, Figs. 8.6 and 8.8). This is also actually not visible in the arrows of figure 8.3, for the same reason, because the values vary from about $2.6 \times 10^{10} \text{ cm}^{-2} \text{ s}^{-1}$ without gas flow, till $7.7 \times 10^{10} \text{ cm}^{-2} \text{ s}^{-1}$ with gas flow of 250 m/s. It should be kept in mind here that the size of the arrows gives the total value of the flux, which is a combination of the axial and radial value.

The calculated density profiles of the Cu atoms are illustrated in Fig. 8.4, for different values of gas flow. It is clear that they are nearly not affected by the gas flow.

The Cu atom density reaches a maximum of $2 \times 10^{10} \text{ cm}^{-3}$ near the sidewalls, at about 3 mm from the cathode bottom. This is the position where most of the sputtering occurs. There is not so much sputtering at the cathode bottom, because of the gas inlet position (hole). The Cu atom density drops towards the cylinder axis, where it reaches a dip of about 10^8 cm^{-3} .

It is apparent from Fig. 8.4 that the Cu density shows a dip at the cylinder axis, and increases towards the sidewalls, for all conditions. This is partly the result of the HCD geometry (with a hole in the center of the cathode bottom) and partly because of the discharge conditions under study. Indeed, Fig 8.5 illustrates the calculated Cu atom density profiles in the same HCD, but without any hole in the cathode bottom, for the pressure of 1 Torr (Fig. 8.5a), as well as for a lower pressure (0.3 Torr, Fig. 8.5b) at the same discharge current as in Fig. 8.4, i.e., 6 mA.

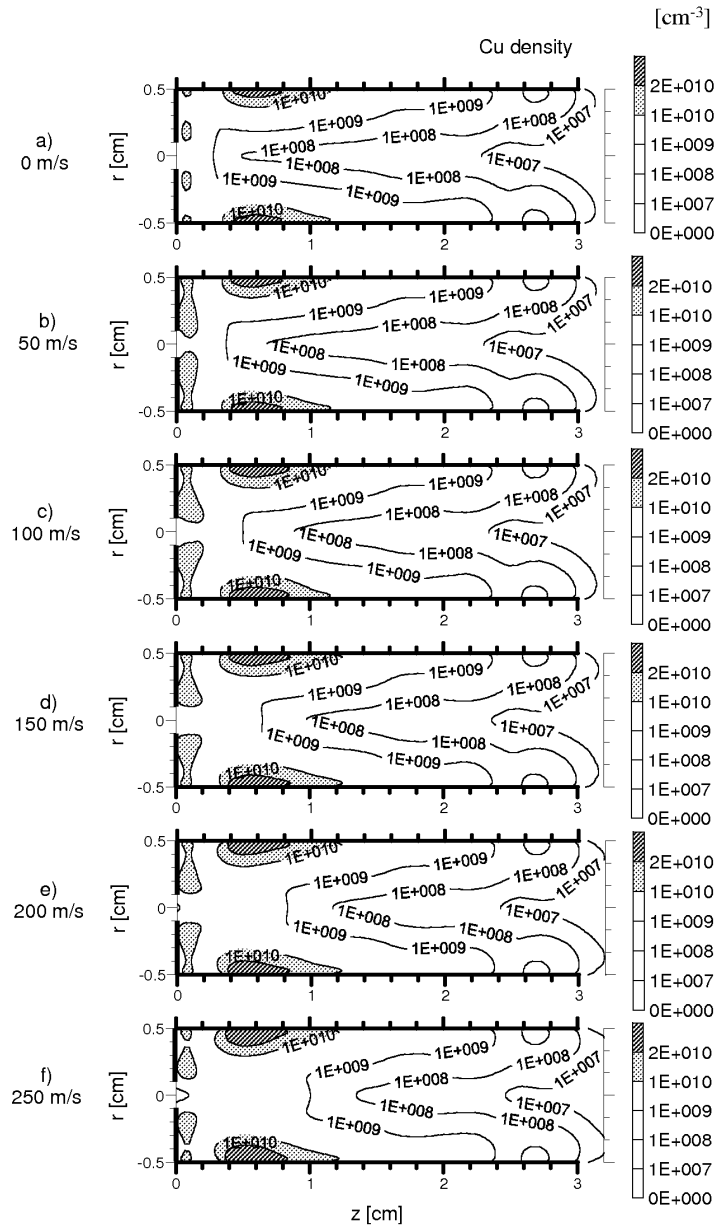


Fig. 8.4 Contour plots of the calculated density profiles of sputtered Cu atoms in the HCD, for different values of gas inlet velocity, including no velocity, at a pressure of 1 Torr.

By comparing Fig. 8.5a with Fig. 8.4a, the effect of the hole in the cathode bottom can be studied. It is clear that the maximum Cu atom density ($2 \times 10^{10} \text{ cm}^{-3}$) is still found near the sidewalls of the HCD, where most of the sputtering occurs at 1 Torr, but there is now also a second maximum (of about 10^{10} cm^{-3}) near the cathode bottom and around the cylinder axis. Of course, in case of a hole in the cathode bottom, no sputtering can take place at the cylinder axis, leading to a lower density in front of the cathode bottom. However, beside this second maximum in front of the cathode bottom, the rest of the profile, in the main part of the HCD, is very similar, and is not much influenced by the hole in the cathode bottom. Indeed, the Cu atom density is still lowest at the cylinder axis and increases towards the sidewalls.

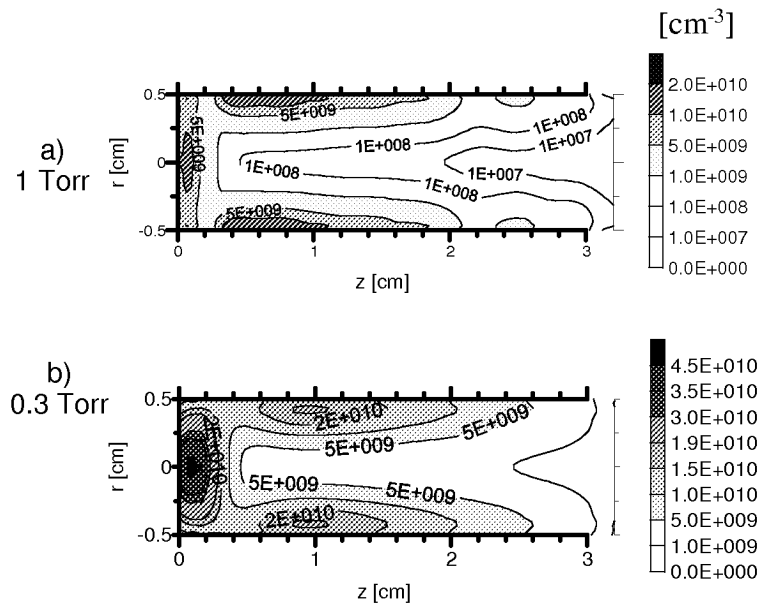


Fig. 8.5 Contour plots of the calculated density profiles of sputtered Cu atoms in the HCD, in case of no hole in the cathode bottom (and hence, no gas flow), for a gas pressure of 1 Torr (a) and 0.3 Torr (b) and a discharge current of 6 mA.

This profile changes when moving to lower pressure, as is illustrated in Fig. 8.5b. Indeed, the maximum Cu atom density, about $7 \times 10^{10} \text{ cm}^{-3}$, is now found in front of the cathode bottom, at the cylinder axis, and a second maximum of about $2 \times 10^{10} \text{ cm}^{-3}$ is located near the side walls (see paragraph 7.4, for more details). Moreover, because of the lower pressure, the mean free path is longer, and thus the diffusion coefficient is larger, leading to more diffusion, both in the axial direction and in the radial directions, away

from the sides towards the middle. Hence, the Cu atom density does not decrease so dramatically towards the cylinder axis as in the higher pressure case, but nevertheless, there is still a dip in density, although less pronounced. Such a dip in the center for the sputtered Cu atom density is found to be characteristic for the HCD, in a wide range of pressures and currents, as we have shown in chapter 7. Because of the dip in density at the cylinder axis, predicted with the model for all conditions and values of gas inlet velocity, it is expected that the flux of Cu atoms at the open end of the HCD, reaches also a minimum in the center. This was already mentioned above, and is indeed shown in Fig. 8.6, for the different values of the gas inlet velocity, at the pressure of 1 Torr. Hence, if a substrate would be placed at the end of the HCD, the deposition flux of sputtered atoms would be highly non-uniform, under the present conditions, with the lowest deposition rate at the center and most deposition at about 4 mm from the center. The relative variation between maximum and minimum flux was found to be slightly higher for lower inlet velocities. Indeed, without gas flow, the minimum value (i.e., $3 \times 10^8 \text{ cm}^{-2} \text{ s}^{-1}$) was about 1% of the maximum value (i.e., $2.6 \times 10^{10} \text{ cm}^{-2} \text{ s}^{-1}$), whereas for the highest gas inlet velocity investigated, the minimum value (i.e., $3.2 \times 10^9 \text{ cm}^{-2} \text{ s}^{-1}$) was calculated to be 4.8 % of the maximum value (i.e., $7.7 \times 10^{10} \text{ cm}^{-2} \text{ s}^{-1}$).

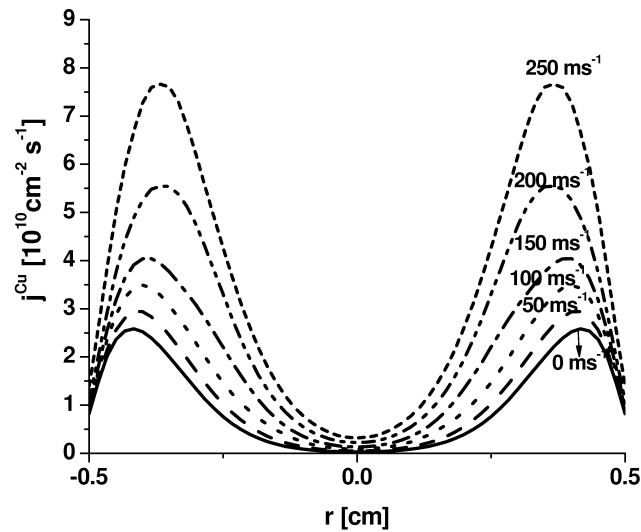


Fig. 8.6 Calculated fluxes of Cu atoms at the open end of the HCD ($z=3.2 \text{ cm}$), as a function of radial position, for different values of inlet gas velocity.

For comparison, the calculated flux at the open end of the HCD, in the case of no hole in the cathode bottom, is depicted in Fig. 8.7, for 1 Torr (left axis, thick solid line). The absolute value of the flux, at the maximum, is a factor of 3.3 higher than with a hole in the cathode bottom (thin solid line), because there can be more sputtering. However, the flux is even more non-uniform than in the case with a hole, i.e., the minimum value (at the center) is calculated to be about 0.6 % of the maximum value. The calculated flux at 0.3 Torr is also shown in Fig. 8.7 (right axis, dashed line). It is found to be much higher, because of the higher Cu atom density in the main body of the HCD (see Fig. 8.5b), and it is not characterized by such a pronounced dip in the center (i.e., the minimum value is about 16% of the maximum value), as is also expected from the density profile in Fig. 8.5b. Hence, this suggests that the uniformity of the deposition rate on a substrate that would be placed near the open end of the HCD could be improved when lowering the gas pressure.

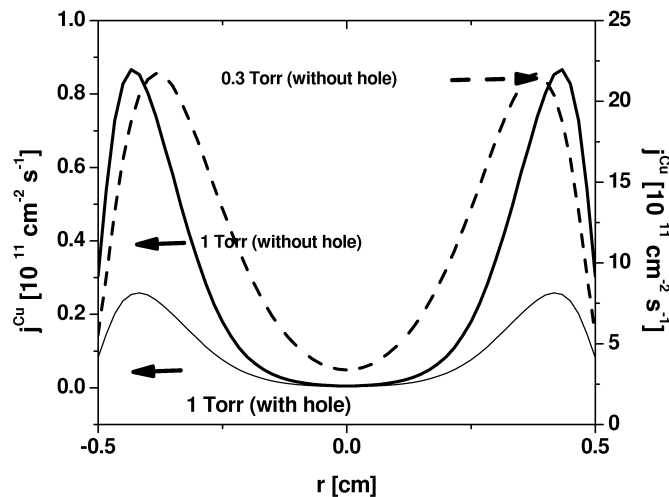


Fig. 8.7 Calculated fluxes of Cu atoms at the open end of the HCD, as a function of radial position, without gas velocity, at 1 Torr, in case of presence or absence of a hole in the cathode bottom (left axis, thin and thicker solid line, respectively), as well as at 1 Torr (without hole in the cathode bottom, right axis, dashed line).

It was shown in Fig. 8.6 that the gas flow does not improve the uniformity of the flux at the open-end of the HCD to a large extent. The absolute value of the flux, on the other hand, increases clearly with rising inlet gas velocity, as is illustrated in Fig. 8.8. Indeed, the Cu atoms are carried away together with the Ar gas flow. It should be mentioned that the total amount of sputtering was found to be roughly the same for all

conditions of gas flow investigated. However, without gas flow, the majority (~ 80 %) of the sputtered atoms was found to be redeposited onto the cathode walls, so that only 20% of the atoms really enter the discharge. This is called the “net sputtered flux”, and this phenomenon was also encountered in dc planar glow discharges.²³ When a significant gas flow is applied, however, the sputtered atoms are entrained with the gas flow, towards the open end of the HCD, and they are prevented from being redeposited at the cathode walls. Hence, the total sputtered flux is then roughly equal to the net sputtered flux.

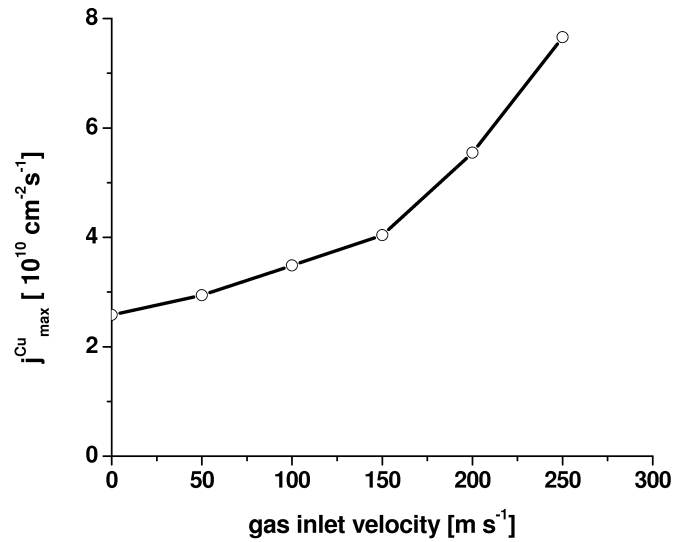


Fig. 8.8 Calculated flux of the Cu atoms at the open end of the HCD, taken at the maximum (i.e., at about 4 mm from the center), as a function of gas inlet velocity.

8.4 Conclusion

A model is developed for a cylindrical HCD with gas flow. The model combines gas flow calculations from a commercial computational fluid dynamics (CFD) code (FLUENT), with self-written models for the plasma behavior. The output of the CFD code, i.e., the argon gas velocity distribution, is used as input in the plasma models, where it is used as an extra term in the flux equations of sputtered neutrals and the corresponding ions, to describe transport by convection. We have focused on how the sputtered Cu atom densities and fluxes are affected by the gas flow, because this is most important for the application of sputter deposition.

It is found that:

1. The gas flow has not much effect on the Cu atom density profile.
2. The gas flow has significant effect on the Cu flux. Indeed, the gas flow carries the Cu atoms away from the gas inlet, in the axial direction, towards the open end of the HCD.
3. The flux of Cu atoms at the open end of the HCD increases with the gas inlet velocity.
4. The model predicts that the external gas flow would enhance the deposition flux of sputtered atoms.
5. The uniformity of the flux, on the other hand, is not much improved.
6. The uniformity was, found to be somewhat better for lower gas pressure, when the Cu atom density was not characterized by such a pronounced dip in the center.
7. Probably, the uniformity can be further improved by modifying the HCD geometry, and more specifically the position of the gas inlet (e.g., gas inlet in the form of a ring or a multi-hole plate at the cathode bottom).

8.5 References

- ¹ T. Jung and A. Westphal, Surf. Coat. Technol. **59**, 171 (1993).
- ² A. Hellmich, T. Jung, A. Kielhorn and M. Reißland, Surf. Coat. Technol. **98**, 1541 (1998).
- ³ C. Panduraru, K. Becker, A. Belkind, A. E. Delahoy, S. Y. Guo and J. Lopez, Proceedings of the "International Conference on Phenomena in Ionized Gases", Greifswald (2003).
- ⁴ L. Bárdos, H. Baránková, Th. Welzel, I. Dani, S. Peter and F. Richter, J. Appl. Phys. **90**, 1703 (2001).
- ⁵ H. Baránková and L. Bárdos, Surf. Coat. Technol. **163-164**, 649 (2003).
- ⁶ D. Korzec, D. Nithammer, J. Engemann, T. Ikeda, T. Aoki and Y. Hatanaka, Surf. Coat. Technol. **142-144**, 21 (2001).
- ⁷ Th. Schurig, S. Menkel, Z. Quan, J. Beyer, B. Güttler, S. Knappe and H. Koch Physica C **262**, 89 (1996).
- ⁸ Z. Hubicka, M. Cada, Z. Potucek, P. Ptacek, H. Síchová, Z. Málková, L. Jastrabík and B. Trunda, Thin Solid Films **447-448**, 656 (2004).
- ⁹ J. Engemann, Surf. Coat. Technol. **169-170**, 14 (2003).
- ¹⁰ Z. Hubicka, G. Pribil, R. J. Soukup and N. J. Ianno, Surf. Coat. Technol. **160**, 114 (2002).
- ¹¹ A. Bogaerts, A. Okhrimovskyy, N. Bager and R. Gijbels, Plasma. Source, Sci. Technol. **14**, 191 (2005).
- ¹² D. A. Benoy, Modeling of Thermal Argon Plasmas, Ph.D. Thesis, Eindhoven University of Technology (1993).
- ¹³ G. M. Janssen, J. van Dijk, D. A. Benoy, M A Tas, K T Burm, W J Goedheer, J. A. M. van der Mullen and D. C. Schram, Plasma Sources Sci. Technol **8**, 1 (1999).
- ¹⁴ G M Janssen, Design of a General Plasma Simulation Model, Fundamental Aspects and Applications, Ph.D. Thesis, Eindhoven University of Technology (2000).
- ¹⁵ J van Dijk, Modeling of Plasma Light Sources: an Object-Oriented Approach, Ph.D. Thesis, Eindhoven University of Technology (2001).
- ¹⁶ D. Van den Abeele, An Efficient Computational Model for Inductively Coupled Air Plasma Flows under Thermal and Chemical Non-Equilibrium, Ph.D. Thesis, von Karman Institute for Fluid Dynamics and University of Leuven (2000).
- ¹⁷ D. P. Lymberopoulos and D. J. Economou, IEEE Trans. Plasma Sci. **23**, 573 (1995).
- ¹⁸ D. Bose, T. R. Govindan and M. Meyyappan, J. Electrochem. Soc. **146**, 2705 (1999).
- ¹⁹ Y. Tanaka and T. Sakuta, J. Phys. D: Appl. Phys. **35**, 468 (2002).
- ²⁰ A. Bogaerts, A. Okhrimovskyy and R. Gijbels, J. Anal. At. Spectrom. **17**, 1076 (2002).
- ²¹ A. Okhrimovskyy, A. Bogaerts and R. Gijbels, J. Appl. Phys. **96**, 3070 (2004).
- ²² Fluent 6.1 User Guide (<http://www.fluent.com>)
- ²³ A. Bogaerts and R. Gijbels, J. Appl. Phys. **79**, 1269 (1996).

Summary & Conclusions

Numerical modeling of a hollow cathode discharge

Summary & Conclusions

Numerical modeling of a hollow cathode discharge

A hollow cathode discharge (HCD) is a special kind of glow discharge. A glow discharge is a partially ionized gas, or plasma, consisting of positive (and sometimes negative) ions and electrons, and a large number of neutral species. It is created by applying a potential difference between two electrodes, which are inserted in a gas. In a HCD, the cathode can be built in different shapes, for example as a spherical segment or as a pair of plane parallel plates or as a hollow cylinder. In the study of a conventional hollow cathode discharge the most important spatial regions are, a dark space adjacent to the cathode surface, where the electric field is strong, which is called the cathode dark space (CDS) or sheath, and a rather luminous part beyond it, where the field is weak and which is called the negative glow (NG) or plasma region. The anode (or anodes) is usually placed close to the cathode surface at such a distance that no positive column can be formed and that the NG can be confined inside the discharge cavity.

The discharge is sustained by the emission of secondary electrons at the cathode, induced by fast ions, atoms and metastable atoms impinging the cathode surface and by the creation of new electron-ion pairs inside the discharge, due to ionization. Conventional HCDs usually operate with a cathode voltage ranging from 200 to 500 Volt, which is lower than in a glow discharge with a single planar cathode, for the same current density. This is possible because the HCD is a very efficient discharge in the use of the charged particle energies. Due to its special geometric configuration, most of the energy of the fast particles is spent inside the discharge, i.e., for the production of new electron-ion pairs, excitation collisions, charge transfer collisions, etc. Indeed, almost all ions that are created in the NG can hit the cathode surface, contributing to the emission of secondary electrons from the cathode. These electrons, being accelerated in the CDS, can use all their energy for ionization and excitation collisions with the gas atoms and the sputtered atoms from the cathode. Moreover, some of these electrons can penetrate into the CDS opposite to the cathode of their origin and cause ionization collisions there, i.e., they can oscillate between opposite cathode surfaces (so-called “pendulum effect”). As a consequence, the ionization and excitation rates in the CDS and in the NG are enhanced.

This enhancement is most evident when the NG regions from facing cathode surfaces overlap, giving rise to a large increase in the current density and light intensity, which is called the “hollow cathode effect”.

These factors have made the HCD a very useful tool for many applications, for example in spectroscopic analysis, where the hollow cathode discharge is used as an emission source, allowing direct excitation and analysis of samples (by sputtering, i.e., the ejection of cathode atoms upon the bombardment of high energetic ions and atoms) and as a light source in atomic absorption spectrometry because of its sharp and intense spectral lines. Moreover, HCDs find applications in plasma processing (ion etching, thin film deposition, surface treatment) as well as in ion gas laser technologies, due to its capability for obtaining high rates of sputtering, while maintaining the discharge voltage relatively low.

To improve the results in these application fields, it is important to understand the different mechanisms involved in the discharge. This can be achieved by means of experimental and theoretical studies, as well as by numerical modeling. Due to the large amount of particles and processes involved in glow discharges, numerical simulations are especially useful in this area.

Many simulations of gas discharge plasmas are based on a fluid model, (i.e., a transport model, where the continuity and flux equations are solved for each plasma species. The transport is described by diffusion and migration in the electric field. In the cases of charged particles, the transport equations are solved together with the Poisson equation, in order to obtain the electric field distribution). In the fluid model (in the drift and diffusion approximation), it is assumed that the velocity distribution of each species present in the discharge (ions, electrons, metastable atoms, etc.) is in hydrodynamic equilibrium with the local electric field. However, when using such a model, the behavior of the energetic electrons, which are responsible for most of the ionization and excitation collisions, cannot accurately be described, and consequently the electron collision rates are not very reliable. Another approach is given by the use of Monte Carlo simulations. With Monte Carlo models (MC) the microscopic nature of a collision can be considered. The particles are followed one after another and the collision rates are calculated based on the energy-dependent cross sections. Hence, a correct energy distribution function for the energetic particles can be calculated. However a MC model is not self-consistent, because the electric field is not calculated in the model, but

needs to be given as input. With the particle-in-cell-Monte-Carlo (PIC-MC) method the problem can be solved self-consistently. The collision rates are calculated based on the energy-dependent cross section, and the particle energy is calculated from the electric field, which is obtained self-consistently from Poisson's equation using the charged species densities. However, this method is very time-consuming because a large number of particles should be followed for statistically valid results. Another way of solving the problem self-consistently is the so-called hybrid model, e.g., a MC model combined with a fluid model. Such a hybrid model combines the advantages of both methods and it is considerably faster than a PIC-MC model.

In the present work an overall picture of the HCD has been presented based on the results of a hybrid model and on the comparison to experimental data. The hybrid approach allows us to calculate in a self-consistent manner the electric field and the energy distribution functions of the energetic particles, which is not only crucial for the correct description of the electrical properties of the discharge but also for the description of the cathode sputtering.

The model as well as the experiments were performed in a dc cylindrical HCD. The model were applied to the two most frequently used configurations of cylindrical HCD's: a HCD where the cathode cylinder is closed at one end, and at some distance from the open end, an anode is placed (asymmetric configuration), and a HCD where the cathode cylinder is open at both ends, close to which the anodes are located (symmetric configuration).

In the study of the asymmetric HCD configuration, argon (Ar) was used as filling gas, the discharge pressure ranges from 0.3 to 1 Torr and the current varies from 1 to 10 mA. A discharge voltage between 246 and 298 V was applied. The anode and the cathode were made both of copper. In the case of the symmetric HCD configuration, helium (He) was used as background gas, while the anodes and cathode were both made from nickel. The gas pressure was 1 Torr, the discharge current ranges from 2 to 6 mA and a discharge voltage from 158 to 170 V was applied. In both cases, the anodes were grounded and the discharge conditions assumed in the model were taken from the experiments.

The species considered in the model were: background argon (helium) atoms at room temperature and uniformly distributed throughout the discharge, singly charged positive argon (helium) and copper ions, metastable argon (helium) atoms, fast and slow electrons, fast Ar atoms, and fast and slow Cu atoms. The movement and collisions of the

fast electrons, fast Ar and Cu atoms and fast Ar⁺ and Cu⁺ ions were described with the Monte Carlo approach, while the slow electrons, Ar⁺, Cu⁺ ions, Cu and Ar (or He) metastable atoms were treated as a continuum in the corresponding fluid models. The above sub-models are coupled to each other due to the interaction processes between the plasma species, and they are solved iteratively until convergence is reached. The latter is determined by the difference in the total current to the anode in two successive iterations, which should be below 1%. Typically, 10-12 iterations were carried out before convergence was reached. Typical results are, among others, the energy distribution and impact collisions rates of the fast particles, the densities and fluxes of all the particles, as well as the electric field and potential distribution throughout the complete discharge.

In the first chapter of this PhD thesis a general description of the conventional HCD, its applications as well as the most frequently used models to describe the behaviour of the gas discharge plasma are given, while in the second chapter a description of all the models is presented.

The third and fourth chapters are concerned to the study of the main physical properties of the HCDs, as well as to the differences due to geometry and filling gas. In that part, we have analyzed in detail the fast electron behavior. We have compared the calculated current-voltage dependence and some spectrometric data of the discharge with experimental data. We have found that the secondary electron emission coefficient (γ) was obtained almost constant in the range of the reduced electric fields studied here, with a value around 0.04, which agrees very well with reported data for a Cu cathode cleaned by sputtering without flashing. Moreover it confirms our assumption that at the conditions studied here the ions are the main source of electron emission from the cathode and that the fundamental process of electron production is by ionization collisions of electrons with Ar atoms.

The electron ionization collisions inside the CDS were found to be important for all conditions investigated, even at high currents. The maximum in the profile of the electron collision rates, the charged particle densities, the potential and electric field was found near the cathode bottom of the HCD cylinder. The plasma potential was found to be negative for all the discharge conditions investigated. When the emission from the cathode bottom was not considered, the maxima in the profiles were axially shifted to the cylinder centre and the plasma potential was found positive at the upper half of the

cylinder cathode. This shows the importance of considering the cathode bottom in order to have a more realistic description of the discharge.

The loss of fast electrons to the anode increases and also the plasma potential becomes more negative with the decrease in pressure and in current.

The best regime for the hollow cathode effect to occur was obtained when at constant voltage the current increases with decreasing pressure, i.e. at pressures between 0.3 and 0.53 Torr and a current of 2 mA. These conditions are characterized in the experimental data by the most intense light emission, and in our calculations, when the maximum of the calculated total electron impact excitation rate is found at the cell axis, i.e., in the form of a disc shape instead of a ring shape.

In chapter 4, we have made a detailed study of an He-Ni HCD, (symmetrical configuration). We found that all the excitation and ionization rates, as well as the plasma species densities, reach a maximum at the discharge center, both in the axial direction (i.e., in the middle of the HC region, at $z = 5.8$ cm) and in the radial direction (i.e., at the cylinder axis). The He metastable atoms reach, however, also a second maximum outside the HC region, i.e., in the region between HC and anode rings. The reason is that the dominant production mechanism of the He metastables, i.e., electron impact excitation to the metastable level, reaches also a second maximum in this region.

The calculated He metastable atom density was found to be an order of magnitude higher than the calculated electron and He^+ ion densities. Consequently, the role of He metastable atoms is clearly not negligible at the conditions under study, both with respect to secondary electron emission at the cathode walls, and to ionization in the plasma, by metastable-metastable collisions. The latter process typically accounts for about 20 % to the total ionization in the HCD, according to our model calculations. Therefore, it was found that including the He metastables in the model was necessary to be able to reproduce the experimental electrical current values.

The comparison made with the experimental data for the electrical current and the radial profiles of electron density, potential and radial electric field (including the value of the plasma potential and the CDS length), shows that the model presents a realistic picture of the He HCD.

In chapter 5, the influence of the fast atoms, fast ions and metastable gas atoms on the discharge properties were analysed for an Ar HCD, as well as the relative importance of different processes determining the metastable atom density in the Ar HCD. The

maximum in the ionization profile due to heavy particles was found very close to the cathode walls. The relative importance of these processes increases with decreasing pressure, as the mean energy of the fast particles, also increases. Especially, at conditions where the ionization inside the CDS is predominant, (i.e., low pressures and currents) we have observed that the net positive charge density inside the CDS increases, followed by a rise in the voltage drop inside the CDS, hence the plasma potential becomes less negative in comparison to the results obtained when only electron ionization was considered. Hence, in spite of the fact that integrated over the total discharge volume, the ionization due to fast Ar atoms and Ar^+ ions contributes only for 3% to the total ionization, the inclusion in the model of Ar^+ and Ar^f ionization collision processes is important for the correct calculation of parameters which directly depend on the ionization distribution in the CDS; i.e., the net charge density distribution in the CDS, the voltage drop in the CDS, as well as the electric field and the plasma potential.

In chapter 6 we have shown the calculation results for the Ar^m metastable atoms compared to their experimental density measured by laser absorption spectroscopy. Experimental results evidence the presence of the metastable atom production source at the cathode surface, probably originating from fast Ar^+ ions and Ar atoms impinging on it, a mechanism that was taken in account in the model. It was found that at low pressure, the metastable atom densities show a nearly parabolic profile at all currents investigated, because of the important role of diffusion. When the pressure increases, the density profiles become flatter, and at high currents, they even exhibit two peaks at the CDS-NG boundaries, with a dip at the discharge axis, which is determined mainly by the enhanced production by electron impact excitation close to the CDS-NG boundaries and the increasing role of the electron quenching as a loss mechanism of the metastable atom population. Comparison between experimental and calculated Ar metastable atom densities shows a good agreement at low pressures, but at 1 Torr the calculated values differ by a factor of two from the measured ones. Several possible explanations for this discrepancy were discussed.

The contribution of metastable atoms to the formation of charges in the Ar-Cu HCD is found to be negligible for the conditions under study, both as ionization source as well as in secondary electron emission from the cathode.

The processes responsible for the sputtering as well as the behavior of the sputtered Cu atoms and Cu^+ ions in a HCD were studied in chapter 7. It was found that

the contribution of the fast Ar^+ ions to the sputtering was the most significant, followed by the fast Ar atoms. The role of self-sputtering was negligible, in contrast to planar GD's, where the contribution of self-sputtering was typically in the order of several %. At the cathode bottom, there is no net sputtered flux, but there is a net amount of redeposition, while at the cathode sidewalls, redeposition predominates only close to the cathode bottom and near the open end towards the anode. Throughout the discharge volume, at all the conditions investigated, the largest concentration of Cu atoms was found in the lower half of the HCD, close to the bottom, at some distance from the cathode surface (both at the cathode bottom and at the cathode sidewalls). At low pressure, the Cu atom population is more uniformly distributed along the discharge length and the density profiles show a maximum at the cylinder axis, close to the cathode bottom, while at high pressures, the maximum was found close to the cathode sidewalls. Moreover at 1 Torr, regions of high Cu atom density alternate with region of low density, which corresponds to the formation of the characteristic consecutive hollow spheres observed experimentally in HCD's. Penning ionization was found the main ionization mechanism for the Cu atoms, followed by Ar^+ ion ACT. The ionization degree of the Cu atoms was found to be in the order of 10^{-5} for all conditions investigated.

In chapter 8, a model was developed for a cylindrical HCD with gas flow. The model combines gas flow calculations from a commercial computational fluid dynamics (CFD) code (FLUENT), with self-written models for the plasma behavior. The output of the CFD code, i.e., the argon gas velocity distribution, is used as input in the plasma models, where it is used as an extra term in the flux equations of neutrals and ions, to describe transport by convection. We have focused on the behavior of sputtered Cu atoms, and how their density and flux are affected by the gas flow, because this is most important for the application of sputter deposition. It was found that the gas flow has not much effect on the Cu atom density profile. However, it has significant effect on the Cu flux. Indeed, the gas flow carries the Cu atoms away from the gas inlet, in the axial direction, towards the open end of the HCD, and the flux of Cu atoms at the open end of the HCD increases with the gas inlet velocity. Hence, the model predicts that the external gas flow would enhance the deposition flux of sputtered atoms. The uniformity of the flux, on the other hand, is not much improved. The uniformity was, however, found to be somewhat better for lower gas pressure, when the Cu atom density was not characterized by such a pronounced dip in the center. Probably, the uniformity can be further improved

by modifying the HCD geometry, and more specifically the position of the gas inlet (e.g., gas inlet in the form of a ring or a multi-hole plate at the cathode bottom).

Finally, we can conclude that from the comparison between results from models and experiments, a better insight in the discharge properties and in the relative importance of different production and loss mechanisms, can be obtained, which helps to improve the use of the HCD as tool for many applications.

Samenvatting & Besluit

*Numeriek model van een holle kathode
ontlading*

Samenvatting & Besluit

Numeriek model van een holle kathode ontleding

Een holle kathode ontleding (HKO) is een speciale soort van glimontleding. Een glimontleding is een gedeeltelijk geïoniseerd gas (of plasma) dat bestaat uit positieve (en soms negatieve) ionen en elektronen en een groot aantal neutrale deeltjes. De glimontleding ontstaat door het aanleggen van een potentiaalverschil tussen twee elektrodes die in een gas geplaatst worden. In een HKA kan de kathode onder verschillende vormen voorkomen, bijvoorbeeld als een sferisch segment of als een paar vlakke evenwijdige platen of als een holle cylinder. In de studie van een conventionele holle kathode ontleding kunnen de volgende belangrijke ruimtelijke gebieden onderscheiden worden: een donkere ruimte grenzend aan het kathodeoppervlak waar het elektrische veld sterk is, die de kathode donkere ruimte (KDR) of grenslaag genoemd wordt, en een gebied daarachter dat eerder verlicht is, waar het veld zwak is en dat het negatieve glimlicht of het plasmagebied genoemd wordt. De anode (of anodes) wordt meestal dicht bij het kathodeoppervlak geplaatst zodat geen positieve kolom kan gevormd worden en zodat het negatieve glimlicht binnenin de ontledingscaviteit kan gehouden worden.

De ontleding wordt in stand gehouden door de emissie van secundaire elektronen aan de kathode; ze wordt geïnduceerd door snelle ionen, atomen en metastabiele atomen die invallen op het kathodeoppervlak en door de creatie van nieuwe elektron-ion paren door ionisatie in de ontleding. Conventionele holle kathode ontledingen werken meestal bij een kathodespanning die ligt tussen 200 V en 500 V, wat lager is dan voor een glimontleding met een enkelvoudige vlakke kathode bij dezelfde stroomdichtheid. Dit is mogelijk omdat de holle kathode ontleding een heel efficiënte ontleding is voor het gebruik van de geladen deeltjesenergieën. Vanwege zijn speciale geometrische configuratie, wordt het grootste deel van de energie van de snelle deeltjes gebruikt binnenin de ontleding, d.w.z. voor de productie van nieuwe elektron-ion paren, excitatie botsingen, ladingsoverdrachtbotsingen, enz. Alle ionen die in het negatieve glimlicht ontstaan, kunnen inderdaad het kathode-oppervlak raken, wat bijdraagt tot de emissie van secundaire elektronen van de kathode. Deze elektronen, die versneld worden in de

kathode donkere ruimte, kunnen al hun energie gebruiken voor ionisatie en excitatiebotsingen met de gasatomen en de gesputterde atomen van de kathode. Sommige van deze elektronen kunnen zelfs binnendringen in de kathode donkere ruimte van de tegenoverliggende kathode en aldaar ionisatiebotsingen veroorzaken, d.w.z. ze kunnen oscilleren tussen de tegenover elkaar liggende kathodeoppervlakken (zgn. “pendulum effect”). Als gevolg daarvan, wordt de efficiëntie van ionisatie en excitatie in de kathode donkere ruimte en in het negatieve glimlicht verhoogd. Deze verhoging in efficiëntie is het duidelijkst wanneer de negatieve glimlicht gebieden van de tegenover elkaar liggende kathode oppervlakken elkaar overlappen. Dit geeft aanleiding tot een grote stijging in stroomdichtheid en lichtintensiteit en wordt het “holle kathode effect” genoemd.

Deze factoren maken de holle kathode ontlading zeer geschikt voor vele toepassingen, bijvoorbeeld voor spectroscopische analyse, waar de holle kathode ontlading gebruikt wordt als een emissiebron, wat een directe excitatie en analyse van monsters toelaat (door sputteren, d.w.z. emissie van kathodeatomen tengevolge van het bombardement van hoogenergetische ionen en atomen); en als een lichtbron in atomaire absorptie spectrometrie, vanwege zijn scherpe en intense spectrale lijnen. Daarnaast vinden holle kathode ontladingen toepassingen in de materiaaltechnologie (etsen, dunne film depositie, oppervlaktebehandeling), in ion gas laser technologieën, vanwege hun vermogen om hoge sputtersnelheden te bekomen terwijl de ontladingsspanning relatief laag kan gehouden worden.

Om de resultaten in deze toepassingsgebieden te verbeteren is het belangrijk om de verschillende mechanismen te begrijpen die in deze ontlading een rol spelen. Dit kan verwezenlijkt worden door middel van experimentele en theoretische studies maar ook door numerieke modellering. Vanwege de grote hoeveelheid aan deeltjes en processen die glimontladingen met zich meebrengen zijn numerieke simulaties zeer nuttig in dit gebied.

Veel simulaties van gasontladingsplasma's zijn gebaseerd op een fluid model (d.w.z. een transportmodel, waar de continuïteits- en fluxvergelijkingen worden opgelost voor elk plasmadeeltje. Het transport wordt beschreven door middel van diffusie en migratie in het elektrische veld. In het geval van geladen deeltjes, worden de transportvergelijkingen samen opgelost met de Poissonvergelijking voor de elektrische veldverdeling. In het fluid model (in de ‘drift-diffusie’ benadering), wordt aangenomen dat de snelheidsverdeling van elk deeltje, aanwezig in de ontlading (ionen, elektronen,

metastabiele atomen, enz.), in hydrodynamisch evenwicht is met het lokale elektrische veld. Wanneer zo'n model echter gebruikt wordt, zal het gedrag van de energetische elektronen, die verantwoordelijk zijn voor het grootste deel van de ionisatie en excitatiebotsingen, niet nauwkeurig kunnen beschreven worden en bijgevolg zijn de elektronenbotsingssnelheden niet erg betrouwbaar.

Een andere benadering wordt gegeven door het gebruik van Monte-Carlo simulaties. Met Monte-Carlo modellen (MC) kan de microscopische aard van de botsingen bestudeerd worden. De deeltjes volgen elkaar op en de botsingssnelheden worden berekend op basis van de energieafhankelijke botsings-werkzame doorsneden. Bijgevolg kan een correcte energiedistributiefunctie voor de energetische deeltjes berekend worden.

Een MC model is niet zelf-consistent, omdat het elektrische veld niet berekend wordt in het model, maar als input moet ingegeven worden. Met de "particle-in-cell" - Monte-Carlo (PIC-MC) methode kan het probleem zelf-consistent opgelost worden. De botsingssnelheden worden berekend op basis van de energie-afhankelijke botsings-werkzame doorsneden en de deeltjesenergie wordt berekend op basis van het elektrische veld, dat zelf-consistent verkregen wordt door middel van de Poisson vergelijking, waarbij gebruik gemaakt wordt van geladen deeltjesdichtheden. Deze methode is echter heel tijdrovend omdat een groot aantal deeltjes moet gevolgd worden om statistisch geldige resultaten te verkrijgen. Een andere manier om het probleem zelf-consistent op te lossen, is het zogenaamde hybride model, bv. een MC model gecombineerd met een fluid model. Zo'n hybride model combineert de voordelen van beide methodes en is aanzienlijk sneller dan een PIC-MC model.

In het huidige werk wordt de holle kathode ontlading beschreven, gebaseerd op de resultaten van een hybride model en op basis van de vergelijking met experimentele gegevens. De hybride benadering laat ons toe om op een zelf-consistente manier het elektrische veld en de energiedistributiefuncties van de energetische deeltjes te berekenen, wat niet alleen cruciaal is voor de correcte beschrijving van de elektrische eigenschappen van de ontlading maar ook voor de beschrijving van de kathodesputtering. Zowel het model als de experimenten werden uitgevoerd in een dc cilindrische HKO. Het model werd toegepast op de meest gebruikte configuraties van cilindrische HKO'en: een HKO waar de kathodecilinder gesloten is aan één uiteinde en waar op een bepaalde afstand van het open einde een anode wordt geplaatst (asymmetrische

configuratie), en een HKO waar de kathodecilinder open is aan beide uiteinden, en met een anode op een bepaalde afstand van beide uiteinden (symmetrische configuratie).

In de studie van de asymmetrische HKO configuratie, wordt argon (Ar) gebruikt als ontladingsgas, ligt de ontladingsdruk tussen 0.3 en 1 Torr en varieert de stroom van 1 tot 10 mA. Een ontladingsspanning tussen 246 en 298 V wordt aangelegd. De anode en de kathode werden beide uit koper vervaardigd. In het geval van de symmetrische HKO configuratie wordt helium als achtergrondgas gebruikt terwijl de anodes en de kathodes beiden uit nikkel vervaardigd werden. De gasdruk is 1 Torr, de ontladingsstroom varieert van 2 tot 6 mA en een ontladingsspanning van 158 tot 170 V werd aangelegd. In beide gevallen, werden de anodes gearde en de ontladingsvoorwaarden die in het model worden aangenomen, werden uit experimenten gehaald.

De volgende soorten deeltjes werden in het model in rekening gebracht : atomen van het achtergrondgas (argon of helium) bij kamertemperatuur en uniform verdeeld over de ontlading, enkelvoudig geladen positieve argon (of helium) en koperionen, metastabiele argon (helium) atomen, snelle en trage elektronen, snelle Ar atomen, en snelle en trage koper atomen. De beweging en botsingen van de snelle elektronen, snelle Ar en Cu atomen en snelle Ar^+ en Cu^+ ionen werden beschreven met de Monte-Carlo benadering, terwijl de trage elektronen, Ar^+ , Cu^+ ionen, Cu atomen en Ar (of He) metastabiele atomen werden behandeld als een continuüm in de overeenkomstige fluid modellen. De bovenstaande submodellen werden aan elkaar gekoppeld vanwege de interactieprocessen tussen de plasmadeeltjes en ze werden iteratief opgelost tot convergentie werd bereikt. Dit werd bepaald door het verschil in de totale stroom aan de anode tussen twee opeenvolgende iteraties, dat onder de 1% zou moeten liggen. 10-12 iteraties werden gewoonlijk uitgevoerd vooraleer convergentie bereikt werd. Typische resultaten zijn onder andere de energieverdeling en botsingsnelheden van de snelle deeltjes, de dichtheden en fluxen van alle deeltjes maar ook het elektrische veld en de potentiaaldistributie over de volledige ontlading.

In het eerste hoofdstuk van deze doctoraatsthesis werd een algemene beschrijving van de conventionele holle kathode ontlading gegeven, samen met zijn toepassingen en ook de meest frequent gebruikte modellen om het gedrag van het gasontladingsplasma te beschrijven. In het tweede hoofdstuk werd een beschrijving gegeven van alle modellen, gebruikt in dit werk.

Het derde en vierde hoofdstuk beschrijven de voornaamste fysische eigenschappen van HKO'en met daarnaast ook de verschillen te wijten aan geometrie en vulgas. In dat deel werd het snelle elektronengedrag tot in detail bestudeerd. De berekende stroom-spanning afhankelijkheid en enkele spectrometrische gegevens van de ontlading werden vergeleken met experimentele gegevens. Er werd vastgesteld dat de secundaire elektronen emissie coëfficiënt (γ) praktisch constant wordt in het gebied van de gereduceerde elektrische velden die hier bestudeerd werden, met een waarde rond 0.04, wat goed overeenkomt met de gerapporteerde gegevens voor een zuivere (d.i. gesputterde) Cu kathode. Dit bevestigt onze veronderstelling dat, bij de voorwaarden die hier bestudeerd werden, de ionen de hoofdbron zijn voor elektronenemissie van de kathode en dat het fundamentele proces van elektronenproductie gebeurt door ionisatiebotsingen van elektronen met Ar atomen.

De elektronen ionisatiebotsingen binnenin de kathode donkere ruimte blijken belangrijk voor alle onderzochte voorwaarden, zelfs bij hoge stromen. Het maximum in het profiel van de elektronen botsingssnelheden, de geladen deeltjesdichtheden, de potentiaal en het elektrische veld is terug te vinden vlakbij de kathodebodem van de HKO cylinder. De plasmapotential blijkt negatief voor al de onderzochte ontladingsvoorwaarden. Als de emissie van de kathodebodem niet in beschouwing genomen wordt, zijn de maxima in de profielen axiaal verschoven naar het midden van de cilinder en de plasmapotential bleek positief te zijn in de bovenste helft van de cilinderkathode. Dit toont het belang aan om rekening te houden met de kathodebodem om een meer realistische beschrijving van de ontlading te verkrijgen.

Het verlies aan snelle elektronen aan de anode verhoogt en ook de plasmapotential wordt meer negatief bij een daling van druk en stroom.

Het beste regime opdat het holle kathode effect zou optreden werd bekomen wanneer bij een constante spanning de stroom stijgt, bij een dalende druk, d.w.z. bij een druk tussen 0.3 en 0.53 Torr en een stroom van 2mA. Deze voorwaarden werden bij de experimentele gegevens gekarakteriseerd door de meest intense lichtemissie; in onze berekeningen, wanneer het maximum van de berekende totale elektronen impact excitatiesnelheid werd bekomen aan de cel-as, d.w.z. in de vorm van een schijf in plaats van een ring.

In hoofdstuk 4 werd een gedetailleerde studie gemaakt van een He-Ni HKO, (symmetrische configuratie). Er werd vastgesteld dat alle excitatie en ionisatiesnelheden,

evenals de plasmadeeltjesdichtheden, een maximum bereiken bij het ontladingscentrum, zowel in de axiale richting (d.w.z. in het midden van het holle kathode gebied, bij $z = 5.8$ cm) en in de radiale richting (d.w.z. aan de cilinder as). De He metastabiele atomen bereiken echter ook een tweede maximum buiten het holle kathode gebied, d.w.z. in het gebied tussen holle kathode en anode ringen. De reden is dat het dominante productiemechanisme van de He metastabielen, d.w.z. elektron impact excitatie tot aan het metastabiele niveau, ook een tweede maximum bereikt in dit gebied.

De berekende metastabiele He atoomdichtheid werd een grootteorde hoger bevonden dan de berekende elektronen en He^+ ionen dichtheden. Bijgevolg is de rol van de He metastabiele atomen duidelijk niet verwaarloosbaar bij de voorwaarden die bestudeerd werden voor wat betreft secundaire elektronenemissie aan de kathodewanden en de ionisatie in het plasma door metastabiele-metastabiele botsingen. Het laatste proces telt typisch voor ongeveer 20% van de totale ionisatie in de HKO, althans zoals voorspeld met onze modelberekeningen. Daarom werd besloten dat het noodzakelijk is om de He-metastabielen mee te nemen in het model om de experimentele elektrische stroomwaarden te kunnen reproduceren.

De vergelijking die gemaakt werd met de experimentele gegevens voor de elektrische stroom en de radiale profielen van elektronendichtheid, potentiaal en radiaal elektrisch veld (inclusief de waarde van de plasmapotential en de lengte van de kathode donkere ruimte), toont aan dat het model een realistisch beeld geeft van de He HKO.

In hoofdstuk 5 werd de invloed van de snelle atomen, snelle ionen en metastabiele gasatomen op de ontladingsvoorwaarden bestudeerd voor een Ar HKO, evenals het relatieve belang van de verschillende processen die de metastabiele atoomdichtheid in de HKO bepalen. Het maximum in het ionisatieprofiel, te wijten aan zware deeltjes, blijkt heel dicht bij de kathodewanden te liggen. Het relatieve belang van deze processen stijgt met dalende druk aangezien de gemiddelde energie van de snelle deeltjes ook toeneemt. Bij voorwaarden waar de ionisatie in de kathode donkere ruimte dominant is (d.w.z. lage druk en stroom), wordt vastgesteld dat de netto positieve ladingsdichtheid binnenin de kathode donkere ruimte toeneemt, gevolgd door een stijging in de spanningsval binnenin de kathode donkere ruimte. Hieruit volgt dat de plasmapotential minder negatief wordt in vergelijking met de resultaten die bekomen worden wanneer alleen elektronenionisatie beschouwd wordt.

Daaruit volgt dat, niettegenstaande het feit dat geïntegreerd over het totale ontladingsvolume, de ionisatie te wijten aan snelle Ar atomen en Ar^+ ionen slechts voor 3% bijdraagt aan de totale ionisatie, het mee in rekening brengen van Ar^+ en Ar^f ionisatiebotsingsprocessen in het model, belangrijk is voor de correcte berekening van parameters die direct afhankelijk zijn van de ionisatieverdeling in de kathode donkere ruimte; d.w.z. de netto ladingsdichtheidsverdeling in de kathode donkere ruimte, de spanningsval in de kathode donkere ruimte, evenals het elektrische veld en de plasmapotential.

In hoofdstuk 6 werden de berekeningsresultaten voor de Ar^m metastabiele atomen vergeleken met hun experimentele dichtheid gemeten door laser absorptie spectroscopie. Experimentele resultaten bevestigen de aanwezigheid van een metastabiele atomen productiebron aan het kathode oppervlak. Waarschijnlijk is die bron afkomstig van snelle Ar^+ ionen en Ar atomen die invallen op de kathode, een mechanisme waar ook mee rekening wordt gehouden in het model. Er werd vastgesteld dat de metastabiele atoomdichtheden, bij lage druk, een nagenoeg parabolisch profiel vertonen bij alle onderzochte stromen vanwege de belangrijke rol van diffusie. Als de druk stijgt worden de dichtheidsprofielen vlakker en bij hoge stromen vertonen ze zelfs twee pieken aan de KDR-NG grenzen met een dip in het centrum van de ontlading, die hoofdzakelijk wordt bepaald door de verbeterde productie door elektronen impact excitatie dicht bij de KDR-NG grenzen en de stijgende rol van de elektronen ‘quenching’ als een verlies mechanisme van de metastabiele atoompopulatie. Vergelijking tussen experimentele en berekende Ar metastabiele atoomdichtheden tonen een goede overeenkomst bij lage druk, maar bij 1 Torr verschillen de berekende waarden met een factor twee van de gemeten waarden. Verschillende mogelijke verklaringen voor deze afwijking werden besproken.

De bijdrage van metastabiele atomen aan de vorming van ladingen in de Ar-Cu HKO blijkt verwaarloosbaar voor de bestudeerde voorwaarden zowel als ionisatiebron als in de secundaire elektronen emissie van de kathode.

De processen die verantwoordelijk zijn voor de sputtering, samen met het gedrag van de gesputterde Cu atomen en Cu^+ ionen in een HKO, werden bestudeerd in hoofdstuk 7. Er werd vastgesteld dat de snelle Ar^+ ionen het meeste bijdragen aan het sputteren gevolgd door de snelle Ar atomen. De rol van zelfsputtering is verwaarloosbaar in tegenstelling tot planaire glimontladingen waar het aandeel van zelfsputtering een grootte-orde heeft van verschillende %. Aan de kathodebodem is er geen netto

gesputterde flux maar er is een netto hoeveelheid aan redepositie terwijl aan de kathode zijwanden redepositie alleen overheerst, dicht bij de kathode bodem en dicht bij het open einde, richting anode. Doorheen het ontladingsvolume werd de grootste concentratie aan Cu atomen gevonden in de onderste helft van de holle kathode ontlading, dicht bij de bodem en op een bepaalde afstand van het kathodeoppervlak (zowel aan de kathode bodem als aan de kathode zijwanden). Bij lagere druk is de Cu atoompopulatie meer uniform verspreid over de ontladingslengte en de dichtheidsprofielen vertonen een maximum aan de cilinderas dichtbij de kathodebodem. Bij hoge druk lag het maximum dicht bij de kathode zijwanden. Bij een druk van 1 Torr wisselen gebieden met hoge Cu atoomdichtheid zich bovendien af met gebieden van lage dichtheid, wat overeenkomt met de vorming van de karakteristieke holle sferen die experimenteel gezien worden in HKO'en. Penning ionisatie blijkt het hoofd ionisatiemechanisme voor de Cu-atomen, gevolgd door asymmetrische ladingsoverdracht met Ar^+ ionen. De ionisatiegraad van de Cu-atomen blijkt een grootteorde van 10^{-5} te hebben voor alle onderzochte voorwaarden.

In hoofdstuk 8 werd een model ontwikkeld voor een cilindrische holle kathode ontlading met gasstroom. Het model combineert gasstroomberekeningen van een commerciële fluid dynamica (CFD) computercode (FLUENT) met zelf geschreven modellen voor het plasmagedrag. De output van de CFD code, d.w.z. de snelheidsdistributie van het argon gas, wordt gebruikt als input voor de plasmamodellen, waar het gebruikt wordt als een extra term in de fluxvergelijkingen van neutralen en ionen om het transport door convectie te beschrijven. Er werd gefocusseerd op het gedrag van gesputterde Cu-atomen, en hoe hun dichtheid en flux worden beïnvloed door de gasstroom omdat dit van groot belang is voor de toepassing van sputterdepositie.

Er werd vastgesteld dat de gasstroom niet veel effect blijkt te hebben op het dichtheidsprofiel van de Cu atomen. De gasstroom heeft nochtans een aanzienlijk effect op de Cu flux. De gasstroom draagt de Cu-atomen immers in axiale richting weg van de gasinlaat naar het open einde van de HKO toe en de flux van de Cu atomen aan het open einde van de HKO stijgt met de snelheid aan de gasinlaat. Het model voorspelt bijgevolg dat de externe gasstroom de depositieflux van gesputterde atomen zal verbeteren. Anderzijds is de uniformiteit van de flux niet veel verbeterd. Er werd vastgesteld dat de uniformiteit toch enigszins verbeterd bij lagere gasdruk wanneer de Cu atoomdichtheid niet gekarakteriseerd wordt door een uitgesproken dip in het midden. De uniformiteit kan verder verbeterd worden door de geometrie van de HKO te verbeteren, meer bepaald de

positie van de gasinlaat (bv. de gasinlaat in de vorm van een ring of een plaat met vele gaatjes in, aan de kathode bodem).

Tot slot, via de vergelijking tussen model resultaten en experimenten kan een beter inzicht verworven worden in de ontladingseigenschappen en in het relatieve belang van de verschillende productie- en verliesmechanismen. Ook kunnen de overkomstige snelheidsconstanten en cross secties bekomen worden, wat ons toelat om de toepassingen van holle kathode ontladingen te verbeteren.

Appendix

a) Publications

1. Hybrid model for a cylindrical hollow cathode discharge and comparison with experiments.
N. Baguer, A. Bogaerts and R. Gijbels, *Spectrochim. Acta Part B* **57**, 311 (2002).
2. Hollow cathode glow discharge in He: Monte- Carlo- Fluid model combined with a transport model for the metastable atoms
N. Baguer, A. Bogaerts and R. Gijbels, *J. Appl. Phys.* **93**, 47 (2003).
3. Role of the fast Ar atoms, Ar⁺ ions and metastable Ar atoms in a hollow cathode glow discharge: Study by a hybrid model.
N. Baguer, A. Bogaerts and R. Gijbels, *J. Appl. Phys.* **94**, 2212 (2003).
4. Hollow cathode discharges with gas flow: numerical modeling for the effect on the sputtered atoms and the deposition flux.
A Bogaerts, A. Okhrimovskyy, N. Baguer and R. Gijbels, *Plasma Sources Sci. Technol.* **14**, 191 (2005).
5. Study of the Ar metastable atom population in a hollow cathode discharge by means of a hybrid model and spectrometric measurements.
N. Baguer, A. Bogaerts, Z. Donko, R. Gijbels and N. Sadeghi, *J. Appl. Phys* **97**, 123305, (2005).
6. Study of the sputtered Cu atoms and Cu⁺ ions in a hollow cathode discharge by using a hybrid model.
N. Baguer and A. Bogaerts, *J. Appl. Phys* **98**, 033303, (2005).

b) Contributions at Conferences

1. Poster at I Euro-Regional Workshop on the Exploration of Low Temperature Plasma Physics, Rolduc, Netherlands, December 3-4, 1998.
2. Poster at XXIV International Conference on Phenomena in Ionized Gases, Warsaw, Poland, July 15, 1999.
3. Poster at II Euro-Regional Workshop on the Exploration of Low Temperature Plasma Physics, Rolduc, Netherlands, December 2-3, 1999.
4. Poster at Winter Conference of Plasma Spectrochemistry, Florida USA, January 13-16, 2000.
5. Poster at General Scientific meeting of the Belgian Physical Society, Louvain, May 26, 2000.
6. Poster at XV Euro-Physics Conference on Atomic and Molecular Physics of Ionized Gases, Lillafured, Hungary, August 25-29, 2000.
7. Oral presentation at NATO meeting for SFP-UV lasers (SFP-97, 1989) March 17, 2001.
8. Poster at General Scientific meeting of the Belgian Physical Society Liege, June 6, 2002.
9. Poster at V Euro-Regional Workshop on the Exploration of Low Temperature Plasma Physics, Rolduc, Netherlands November 28-29, 2002.
10. Poster at XXVI International Conference on Phenomena in Ionized Gases, Greifswald, Germany, July 12-16, 2003.

c) Scientific Visits

Research and training visit at the group of Dr. Z. Donko, at the Research Institute for Solid State Physics and Optics, Hungarian Academy of Sciences, P.O. Box 49, H-1525, Budapest, Hungary, in the framework of a joint NATO SFP project (Experiment to validate the modeling) (SFP-971989), May 28 to June 8, 2000.